

Fundamental Studies on Li Diffusion
in Materials Considered for
Battery Applications

Von der Naturwissenschaftlichen Fakultät der
Gottfried Wilhelm Leibniz Universität Hannover
zur Erlangung des Grades
Doktor der Naturwissenschaften
Dr. rer. nat.

genehmigte Dissertation

von
Dipl.-Chem. Alexander Kuhn
geboren am 16.04.1984 in Freiburg i. Br.

2012

Referent: Prof. Dr. Paul Heitjans
Korreferent: Prof. Dr. Jürgen Caro

Tag der Promotion: 07.09.2012

La lutte elle-même vers les sommets suffit à remplir un cœur d'homme.

Il faut imaginer Sisyphe heureux.

Albert Camus

Erklärung

Hierdurch erkläre ich, dass ich die vorliegende Dissertation selbständig verfasst und die benutzten Hilfsmittel und Quellen sowie die zu Hilfeleistungen herangezogenen Institutionen vollständig angegeben habe. Die Dissertation wurde nicht schon als Masterarbeit, Diplomarbeit oder andere Prüfungsarbeit verwendet.

Stuttgart, den 3. Juni 2012

Alexander Kuhn, Dipl.-Chem.

Abstract

This thesis contains fundamental studies on the Li ion dynamics in solid-state model systems which are discussed as potential materials in electrochemical applications such as Li-ion batteries: the garnet-type electrolyte $\text{Li}_7\text{La}_3\text{Zr}_2\text{O}_{12}$ (LLZ), and the Zintl phase $\text{Li}_{12}\text{Si}_7$. The Li ion dynamics occurring in these materials is thoroughly characterized over a wide dynamic range corresponding to a wide temperature range. With the help of atomic-scale nuclear methods, long-range nuclear methods, long-range non-nuclear methods, and short-range non-nuclear methods, the macroscopically observed Li transport is traced back to the single correlated ionic hop. For a higher level of understanding, the observed dynamics has to be correlated with structural features of the model systems. For this purpose, comparative studies and/or high-resolution NMR studies are used.

Li ion dynamics, solid-state NMR, impedance spectroscopy, $\text{Li}_7\text{La}_3\text{Zr}_2\text{O}_{12}$, $\text{Li}_{12}\text{Si}_7$

Zusammenfassung

Diese Dissertation beinhaltet Grundlagenstudien zur Li-Ionendynamik in Festkörpern anhand von Modellsystemen, die als potentielle Materialien für elektrochemische Anwendungen wie Li-Ionenbatterien diskutiert werden: der Elektrolyt $\text{Li}_7\text{La}_3\text{Zr}_2\text{O}_{12}$ (LLZ) mit granatähnlicher Struktur und die Zintl-Phase $\text{Li}_{12}\text{Si}_7$. Die Li-Ionendynamik in diesen Materialien wurde über einen großen dynamischen Bereich charakterisiert und auf unterschiedlichen Längen- und Zeitskalen mit nicht-nuklearen und nuklearen Methoden untersucht. Der makroskopisch beobachtete Li-Transport wird auf den elementaren korrelierten Li-Sprung zurückgeführt werden. Für ein tieferes Verständnis der Dynamik muss diese mit der Struktur der Modellsysteme korreliert werden. In diesem Zusammenhang werden vergleichende Studien sowie Hochauflösungs-NMR-Methoden herangezogen.

Li-Ionendynamik, Festkörper-NMR-Spektroskopie, Impedanzspektroskopie, $\text{Li}_7\text{La}_3\text{Zr}_2\text{O}_{12}$, $\text{Li}_{12}\text{Si}_7$

Contents

1	Introduction	1
2	Li Ion Diffusion in Solids	3
2.1	Hopping ion dynamics in solids	3
2.1.1	Diffusion in solids - theoretical background, diffusion parameters	3
2.1.2	Li-ion batteries	6
2.1.3	Fast Li-ion conductors	9
2.2	Techniques to determine diffusion parameters	11
2.2.1	Overview: techniques and their length scales and time scales	11
2.2.2	Basics of impedance spectroscopy	12
2.2.3	Basics of solid-state NMR spectroscopy	15
	Article: “NMR relaxometry as a versatile tool to study Li ion dynamics in potential battery materials”	40
3	Li Ion Dynamics in Garnet-type Li Electrolytes $\text{Li}_7\text{La}_3\text{Zr}_2\text{O}_{12}$	47
3.1	Garnet-type Li electrolytes and LLZ	47
3.2	LLZ crystallizing with tetragonal symmetry \leftrightarrow LLZ crystallizing with cubic symmetry	47
	Article: “Li self-diffusion in garnet-type $\text{Li}_7\text{La}_3\text{Zr}_2\text{O}_{12}$ as probed by diffusion-induced ^7Li spin-lattice relaxation NMR spectroscopy”	50
	Article: “Spin-alignment echo NMR: probing Li^+ hopping motion in the solid electrolyte $\text{Li}_7\text{La}_3\text{Zr}_2\text{O}_{12}$ with garnet-type tetragonal structure”	61
3.3	SFG NMR on the tetragonal LLZ	69
3.3.1	Results	69
3.3.2	Concluding remarks	70
	Article: “Li ion dynamics in Al-doped garnet-type $\text{Li}_7\text{La}_3\text{Zr}_2\text{O}_{12}$ crystallizing with cubic symmetry”	71
	Article: “Structure and dynamics of the fast lithium ion conductor $\text{Li}_7\text{La}_3\text{Zr}_2\text{O}_{12}$ ” . . .	84
3.4	Recent results on cubic LLZ	99
3.4.1	Samples	99
3.4.2	Impedance spectroscopy on LLZ14	99
3.4.3	^6Li , ^7Li NMR relaxometry and ^7Li SFG NMR on LLZ14/LLZ911	102
3.4.4	Conclusion	104
	Article: “Mechanosynthesis of solid electrolytes for lithium-ion batteries - Li^+ transport properties of garnet-type Al-doped $\text{Li}_7\text{La}_3\text{Zr}_2\text{O}_{12}$ ”	105

4	Structure and Dynamics in the Binary Zintl-type Silicide $\text{Li}_{12}\text{Si}_7$	116
4.1	The Li-Si system	116
4.2	Li dynamics in $\text{Li}_{12}\text{Si}_7$	117
4.3	Structural aspects of $\text{Li}_{12}\text{Si}_7$	118
4.4	Correlating Structure and Dynamics in $\text{Li}_{12}\text{Si}_7$	120
	Article: “Li ion Diffusion in the Anode Material $\text{Li}_{12}\text{Si}_7$: Ultrafast Quasi-1D Diffusion and Two Distinct Fast 3D Jump Processes Separately Revealed by ^7Li NMR Relaxometry”	121
	Article: “Li NMR Spectroscopy on Crystalline $\text{Li}_{12}\text{Si}_7$: Experimental Evidence for the Aromaticity of the Planar Cyclopentadienyl-Analogous Si_5^{6-} Rings”	126
	Poster: “Insight into the Li ion dynamics in $\text{Li}_{12}\text{Si}_7$: Combining PFG NMR, 1D/2D MAS NMR, and NMR relaxometry”	134
5	Conclusion	135
	Bibliography	138
	Appendix	147
A	Experimental	147
A.1	Equipment	147
A.1.1	Impedance spectroscopy measurements	147
A.1.2	NMR spectroscopy measurements	147
A.1.3	Miscellaneous	148
A.2	Pulse sequences	149
A.3	Software	150
	Curriculum Vitae	152
	List of Publications	154
	Acknowledgment	157

Chapter 1

Introduction

Understanding Li ion dynamics in solids is not only interesting from the point of view of fundamental research but also crucial for the characterization and development of new materials suitable for electrochemical devices. Hereby, new technologies require new materials; the precondition for the development of new materials is to understand existing materials and the structural properties which determine their electrochemical performance. This underlines the importance of fundamental research in the field of solid state ionics. This thesis contains fundamental studies on Li ion dynamics in ion-conducting solids of very different nature. These include purely ionic conductors - potential electrolytes in Li-ion batteries (LLZ) - and mixed ionic-electronic conductors ($\text{Li}_{12}\text{Si}_7$) which may serve as electrode materials in Li ion batteries. The studied model systems are discussed as potential materials for future battery applications.

This work should not be considered as isolated research project but it is placed in the context of prosperous developments in Li-ion research in Germany and beyond. Novel energy storage technologies are required for the transformation from economics depending on fossil energy towards a renewable-energy based economy. Hereby, Li-ion batteries are considered to play a key role, especially in the framework of electro-mobility. Governmental projects (BMBF projects: “Hochenergie-Lithiumionenbatterien (HE-Lion)”, Förderkennzeichen 03X4612N; “Steigerung der Kompetenz in der Elektrochemie für die Elektromobilität - Kompetenzverbund Nord (KVN)”, Förderkennzeichen 13N9973) have brought additional impetus into the community of solid state ionics in Germany - well beyond simple financing. New cooperations have been brought to life and networks of fundamental research, applied research and industry have been established. The cooperations within the networks have also led to new strategic partnerships between research groups in the framework of pure fundamental research and, altogether, to a more vivid scientific exchange. This is the background that made this work possible.

Understanding Li ion dynamics contains three steps: (i) a thorough structural characterization of the examined material, (ii) a characterization of the dynamic processes taking place on different time scales and length scales, and (iii), correlating structure and dynamics. Very often, point (iii) is only possible in systematic studies of a series of materials, or, if possible, with the help of high-resolution techniques. Additionally, theoretical studies may assist to understand the structure-dynamics relations.

The experimental part of this work is divided into two parts:

- Studies on various samples of the garnet-type electrolyte $\text{Li}_7\text{La}_3\text{Zr}_2\text{O}_{12}$ (LLZ). (i) LLZ crystallizing with tetragonal symmetry at room temperature provided by Prof. Dr. V. Thangadurai (University of Calgary, Canada). (ii) Al-doped cubic LLZ provided by Dr. F. Tietz (FZ Jülich, Germany) (iii) Al-doped cubic LLZ provided by Prof. Dr. J. Janek (University of Gießen, Germany), and (iv) mechanothesized Al-doped LLZ prepared by A. Düvel (University of Hannover, Germany) in a cooperation project of A. Düvel and myself. The LLZ samples were studied by ^7Li NMR relaxometry (sample (iii) also with ^6Li NMR relaxometry) and line shape analysis, impedance spectroscopy, and ^7Li SFG NMR. The structural characterization included temperature-dependent XRD, ^{27}Al MAS NMR, and IR spectroscopy. For sample (iii), under the coordination of Prof. Dr. J. Janek, various other methods for the characterization were applied. For this sample, the Li dynamics was characterized over a dynamic range of 12 orders of magnitude (from 118 K to 920 K).

The overall aim of the studies on LLZ was (a) to check the Li ion mobility in LLZ with a nuclear method for the first time and (b) to contribute to the scientific process of understanding the high Li mobility in some samples of Al-doped cubic LLZ.

- A study on the Li ion dynamics in the binary Zintl-type silicide $\text{Li}_{12}\text{Si}_7$. While in oxidic solid electrolytes like those described above, the bounding situations of Li varies only slightly (4-6 oxygen atoms as nearest neighbors) this is certainly not the case for the complex-structured Zintl-type silicide $\text{Li}_{12}\text{Si}_7$ which contains two types of Zintl-anions, Si_5^{6-} -rings and Si_4^{10-} -stars surrounded by Li ions. The different surrounding and binding situations of Li ions on different crystallographic sites result in very different mean residence times of Li ions on different sites as revealed by ^7Li NMR relaxometry and line shape analysis, 1D and 2D ^7Li and ^6Li MAS NMR, and, ^7Li PFG NMR and SFG NMR. The different electronic surrounding leads to distinct chemical shifts of the $^6,7\text{Li}$ MAS NMR lines. One of the Li sites is a Li ion sandwiched between two Si_5^{6-} -rings. The chemical shift of this Li site amounts to -17.2 ppm. This is the first experimental evidence of the aromaticity of a ring solely consisting of silicon. With the help of recently published NMR studies on structural aspects of $\text{Li}_{12}\text{Si}_7$, a consistent picture of the structure and dynamics occurring in $\text{Li}_{12}\text{Si}_7$ is obtained.

Chapter 2

Li Ion Diffusion in Solids

2.1 Hopping ion dynamics in solids

2.1.1 Diffusion in solids - theoretical background, diffusion parameters

Diffusion in solids is an ubiquitous phenomenon in nature. It most prominently becomes visible in solid state reactions (including those taking place in electrochemical devices), many solid-solid phase transitions or interdiffusion phenomena. But diffusion phenomena have an even more general background: the dynamics of atoms or ions is an equilibrium property of any material and, as such, it only depends on the external free variables of the considered thermodynamic system such as *e. g.* temperature and pressure. In the framework of this study, by dynamic processes we mean atom or ion dynamics, *i. e.* when the position of atoms or ions is subject to change with time. Atom/ion dynamics may be classified into vibration, rotation, and translation (free translation with elastic collisions or, for bound states, either tunneling or hopping processes). In this work we will define a dynamic process as a diffusive process when the limit of the respective mean square displacement for $t = \infty$ approaches infinity, *i. e.* a long-range translational process. In addition, there may exist non-diffusive translational processes which are strictly localized.

In solids, diffusive processes of ions are usually thermally activated hopping processes according to

$$\tau^{-1} = \tau_0^{-1} \cdot \exp\left(-\frac{E_A}{k_B T}\right). \quad (2.1)$$

Hereby, τ^{-1} is the hopping or jump rate, τ_0^{-1} the so-called attempt frequency, E_A is the activation energy for the jump process, k_B Boltzmann's constant, and T the absolute temperature. In order to get a rough picture of the physical meaning of the quantities determining ion dynamics in solids, τ_0^{-1} and E_A , let us consider an ion in a potential landscape such as in Fig. 2.1. Near the bottom of a well, the potential can be considered as harmonic giving rise to vibrations according to the harmonic oscillator whose eigenfrequency $\omega_0 = \sqrt{k/m}$ is defined by the ion mass m and a force constant k given by the curvature of the potential well. This vibrational eigenfrequency can be identified with the attempt frequency τ_0^{-1} in Eqn. 2.1. Indeed, for solids, the attempt frequency is expected to be in the order of phonon frequencies, *i. e.* the THz range. Experimental data pointing to considerably lower attempt frequencies are due to (i) inappropriate interpretation of data, (ii) inappropriate extrapolation of the jump rates from an extrinsic range, or (iii) a highly collective jump process.

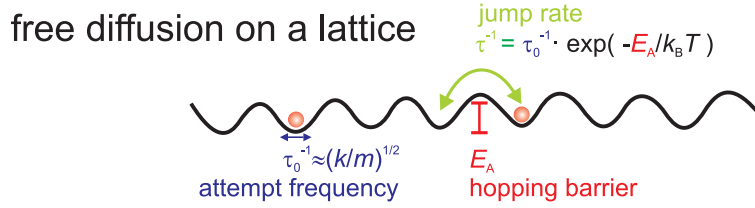


Figure 2.1: Free diffusion on a lattice: understanding the parameters determining the jump rate

defects	thermodynamically stable	metastable
1D	Frenkel and Schottky defects partially occupied site dopant atom	partially occupied site dopant atom
2D	-	grain boundary nanostructured materials dislocation
3D	solid solution	solid solution inclusion, composite material amorphous state

Table 2.1: Defects in solids I

The second relevant parameter determining the diffusion process, is the activation energy E_A . In the case of unhindered diffusion, it is simply given by the potential threshold the ion has to overcome when jumping from one potential well to the other. The Boltzmann-term in Eqn. 2.1 then is a measure of the probability that, at a given temperature T , the vibrating ion has enough thermal energy to overcome the barrier E_A . Unlike the attempt frequency, in reality, the measured activation energies for a diffusion process are regularly not equal to the hopping barrier in this simple picture. This has a simple reason: clearly, the jump will only be possible if the adjacent potential well is vacant. Therefore, the mean jump rate of the diffusing ions has to be rewritten as

$$\bar{\tau}^{-1} = \gamma \tau^{-1} \quad (2.2)$$

Hereby, γ is the probability that there is a vacancy adjacent to the ion. Eqn. 2.2 underlines the importance of defects in solid state diffusion phenomena - there is no diffusion without defects. Understanding and engineering defects, therefore, is a crucial point in designing new materials with high diffusivity. Solid state defects may be categorized into either their dimensionality (1D, 2D, and 3D) defects, or into thermodynamically stable ones and metastable ones. This is summarized in Table 2.1. Obviously, sometimes, structurally very similar systems may be either stable or metastable. However, it is the structural features which determine the ion dynamics of the material - independent of it being stable or metastable. Additionally, dopant atoms in a crystal (1D) can be considered as a solid solution (3D). Therefore we will try another categorization: Let us first consider the thermally activated defects which occur in any material above 0 K for thermodynamical reasons. A Frenkel defect is formed by a jump of an atom into a nearby interstitial. Thereby, an interstitial and a vacancy are formed. A Schottky defect occurs in ionic materials and includes the formation of vacancies (anionic and cationic) without interstitials. The first step

defect type	γ thermally activated	resists high T	stable/metastable
Frenkel, Schottky (F&S)	yes	yes	stable
partially occupied site (POS)	no	yes	both
aliovalent dopant	no (POS)	see phase diagram	both
isovalent dopant	yes (F&S)	see phase diagram	both
nanostructured materials	??	usually not	metastable
amorphous state	??	up to T_g	metastable

Table 2.2: Defects in solids II

in the formation are jumps on the surface of the material - it thus goes along with expansion of the material. Afterwards, the defects diffuse into the bulk of the crystal. But what is the driving force of the defect formation? To answer this question the defect formation reaction has to be considered, here for the example of a Frenkel defect



whereby A is the regular crystal position and I is the interstitial position. Let us consider the Gibbs free enthalpy (per number) for this reaction:

$$\Delta g_f = \Delta h_f - T\Delta s_f \quad (2.4)$$

Hereby, the defect formation enthalpy Δh_f can be estimated to be in the order of the binding energy of the given atom on the site. In ionic conductors, it is in the order of the jump barrier. It is positive in sign. Therefore, the driving force for the defect formation must be the defect formation entropy, Δs_f . Indeed, Δs_f is positive in sign, and its absolute value can be estimated from the mixing entropies of occupied and vacant site A_{vac} and A_{occ} , and of occupied and vacant interstitial I_{vac} and I_{occ} . In the framework of this simple estimation, the number of interstitial positions can be assumed to be in the same order of magnitude as the number of regular sites ($A_{\text{occ}} + A_{\text{vac}} \approx I_{\text{occ}} + I_{\text{vac}}$). Then, the mixing entropy is obtained from simple statistics:

$$S_{\text{mix}} = -k_B \left[A_{\text{occ}} \ln \frac{A_{\text{occ}}}{A_{\text{occ}} + A_{\text{vac}}} + A_{\text{vac}} \ln \frac{A_{\text{vac}}}{A_{\text{occ}} + A_{\text{vac}}} + I_{\text{occ}} \ln \frac{I_{\text{occ}}}{I_{\text{occ}} + I_{\text{vac}}} + I_{\text{vac}} \ln \frac{I_{\text{vac}}}{I_{\text{occ}} + I_{\text{vac}}} \right] \quad (2.5)$$

The fraction of vacant sites $x = A_{\text{vac}}/(A_{\text{occ}} + A_{\text{vac}}) = I_{\text{occ}}/(I_{\text{occ}} + I_{\text{vac}})$ will be very small and, as a result, $A_{\text{occ}} + A_{\text{vac}} \approx A_{\text{occ}}$ and $I_{\text{occ}} + I_{\text{vac}} \approx I_{\text{occ}}$. Therefore, Eqn 2.5 reduces to

$$S_{\text{mix}} \approx -k_B \left[A_{\text{vac}} \ln \frac{A_{\text{vac}}}{A_{\text{occ}} + A_{\text{vac}}} + I_{\text{occ}} \ln \frac{I_{\text{occ}}}{I_{\text{occ}} + I_{\text{vac}}} \right] = -2k_B x (A_{\text{occ}} + A_{\text{vac}}) \ln x \quad (2.6)$$

and the reaction entropy of the vacancy formation can be calculated as

$$\Delta s_f = \frac{\partial S_{\text{mix}}}{\partial \xi} = -2k_B \ln x \quad (2.7)$$

Hereby, ξ is the number extent of reaction for the defect formation reaction. Due to $x \ll 1$, the defect formation entropy is positive in sign. This is the thermodynamic reason for the existence of vacancies at equilibrium at any temperature above 0 K. With Eqn. 2.7, Eqn. 2.4 and the

equilibrium condition $\Delta g_f = 0$, we obtain

$$\Delta h_f = -2k_B T \ln x \quad (2.8)$$

$$x(T) = \exp(-\Delta h_f/(2k_B T)) \quad (2.9)$$

Although Eqn. 2.9 contains some simplifications, the characteristics are still maintained. The fraction of vacant sites x in systems only containing Frenkel or Schottky defects, is Arrhenius-activated. Therefore, going back to Eqn. 2.2, the effective mean hopping rate of the atoms which determines the diffusivity is given as:

$$\bar{\tau}^{-1} = \exp(-\Delta h_f/(2k_B T)) \tau^{-1} = \exp\left(-\frac{\Delta h_f}{2k_B T}\right) \tau_0^{-1} \cdot \exp\left(-\frac{E_A}{k_B T}\right) \quad (2.10)$$

with τ^{-1} being the jump rate of the vacancy (or the jump rate of the atom/ion for unhindered diffusion). For this class of materials, the activation energy measured in any diffusion experiment is a function of both the hopping barrier AND the vacancy formation enthalpy. Since τ_0^{-1} varies only slightly for different materials, we can already conclude that this class of materials will probably not contain the best ionic conductors.

On the other hand, in most superionic conductors, the sites are only partially occupied. Then, the vacancy concentration hardly depends on temperature and the measured activation enthalpy is largely dominated by the actual hopping process. In this case, the hopping process can be described with the mean hopping rate

$$\bar{\tau}^{-1} = \gamma \cdot \tau_0^{-1} \cdot \exp\left(-\frac{E_A}{k_B T}\right) \quad (2.11)$$

whereby the constant $\gamma = f(x, (1-x))$ is the effective fraction of mobile ions which does not depend on the temperature.

In a 3D isotropic medium, these activated jumps give rise to long range diffusion, described by the scalar self- or tracer diffusion coefficient via the Einstein-Smoluchowski equation:

$$D = f \cdot \frac{a^2}{6} \cdot \bar{\tau}^{-1} = f \cdot \frac{a^2}{6} \cdot \gamma \cdot \tau_0^{-1} \cdot \exp\left(-\frac{E_A}{k_B T}\right) \quad (2.12)$$

with the correlation factor f which depends on the lattice geometry and usually lies between 0.5 and 1. In non-isotropic solids (symmetry lower than cubic), the diffusion coefficient is no longer a scalar, but a 3×3 tensor. Then, the self-diffusion occurring in equilibrium is best described by Einstein's interpretation [1] of Fick's second law which connects the probability density ρ to find an ion at time t at its original site ($t = 0$) with the diffusion tensor \underline{D} :

$$\frac{\partial \rho}{\partial t} = \underline{D} \Delta \rho \quad (2.13)$$

Hereby, Δ is the Laplacian.

2.1.2 Li-ion batteries

Although Li ion batteries are not directly in the focus of this thesis, the materials studied are considered for applications in Li-ion batteries. Therefore, this important application will be presented in a brief manner that allows one to understand the requirements, materials have to meet in order to be suited as a battery material.

A Li ion battery most importantly consists of three parts, the anode, the cathode, and the electrolyte. Both anode and cathode are materials with variable Li stoichiometry and they are both electronic and ionic conductors. The Li uptake or loss reactions for the anode material A and the cathode material (B) can be written as:



When Li is inserted (intercalated) into the respective material, the valence electrons of the Li atoms occupy states in the band structure of the electron-conducting host material. Therefore, the Fermi energy E_F depends on the degree of intercalation. The Fermi energy range of an anode material lies at higher energies than that of a cathode material (cf. Fig. 2.2A and B).

Let us now consider an anode material filled with Li Li_xA (maximum E_F) and a deintercalated cathode material B (minimum E_F) (Fig. 2.2A). The potential difference (at zero current) U_0 between the two materials is the difference of the two Fermi levels E_F and determines the maximum voltage of a battery built up of these two materials. Obviously, the two materials cannot coexist in equilibrium. If the two materials are contacted, due to the difference of the Fermi levels, an electronic current will occur from the anode to the cathode leading to a charge separation. Subsequently, Li ions will diffuse from the anode to the cathode in order to compensate for the negative charge transported to the cathode by the electronic current.¹

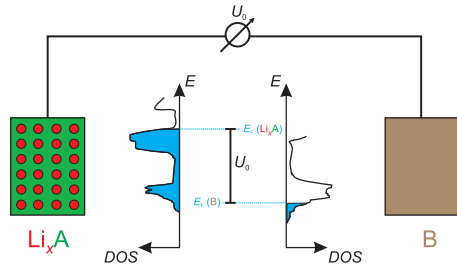
So, if anode and cathode material are simply contacted the system will equilibrate simply by dissipating thermal energy. Now, a battery contains a third component which allows the energy to be used as electric energy: the electrolyte. The electrolyte separates anode and cathode (see Fig. 2.2E and F). It is an ionic conductor and an electronic insulator. Then, if the anode and cathode are, additionally, contacted via an electronic conductor and ionic insulator, the electronic current and the ionic current are perfectly separated. The electronic current (outside the battery) is used to power devices, the ionic current occurs in the battery to account for the charge compensation. In sum, Li atoms are transported from the anode to the cathode.

In rechargeable batteries, the process can be reversed by applying a reversed voltage (a little higher than the voltage of the charged battery). Effectively, this shifts the energy of the electronic band structure of the cathode to a higher level and that of the anode to a lower level such that the Fermi niveau of the cathode (discharged state) is higher than that of the anode (see Fig. 2.2C). As a result, an electronic current occurs from the cathode to the anode - followed by an ionic current from the anode to the cathode until the Fermi levels are balanced again (see Fig. 2.2D and F). When the charging voltage is disconnected, anode and cathode are in the original, charged state (Fig. 2.2A and E).

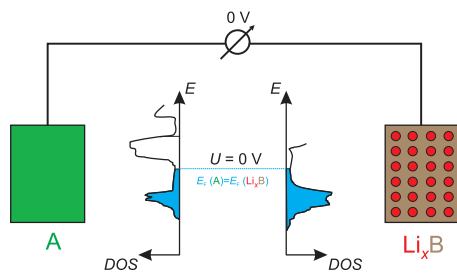
The most important requirements for anode, cathode and electrolyte materials are summarized in table 2.3. Hereby, the third row, the density of states (DOS) at Fermi level requires some extra discussion. For the electrolyte, the large band gap above the Fermi level (=filled band) simply is

¹usually, the electronic mobility is higher than the ionic one. Otherwise, due to the chemical potential gradient, Li would diffuse to the cathode, followed by an electronic current to compensate for the charge. The effects of the chemical potential of Li and the electric potential may be summarized with one physical quantity, the electrochemical potential of Li. Indeed, more precisely, the voltage of a battery is the difference between the two electrochemical potentials of the anode and cathode material. In equilibrium, the electrochemical potential of anode and cathode material is equal. For the sake of clarity, Fig. 2.2 concentrates on the electronic potential, only.

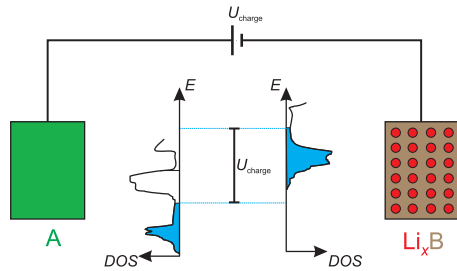
(A) anode and cathode material in the charged state



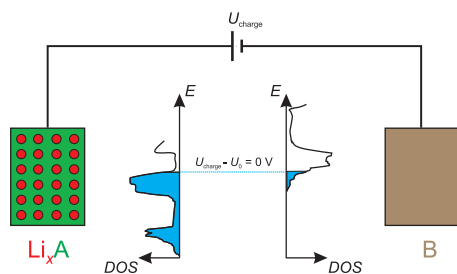
(B) anode and cathode material in the discharged state



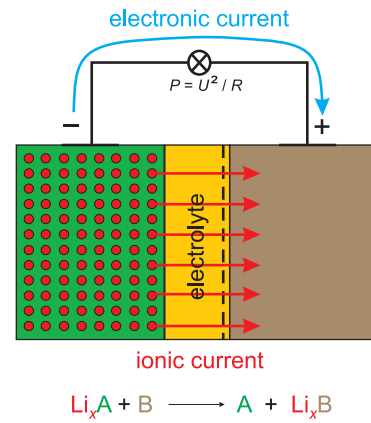
(C) anode and cathode material in the discharged state charging voltage applied



(D) anode and cathode material in the charged state charging voltage still applied



(E) discharging the battery



(F) charging the battery

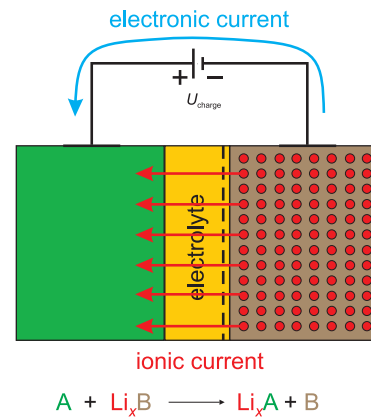


Figure 2.2: A-B: schematic picture of the electronic properties of charged and discharged anode and cathode material. Both cathode and anode material have a high density of states (DOS) in the working regime of the battery. The working regime of the anode is at higher E than the one of the cathode. C-D: shifting the energy of the electronic states by applying an external voltage as background for the recharging process. E-F: Basic principle of a rechargeable Li ion battery.

	Li stoichiometry	DOS	conductivity
anode	variable	high below E_F	mixed
cathode	variable	high above E_F	mixed
electrolyte	fixed	large band gap above E_F	purely ionic $>10^{-3}$ S/cm

Table 2.3: Requirements for Li ion battery materials

the requirement for an electronic insulator even if contacted between anode and cathode (=large electrochemical window). The unoccupied band (or LUMO) should lie at higher energies than the Fermi level of the anode in the charged state in order to prevent reduction of the electrolyte; the valence band (or HOMO) of the electrolyte should lie at lower energies than the Fermi level of cathode in the charged state in order to prevent oxidation of the electrolyte.² For anode and cathode materials, which need to be electronic conductors, clearly, the Fermi level is in a band. For a charged battery, the Fermi level of the anode is above a region with very high DOS, while the Fermi level of the cathode in the charged state is below such a region. The high DOS of both cathode and anode in the working regime of the battery guarantees that the battery has a nearly constant voltage in the working regime (see Fig. 2.2A-D).

2.1.3 Fast Li-ion conductors

As mentioned above, Li electrolytes suitable for battery applications have to meet several requirements, the most important ones being (i) high room-temperature (RT) ionic conductivity ($>10^{-3}$ S/cm), (ii) negligible electronic conductivity (iii) large electrochemical window resulting in stability in contact with both anode and cathode materials. The solid-state electrolytes reported so far don't meet all requirements sufficiently well.

In the literature, many reviews on fast Li-ion conductors are found. Therefore I will not add another complete review, here, but refer to Refs. [2–9]. Fig. 2.3 shows the conductivity Arrhenius plots of a selection of electrolytes.

The fastest Li solid electrolytes known so far are phospho-sulfides of both amorphous and crystalline nature (see Ref. [10] and references therein). Some of these solid electrolytes have been applied in all-solid state batteries already. [11] The Li mobility is often higher in sulfidic compounds than in similar oxidic ones. This may be explained by (i) the higher polarizability of S and (ii) by the lower binding energy of Li and S.

H-doped Li_3N is known as a good solid electrolyte but it reacts with metallic Li. [12] The electrochemical window is too small for battery applications.

Heavily doped rocksalt-structured lithium chlorides and bromides are also very good Li ion conductors in their high-temperature modification. [3, 4, 17]

The oxidic solid electrolytes shown here can be classified into the following sub-categories: (i) LISICON electrolytes with the $\gamma\text{-Li}_3\text{PO}_4$ or the related Li_4SiO_4 structure [2, 4, 22–24] (ii) perovskite-structured oxides [6, 14], (iii) Li_2SO_4 , and related phases [13, 25] and, (iv) garnet-type solid electrolytes [7, 18, 20, 21, 26].

²This would require band gaps of >4 eV for high-energy cells, a value that is hardly achievable and not possible for organic-polymeric electrolytes. In reality, it will be sufficient to have kinetic hindering of the reduction.

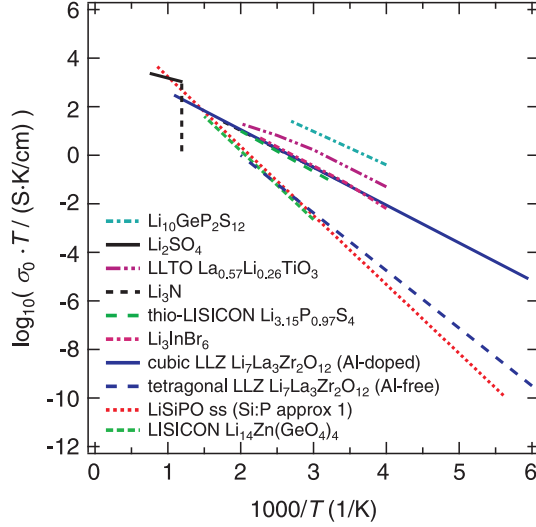


Figure 2.3: Conductivities of a selection of Li electrolytes: $\text{Li}_{10}\text{GeP}_2\text{S}_{12}$ [10], Li_2SO_4 [13], LLTO [14], Li_3N [15], thio-LISICON, [16], Li_3InBr_6 [17], Al-doped cubic LLZ [18, 19], tetragonal LLZ [20, 21], LiSiPO ss this study and [22, 23], LISICON [24]. See text for discussion.

There seems to be a general "magic" limit of the conductivity in the oxidic Li ion conductors. This "magic" limit is given by LiSiPO [22, 23], LISICON [24], undoped LLZ [20, 21] and many other systems not shown here for the sake of clarity (see the above-mentioned review articles). The conductivity is roughly characterized by an activation energy of 0.5 eV and a prefactor of the Arrhenius law being in accordance with typical phonon frequencies. All these ion conductors share the two structural features: a closest packing of oxygen atoms (or a very similar one) and stoichiometric Li vacancies or readily available interstitials. Thus, this limit might represent correlated dynamics of Li ions through an intact regular oxygen lattice with an extrinsic, nearly temperature-independent concentration of effectively mobile Li.

The LLTO oxidic electrolytes which are characterized by a higher Li conductivity, show oxygen deficiencies and clearly have strong distortions in the oxygen sublattice, thus making the different diffusivity understandable. The higher conductivity in Al-doped LLZ [18, 19, 27, 28] seems to have a similar reason - as pointed out in this study. The Al-doping directly affects the garnet network and most probably leads to considerable distortion of the oxygen sublattice. Whether oxygen vacancies play a role or not still remains unclear. Al-doped LLZ has been successfully applied in prototype all-solid-state batteries. [29–32]. An all-solid-state battery using Nb-doped LLZ [33] showed an interfacial resistance comparable with liquid organic electrolytes and good cycling performance. [34] The high conductivity in the high-temperature phase Li_2SO_4 seems to be connected with rotations of the sulfate ion which facilitates the Li jumps. Similar behavior is found in Na_3PO_4 [25] and LiBH_4 [35, 36].

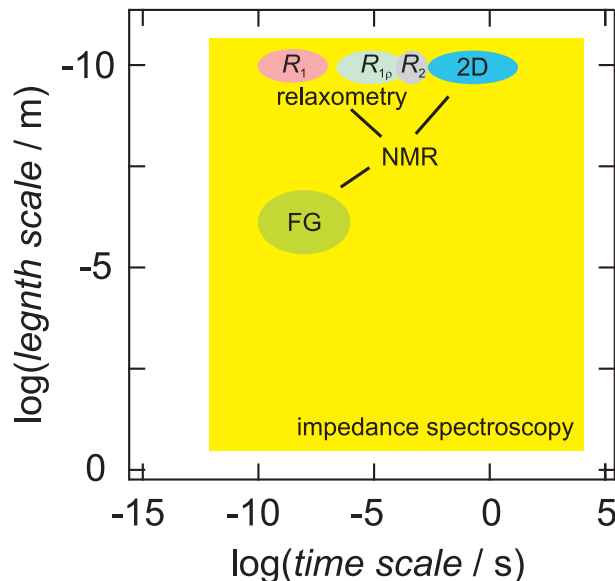


Figure 2.4: Time scales and length scales of experimental techniques capable of determining hopping ion dynamics in Li conductors. For a better readability, only the techniques used in this work are included into the graph. See text for other available techniques. The yellow box for impedance spectroscopy is explained further in the text.

2.2 Techniques to determine diffusion parameters

2.2.1 Overview: techniques and their length scales and time scales

Most generally, any measurement goes along with a perturbation of the system to be measured. Therefore, it is not possible to truly study equilibrium. However, Linear Response Theory [37,38] provides the theoretical foundation for the characterization of equilibrium dynamics via the response of a dynamic system to a small perturbation. There are many techniques available for the measurement of atom/ion dynamics. It is sensible to classify these into time scales and length scales they are sensitive to. Fig. 2.4 provides such an overview for the techniques used in this work. The graph should be read in the following way:

NMR relaxometry is sensitive to motions on the atomic length scale. NMR spin-lattice relaxation rate R_1 measurements are sensitive to very fast motion with jump rates in the order of $\tau^{-1} = 10^{10} \dots 10^7 \text{ s}^{-1}$. $R_{1\rho}$ stands for NMR spin-lattice relaxation in the rotating frame, R_2 for NMR spin-spin relaxation. The whole range of NMR relaxometry can also be covered by (i) β -NMR [39–46] and (ii) field-cycling NMR [47, 48] (not shown for the sake of clarity). 2D (and nD) NMR techniques (including 2D exchange NMR, spin-alignment echo (SAE) NMR, and many others) are sensitive to much slower dynamics occurring on a time scale determined by the second or third dimension in the pulse sequence. These techniques usually do not provide information on the length scale of the underlying dynamics. Again, only NMR frequencies (which do not contain spatial information) are correlated. Another technique being sensitive to the atomic length scale is quasi-elastic neutron scattering (also not shown) which is sensitive to a similar time-scale like NMR R_1 . From all these techniques, it is not possible to tell whether the observed dynamics give rise to a long-range diffusive transport. Therefore, it is necessary to use long-range techniques such as tracer

techniques. Since there is no suitable radioactive tracer for Li, the radioactive tracer method is not applicable. Instead, (i) field-gradient NMR methods, or (ii) secondary ion mass spectroscopy (SIMS) [49] or laser ablation mass spectroscopy with ${}^6\text{Li}$ - ${}^7\text{Li}$ diffusion couples [50] can be used. Additionally, dc-conductivity can be used to determine long-range transport.

The yellow box for impedance spectroscopy requires some explanation: Although impedance spectroscopy is indeed sensitive to motions on very short and very long length and time scales, it is only possible to extract the information on the time scale from the measurement without further assumptions.

Clearly, understanding ion dynamics means to understand it from the single (correlated) hop to the long-range dynamics measured in tracer-like diffusion experiments. Therefore, any fundamental study on the ion dynamics must contain both short-range methods which are necessary to study the single hop, and long-range methods which characterize the diffusion the successful single hops give rise to.

2.2.2 Basics of impedance spectroscopy

Impedance spectroscopy (IS) is one of the most simple and direct techniques to obtain information on ion dynamics in ionic conductors given that their electronic conductivity is negligible. It can be understood as an extension of dc conductivity measurements to non-zero frequencies. This allows one to study the dynamics of charges even in absence of long-range conductivity. The principle of the measurement is outlined in Fig. 2.5.

An alternating voltage $U(t) = U_0 \cdot \exp(i\omega t)$ is applied to the sample studied. This results in an alternating current $I(t) = I_0 \cdot \exp(i\omega t - i\varphi)$ with φ being the phase angle between current and voltage. Although there are different technical possibilities to build an impedance spectrometer (impedance bridge, capacitance bridge) with different primary quantities measured, always the same information is available. This information may be derived into several commonly used complex quantities. The complex admittance Y^* is defined as

$$Y^* = \frac{I_0 \cdot \exp(i\omega t - i\varphi)}{U(t) = U_0 \cdot \exp(i\omega t)} = |Y| \cdot \exp(-i\varphi) = Y' + Y'' \quad (2.16)$$

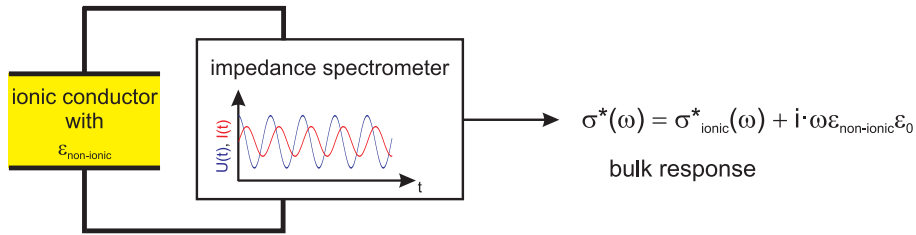


Figure 2.5: Principle of the impedance spectroscopy measurement of ionic conductors. The ionic conductor is contacted with (usually ion-blocking) electronically conducting electrodes. Two contributions are measured in parallel: the capacitor made up by the electrodes and filled with a dielectric medium characterized by the permittivity $\epsilon_{\text{non-ionic}}$. Additionally, ion dynamics occurring in the sample give rise to a dielectric answer.

The respective normalized quantity is the conductivity σ^* . For a parallelepiped it is given as:

$$\sigma^* = Y^* \cdot \frac{d}{A} \quad (2.17)$$

with A being the area of the parallelepiped and d being the thickness.

Three other representations are commonly used: the complex resistivity

$$\rho^* = \frac{1}{\sigma^*} \quad (2.18)$$

(or the non-normalized complex impedance $Z^* = \frac{1}{Y^*}$), the complex dielectric constant (or permittivity)

$$\epsilon^* = \frac{\sigma^*}{i\omega\epsilon_0}, \quad (2.19)$$

and the electric modulus

$$M^* = \frac{1}{\epsilon^*} = \rho^* \cdot i\omega\epsilon_0. \quad (2.20)$$

Which representation is the most suitable one for the analysis of data depends on the system studied. For ionic conductors, there is a clear preference to use the complex conductivity or permittivity - simply because here, non-ionic effects only give rise to additive effects: it is intrinsic to the method of impedance spectroscopy that in parallel to the ionic contribution non-ionic contributions to the bulk permittivity affect the total dielectric response.

$$\sigma^* = \sigma_{\text{ionic}}^* + i\omega\epsilon'_{\text{non-ionic}}\epsilon'_v \quad (2.21)$$

Hereby, "ionic" means contributions due to ionic hopping, "non-ionic" includes *e. g.* ionic vibration and electronic excitation. σ_{hop}^* should not be mixed up with the definition of the conductivity σ^* above - it will be defined below. For this purpose, it is necessary to introduce the complex susceptibility χ^*

$$\chi^* = \epsilon^* - 1 = \chi_{\text{ionic}}^* + (\epsilon_{\text{non-ionic}}^* - 1) \quad (2.22)$$

Now, σ_{ionic}^* is related to χ_{ionic}^* :

$$\sigma_{\text{ionic}}^* = i\omega\epsilon_0 \cdot \chi_{\text{ionic}}^* \quad (2.23)$$

The real part χ'_{ionic} and the imaginary part χ''_{ionic} of the complex susceptibility reflect the part of the electric field energy stored and lost per cycle in radians due to the ion dynamics. The two quantities are not independent, but coupled via the Kramers-Kronig (KK) relation. [51]:

$$\chi''_{\text{ionic}}(\omega) = -\frac{2\omega}{\pi} P \int_0^\infty \frac{\chi'_{\text{hop}}(\omega')}{\omega'^2 - \omega^2} d\omega' \quad (2.24)$$

$$\chi'_{\text{ionic}}(\omega) = \frac{2}{\pi} P \int_0^\infty \frac{\omega' \chi''_{\text{hop}}(\omega')}{\omega'^2 - \omega^2} d\omega' \quad (2.25)$$

whereby P is the principle value of the integral. These Kramers-Kronig relations, naturally, also couple σ'_{ionic} and σ''_{ionic} . The quantity measured in impedance spectroscopy, however, is σ^* which is related to ϵ^* . However, if the dielectric answer is simply given by the ionic response and a frequency independent $\epsilon_{\text{non-ionic}}^*$ which only appears in σ'' , not in σ' , we get the important result:

$$\sigma' = \sigma'_{\text{ionic}} \quad (2.26)$$

$$\epsilon' = \chi'_{\text{ionic}} + \epsilon'_{\text{non-ionic}} \quad (2.27)$$

Concluding, the real part of the conductivity σ' contains the complete information on the ion dynamics (unless covered by other effects). In real situations, however, the impedance data is influenced by further effects such as: electrode polarization effects, grain boundary impedance effects, possibly additional purely dielectric responses, etc. Therefore, in order to extract the ionic bulk properties, it is necessary to look at the whole complex data set, *e. g.* in terms of σ' and ϵ' . The disadvantages of the ρ^* and M^* representations have been discussed in the literature, see *e. g.* Roling *et al.* [52]: in these representations, non-ionic and ionic effects are mixed and, thus, the graphical inspection of the data may be misleading. Nevertheless, by including the non-ionic parameters - which can easily be extracted from the data, the data can be fitted, too. This regression must (since the inversion is a conservative mathematical procedure) yield the same results as in the non-inverted levels within the errors of the fit (*cf.* Macdonald *et al.* [53]). However, this data does not contain additional information on the ion dynamics that would not be obtained from the conductivity level.

2.2.3 Basics of solid-state NMR spectroscopy

(i) Angular momentum in quantum mechanics and nuclear spin

The nuclear spin \hat{I} is a basic property of nuclei like *e. g.* mass or charge.³ The spin is the quantum-mechanical analogue of the classical intrinsic angular momentum. Other angular momenta in quantum mechanics like the orbital angular momentum and molecular rotations follow the same equations which will be outlined in this section. The treatment of the angular momentum in quantum mechanics provides the information necessary to understand the most basic principles in chemistry, from the periodic table of elements to chemical bonding, from spectroscopy to statistical thermodynamics.

In classic physics, the angular momentum is given as

$$\vec{l} = \vec{r} \times \vec{p} \quad (2.28)$$

Using the definition of the vector product, the following components are obtained:

$$\vec{l}_x = \vec{e}_x (\vec{y} \cdot \vec{p}_z - \vec{z} \cdot \vec{p}_y) \quad (2.29)$$

$$\vec{l}_y = \vec{e}_y (\vec{z} \cdot \vec{p}_x - \vec{x} \cdot \vec{p}_z) \quad (2.30)$$

$$\vec{l}_z = \vec{e}_z (\vec{x} \cdot \vec{p}_y - \vec{y} \cdot \vec{p}_x) \quad (2.31)$$

$$\vec{l}^2 = \vec{l}_x^2 + \vec{l}_y^2 + \vec{l}_z^2; \quad |\vec{l}| = \sqrt{\vec{l}^2} \quad (2.32)$$

In quantum mechanics, the quantities are described by operators. The space coordinates are simply product operators $x \cdot$ and the operator for the momentum is $p_x = \frac{\hbar}{i} \frac{\partial}{\partial x}$:

$$\hat{l}_x = \frac{\hbar}{i} \left(\hat{y} \frac{\partial}{\partial z} - \hat{z} \frac{\partial}{\partial y} \right) \quad (2.33)$$

$$\hat{l}_y = \frac{\hbar}{i} \left(\hat{z} \frac{\partial}{\partial x} - \hat{x} \frac{\partial}{\partial z} \right) \quad (2.34)$$

$$\hat{l}_z = \frac{\hbar}{i} \left(\hat{x} \frac{\partial}{\partial y} - \hat{y} \frac{\partial}{\partial x} \right) \quad (2.35)$$

$$\hat{l}^2 = \hat{l}_x^2 + \hat{l}_y^2 + \hat{l}_z^2 \quad (2.36)$$

The unit of the angular momentum is the one of $[\hbar]=\text{Js}$. In practical use in the framework of NMR theory, however, it is very useful to define a new set of operators without \hbar .⁴ The nuclear spin operators are then defined as

$$\hat{I}_x = \frac{1}{i} \left(\hat{y} \frac{\partial}{\partial z} - \hat{z} \frac{\partial}{\partial y} \right) \quad (2.37)$$

$$\hat{I}_y = \frac{1}{i} \left(\hat{z} \frac{\partial}{\partial x} - \hat{x} \frac{\partial}{\partial z} \right) \quad (2.38)$$

$$\hat{I}_z = \frac{1}{i} \left(\hat{x} \frac{\partial}{\partial y} - \hat{y} \frac{\partial}{\partial x} \right) \quad (2.39)$$

$$\hat{I}^2 = \hat{I}_x^2 + \hat{I}_y^2 + \hat{I}_z^2 \quad (2.40)$$

³Great parts of the NMR basics were taken from Ref. [54] - corrected and adjusted where necessary. Additionally, the well-known textbooks Refs. [55–59] have been used. For a closed introduction into the treatment of angular momenta in quantum mechanics with the help of group theory and irreducible tensor operators see Refs. [60–64]

⁴In atomic units, $\hbar = 1$ anyway. However, in NMR theory, atomic units are not commonly used. Usually, the Hamiltonians are given in frequency units (rad/s) and the \hbar is introduced into the Hamiltonians and equations as prefactors to compensate for the missing \hbar in the definition of \hat{I} .

The advantage of this definition is that this set of operators can be used to describe rotations in spin space. The operators have the following commutators:

$$[\hat{I}_x, \hat{I}_y] = i\hat{I}_z \quad (2.41)$$

$$[\hat{I}_y, \hat{I}_z] = i\hat{I}_x \quad (2.42)$$

$$[\hat{I}_z, \hat{I}_x] = i\hat{I}_y \quad (2.43)$$

$$[\hat{I}_x, \hat{I}^2] = 0 \quad (2.44)$$

$$[\hat{I}_y, \hat{I}^2] = 0 \quad (2.45)$$

$$[\hat{I}_z, \hat{I}^2] = 0 \quad (2.46)$$

As the components of the spin do not commute, only its absolute value and one component are determined while the other two components carry quantum-mechanical uncertainty.

It is useful to define the step operators

$$\hat{I}_+ = \hat{I}_x + i\hat{I}_y \quad (2.47)$$

$$\hat{I}_- = \hat{I}_x - i\hat{I}_y \quad (2.48)$$

with the commutators

$$[\hat{I}_z, \hat{I}_+] = \hat{I}_+ \quad (2.49)$$

$$[\hat{I}_z, \hat{I}_-] = -\hat{I}_- \quad (2.50)$$

$$[\hat{I}^2, \hat{I}_+] = 0 \quad (2.51)$$

$$[\hat{I}^2, \hat{I}_-] = 0 \quad (2.52)$$

The product of the step-up and step-down operators is Hermitian:

$$\hat{I}_- \hat{I}_+ = \hat{I}_x^2 + \hat{I}_y^2 - \hat{I}_z = \hat{I}^2 - \hat{I}_z^2 - \hat{I}_z \quad (2.53)$$

$$\hat{I}_+ \hat{I}_- = \hat{I}_x^2 + \hat{I}_y^2 + \hat{I}_z = \hat{I}^2 - \hat{I}_z^2 + \hat{I}_z \quad (2.54)$$

With these definition, all basic properties of the spin operators, all important properties can be deduced. Let $|I, m\rangle$ be a normalized eigenfunction (EF) of \hat{I}^2 and \hat{I}_z . The expectation values are defined as

$$\rightarrow \langle I, m | \hat{I}^2 | I, m \rangle = \lambda \geq 0 \quad (2.55)$$

$$\langle I, m | \hat{I}_z | I, m \rangle = m \quad (2.56)$$

Hereby, λ and m are simply parameters which will be characterized more accurately below. λ is the eigenvalue (EV) of a squared Hermitian operator. It is real and positive since Hermitian operators have real eigenvalues. Since \hat{I}_z is a component of \hat{I} , it follows:

$$\langle I, m | \hat{I}^2 - \hat{I}_z^2 | I, m \rangle = \lambda - m^2 \geq 0 \quad (2.57)$$

$$\rightarrow \lambda \geq m^2 \quad (2.58)$$

Thus, the maximum value of $|m|$ is limited by λ . As a next step the effect of the step-up operator on the EF is examined. Therefore, the above-given commutators will be used.

$$\hat{I}^2 \hat{I}_+ | I, m \rangle = \hat{I}_+ \hat{I}^2 | I, m \rangle = \lambda \hat{I}_+ | I, m \rangle \quad (2.59)$$

The step-up operator \hat{I}_+ commutes with \hat{I}^2 and therefore generates a new EF $\hat{I}_+ |I, m\rangle$ of \hat{I}^2 with the same EV λ . On the other hand, \hat{I}_+ does not commute with \hat{I}_z . Nevertheless, $\hat{I}_+ |I, m\rangle$ has to be an eigenfunction also of \hat{I}_z because of $[\hat{I}_z, \hat{I}^2] = 0$. Using the commutator $[\hat{I}_z, \hat{I}_+] = \hat{I}_+$, the EV of \hat{I}_z of the EF $\hat{I}_+ |I, m\rangle$ can be easily deduced:

$$\hat{I}_z \hat{I}_+ |I, m\rangle = \hat{I}_+ \hat{I}_z |I, m\rangle + \hat{I}_+ |I, m\rangle = (m+1) \hat{I}_+ |I, m\rangle \quad (2.60)$$

As expected, $\hat{I}_+ |I, m\rangle$ is an EF of \hat{I}_z but with an EV increased by 1. The effect of \hat{I}_+ on $|I, m\rangle$ can be summarized as:

$$\hat{I}_+ |I, m\rangle = c_+ |l, m+1\rangle \quad (2.61)$$

For the step-down operator, we obtain, respectively

$$\hat{I}_- |I, m\rangle = c_- |l, m-1\rangle \quad (2.62)$$

Due to $m^2 \leq \lambda$, there must be a maximum and minimum value $m_{\max} = -m_{\min}$. Therefore, applying the step-up operator to the EF $|l, m_{\max}\rangle$ must yield zero:

$$\hat{I}_+ |I, m_{\max}\rangle = 0 \quad (2.63)$$

$$\hat{I}_- |I, m_{\min}\rangle = 0 \quad (2.64)$$

Applying the step-down operator \hat{I}_- on $\hat{I}_+ |I, m_{\max}\rangle$ must still be zero:

$$\hat{I}_- \hat{I}_+ |I, m_{\max}\rangle = 0 \quad (2.65)$$

As shown above, the product of step-down and step-up operators is a Hermitian operator:

$$\hat{I}_- \hat{I}_+ = \hat{I}_x^2 + \hat{I}_y^2 - \hat{I}_z = \hat{I}^2 - \hat{I}_z^2 - \hat{I}_z \quad (2.66)$$

From Eqns. 2.65 and 2.66 follows:

$$(\hat{I}^2 - \hat{I}_z^2 - \hat{I}_z) |I, m_{\max}\rangle = 0 \quad (2.67)$$

$$\rightarrow (\lambda - m_{\max}^2 - m_{\max}) |l, m_{\max}\rangle = 0 \quad (2.68)$$

$$\rightarrow \lambda - m_{\max}^2 - m_{\max} = 0 \quad (2.69)$$

$$\rightarrow \lambda = m_{\max}(m_{\max} + 1) \quad (2.70)$$

Accordingly, for the lower limit, one obtains:

$$\lambda = m_{\min}(m_{\min} - 1) \quad (2.71)$$

Now, we define the spin quantum number I as:

$$I = m_{\max} = -m_{\min} \quad (2.72)$$

The EV's (= expectation value, since the EF's were defined to be normalized) of the nuclear spin operators \hat{I}^2 and \hat{I}_z are, thus, given as:

$$\hat{I}^2 |I, m\rangle = I(I+1) |I, m\rangle \quad (2.73)$$

$$\hat{I}_z |I, m\rangle = m |I, m\rangle \quad (2.74)$$

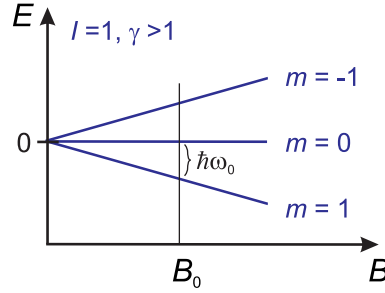


Figure 2.6: Zeeman splitting of an $I = 1$ -nucleus with positive γ .

For simple reasons of symmetry, I is integer or half-integer; m assumes values of $-I, (-I+1) \dots (I-1), I$. These are the most fundamental properties of angular momenta in quantum mechanics and suffice *e. g.* to explain the periodic table of elements or the H-atom emission spectrum.

The nuclear spin quantum number I depends on the number of neutrons and protons of the nuclei and on the nuclear state. In NMR, only the nuclear ground state is of any importance. Therefore, I can be considered as an isotope-specific constant for most practical uses.

(ii) Interaction of an isolated nuclear spin with an external magnetic field

Since the nucleus is not a point charge, the nuclear spin goes along with a magnetic moment $\hat{\mu}$

$$\hat{\mu} = \gamma \cdot \hat{I} \quad (2.75)$$

whereby γ is an isotopic constant (again, only for the nuclear ground state). The Hamiltonian describing the interaction between the magnetic moment $\hat{\mu}$ and an external magnetic field B_0 in frequency units is - in complete analogy to the classical interaction energy of a magnetic moment and an external field - given as:

$$\hat{H} = -\hat{\mu} \cdot \underline{B}_0 = -\gamma \cdot \hat{I} \cdot \underline{B}_0 \quad (2.76)$$

With the static field (by definition) aligned in the z -direction, Eqn. 2.76 reduces to:

$$\hat{H} = -\gamma \cdot \hat{I}_z \cdot B_0 \quad (2.77)$$

Accordingly, the expectation values of the energy are given as

$$\langle I, m | \hat{H} | I, m \rangle = -\gamma m B_0 \quad (2.78)$$

In the absence of an external field, the spin states are degenerate. In the presence of an external field, the so-called Zeeman states have different energies. Two adjacent Zeeman states are separated by

$$\omega_0 = \gamma B_0 \quad (2.79)$$

ω_0 is called the Larmor frequency. The Zeeman splitting energy in Joule is, accordingly, $\hbar\omega_0$. This situation is depicted in Fig. 2.6

(iii) The density operator

The density operator is of central importance for understanding the outcome of NMR experiments. Therefore, I will give a short introduction into the nuclear spin density operator.

In a canonical ensemble of spins, the probability of finding a spin in the state $|m\rangle$ (I will be left out from here on since it is constant for a given nucleus) corresponds to Boltzmann's distribution:

$$p_m = \frac{\exp(-\frac{E_m}{k_B T})}{\sum_n \exp(-\frac{E_n}{k_B T})} = \frac{\exp(-\frac{E_m}{k_B T})}{Z} \approx \frac{1 + \frac{E_m}{k_B T}}{Z} \quad (2.80)$$

Thus, one EF is not sufficient to describe a spin in a canonical ensemble. Rather, it is necessary to define a superposition state Ψ

$$\Psi = \sum_m \sqrt{p_m} |m\rangle \quad (2.81)$$

Ψ is the quantum-mechanical wave function describing the canonical ensemble of, so far, non-interacting spins in thermal equilibrium in a complete manner. Non-equilibrium states are included in the more general definition

$$\Psi = \sum_m c_m |m\rangle \quad (2.82)$$

As usual, the expectation value of an operator \hat{A} is given as

$$\langle \hat{A} \rangle = \langle \Psi | \hat{A} | \Psi \rangle \quad (2.83)$$

The orthonormalized spin eigenfunctions $|m\rangle$ (for a fixed spin quantum number I) form an orthonormal basis of the spin space. Like for any complete set of basis functions, the following completeness relation holds:

$$\sum_m |m\rangle \langle m| = \hat{1} \quad (2.84)$$

Twice including Eqn. 2.84 into Eqn. 2.83 yields:

$$\langle \hat{A} \rangle = \sum_{mn} \langle \Psi | m \rangle \langle m | \hat{A} | n \rangle \langle n | \Psi \rangle \quad (2.85)$$

$$\langle \hat{A} \rangle = \sum_{mn} c_m^* A_{mn} c_n \quad (2.86)$$

Hereby, for the second step Eqn. 2.82 was used. Now, Eqn. 2.86 is the matrix formulation of Eqn. 2.83:

$$\langle \hat{A} \rangle = \underline{c}^* \underline{A} \underline{c} \quad (2.87)$$

The matrix \underline{A} is the projection of the abstract operator \hat{A} into the basis of the spin EF's. The eigenvector \underline{c} is the projection of Ψ into the the basis of the spin EF's. Now the (probability) density operator $\hat{\rho}$ is defined as the outer product of the abstract superposition state Ψ :

$$\hat{\rho} = |\Psi\rangle \langle \Psi| \quad (2.88)$$

The vector components of the projection of $\hat{\rho}$ into the basis of the spin EF's are:

$$\rho_{nm} = \langle n | \Psi \rangle \langle \Psi | m \rangle = c_n c_m^* \quad (2.89)$$

Now, clearly, Eqn. 2.86 can be reformulated:

$$\langle \hat{A} \rangle = \sum_{mn} A_{mn} \rho_{nm} = \text{Tr}(\underline{\underline{A}} \underline{\underline{\rho}}) = \text{Tr}(\hat{A} \hat{\rho}) \quad (2.90)$$

The density operator completely describes the canonical ensemble of spins - in a similar fashion as the superposition state Ψ . The time-dependent Schrödinger equation which describes the evolution of Ψ relates to the Liouville-von Neumann equation which describes the evolution of the density matrix operator:

$$\frac{\partial \hat{\rho}}{\partial t} = i[\hat{\rho}, \hat{H}] \quad (2.91)$$

For a time-independent Hamiltonian \hat{H} , the following simple general solution is given:

$$\hat{\rho}(t) = e^{-i\hat{H}t} \hat{\rho}(0) e^{i\hat{H}t} \quad (2.92)$$

For time-dependent Hamiltonians, two main procedures are typically used to solve the Liouville-von Neumann equation: (i) A unitarian axis transformation into a time-dependent coordinate system (*e.g.* a rotating frame) in which the Hamiltonian is no longer time-dependent. If this procedure still leaves us with time-dependencies, (ii) average Hamiltonian theory can be applied: Hereby, the time-dependent (*e.g.* rotating-frame) Hamiltonian is developed as a Magnus expansion of time-independent Hamiltonians.⁵ The first-order average Hamiltonian is simply the mean Hamiltonian considered time interval (*e.g.* Larmor precession period), the higher order terms in the Magnus expansion contain n^{th} order commutators of the Hamiltonians acting on the spin system at different times. The averaged commutators, then, yield the higher-order average Hamiltonians.

(iv) Density operator of an ensemble of non-interacting $I = 1/2$ -nuclei in equilibrium

For non-interacting $I=1/2$ -nuclei, the two EF's $|\alpha\rangle$ and $|\beta\rangle$ span the spin space which conclusively can be described as a 2x2 matrix. Accordingly, the spin operators are

$$\hat{I}_x = \frac{1}{2} \begin{pmatrix} 0 & 1 \\ 1 & 0 \end{pmatrix} \quad (2.93)$$

$$\hat{I}_y = \frac{1}{2i} \begin{pmatrix} 0 & 1 \\ -1 & 0 \end{pmatrix} \quad (2.94)$$

$$\hat{I}_z = \frac{1}{2} \begin{pmatrix} 1 & 0 \\ 0 & -1 \end{pmatrix} \quad (2.95)$$

and the step operators are

$$\hat{I}_+ = |\alpha\rangle\langle\beta| = \begin{pmatrix} 0 & 1 \\ 0 & 0 \end{pmatrix} \quad (2.96)$$

$$\hat{I}_- = |\beta\rangle\langle\alpha| = \begin{pmatrix} 0 & 0 \\ 1 & 0 \end{pmatrix} \quad (2.97)$$

⁵Usually, the Magnus expansion deals with discrete time-dependences of the Hamiltonians. The transition to a continuous time-dependence can be achieved by using integrals instead of sums.

It is useful to define another pair of operators, the projection operators:

$$\hat{I}_\alpha = |\alpha\rangle\langle\alpha| = \begin{pmatrix} 1 & 0 \\ 0 & 0 \end{pmatrix} \quad (2.98)$$

$$\hat{I}_\beta = |\beta\rangle\langle\beta| = \begin{pmatrix} 0 & 0 \\ 0 & 1 \end{pmatrix} \quad (2.99)$$

Applying the projection operators on the density matrix yields the population of the respective Zeeman state. The density matrix can be constructed from the projection operators and step operators:

$$\hat{\rho} = \rho_\alpha \hat{I}_\alpha + \rho_+ \hat{I}_+ + \rho_\beta \hat{I}_\beta + \rho_- \hat{I}_- = \begin{pmatrix} \rho_\alpha & \rho_+ \\ \rho_- & \rho_\beta \end{pmatrix} \quad (2.100)$$

The diagonal elements are called populations, the off-diagonal elements are called coherences. Populations are the probability to find a spin in state $|\alpha\rangle$ or $|\beta\rangle$ while coherences describe the probability of transitions (step operators!!) between the the states. With Eqns.2.80 and 2.79, the density matrix in thermal equilibrium is given as:

$$\hat{\rho}(0) \approx \frac{1}{Z} \begin{pmatrix} 1 + \frac{\hbar\omega_0}{2kT} & 0 \\ 0 & 1 - \frac{\hbar\omega_0}{2kT} \end{pmatrix} \quad (2.101)$$

Below, I will use the abbreviation \mathbf{B} for the population difference $\frac{\hbar\omega_0}{kT}$. In NMR, thermal energy is usually larger than the Zeeman splitting ($\hbar\omega_0 < kT$) which allows one to use the high-temperature approximation $Z \approx 2$. Therefore, the equilibrium density matrix of an ensemble of non-interacting spins can be written as:

$$\hat{\rho}(0) = \frac{1}{2} \left(\hat{1} + \mathbf{B} \hat{I}_z \right) \quad (2.102)$$

From $\hat{\rho}(0)$ as a starting point, using the Liouville-von Neumann equation (Eqn. 2.92), the evolution of $\hat{\rho}$ can be calculated.

(v) The effect of an on-resonance RF pulse on the density matrix

The oscillating magnetic field of an RF pulse $2B_1 \cos(\omega_0 t + \varphi)$ interacts with the spin system. Usually, the RF coil is mounted perpendicular to the external field - let us define it to be aligned along the x-axis. Then, the total Hamiltonian describing the interaction with the static field B_0 along z and with the oscillating field $2B_1 \cos(\omega_0 t)$ (for simplicity with phase $\varphi = 0$) can be written as:

$$\hat{H} = -\omega_0 \hat{I}_z - 2\omega_1 \hat{I}_x \cos(\omega_0 t) \quad (2.103)$$

Hereby, $\omega_0 = \gamma B_0$ and $\omega_1 = \gamma B_1$. The linearly polarized RF field in Eqn. 2.103 can be written as a superposition of two circularly polarized RF fields:

$$\hat{H} = -\omega_0 \hat{I}_z - \omega_1 \left[\left(\hat{I}_x \cos(\omega_0 t) + \hat{I}_y \sin(\omega_0 t) \right) + \left(\hat{I}_x \cos(\omega_0 t) - \hat{I}_y \sin(\omega_0 t) \right) \right] \quad (2.104)$$

With the property of the dimensionless spin operators

$$e^{-i\phi \hat{I}_z} \hat{I}_x e^{i\phi \hat{I}_z} = \hat{I}_x \cos \phi + \hat{I}_y \sin \phi, \quad (2.105)$$

this can be rewritten as

$$\hat{H} = -\omega_0 \hat{I}_z - \omega_1 \left(e^{-i\omega_0 t \hat{I}_z} \hat{I}_x e^{i\omega_0 t \hat{I}_z} + e^{i\omega_0 t \hat{I}_z} \hat{I}_x e^{-i\omega_0 t \hat{I}_z} \right) \quad (2.106)$$

The two components rotate along z with the angular frequencies $\pm\omega_0$. It can be shown that only the component rotating with $-\omega_0$ has significant impact on the spin system. Thus, the Hamiltonian reduces to:

$$\hat{H} = -\omega_0 \hat{I}_z - \omega_1 e^{i\omega_0 t \hat{I}_z} \hat{I}_x e^{-i\omega_0 t \hat{I}_z} \quad (2.107)$$

The total Hamiltonian is time-dependent. However, the time dependence can be eliminated with the help of a unitarian transformation into the rotating frame using the unitarian operator

$$\hat{U} = e^{i\omega_0 t \hat{I}_z} \quad (2.108)$$

In order to understand the axis transformation, let us first consider the unitarian transformation of the wave function $|\Psi\rangle$ which is simply

$$|\Psi\rangle_{rot} = \hat{U}^\dagger |\Psi\rangle \quad (2.109)$$

It follows for the density operator $\hat{\rho} = |\Psi\rangle\langle\Psi|$:

$$\hat{\rho}_{rot} = \hat{U}^\dagger \hat{\rho} \hat{U} \quad (2.110)$$

When $|\Psi\rangle_{rot}$ is introduced into the Schrödinger equation (or the transformed density operator $\hat{\rho}_{rot}$ into the Liouville-von Neumann equation), the Schrödinger equation (or Liouville-von Neumann equation) is fulfilled if the Hamiltonian is transformed according to:

$$\hat{H}_{rot} = \hat{U}^\dagger \hat{H} \hat{U} + \omega_0 \hat{I}_z \quad (2.111)$$

This is why the rotating-frame transformation is also called interaction representation or Zeeman picture. Now, let us first transform $\hat{\rho}(0)$ into the rotating frame:

$$\hat{\rho}_{rot}(0) = e^{-i\omega_0 t \hat{I}_z} \hat{\rho}(0) e^{i\omega_0 t \hat{I}_z} \quad (2.112)$$

$$= e^{-i\omega_0 t \hat{I}_z} \frac{1}{2} \left(\hat{1} + \mathbf{B} \hat{I}_z \right) e^{i\omega_0 t \hat{I}_z} \quad (2.113)$$

$$= \frac{1}{2} \left(\hat{1} + \mathbf{B} \hat{I}_z \right) \quad (2.114)$$

$$\hat{\rho}_{rot}(0) = \hat{\rho}(0) \quad (2.115)$$

Since \hat{I}_z commutes with \hat{I}_z , the rotating-frame equilibrium density matrix is simply the laboratory-frame density matrix.

As a next step, let us transform the Hamiltonian:

$$\hat{H}_{rot} = e^{-i\omega_0 t \hat{I}_z} \hat{H} e^{i\omega_0 t \hat{I}_z} + \omega_0 \hat{I}_z \quad (2.116)$$

$$= e^{-i\omega_0 t \hat{I}_z} \left(-\omega_0 \hat{I}_z - \omega_1 e^{i\omega_0 t \hat{I}_z} \hat{I}_x e^{-i\omega_0 t \hat{I}_z} \right) e^{i\omega_0 t \hat{I}_z} + \omega_0 \hat{I}_z \quad (2.117)$$

$$= -\omega_0 \hat{I}_z - \omega_1 \hat{I}_x + \omega_0 \hat{I}_z \quad (2.118)$$

$$\hat{H}_{rot} = -\omega_1 \hat{I}_x \quad (2.119)$$

In the rotating-frame, the Zeeman-Hamiltonian vanishes and the RF Hamiltonian has lost its time dependence. Now, in the rotating frame, the Liouville-von Neumann equation is easily solved as

$$\hat{\rho}_{rot}(t) = e^{-i\hat{H}_{rot}t} \hat{\rho}_{rot}(0) e^{i\hat{H}_{rot}t} \quad (2.120)$$

$$= e^{i\omega_1 t \hat{I}_x} \frac{1}{2} \left(\hat{1} + \mathbf{B} \hat{I}_z \right) e^{-i\omega_1 t \hat{I}_x} \quad (2.121)$$

$$= \frac{1}{2} \left[\left(\hat{1} + \mathbf{B} e^{i\omega_1 t \hat{I}_x} \hat{I}_z e^{-i\omega_1 t \hat{I}_x} \right) \right] \quad (2.122)$$

$$= \frac{1}{2} \left[\hat{1} + \mathbf{B} \left(\hat{I}_z \cos \omega_1 t - \hat{I}_y \sin \omega_1 t \right) \right] \quad (2.123)$$

$$= \frac{1}{2} \left[\hat{1} + \mathbf{B} \left(\frac{1}{2} \begin{pmatrix} 1 & 0 \\ 0 & -1 \end{pmatrix} \cos \omega_1 t - \frac{1}{2i} \begin{pmatrix} 0 & 1 \\ -1 & 0 \end{pmatrix} \sin \omega_1 t \right) \right] \quad (2.124)$$

$$= \begin{pmatrix} \frac{1}{2} + \frac{\mathbf{B}}{4} \cos \omega_1 t & i \frac{\mathbf{B}}{4} \sin \omega_1 t \\ -i \frac{\mathbf{B}}{4} \sin \omega_1 t & \frac{1}{2} + \frac{\mathbf{B}}{4} \cos \omega_1 t \end{pmatrix} \quad (2.125)$$

The x' -pulse ($\varphi = 0$) rotates the population difference \mathbf{B} along the rotating-frame x' axis. The rotation angle α depends on the pulse duration t_p :

$$\alpha = \omega_1 t_p \quad \omega_1 = \gamma B_1 \quad (2.126)$$

The laboratory-frame density matrix after the pulse is obtained by transforming back to the laboratory frame:

$$\hat{\rho}(t) = \hat{U} \hat{\rho}_{rot}(t) \hat{U}^\dagger \quad (2.127)$$

$$= e^{i\omega_0 t \hat{I}_z} \begin{pmatrix} \frac{1}{2} + \frac{\mathbf{B}}{4} \cos \omega_1 t & i \frac{\mathbf{B}}{4} \sin \omega_1 t \\ -i \frac{\mathbf{B}}{4} \sin \omega_1 t & \frac{1}{2} + \frac{\mathbf{B}}{4} \cos \omega_1 t \end{pmatrix} e^{-i\omega_0 t \hat{I}_z} \quad (2.128)$$

$$\hat{\rho}(t) = \begin{pmatrix} \frac{1}{2} + \frac{\mathbf{B}}{4} \cos \omega_1 t & i \frac{\mathbf{B}}{4} \sin \omega_1 t \cdot e^{i\omega_0 t} \\ -i \frac{\mathbf{B}}{4} \sin \omega_1 t \cdot e^{-i\omega_0 t} & \frac{1}{2} + \frac{\mathbf{B}}{4} \cos \omega_1 t \end{pmatrix} \quad (2.129)$$

Hereby, only the coherences are time-dependent since \hat{I}_z , and thus, the diagonal elements are invariant under rotation along z .

(vi) The magnetization vector

The classical magnetization vector describes the macroscopic magnetization of a spin system. It is the measurable quantity of the quantum-mechanic spin system. The magnetization vector is proportional to the vector built up of the expectation values of the magnetic moment operators $\hat{\mu}_{x,y,z} = \gamma \hat{I}_{x,y,z}$:

$$\vec{M}(t) = \begin{pmatrix} \text{Tr}(\hat{\rho}(t) \gamma \hat{I}_x) \\ \text{Tr}(\hat{\rho}(t) \gamma \hat{I}_y) \\ \text{Tr}(\hat{\rho}(t) \gamma \hat{I}_z) \end{pmatrix} = \frac{\gamma}{2} \begin{pmatrix} \rho_- + \rho_+ \\ i\rho_- - i\rho_+ \\ \rho_\alpha - \rho_\beta \end{pmatrix} \quad (2.130)$$

Conclusively, the equilibrium magnetization vector is obtained as:

$$\vec{M}_{eq} = \begin{pmatrix} 0 \\ 0 \\ \frac{\gamma \mathbf{B}}{4} \end{pmatrix} \equiv \begin{pmatrix} 0 \\ 0 \\ \mathbf{M} \end{pmatrix} \quad (2.131)$$

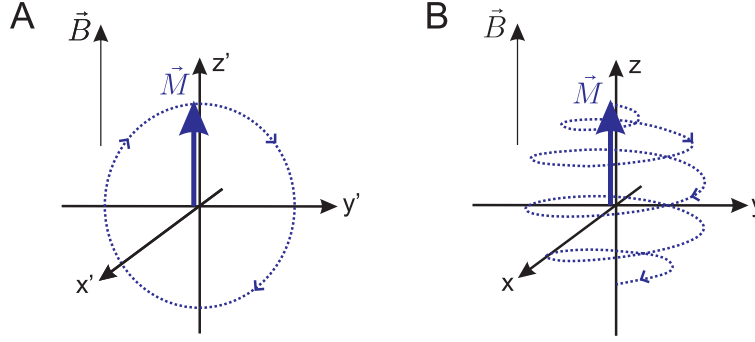


Figure 2.7: Evolution of the magnetization vector during a x' pulse in A: the rotating frame and B: the laboratory frame.

with the equilibrium magnetization \mathbf{M} (to obtain the result in SI units, it has to be multiplied by \hbar).

Similarly, the rotating-frame and laboratory-frame magnetization vector during an x' pulse is obtained from the respective density operators (Eqns. 2.125 and 2.129) as:

$$\vec{M}_{rot}(t_p) = \begin{pmatrix} 0 \\ \mathbf{M} \sin \omega_1 t_p \\ \mathbf{M} \cos \omega_1 t_p \end{pmatrix} \quad (2.132)$$

$$\vec{M}(t_p) = \begin{pmatrix} \mathbf{M} \sin \omega_1 t_p \sin \omega_0 t_p \\ \mathbf{M} \sin \omega_1 t_p \cos \omega_0 t_p \\ \mathbf{M} \cos \omega_1 t_p \end{pmatrix} \quad (2.133)$$

The evolution of the magnetization vector under the influence of an x' pulse on resonance is depicted in Fig. 2.7. It is possible to create defined non-equilibrium states by applying a pulse of defined pulse length t_p . After a $\pi/2$ pulse, *e. g.*, the population difference is completely “rotated” into the 1-quantum coherences. After such a pulse, the magnetization vector in the laboratory frame is obtained as

$$\vec{M}(t_p) = \begin{pmatrix} \mathbf{M} \sin \omega_0 t_p \\ \mathbf{M} \cos \omega_0 t_p \\ 0 \end{pmatrix} \quad (2.134)$$

After a $\pi/2$ pulse, the magnetization rotates in the xy -plane and, thus, induces an alternating voltage in the measuring coil. Thus, populations are not detected but the (-1)-coherence. The Fourier-Transform of such a signal would be a delta-function at ω_0 . Spin-spin relaxation leads to a decay of the oscillating magnetization and, as a result, to finite linewidths. Relaxation will be dealt with below.

(vii) Nuclear spin interactions

Chemical shift The Larmor frequency of a spin depends on the local magnetic field at the nucleus. The local field usually differs from the external field since the electronic structure surrounding the nucleus shields or deshields the magnetic field due to induced ring currents. The

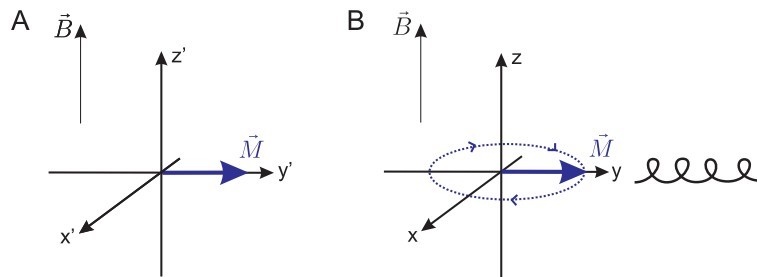


Figure 2.8: Magnetization vector after a $\pi/2$ pulse in A: the rotating frame and B: the laboratory frame.

resulting shift of the Larmor frequency is called chemical shift (CS). The CS Hamiltonian is linear with \hat{I} . In frequency units (rad/s) it is given as:

$$\hat{H}_{\text{CS}} = \gamma \hat{I} \underline{\underline{\sigma}} B_0 \quad (2.135)$$

Generally, $\underline{\underline{\sigma}}$ is a 3x3-tensor and belongs to the same point group as the nuclear site. The chemical shift tensor is usually characterized by the following values

$$\sigma_{\text{iso}} = \frac{1}{3} \text{Tr}(\underline{\underline{\sigma}}) = \frac{1}{3} (\sigma_{xx}^{\text{PAF}} + \sigma_{yy}^{\text{PAF}} + \sigma_{zz}^{\text{PAF}}) \quad (2.136)$$

$$\Delta_{\text{CS}} = \sigma_{zz}^{\text{PAF}} - \sigma_{\text{iso}} \quad (2.137)$$

$$\eta_{\text{CS}} = \frac{\sigma_{xx}^{\text{PAF}} - \sigma_{yy}^{\text{PAF}}}{\Delta} \quad (2.138)$$

whereby PAF stands for the principle axis frame. The z -axis of the PAF z^{PAF} is defined for point groups with rotation axes as the n -fold rotation axis C_n with the highest value of n . If there is a rotation axis C_n with $n > 2$, the tensor is axialsymmetric and $\eta_{\text{CS}} = 0$. Otherwise, $\eta_{\text{CS}} \neq 0$. Clearly, in the absence of a C_n axis, no PAF can be defined, and three parameters σ_{iso} , Δ_{CS} and η_{CS} are not sufficient to characterize the CS tensor, but it can be shown that the additional antisymmetric components do not have a significant impact on the spectrum. [57,65] The secular CS Hamiltonian obtained from first-order perturbation theory (or zero-order average Hamiltonian theory) is

$$\hat{H}_{\text{CS}}^{(0)} = \gamma \hat{I}_z B_0 [\sigma_{\text{iso}} + \frac{1}{2} \Delta_{\text{CS}} (3 \cos^2 \Theta - 1 + \eta_{\text{CS}} \sin^2 \Theta \cos 2\Phi)] \quad (2.139)$$

Hereby, Θ and Φ are the polar angles determining the orientation of the PAF z -axis z^{PAF} and the magnetic field axis (=laboratory-frame z -axis). In the powder average, all possible orientations occur with the same probability. Simulated rigid-lattice CS powder spectra are shown in Fig. 2.9. For the simulation, the software WinSolids [66] developed by K. Eichele at the University of Tübingen, Germany, was used. Since isolated nuclei are usually not accessible for NMR experiments, chemical shift is always present. Therefore, the chemical shift scale δ_{CS} is defined in reference to an arbitrary reference compound:

$$\delta_{\text{CS}} = \frac{\nu_{\text{iso}} - \nu_{\text{ref}}}{\nu_{\text{ref}}} \quad (2.140)$$

Dipolar interaction The magnetic dipolar interaction is the interaction between the magnetic moments of two adjacent nuclear spins. The interaction Hamiltonian in angular frequency units

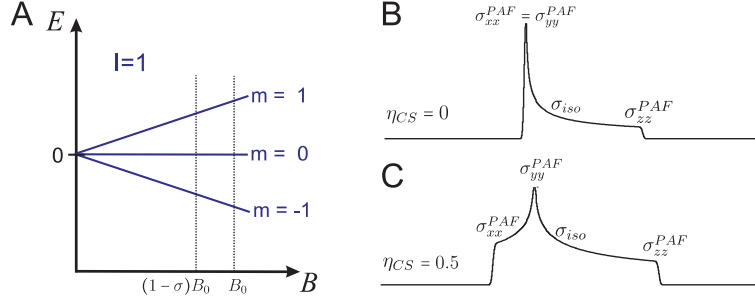


Figure 2.9: A: Shielding of the magnetic field and chemical shift. B: Powder spectrum for axial-symmetric CS tensor. C: powder spectrum for a CS tensor with $\eta_{CS} = 0.5$.

(rad/s) is given as:

$$\hat{H}_D = -2\hat{I}\underline{\underline{D}}\hat{S} \quad (2.141)$$

\hat{I} is the spin operator of the considered spin, \hat{S} is the spin operator of the interacting spin (not necessarily the same nucleus) which is the source of the local field felt by spin \hat{I} . $\underline{\underline{D}}$ is the dipolar coupling tensor which is traceless and invariant under rotation along the PAF z -axis (= the internuclear vector). With the definition of the dipolar coupling constant (in rad/s)

$$d = \hbar \frac{\mu_0}{4\pi} \frac{\gamma_I \gamma_S}{r_{IS}^3} \quad (2.142)$$

the diagonal components of the symmetric dipolar coupling tensor in the PAF are

$$D_{xx}^{PAF} = -d/2 \quad (2.143)$$

$$D_{yy}^{PAF} = -d/2 \quad (2.144)$$

$$D_{zz}^{PAF} = d \quad (2.145)$$

Due to the r_{IS}^{-3} dependence of the coupling constant, the dipolar interaction is a short-distance interaction. The coupling with nearest neighbors will dominate the overall coupling.

The Hamiltonian for homonuclear dipolar coupling between the spin k and l can be split up into spin-dependent and orientation-dependent operators according to

$$\hat{H}_D = \sum_{q=-2}^2 \hat{F}_{kl}^{(q)} \hat{A}_{kl}^{(q)} \quad (2.146)$$

with

$$\begin{aligned} \hat{A}_{kl}^{(0)} &= -[\hat{I}_{zk}\hat{I}_{zl} - \frac{1}{4}(\hat{I}_k^+ \hat{I}_l^- + \hat{I}_k^- \hat{I}_l^+)] & \hat{F}_{kl}^{(0)} &= d_{kl}(3 \cos^2 \Theta - 1) \\ \hat{A}_{kl}^{(\pm 1)} &= -\frac{3}{2}[\hat{I}_{zk}\hat{I}_l^\pm + \hat{I}_k^\pm \hat{I}_{zl}] & \hat{F}_{kl}^{(\pm 1)} &= d_{kl} \sin \Theta_{kl} \cos \Theta_{kl} e^{\mp i\Phi_{kl}} \\ \hat{A}_{kl}^{(\pm 2)} &= -\frac{3}{4}\hat{I}_k^\pm \hat{I}_l^\pm & \hat{F}_{kl}^{(\pm 2)} &= d_{kl} \sin^2 \Theta_{kl} e^{\mp 2i\Phi_{kl}} \end{aligned} \quad (2.147)$$

The operator $\hat{A}_{kl}^{(q)}$ with $q=0$ describes energy-conserving interaction processes (giving rise to spin diffusion or spin-spin relaxation) while the processes with $q = \pm 1$ and $q = \pm 2$ go along with a net change of the longitudinal magnetization (and will give rise to spin-lattice relaxation). In the low-temperature (or high-field) approximation, only the terms with $q=0$ affect the NMR line shape.

From these terms (=secular terms), the first-order Hamiltonian for homonuclear dipolar coupling is obtained as

$$\hat{H}_D^{homo,(0)} = -\frac{d}{2}[3\hat{I}_z\hat{S}_z - \hat{I}\hat{S}](3\cos^2\Theta - 1) \quad (2.148)$$

For heteronuclear dipolar coupling, similarly, one obtains:

$$\hat{H}_D^{hetero,(0)} = -d\hat{I}_z\hat{S}_z(3\cos^2\Theta - 1) \quad (2.149)$$

Hereby, the polar angle Θ is given by the orientation internuclear vector with respect to the external field.

In solids with immobile spins (rigid lattice), the static dipolar interaction of all the spins gives rise to a broad, approximately Gaussian-shaped NMR spectrum determined by the $\hat{A}_{kl}^{(0)}$ operator which describes the energy-conserving flip-flop processes leading to spin-spin relaxation, *i. e.* the decay of the transversal magnetization. The coupling constant determines the mean interaction rate (corresponding to the time scale of the interaction). If the spins become mobile at higher temperatures, the line narrows (motional narrowing) once the jump rate is higher than the interaction rate. Then, the nuclei do not reside adjacent to each other for a time long enough for the interaction process to become effective. Less effective relaxation translates into a narrower line.

Quadrupolar Interaction All nuclei with $I > 1/2$ possess an electric quadrupole moment eQ which is aligned along the spin axis. Therefore, the interaction of the electric quadrupole moment with an electric field gradient gives rise to an energy shift of the Zeeman niveaus. The quadrupolar Hamiltonian is given as:

$$\hat{H}_Q = \frac{eQ}{2I(2I-1)\hbar}\hat{I}\underline{V}\hat{I} \quad (2.150)$$

whereby \underline{V} is the traceless electric field gradient tensor (EFG) built up from the partial derivatives of the electric field (*e. g.* $V_{zz}^{\text{PAF}} = \frac{\partial^2 V}{\partial z_{\text{PAF}}^2}$). The EFG belongs to the same point group as the nuclear site. The PAF EFG is usually characterized by the quadrupolar coupling constant δ_Q (in angular frequency units) and the asymmetry parameter η_Q :

$$\delta_Q = \frac{V_{zz}^{\text{PAF}}eQ}{\hbar} \quad (2.151)$$

$$\eta_Q = \frac{V_{xx}^{\text{PAF}} - V_{yy}^{\text{PAF}}}{V_{zz}^{\text{PAF}}} \quad (2.152)$$

Again, for a point group with a symmetry axis C_n with $n > 2$, the tensor is axial-symmetric and $\eta_Q = 0$, otherwise $\eta_Q \neq 0$. In the rigid lattice, the site-specific point group determines the point group of the EFG tensor while in the limit of fast diffusion, the mean EFG tensor shows the same point group as the crystal. For isotropic random-network glasses, a mean cubic symmetry is expected. Residual EFG coupling points to a non-isotropic or non-random glass structure.

The first-order quadrupolar Hamiltonian of the secular parts is given as

$$\hat{H}_Q^{(0)} = \frac{\delta_Q}{8\hbar I(2I-1)}(3\hat{I}_z^2 - \hat{I}^2)[(3\cos^2\Theta - 1) + \eta_Q \sin^2\Theta \cos 2\Phi] \quad (2.153)$$

Table 2.4: Quadrupolar contribution to the Zeeman energies ($I=1$ bzw. $I=3/2$):

m	ω_Q
1, -1	$\hbar\delta_Q/8 \cdot W$
0	$-\hbar\delta_Q/4 \cdot W$
1/2, -1/2	$-\hbar\delta_Q/8 \cdot W$
3/2, -3/2	$\hbar\delta_Q/8 \cdot W$

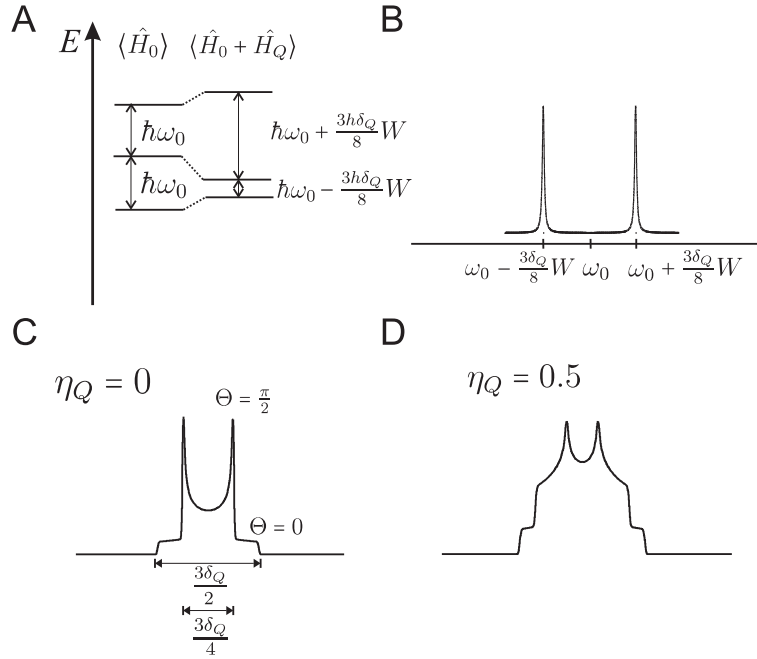


Figure 2.10: Quadrupolar Interaction for $I=1$ -nuclei. A: quadrupolar shifts of the Zeeman states. B: single crystal spectrum at a given orientation. C: powder spectrum for $\eta_Q=0$ D: powder spectrum for $\eta_Q=0.5$

Hereby, Θ and Φ describe the relative orientation of the EFG PAF (=site PAF) and the external magnetic field. The first-order angular frequency shifts of the Zeeman Niveaus are, accordingly:

$$\omega_Q^{(0)} = \frac{\delta_Q}{8\hbar I(2I-1)}(3m^2 - I(I+1))[(3\cos^2\Theta - 1) + \eta_Q \sin^2\Theta \cos 2\Phi] \quad (2.154)$$

$$\equiv \frac{\delta_Q}{8\hbar I(2I-1)}(3m^2 - I(I+1)) \cdot W \quad (2.155)$$

with W being an abbreviation for the orientation-dependent term in brackets. Table 2.4 shows the first-order quadrupolar shifts for $I = 1$ and $I = 3/2$ nuclei. Figs. 2.10 and 2.11 visualize the impact of the quadrupolar coupling on the Zeeman states (A), on a single-crystal spectrum (B), and on a powder spectrum (C and D) for $I = 1$ and $I = 3/2$ -nuclei, respectively.

J-Coupling J-coupling has the same form as the dipolar interaction with the j-coupling tensor $\underline{\underline{J}}$ instead of the dipolar coupling tensor $\underline{\underline{D}}$. It is an indirect dipolar interaction mediated via electrons

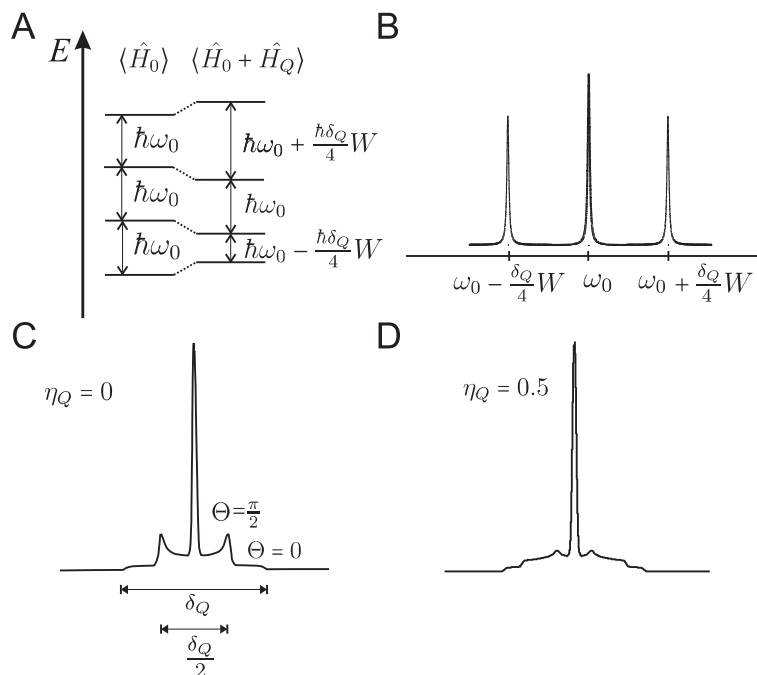


Figure 2.11: Quadrupolar Interaction for $I=3/2$ -nuclei. A: quadrupolar shifts of the Zeeman states. B: single crystal spectrum at a given orientation. C: powder spectrum for $\eta_Q=0$ D: powder spectrum for $\eta_Q=0.5$

in covalent bonds. It is of central importance in NMR on organic molecules whereby in liquids the tensor reduces to a scalar.

Dipolar interaction with electron spins Here, again, direct and indirect dipolar interactions with the electron spin \hat{S} are possible. The indirect spin-spin interaction with electron spins mediated via bonds is called hyperfine interaction. Usually (at least in compounds with a high density of paramagnetic centers), the spin-lattice and spin-spin relaxation of the electron spin occurs on a shorter time scale than the dipolar coupling between the nuclear spin and the electron spin. Then, the nuclear spin does not couple to single spin states $|m_S\rangle$ but to a time-averaged spin state which is the expectation value $\langle \hat{S}_z \rangle$. [67]

The Knight shift is very similar to the hyperfine interaction: it is the interaction with unpaired electrons (in s -states) on the Fermi surface in conductive materials. [68]

Higher-order energy shifts Higher order perturbation theory has to be considered when the perturbations are not very small with respect to the Zeeman interaction. For instance, the quadrupolar interaction is very often large enough to make it necessary to consider second-order perturbation theory (or first-order average Hamiltonian theory). The higher-order terms are characterized by a Larmor frequency dependence according to ω_0^{-n+1} with n being the n^{th} order of the perturbation. Thus, the higher-order effects are less pronounced in large magnetic fields.

(viii) Relaxation

As shown above, by using RF pulses, defined non-equilibrium states of the spin system (and the magnetization vector) can be created. Hereby, two different kinds of non-equilibrium can be discerned:

- The populations (diagonal elements of the density matrix) do not follow Boltzmann's distribution. Then, the z -component of the magnetization vector does not show the equilibrium value. The spin system has to exchange energy in order to return to equilibrium. The relaxation process is called longitudinal relaxation or spin-lattice relaxation (SLR) and occurs at a rate R_1 , the SLR rate.
- The (-1)-coherences (off-diagonal elements in the density matrix) are non-zero which goes along with a magnetization vector rotating in the xy -plane. Spin-interactions lead to a loss of coherence and a decay of the transversal magnetization which is measured as free induction decay (FID) in FT-NMR experiments. The transversal relaxation is called spin-spin relaxation (SSR) and occurs at a rate R_2 , the SSR rate. Since the FID is the inverse Fourier-Transform of the line shape, the SSR was indirectly introduced in the foregoing section where the influence of the spin-interactions on the line shape were considered with the help of the secular parts of the interaction Hamiltonians.

The Bloch equation phenomenologically describes the dynamics of the magnetization vector after a pulse:

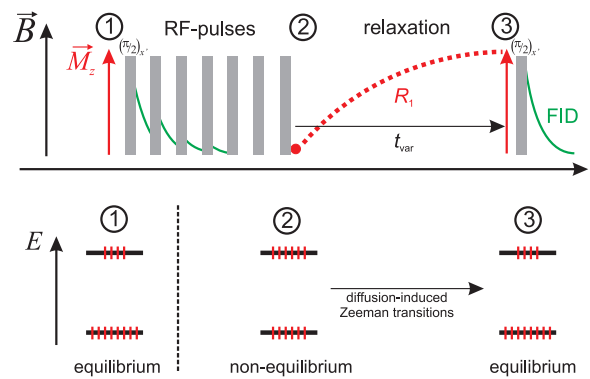
$$\frac{\partial \vec{M}(t)}{\partial t} = \gamma \vec{M}(t) \times \vec{B}(t) - \underline{\underline{R}}(\vec{M}(t) - \vec{M}_{eq}) \quad (2.156)$$

Hereby, the relaxation matrix $\underline{\underline{R}}$ is a diagonal matrix with the components R_2 , R_2 , and R_1 . Very often, the relaxation process back to equilibrium shows non-exponential behavior. Then, the Bloch equations are not a suitable description of the dynamics of the magnetization vector.

Techniques to measure R_1 , $R_{1\rho}$, and R_2 The spin lattice relaxation rate can be *e.g.* measured by using the saturation recovery pulse sequence $[n \times (90^\circ - \tau) - t_{\text{delay}} - 90^\circ - FID]$ shown in Fig. 2.12A. The comb of n closely spaced pulses destroys the magnetization. Its return to equilibrium is monitored by several experiments with different delay times t_{delay} . The amplitude of the $FID(t_{\text{delay}})$ yields the relaxation transient. The relaxation process goes along with transitions between the Zeeman states.

The so-called spin-lattice relaxation in the rotating frame enables the measurement of SLR for much smaller Zeeman splittings. It is measured with the spin-locking pulse sequence shown in Fig. 2.12B. An 90°_x pulse tips the magnetization to the $-y'$ axis. After that, the locking pulse of variable length t_{lock} and phase $-y'$ is applied. In the rotating frame, the locking pulse appears as a constant magnetic field B_1 giving rise to a Zeeman splitting with $\omega_1 = 10^4 \leq 10^6 \text{ s}^{-1}$. The population difference of the rotating-frame Zeeman states directly after the first pulse represents Boltzmann's distribution for the Zeeman splitting ω_0 which is far too large for the much smaller rotating-frame Zeeman splitting ω_1 . The system returns to equilibrium by transitions between the rotating-frame Zeeman niveaus. The rotating-frame SLR transients are recorded by subsequent

A) SLR in the laboratory frame



B) SLR in the rotating frame

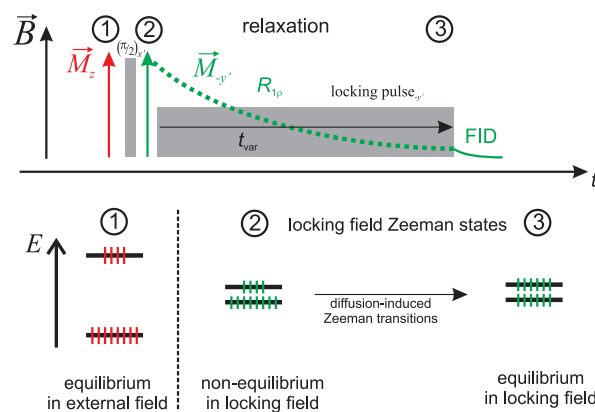


Figure 2.12: A: Top section: saturation recovery pulse sequence for the measurement of SLR rates R_1 . Bottom section: population of the Zeeman states in the course of the experiment. (1): equilibrium magnetization, Zeeman states populated according to Boltzmann's distribution (2) fully destroyed magnetization, Zeeman states equally populated. (2)→(3) SLR goes along with transitions between the Zeeman states. B: Top section: spin-locking pulse sequence for the measurement of $R_{1\rho}$. Bottom Section: population of the locking-field Zeeman states in the course of the experiment.

measurements with different t_{lock} .

The spin-spin relaxation rate R_2 can be understood as the zero-locking-field limit of $R_{1\rho}$. It can be measured by the use of echo pulse sequences. In solids, the solid echo pulse sequence $[90^\circ - \tau - 64^\circ - \tau - \text{echo}]$ can be used. Hereby, τ is varied in a series of measurements. The amplitude of the echo as a function of 2τ yields the SSR transients.

Diffusion-induced relaxation In the coming section, I will present a very rough picture which provides qualitative understanding of diffusion-induced spin-lattice relaxation (see also the paper “NMR relaxometry as a versatile tool to study Li ion dynamics in potential battery materials” which is attached at the end of this chapter (page 40-46)). Let us consider a non-equilibrium state created by a series of $\pi/2$ -pulses which fully destroy the magnetization as shown in Fig. 2.12. Now, the system will tend to return back to equilibrium. Therefore, transitions between the Zeeman states are necessary. Spontaneous emissions ($\propto \nu^3$) can be neglected in the radio-frequency regime, since induced emissions occur at a higher rate. Resonant fluctuations of spin interactions, for example due to hopping motion of the spins, induce Zeeman transitions. In solids, the energy is exchanged with lattice phonons which is why the process is called spin-lattice relaxation. Now, it is necessary to examine the fluctuations of the spin interactions. Clearly, it is expected that relaxation is most efficient when the hopping rate is in the order of the NMR frequency which is an internal resonance situation. But what is the situation like when the jump rate is smaller or larger than the NMR frequency? Therefore, a description of the fluctuations due to the hopping dynamics is necessary. The fluctuations of the spin interactions can be described (in a quite rough manner) by an NMR frequency correlation function $G(t)$:

$$G(t) = \langle \Delta\omega(0) \cdot \Delta\omega(t) \rangle \quad (2.157)$$

$$G(0) = \langle \Delta\omega(0) \cdot \Delta\omega(0) \rangle \equiv M_2 \quad (2.158)$$

$$G(t) = M_2 \cdot g(t) \quad (2.159)$$

Hereby, the bracket denotes the ensemble average. When the NMR frequency is altered due to a jump, the NMR frequency correlation function $G(t)$ decays. In the most simple case, $g(t)$ can be identified with the one-particle-two-time correlation function. $G(0)$ is, according to the above-given definition of the NMR frequency correlation function, the second moment of the interaction, also called interaction strength. Now, we were interested in the fluctuations on resonance. These may be obtained from the one-sided Fourier-Transform of $G(t)$, the spectral density $J'\omega$:

$$J'(\omega) = M_2 \cdot \text{Re} \left[\int_0^\infty g(t) e^{-i\omega t} dt \right] = M_2 \cdot j'(\omega) \quad (2.160)$$

Now, without any deeper theoretical foundation, one might assume that the diffusion-induced NMR relaxation rates R_1 and R_2 are:

$$R_1 \approx M_2 \cdot j'(\omega_0) \quad (2.161)$$

$$R_{1\rho} \approx M_2 \cdot j'(\omega_1) \quad (2.162)$$

$$R_2 \approx M_2 \cdot j'(0) \quad (2.163)$$

From these equations, the temperature dependence of diffusion-induced SLR rates R_1 can be understood qualitatively by assuming that $g(t)$ and $j'(\omega)$ is equal to the one-particle-two-time

Table 2.5: Limiting cases of diffusion-induced SLR and SSR.

limit	R_1
$\tau^{-1} \ll \omega_0$	$\propto \omega_0^{-2+n} \tau^{-1+n}$
$\tau^{-1} = \omega_0$	maximum
$\tau^{-1} \gg \omega_0$	$\propto \tau$

limit	R_2
$\tau^{-1} < \sqrt{M_2}$	$= \sqrt{M_2}$
$\tau^{-1} = \sqrt{M_2}$	onset of narrowing
$\tau^{-1} > \sqrt{M_2}$	$\propto \tau$

correlation function describing the hopping dynamics. For example, in the case of Brownian motion, the correlation function is a single exponential correlation function. Then, the SLR rate will show the well-known symmetric BPP-behavior [69] and the SLR rate peaks when the correlation rate equals the NMR frequency which is the internal resonance condition mentioned above:

$$\tau^{-1} = \omega_0 \quad (2.164)$$

Deviations from uncorrelated Brownian motion can often be well described by KWW-stretched exponentials. The respective limiting cases of R_1 for $\tau^{-1} \gg \omega_0$ and $\tau^{-1} \ll \omega_0$ are summarized in Table 2.5. The behavior of R_2 will only apply at high temperatures, in the weak collisions regime ($\tau^{-1} > \sqrt{M_2}$). At lower temperatures in the rigid lattice, the so-called strong-collisions regime, flip-flop processes of interacting spins (= spin diffusion) occur at a constant rate defined by the interaction strength $\sqrt{M_2}$ for dipolar interaction. Thus, in the strong-collision regime, $R_2 = \sqrt{M_2}$. An important result is obtained from this simplistic approach: the measurement of diffusion-induced R_1 , $R_{1\rho}$ and R_2 provides insight into the hopping dynamics. Absolute jump rates can be determined from the maximum of R_1 and from the onset of narrowing of R_2 . Since ω_0 is in the order of $10^7 \dots 10^9 \text{ s}^{-1}$, R_1 is sensitive to very fast hopping dynamics while R_2 and $R_{1\rho}$ are sensitive to relatively slow dynamics.

Clearly, the simplistic approach given above can only be valid in a qualitative manner because the quantum-mechanic nature of the NMR interactions was neglected. Furthermore, (i) the reservoir which the energy is exchanged with, the lattice phonons, was not included into the considerations, (ii) most spin interactions are bilinear in \hat{I} (dipolar coupling, quadrupolar coupling) which leads to the influences of two-quantum transitions.

Weak-collisions and strong-collisions regime For the treatment of diffusion-induced relaxation, two regimes have to be discerned: the strong-collisions regime where the jump rate of mobile spins is smaller than the rigid-lattice SSR rate ($R_{2,r1} > \tau^{-1}$) and the weak-collisions regime ($R_{2,r1} < \tau^{-1}$). In the strong collision regime, the spin-spin interaction rate (energy-conserving flip-flop processes) is higher than the hopping rate, *i. e.* the so-called rigid lattice regime. Then, between two successive hops of a spin, the spin system has a common spin temperature. This theory has to be applied for the evaluation of SSR in the rigid lattice (as given above). Hereby,

the SSR rate is determined by spin dynamics due to spin-spin interactions and not due to hopping of the spins. Flip-flop processes which connect the homonuclear spin reservoir occur on a shorter time scale than atomic jumps. The rate of the flip-flop processes is determined by the strength of the spin-spin interaction. [59, 70]

Strong-collisions theory also has to be applied for diffusion-induced SLR at low temperatures ($R_{2,\text{rl}} > \tau^{-1}$) in small fields which is relevant for the rotating-frame SLR and field-cycling NMR. [71–75]

At high temperatures ($R_{2,\text{rl}} < \tau^{-1}$), in the motional-narrowing regime, the weak-collisions theory can be applied for SSR and SLR in both high and low fields.

An attempt of a rigorous treatment of NMR relaxation which includes both regimes is given in Ref. [71].

Homonuclear dipolar relaxation and quadrupolar relaxation Since the Hamiltonians for the homonuclear dipolar interaction and quadrupolar interaction are both bilinear in \hat{I} , the mathematical treatment of both interactions is parallel. The relaxation rates for homonuclear dipolar relaxation and quadrupolar relaxation according to the weak-collisions theory are given as [55, 65, 69, 75–79]:

$$R_1 = M_2 \cdot \left[\frac{2}{3}j'(\omega_0) + \frac{8}{3}j'(2\omega_0) \right] \quad (2.165)$$

$$R_{1\rho} = M_2 \cdot \left[j'(2\omega_{1,\text{eff}}) + \frac{5}{3}j'(\omega_0) + \frac{2}{3}j'(2\omega_0) \right] \quad (2.166)$$

$$R_2 = M_2 \cdot \left[j'(0) + \frac{5}{3}j'(\omega_0) + \frac{2}{3}j'(2\omega_0) \right] \quad (2.167)$$

Hereby, the effective locking frequency $\omega_{1,\text{eff}} = \sqrt{\omega_1^2 + M_2}$ whereby $\sqrt{M_2} = R_{2,\text{rl}} = \omega_{\text{loc}}$ is the mean local field due to the interaction.

In experimental situations, ω_1^2 is regularly not much larger or even smaller than M_2 . Clearly, then, the weak-collisions approximation is not valid any more and the strong-collisions theory applies, instead. This has no effect on the slope of $R_{1\rho}$ low temperature flank but on its absolute value which appears to be a similar outcome as if the effective locking field is altered. When the weak-collisions expressions are used for the interpretation of experimental data, this leaves us with some uncertainty of the maximum condition and of the apparent effective locking frequency. Around the $R_{1\rho}$ maximum, the transition to the weak-collision regime occurs. [71–75, 80]

Heteronuclear dipolar relaxation The NMR relaxation rates due to fluctuations of the heteronuclear dipolar interaction between the observed spin \hat{I} and the coupling spin \hat{S} in the framework of weak-collisions theory is given as [59, 65, 79, 81]:

$$R_1^{\text{IS}} = M_2^{\text{IS}} \cdot \left[\frac{3}{2}j'(\omega_{\text{I}}) + \frac{1}{2}j'(\omega_{\text{I}} - \omega_{\text{S}}) + 3j'(\omega_{\text{I}} + \omega_{\text{S}}) \right] \quad (2.168)$$

$$R_{1\rho}^{\text{IS}} = M_2^{\text{IS}} \cdot \left[k^{\text{IS}} \cdot j'(\omega_{1,\text{eff}}) + \frac{3}{4}j'(\omega_{\text{I}}) + \frac{1}{4}j'(\omega_{\text{I}} - \omega_{\text{S}}) + \frac{3}{2}j'(\omega_{\text{I}} + \omega_{\text{S}}) + \frac{3}{2}j'(\omega_{\text{S}}) \right] \quad (2.169)$$

$$R_2^{\text{IS}} = M_2^{\text{IS}} \cdot \left[k^{\text{IS}} \cdot j'(0) + \frac{3}{4}j'(\omega_{\text{I}}) + \frac{1}{4}j'(\omega_{\text{I}} - \omega_{\text{S}}) + \frac{3}{2}j'(\omega_{\text{I}} + \omega_{\text{S}}) + \frac{3}{2}j'(\omega_{\text{S}}) \right] \quad (2.170)$$

Hereby, again, the effective locking frequency is $\omega_{1,\text{eff}} = \sqrt{\omega_1^2 + M_2^{\text{IS}}}$. $k^{\text{IS}} = 1$ for $\omega_1^2 \gg M_2^{\text{IS}}$, otherwise $k^{\text{IS}} > 1$. Concerning the applicability of the weak-collisions theory, the same considerations as given above hold.

Relaxation due to coupling with the electron spins of paramagnetic impurities Hereby, in principle, two different scenarios are possible. (i) the electron spin of the paramagnetic ion possesses a relaxation rate R_p which is independent of the coupling with mobile nuclear spins. (ii) the relaxation of the electron spin ion is due to coupling with mobile nuclear spins. [82]

The first case (i) is commonly considered in textbooks and publications on NMR theory. [55, 56, 77, 82–86] This situation applies to paramagnetic materials [67] and to diamagnetic host materials with paramagnetic impurities of, *e. g.*, Fe [87] or Gd [82].

Considering the second case (ii) is - to my knowledge - not discussed in the literature⁶ although there is a large amount of experimental data supporting this hypothesis for materials with paramagnetic impurities of *e. g.*, Mn^{2+} or Cr^{3+} [21, 77, 87–90]. In this case, it should be justified to treat the problem parallel to the usual heteronuclear dipolar coupling.

For the first case (i), the spin-lattice relaxation rate of the nuclear spin is given as: [55, 56, 77, 86]

$$R_1 \propto \frac{\tau_p}{1 + (\omega_0 \tau_p)^2} \cdot r^{-6} \quad (2.171)$$

Hereby, $\tau_p = 1/R_p$ is the inverse of the independent spin-lattice relaxation rate of the electron spin. Due to the r^{-6} -dependence, nuclear spins close to the interacting ions will relax very fast while in longer distance, the nuclei are unaffected. Now, let us consider mobile nuclear spins in a solid with a very low concentration of such paramagnetic impurities. Then, at low temperatures, the relaxation will be limited by the diffusion of the nuclear spins to the vicinity of the paramagnetic ion, while at high temperatures, the contact time of the nuclear spin with the impurity limits the rate. This leads to a relaxation rate maximum at a temperature where the jump rate equals the relaxation rate of a spin residing adjacent to the impurity. [86] The low-temperature limit is $R_1 \propto \tau^{-1}$, the high-temperature limit is $R_1 \propto \tau$ in the case of uncorrelated dynamics. [82, 86] The ω_0 dependence enters via Eqn. 2.171.

In the second case (ii), the relaxation rate might follow the same behavior as heteronuclear dipolar coupling (a suggestion of mine, a similar treatment of relaxation at paramagnetic impurities is given in Ref. [91]). This leads to

$$R_1^{\text{para}} = M_2^{\text{para}} \cdot \left[\frac{3}{2} j'(\omega_I) \right] \quad (2.172)$$

$$R_{1\rho}^{\text{para}} = M_2^{\text{para}} \cdot \left[k^{\text{para}} \cdot j'(\omega_{1,\text{eff}}) + \frac{3}{4} j'(\omega_I) \right] \quad (2.173)$$

whereby the terms in ω_S were neglected since the spectral densities in the relevant temperature range will be nearly zero at ω_S . M_2^{para} should be a function of the actual interaction strength near the impurity, where the relaxation event takes place, and of the concentration of impurities and nuclear spins. The SLR rate maximum in this case is $\tau^{-1} = \omega_0$ and the paramagnetic impurity centers simply enhance the relaxation.

The two scenarios as found in experimental data (see above) are depicted in Fig. 2.13:

⁶An exception is a paper by Abou-Ghaloun *et al.* [88] which has never been cited. There, the effect of paramagnetic impurities on R_1 is derived from the fluctuation of the local field the ions are exposed while diffusing past paramagnetic impurities. This is quite parallel to the simplistic model to explain R_1 given in this work, see above.

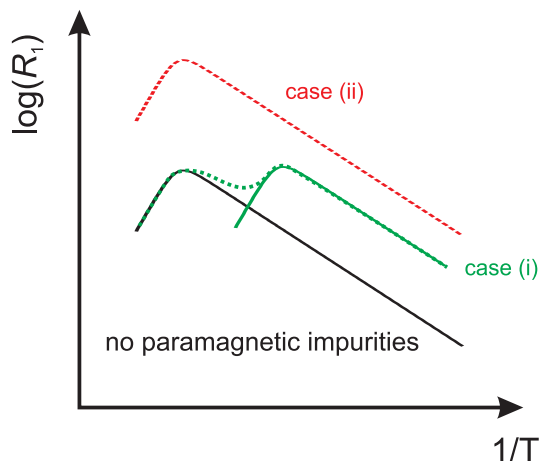


Figure 2.13: The effect of paramagnetic impurities found in experimental data. black line: SLR rate in the absence of paramagnetic impurities. red line, case (ii): enhanced relaxation due to the paramagnetic centers, no effect on the form of the diffusion-induced SLR rate peak. green line, case(i): additional peak due to paramagnetic ions which may appear as a shoulder.

Background relaxation and NCL-type relaxation Korringa relaxation and vibrational relaxation are typical background relaxations. The Korringa relaxation is due to coupling to unpaired conduction electrons near the Fermi surface and roughly follows linear temperature dependence. [68] Vibrational relaxation is due to fluctuations of the quadrupolar coupling due to lattice vibrations and follows a T^2 dependence at temperatures above the Debye temperature and a T^7 dependence well below the Debye temperature. [92] Both relaxation types (if present) are simply superimposed to the diffusion-induced relaxation rates and appear at low and at high temperatures. A "background" that does not appear at high temperatures but at low temperatures is not a background but associated with ionic motion - most probably NCL-type caged dynamics of the ion [93–96]. For NCL dynamics, at a certain temperature, the hopping correlation rate will exceed the correlation rate of the NCL dynamics which does not allow the NCL to exist at higher temperatures. For vibrational dynamics, however, the correlation rate will always be higher than the hopping correlation rate.

(ix) Field-gradient NMR

Field-Gradient (FG) NMR is a powerful tool for the determination of tracer diffusion coefficients. Two variants of the FG NMR can be used: pulsed field-gradient (PFG) NMR and static field-gradient (SFG) NMR.

FG NMR techniques use (stimulated) echo pulse sequences, in the most simple case a Hahn echo [$90^\circ - \tau - 180^\circ - \tau - echo$]. During the two τ -periods, the magnetization is in the transversal plane and will decay with R_2 due to spin-spin interactions (flip-flop processes) which lead to frequency fluctuations of the spins. Therefore, the refocused echo has a smaller amplitude than the FID has after a single pulse. It is important to realize that the reason for the echo decay is the fact that the spins do not carry an individual NMR frequency due to the interactions. Any fluctuation of the NMR frequency whatever cause it has will cause the echo to decay. In FG NMR, the diffusion of spins in a static or pulsed field gradient $g = \partial B / \partial z$ leads to z -dependent NMR frequency

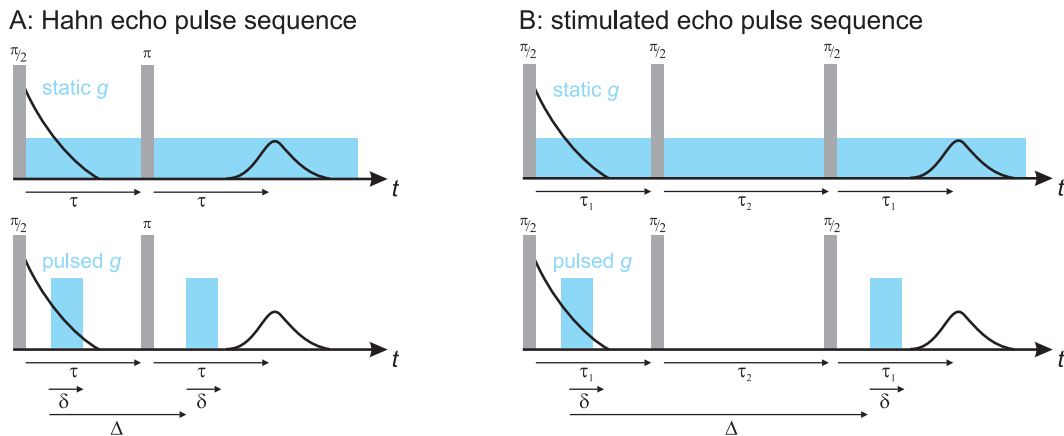


Figure 2.14: Pulse sequences for static and pulsed FG NMR. A: Hahn echo pulse sequence, B: stimulated echo pulse sequence.

fluctuations and, thus, to an echo decay.

Commonly used pulse sequences for FG NMR are shown in Fig. 2.14. The respective decay of the echo amplitude due to relaxation and 3D isotropic diffusion is given as:

For the Hahn echo and SFG NMR:

$$I/I_0(2\tau) = \exp\left(-2\tau R_2 - \frac{2}{3}D\gamma^2 g^2 \tau^3\right) \quad (2.174)$$

For the stimulated echo and SFG NMR:

$$I/I_0(2\tau_1 + \tau_2) = \exp\left(-2\tau_1 R_2 - \tau_2 R_1 - D\gamma^2 g^2 \tau_1^2 (\tau_1 + \tau_2)\right) \quad (2.175)$$

or the Hahn echo and PFG NMR:

$$I/I_0(2\tau) = \exp\left(-2\tau R_2 - D\gamma^2 g^2 \delta^2 \left(\Delta - \frac{\delta}{3}\right)\right) \quad (2.176)$$

For the stimulated echo and PFG NMR:

$$I/I_0(2\tau_1 + \tau_2) = \exp\left(-2\tau_1 R_2 - \tau_2 R_1 - D\gamma^2 g^2 \delta^2 \left(\Delta - \frac{\delta}{3}\right)\right) \quad (2.177)$$

Hereby, the meaning of the different time constants τ , τ_1 , τ_2 , Δ and δ is visualized in Fig. 2.14. D is the tracer diffusion coefficient, g is the field gradient and γ the gyromagnetic ratio of the observed nucleus. R_1 and R_2 are the SLR and SSR rates. PFG NMR experiments are usually performed with constant times τ_1 , τ_2 , Δ and δ . The only quantity that is changed in a series of measurements is the amplitude of the pulsed field gradient g . Then, the decay of the echo due to relaxation does not play any role. This, of course, is not possible in SFG NMR. However, the decay due to diffusion shows a different dependence on τ than relaxation. Therefore, from the shape of the decay, it is possible to decide whether it is due to diffusion or relaxation. Measuring the relaxation rates R_1 and R_2 at the same field but without a gradient in a separate experiment allows one to reduce the quantity of adjustable fit parameters and usually leads to more accurate diffusion coefficients.

For further details, see, *e. g.* Refs. [97–105]

Stimulated echo and two-site exchange

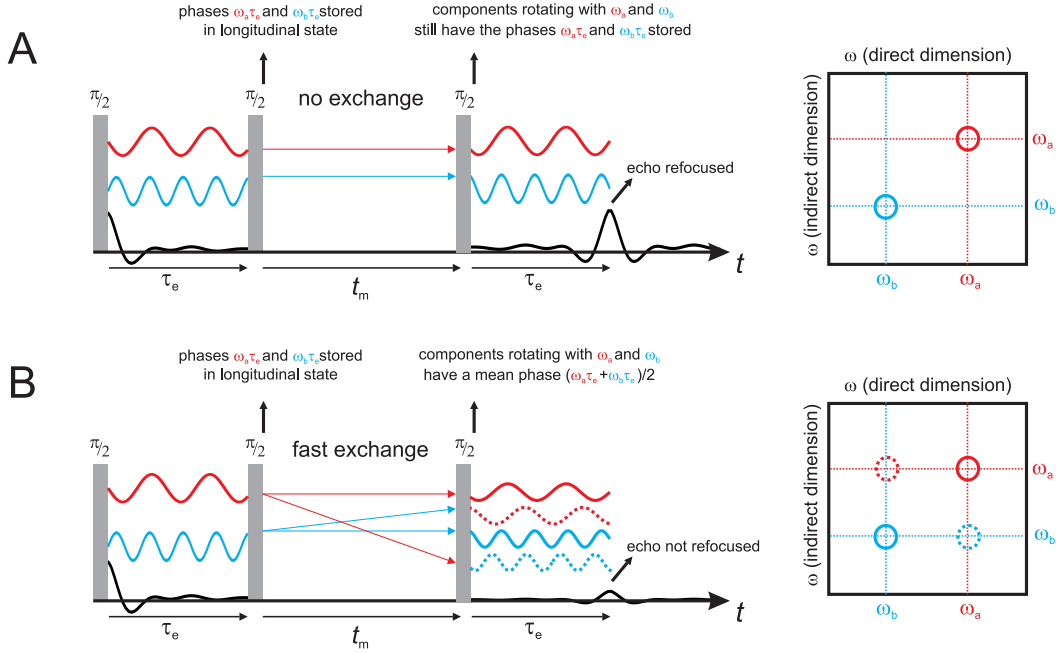


Figure 2.15: Scheme of the 2D exchange NMR and SAE NMR. See text for further details.

(x) Stimulated Echoes and 2D exchange NMR

Stimulated echo pulse sequences $[90_{\phi_1}^{\circ} - \tau_e - 90_{\phi_2}^{\circ} - t_m - 90_{\phi_3}^{\circ} - \tau_e - echo]$ with $\phi_2 = \phi_1 \pm 90^{\circ}$ and suitable phase cycling can be used to study exchange between sites with (i) different chemical shift, and thus, different Larmor frequency $\omega_{\delta} = (1 - \sigma)\omega_0$ or (ii) with different quadrupolar frequency ω_Q . The underlying principle is shown in Fig. 2.15: the first, say, x' pulse rotates the magnetization to the $-y'$ axis. Now, due to different site-specific frequencies ω_i (ω_{δ} or ω_Q), the respective spin packages M_i will acquire a phase shift $\omega_i\tau_e$ during τ_e . The second pulse rotates the components $M_i \sin(\omega_i\tau_e)$ into a longitudinal state. In the absence of exchange processes during t_m (Fig. 2.15A), the third pulse simply rotates the spin packages $M_i \sin(\omega_i\tau_e)$ back into the transversal plane and after τ_e , the echo is observed. However, if the spin packages have another frequency ω_i after t_m , they will not be refocused at the echo after τ_e (Fig. 2.15B). In 2D exchange NMR, the evolution time τ_e is varied. Performing a Fourier transformation along the direct dimension (echo decay) and the indirect dimension τ_e yields the 2D spectra shown on the right-hand side of Fig. 2.15. In the absence of exchange, only diagonal peaks (auto-correlations) are observed. Exchange (due to jumps or spin diffusion) gives rise to off-diagonal peaks (cross-correlations). By varying the mixing time t_m , the exchange dynamics can be studied.

Clearly, to obtain resolved 2D spectra, single crystals or MAS conditions are required. However, for powder samples it is still possible to study the decay of the amplitude at the echo top with t_m . Only the auto-correlations give rise to the amplitude at the echo top. In the case of Li, the chemical shift range is not large enough to record Larmor-frequency auto-correlation functions, but it is possible to record quadrupolar frequency auto-correlation functions, *e. g.* by using the Jeener-Broekaert spin-alignment-echo (SAE) pulse sequence [106] $[90_{\phi_1}^{\circ} - \tau_e - 45_{\phi_2}^{\circ} - t_m - 45_{\phi_3}^{\circ} - \tau_e - echo]$

with $\phi_2 = \phi_1 \pm 90^\circ$ and a suitable phase cycling generating the \hat{T}_{20} (for the definition of irreducible tensor operators, see *e.g.* Refs. [60–64]) state during the mixing time. Then, the echo amplitude (neglecting relaxation) is given as:

$$I/I_0(t_m, \tau_e) = \frac{\langle \sin(\omega_Q(0) \cdot \tau_e) \sin(\omega_Q(t_m) \cdot \tau_e) \rangle}{\langle \sin(\omega_Q(0) \cdot \tau_e) \sin(\omega_Q(0) \cdot \tau_e) \rangle} \quad (2.178)$$

The decay of the echo function is the auto-correlation function of the quadrupolar frequencies. If every jump goes along with a change of the quadrupolar frequency, the one-particle-two-time correlation function is equal to this correlation function. Therefore, in many cases, the SAE technique can be used to study slow Li dynamics. [26, 107–113]

Note that atomic jumps are not the only mechanism that can lead to an echo decay. Spin diffusion (T-independent!) and relaxation may lead to an echo decay which is not related to atomic jumps. Very fast fluctuations of the quadrupolar frequency (faster than SSR) are not observed since in this case, the quadrupolar frequencies are already averaged during τ_e . This rules out an SAE decay due to fast forward-backward jumps or (generally) jumps to sites with very short life time and limits the technique to be used in and slightly above the rigid lattice. The same, clearly, holds for 2D exchange.

(xi) Magic-Angle Spinning NMR

The secular components of the first-order Hamiltonians of the chemical shift interaction, magnetic dipolar interaction, and the electric quadrupolar interaction show an orientation dependence containing the term $(3 \cos^2 \Theta - 1)$. For $\Theta \approx 54.74^\circ$, the magic angle, this term is zero. In a powder sample, there are always many different orientations of Θ , (i) due to different orientations of crystallites and (ii) due to different orientations of the site-specific principle axis frames within one crystallite. However, if the powder sample with many different orientations is rotated along the magic-angle axis (with respect to the external field B_0), averaged over a rotation period, all sites are aligned at the magic angle. Therefore, if a sample is rotated along the magic angle fast enough (much faster than the respective coupling constants), sharp lines and high resolution is obtained. Line broadening due to dipolar interactions and chemical shift anisotropies can usually be eliminated by MAS NMR. In contrast, for many quadrupolar nuclei residing in non-cubic sites, the quadrupolar coupling constants are larger than technically available spinning rates. However, for half-integer nuclei, the central transition - which is not affected by the quadrupolar coupling to first order - is often narrowed by the MAS technique. However, now, the intensities are no longer proportional to the spin density in the sample. Additionally, in the case of very strong quadrupolar coupling, second-order effects affect the central transition, as well. The second order interactions have a different orientation dependence and therefore are not averaged to zero by the MAS technique. So, other NMR techniques like MQMAS NMR [114] or higher fields (which reduce the second-order interactions) allow one to improve the resolution further.



Contents lists available at SciVerse ScienceDirect

Solid State Nuclear Magnetic Resonance

journal homepage: www.elsevier.com/locate/ssnmr

NMR relaxometry as a versatile tool to study Li ion dynamics in potential battery materials

A. Kuhn^a, M. Kunze^b, P. Sreeraj^c, H.-D. Wiemhöfer^c, V. Thangadurai^d, M. Wilkening^{a,e,*}, P. Heitjans^{a,e}^a Institute of Physical Chemistry and Electrochemistry, Leibniz University Hannover, Callinstr. 3-3a, 30167 Hannover, Germany^b MEET – Münster Electrochemical Energy Technology, University of Münster, Corrensstr. 46, D-48149 Münster, Germany^c Institute of Inorganic and Analytical Chemistry, University of Münster, Corrensstr. 28-30, D-48419 Münster, Germany^d Department of Chemistry, University of Calgary, 2500 University Drive NW, Calgary, Alberta, Canada T2N 1N4^e ZFM – Center for Solid State Chemistry and New Materials, Leibniz University Hannover, D-30167 Hannover, Germany

ARTICLE INFO

Available online 9 February 2012

Keywords:

Li ion dynamics
NMR spin–lattice relaxation
Battery materials
Li₇La₃Zr₂O₁₂
Li₁₂Si₇

ABSTRACT

NMR spin relaxometry is known to be a powerful tool for the investigation of Li⁺ dynamics in (non-paramagnetic) crystalline and amorphous solids. As long as significant structural changes are absent in a relatively wide temperature range, with NMR spin–lattice (as well as spin–spin) relaxation measurements information on Li self-diffusion parameters such as jump rates and activation energies are accessible. Diffusion-induced NMR relaxation rates are governed by a motional correlation function describing the ion dynamics present. Besides the mean correlation rate of the dynamic process, the motional correlation function (i) reflects deviations from random motion (so-called correlation effects) and (ii) gives insights into the dimensionality of the hopping process. In favorable cases, *i.e.*, when temperature- and frequency-dependent NMR relaxation rates are available over a large dynamic range, NMR spin relaxometry is able to provide a comprehensive picture of the relevant Li dynamic processes. In the present contribution, we exemplarily present two recent variable-temperature ⁷Li NMR spin–lattice relaxation studies focussing on Li⁺ dynamics in crystalline ion conductors which are of relevance for battery applications, *viz.* Li₇La₃Zr₂O₁₂ and Li₁₂Si₇.

© 2012 Elsevier Inc. All rights reserved.

1. Introduction

Materials being suitable for all-solid-state lithium-ion battery applications benefit from a high Li⁺ self-diffusivity [1–3]. Investigating the Li ion dynamics by nuclear magnetic resonance (NMR) methods helps to identify potential electrode and electrolyte materials. In particular, classical NMR spin–lattice relaxometry is a powerful and reliable tool to determine Li self-diffusion parameters in (non-paramagnetic) ion conductors fairly independent of a diffusion model [4–11]. A complete NMR spin–lattice relaxation (SLR) study, if applicable, includes the temperature- and frequency-dependent measurement of spin–lattice relaxation rates in both the laboratory (R_1) and rotating frame of reference ($R_{1\rho}$). While R_1 measurements are sensitive to jump rates in the order of the Larmor frequency ω_0 ($\approx 10^9$ s⁻¹), with the help of $R_{1\rho}$ measurements, lithium jump rates in the order of the applied

locking frequency ω_1 ($\approx 10^5$ s⁻¹) can be probed. NMR spin–spin relaxation (SSR) measurements, which are sensitive to slower Li diffusion processes with rates of the order of approximately 10⁴ s⁻¹, complement an NMR spin relaxometry study. Even slower Li hopping dynamics can be probed by analyzing stimulated echoes generated with the Jeener-Broekaert pulse sequence [10,12–19].

Since quantitative information is obtained from the maximum, the slopes and the absolute value of the characteristic diffusion-induced SLR NMR rate peaks, ideally a large temperature range has to be covered. The informative value of a single SLR or SSR measurement is very limited. As a result, the applicability of the technique is restricted to materials which do not undergo significant structural changes. Provided such changes are absent, activation energies (E_A) and jump rates (τ^{-1}) of the underlying diffusion processes can be extracted from NMR relaxation data. Usually, the jump rates (τ^{-1}) follow Arrhenius behavior according to

$$\tau^{-1} = \tau_0^{-1} \exp(-E_A/(k_B T)) \quad (1)$$

with the pre-exponential factor τ_0^{-1} being expected in the order of phonon frequencies. Additionally, the analysis of the measured NMR SLR rates yields information on the auto-correlation function

* Corresponding author. Present address: Graz University of Technology, Institute for Chemistry and Technology of Materials, Stremayrgasse 9/Z3, A-8010 Graz, Austria.

E-mail addresses: kuhn@pci.uni-hannover.de (A. Kuhn), wilkening@pci.uni-hannover.de, wilkening@tugraz.at (M. Wilkening), heitjans@pci.uni-hannover.de (P. Heitjans).

describing the motional process. Moreover, by comparing features of the NMR relaxation data with those expected from different diffusion models, the dimensionality of a diffusion process can be probed [4,5,14,20–26].

After presenting the basics of NMR relaxation measurements in Section 2, in Sections 3 and 4, we showcase two recent NMR SLR studies on Li ion conductors viz. garnet-like $\text{Li}_7\text{La}_3\text{Zr}_2\text{O}_{12}$ and the Zintl-phase $\text{Li}_{12}\text{Si}_7$, respectively. While garnets are currently investigated to be used as solid electrolytes, Li containing silicides are considered to act as efficient (high-capacity) anode materials.

2. Basics of NMR relaxometry

2.1. Principle ideas of the most common measuring techniques

In a simplified view Fig. 1(A) depicts the basic idea of an NMR SLR rate measurement. Let us consider a spin system exposed to a homogeneous external magnetic field \vec{B}_0 . In thermal equilibrium, the Zeeman levels are populated according to Boltzmann's distribution giving rise to an equilibrium magnetization $\vec{M}_z = \vec{M}_{\text{eq}}$ which is parallel to \vec{B}_0 . By using appropriate radio frequency (RF) pulses, well-defined non-equilibrium states can be generated. For example, a saturation comb, consisting of a number of $(\pi/2)_x$ -pulses, can be used to fully destroy the initial magnetization, see Fig. 1(A). After this perturbation, the spin system will tend to relax back to thermal equilibrium. In many cases, the corresponding SLR transients $M_z(t_{\text{var}})$, reflecting the recovery of longitudinal magnetization, follow exponential time behavior. The associated rate constant is the so-called NMR spin–lattice relaxation rate R_1 which is a measure of the transition probability of the spins between distinct Zeeman levels. The transients $M_z(t_{\text{var}})$ can be recorded in several measurements by applying a detection pulse after a variable delay time t_{var} .

The NMR SLR process is caused by transitions between the Zeeman levels. Due to the low Zeeman splitting energy, only induced transitions play a role. For example, resonant fluctuations of spin interactions due to motional processes induce Zeeman transitions. NMR SLR becomes effective, i.e., the transition probability is at its maximum, when the correlation rate of the motional process τ_c^{-1} is similar to the Larmor frequency ω_0 characterizing the splitting of the Zeeman levels according to $\omega_0 = -\gamma_m \vec{B}_0$. γ_m denotes the magnetogyric ratio of the nucleus under investigation [20]. Therefore, in an external magnetic field of several Tesla, an NMR SLR rate maximum is expected at a temperature where the correlation rate of the motional process τ_c^{-1} is in the order of $\omega_0 \approx 10^9 \text{ s}^{-1}$. This is the regime of very fast motion. Increasing or decreasing the magnetic field B_0 (usually in the range from 1 to 21 T) shifts the maximum of the diffusion-

induced rate peak $R_1(1/T)$ towards higher and lower temperatures, respectively.

Owing to the bad signal-to-noise ratio at very low magnetic fields it is not feasible to perform conventional NMR experiments at B_0 values smaller than 1 T. Therefore, slow motions are difficult to extract with NMR SLR measurements performed in the laboratory frame of reference. These might be probed by field-cycling NMR techniques [27,28] which, to our knowledge, have up to now not been applied to the study of Li ion dynamics with ^7Li or ^6Li probes.

Another NMR technique capable of measuring SLR rates in the laboratory reference frame at $B_0 (< 1 \text{ T})$ is β -radiation detected NMR (β -NMR) [29]. A well suited probe is the β -active isotope ^8Li ($t_{1/2} = 0.8 \text{ s}$). The ^8Li nuclei (spin quantum number $I=2$) are produced and spin-polarized *in situ* by capture of polarized cold neutrons ($I=1/2$) by ^7Li ($I=3/2$) in the sample to be studied. The resulting ^8Li spin polarization is, thus, not governed by Boltzmann's distribution, and its relaxation to equilibrium due to, e.g., resonance with internal fluctuating fields can be readily monitored via the angular β -radiation distribution. The measurement of the spin–lattice relaxation rate is restricted to a window of at most $0.01/t_{1/2} < R_1 < 100/t_{1/2}$ [29,30]. Investigations of Li ion dynamics in quite a number of crystalline and amorphous Li containing solids were carried out at an early date via ^8Li β -NMR SLR rate measurements (see Refs. [30,31] for reviews). While these studies were mainly oriented towards fundamental aspects of Li diffusion, some of the investigated model systems, e.g., LiC_6 , [32,33] LiC_{12} , [34] LiAl , [35], and LiMg [36] have also been considered as Li battery materials. It is noted that in a study on diffusion-induced ^8Li SLR in Li metal [37] it was exemplarily shown that the gap between the field/frequency ranges covered by conventional ^7Li NMR SLR measurements in (i) the laboratory and (ii) the rotating reference frame (to be discussed below) can be bridged by β -NMR.

Diffusion processes with jump rates in the order of 10^5 s^{-1} can be studied by NMR SLR measurements using the spin-locking technique being carried out in the rotating frame of reference [38–43]. The principle idea of a $R_{1\varrho}$ measurement is depicted in Fig. 1(B). The first $(\pi/2)_x$ pulse tips the magnetization to the $(-y')$ axis. (The prime ' denotes the axes of the rotating frame which rotates at a frequency ω_0 along the magnetic field axis). This pulse is followed by the so-called locking pulse with the phase $-y'$. In the rotating frame, it appears as a static magnetic field along the $(-y')$ -axis and gives rise to Zeeman splitting along the rotating frame quantization axis $-y'$. Usually, the pulsed field $B_1 = \omega_1/\gamma_m$ is in the order of some mT which is about three orders of magnitude lower than the external field B_0 . Accordingly, the corresponding Zeeman splitting is much smaller than that for NMR SLR performed in the laboratory frame of reference. Because the initial population difference is much higher than the expected value for Boltzmann's distribution, the spin system relaxes towards the new state defined by the locking field B_1 being characterized by a much lower y' -magnetization. The associated magnetization transients $M_{-y'}(t_{\text{lock}})$, containing the temperature-dependent rate constant $R_{1\varrho}$, can be recorded by varying the length t_{lock} of the locking pulse. Since the residual transversal magnetization, showing up after the locking pulse, directly gives rise to a free induction decay (FID) no additional detection pulse is needed.

Again, the (rotating frame) Zeeman transitions are induced by fluctuating interactions of the spins with internal magnetic dipolar or electric quadrupolar fields. In contrast to NMR SLR in the laboratory frame, $R_{1\varrho}$ measurements are, due to the much smaller Zeeman splitting, sensitive to fluctuations in the kHz range, thus, useful to close the gap between NMR SLR and methods able to probe motions with jump rates smaller than 10^4 s^{-1} [19,14].

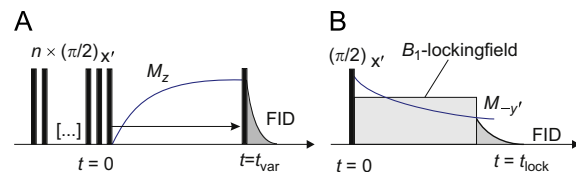


Fig. 1. (A) Principle of an NMR R_1 measurement with the saturation recovery pulse sequence: A comb of closely spaced rf-pulses $(\pi/2)_x$ ($n \approx 10$) destroys the (initial) longitudinal magnetization ($M_z = M_{\text{eq}}$) so that $M_z = 0$ at $t = 0$. The subsequent recovery of $M_z(t)$ is probed with a single $\pi/2$ -pulse which is sent after a variable relaxation delay $t = t_{\text{var}}$. In most cases, $M_z(t_{\text{var}})$ can be approximated by a (stretched) exponential function: $M_z(t_{\text{var}}) = M_{\text{eq}} - \exp(-(t_{\text{var}} \cdot R_1)^y)$ with $0 < y \leq 1$. (B) Principle of an $R_{1\varrho}$ measurement: After a $\pi/2$ -pulse the magnetization $M_{-y'}$ is locked by a B_1 -field. Compared to the preparation pulse, the corresponding locking pulse is phase-shifted by $-\pi/2$. The decay of $M_{-y'}$ is probed as a function of the locking pulse length t_{lock} .

The spin–spin (or transverse) relaxation (SSR) rate R_2 can be understood as the limit of $R_{1\rho}$ for $\omega_1 \rightarrow 0$. It is, however, measured differently, e.g., by using the well-known Hahn-Echo pulse sequence or, as in the case of solids, by the solid-echo pulse sequence.

2.2. NMR relaxation in terms of spectral densities $j(\omega)$

As mentioned in the foregoing section, fluctuating spin interactions, being caused by diffusion processes, for example, are responsible for NMR relaxation. These include homo- and heteronuclear dipole–dipole couplings (also those to paramagnetic centers) and, if nuclei with a spin-quantum number I larger than $1/2$ nuclei are considered, the quadrupolar coupling to (non-vanishing) electric field gradients. The various interactions influence the Zeeman levels resulting in distinct shifts $\Delta\omega$ of the Larmor frequencies of the interacting spin(s). Since the interactions depend on the (relative) positions of the spin(s), they are altered by motional processes giving rise to the aforementioned fluctuations of $\Delta\omega$. In a simple approach, they can be described by an NMR correlation function $G(t)$:

$$G(t) = \langle \Delta\omega(0) \cdot \Delta\omega(t) \rangle = G(0) \cdot g(t) \quad (2)$$

Hereby the brackets denote the ensemble average of a powder sample. Let us note that $G(t)$ is not identical with the motional correlation function. However, the correlation function certainly contains the temporal information on the dynamic processes because it reflects the spatial and angular dependences of the spin interactions described by the associated Hamiltonians. The exact form of $G(t)$ depends on both the (relevant) spin interactions and the diffusion mechanism. For random dynamics, $G(t)$ is a function which monotonically decays from $G(0)$ to zero with $G(0)$ being a measure of the interaction strength. In the most simple case, i.e., for isotropic random motion, $g(t)$ is a single exponential (see also the next section) with the decay constant being the correlation rate of the motional process τ_c^{-1} . Certainly, the consideration of multiple interactions of the spins as well as anisotropic and/or non-random (correlated) motion gives rise to more complex correlation functions, see Section 2.3.

In order to describe an NMR relaxation process, we are interested in the components of the spectral density function $j(\omega)$ at $\omega = \omega_0$ (and $\omega = \omega_1$). $j(\omega)$, which is directly proportional to R_1 (and $R_{1\rho}$), is readily obtained by Fourier transformation of the correlation function $g(t)$:

$$j(\omega) = \int_{-\infty}^{\infty} g(t) \exp(-i\omega t) dt \quad (3)$$

A stringent derivation and closed theoretical description based on first order perturbation theory for (homonuclear) magnetic dipolar (as well as electric quadrupolar) relaxation [5,20–22,44] yields:

$$R_1 = G(0) \cdot \left[\frac{1}{3} j(\omega_0) + \frac{4}{3} j(2\omega_0) \right] \quad (4)$$

$$R_{1\rho} = G(0) \cdot \left[\frac{1}{2} j(2\omega_1) + \frac{5}{6} j(\omega_0) + \frac{1}{3} j(2\omega_0) \right] \quad (5)$$

$$R_2 = G(0) \cdot \left[\frac{1}{2} j(0) + \frac{5}{6} j(\omega_0) + \frac{1}{3} j(2\omega_0) \right] \quad (6)$$

As mentioned above, $G(0)$ reflects the interaction strength of the spins with local magnetic fields or electric field gradients. In case of homonuclear dipolar relaxation it is equal to the second moment which can be either calculated using the well-known van-Vleck formula [45] or determined from the static line in the rigid lattice.

2.3. BPP model for 3D isotropic random diffusion

As mentioned above, the function $g(t)$ introduced in Eq. (2), is not identical with the motional correlation function; rather, it has the character of an NMR (frequency) correlation function. Therefore, also the angular dependencies of the interaction Hamiltonians have an impact on $g(t)$ which is by no means negligible in the case of anisotropic or even spatially confined motion. In such cases, i.e., when NMR has to be used to collect information on geometric properties of a given diffusion process, the predictions of suitable diffusion models are helpful to interpret the data, which, at the best, have been measured as a function of both temperature and frequency.

When the diffusion process is isotropic, quite often, the temperature and frequency dependence of NMR rates can be well described with the model introduced by Bloembergen, Purcell and Pound. In the so-called BPP-ansatz [20], which is valid for uncorrelated three-dimensional motion, the corresponding correlation function $g(t)$ is given by a single exponential, $g(t) = \exp(-|t|/\tau_c)$ with the correlation rate τ_c^{-1} given by $\tau_c^{-1} = \tau_{c0}^{-1} \exp(-E_A/(k_B T))$, which results in a Lorentzian shaped spectral density term $j(\omega) (\propto R_{1(\omega)})$:

$$j(\omega) = \frac{2\tau_c}{1 + (\omega\tau_c)^2} \quad (7)$$

For example, in the case of $R_1(\omega_0)$ this yields

$$R_1(\omega_0) = \frac{2}{3} G(0) \cdot \left[\frac{\tau_c}{1 + (\omega_0\tau_c)^2} + \frac{4\tau_c}{1 + (2\omega_0\tau_c)^2} \right] \quad (8)$$

Again, in the case of homonuclear magnetic dipolar interaction, the interaction strength $G(0)$ can be obtained from the van-Vleck formula [45] by taking into account the distances and coordination numbers of the interacting spins in the structure. Alternatively, the order of the dipolar coupling constant can be estimated from the NMR line width or the R_2 rate recorded in the temperature regime of the rigid-lattice ($R_{20} = \sqrt{G(0)}$). For comparison, the interaction strength of electric quadrupolar coupling is related to the different electric field gradients the nuclei are “sensing” while diffusing. It is in the order of the squared quadrupole coupling constant δ_q (see above) [21,46,47,44] that can also be extracted from NMR spectra recorded at low T . Provided the orientation of the corresponding quadrupole coupling tensor remains unchanged, not the absolute value of δ_q but the difference of two (or more) coupling constants at different crystallographic sites lead to the fluctuations responsible for relaxation. If ion hops between sites with practically the same δ_q are considered, then the orientation dependence of the tensor determines spin–lattice relaxation. For heteronuclear dipolar relaxation and dipolar relaxation at paramagnetic impurity centers, the theoretical description is more complicated [21,48,5,49] and will be briefly discussed in the next sections where necessary.

Deviations from a single exponential NMR correlation function $g(t)$ are rather the rule than the exception. Quite often, such deviations reflect correlated motion which may be caused by, for example, (i) a vacancy diffusion mechanism, (ii) structural disorder, and (iii) Coulombic interactions of the spins. However, irrespective of the microscopic origin, the deviations from uncorrelated motion can satisfactorily taken into account by replacing the single exponential by a stretched exponential [50,4,51–54]:

$$g(t) = \exp(-(|t|/\tau_c)^\alpha) \quad (9)$$

The stretching exponent α ranges from 0 to 1. The corresponding Fourier transform is given by

$$j(\omega) = \frac{2\tau_c}{1 + (\omega\tau_c)^{1+\alpha}} \quad (10)$$

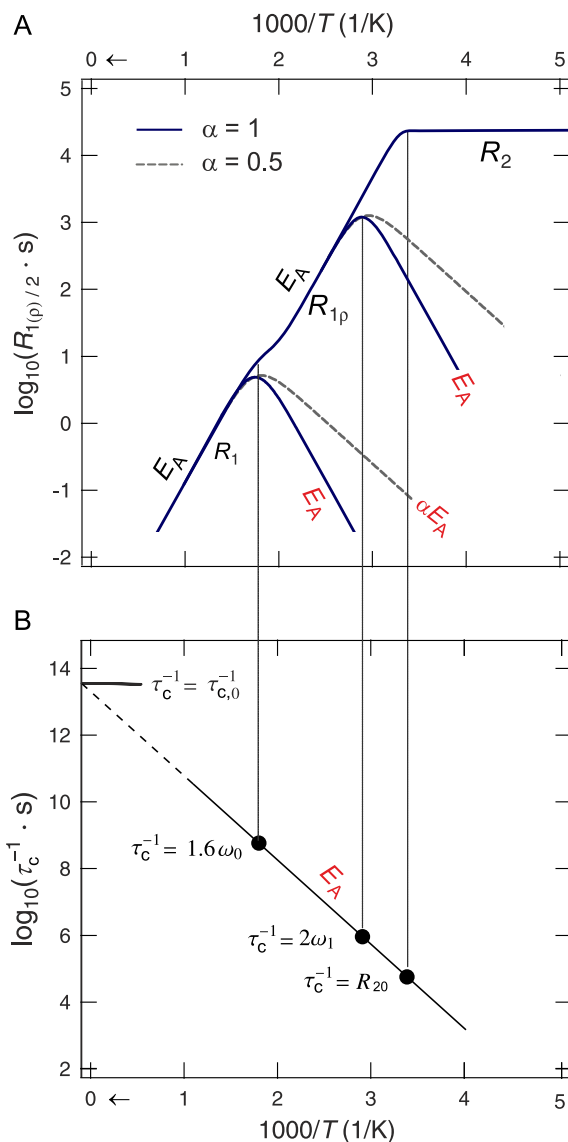


Fig. 2. (A) Calculated relaxation rates R_1 , $R_{1\rho}$, and R_2 for homonuclear dipolar relaxation and 3D, isotropic diffusion using $\omega_0/2\pi=77.7$ MHz and $\omega_1/2\pi=80$ kHz. The Arrhenius parameters were chosen to be $E_A=0.5$ eV and $\tau_0^{-1}=5 \times 10^{-14} \text{ s}^{-1}$. The rate R_2 in the rigid-lattice was $R_{20}=2 \times 10^4 \text{ s}^{-1}$. While the solid lines represent uncorrelated motion ($\alpha=1$), the dashed line shows the behavior found for correlation effects, here $\alpha=0.5$. (B) Arrhenius plot illustrating how NMR correlation rates can be determined from the curves shown in (A). Li jump rates can be extracted from the corresponding NMR SLR rate peaks and the temperature dependence of R_2 . Within a factor of two, the Li jump rate τ^{-1} is identical with the correlation rate τ_c^{-1} , see, e.g., Ref. [37].

As an example, in the Arrhenius diagram of Fig. 2(A), the temperature dependencies of the various BPP-type NMR relaxation rates are shown. The maximum conditions of the NMR rate peaks are given by $\omega_0 \approx 0.6\tau_c^{-1}$ and $\omega_1 = 0.5\tau_c^{-1}$, respectively [20,42]. For uncorrelated, three-dimensional motion, the rate peaks are symmetric with the slope representing the activation energy E_A of the motional process, see, e.g., Ref. [55]. In the low-temperature ($\omega\tau_c \gg 1$) and high-temperature ($\omega\tau_c \ll 1$) limit, the NMR SLR rates

are proportional to $\tau_c^{-1}\omega^{-2}$ and τ , respectively. Additionally, in Fig. 2 NMR SLR rates calculated using the modified BPP model (see Eq. (10)), which accounts for deviations from uncorrelated motion, are included. Note that the effects arising from correlated motion appear on the low-temperature flank only. The corresponding slope is reduced by α yielding E_A which is given by αE_A .

This is in contrast to those effects which arise from diffusion in confined dimensions. In such cases, characteristic deviations from BPP-behavior appear on the high-temperature flank [5,4]. It is typical of low-dimensional diffusion that the flanks in the limit $\omega\tau_c \ll 1$ reveal a smaller slope compared to the 3D BPP case [5]. Moreover, the diffusion-induced NMR SLR rates in the high-temperature range depend on the Larmor (and locking frequency) applied. The limiting cases are, however, sensitive to the exact microscopic diffusion model.

Note that the foregoing results exclusively deal with spin-1/2 nuclei. However, both natural Li isotopes are quadrupolar nuclei [$I(^6\text{Li})=1$, $I(^7\text{Li})=3/2$]. In this case, most prominently quadrupolar relaxation can take place. Consequently, the relaxation transients are no longer governed by a single exponential but by the sum of two exponentials [47] (see also ref. [36], the Appendix in particular). Further effects leading to non-exponential relaxation transients might include, for example, (i) the presence of two or more dynamically separated spin reservoirs [56,57,4] or (ii) the effect of inhomogeneous averaging when relaxation takes place at localized relaxation centers and spin diffusion, i.e., magnetization transfer among neighboring nuclei, is absent, which results in a stretched exponential of the nuclear magnetization with $\gamma=0.5$, see Refs. [58,59].

3. Case studies – probing Li jump rates by NMR spin–lattice relaxation

3.1. Li NMR spin–lattice relaxation rates of garnet-type tetragonal $\text{Li}_7\text{La}_3\text{Zr}_2\text{O}_{12}$

In Fig. 3(A), NMR relaxometry data for $\text{Li}_7\text{La}_3\text{Zr}_2\text{O}_{12}$ crystallizing with tetragonal symmetry are shown. The NMR SLR rates R_1 were measured at two Larmor frequencies $\omega_0/2\pi$ (77.7 MHz and 155.4 MHz) using the saturation recovery technique (see above). The corresponding NMR SLR rates in the rotating frame ($R_{1\rho}$) were recorded at $\omega_0/2\pi=77.7$ MHz using the spin-lock technique with a pulsed locking frequency $\omega_1/2\pi=30$ kHz. At first glance, the diffusion-induced rate peaks are very similar to the calculated ones shown in Fig. 2. From the maxima of the SLR peaks, the motional correlation rates can be obtained which are within a factor of two identical with the Li jump rates, see, e.g., Ref. [37]. The rates are included in the Arrhenius diagram of Fig. 3(B). For comparison, Li jump rates deduced from dc-conductivity measurements [60,11] are also shown. The solid line in Fig. 3(B) represents an Arrhenius fit according to Eq. (1) and yields an activation energy of $E_A=0.52(2)$ eV, see Ref. [11].

A closer look at the NMR data shown in Fig. 3(A) exhibits an interesting deviation from the behavior expected for pure homonuclear dipolar relaxation (cf. Fig. 2). Interestingly, the $R_{1\rho}$ (and R_2) rates measured at high temperatures do not coincide with the R_1 rates. In this temperature range, the rates R_2 are much larger than expected from an estimation of the interaction strength from R_{20} . This is accompanied by a shift of the onset of the diffusion-induced decrease of the R_2 towards higher temperatures. For comparison, the interaction strength, which can be estimated from R_{20} under the assumption of homonuclear dipolar relaxation, turned out to be an order of magnitude too low to account for the absolute rates measured in the narrowing regime. In contrast to that, but as expected, ^7Li NMR line narrowing sets in

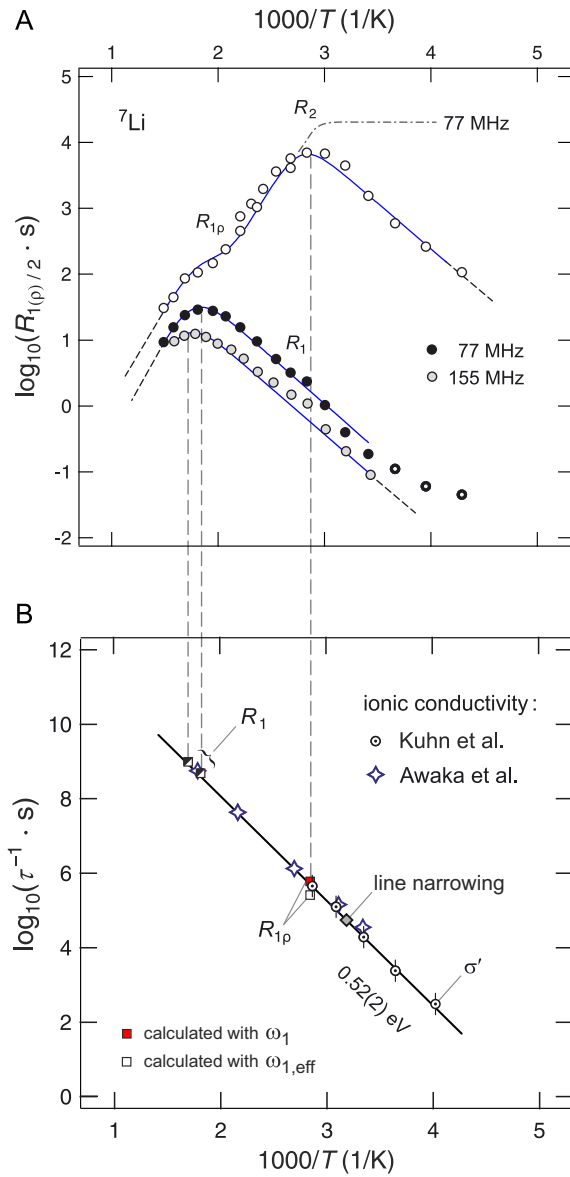


Fig. 3. (A) ${}^7\text{Li}$ NMR SLR rates R_1 and $R_{1\rho}$ of tetragonal $\text{Li}_7\text{La}_3\text{Zr}_2\text{O}_{12}$ measured with the saturation recovery pulse sequence at 77 and 155 MHz. Data were taken from Ref. [11] where the experimental details are described. The solid lines represent a global fit with the Arrhenius parameters given by the Arrhenius line in (B). The dashed-dotted line indicates the temperature dependence of R_2 . (B) Li jump rates extracted from the NMR spin-lattice relaxation data. For comparison, corresponding Li jump rates deduced from conductivity data, see Awaka et al. [60] and Kuhn et al. [11], are also shown. The solid line represents the Arrhenius line obtained from the global fit analysis, see also Ref. [11], of the NMR relaxation rates. Note that the rates deduced from $R_{1\rho}$ measurements were either calculated by using $\omega_1\tau \approx 0.5$ or by using an effective locking frequency, $\omega_{1\text{eff}}\tau \approx 0.5$, taking into account local magnetic fields.

at much lower temperatures (cf. Ref. [49]). Note that in samples with a large concentration of paramagnetic centers, even a motional broadening may be observed [5]. For the sake of completeness, the Li jump rate estimated from ${}^7\text{Li}$ NMR line narrowing, taken from Ref. [11], is also included in Fig. 3(B).

Here, the ratio of $R_{1\rho}$ (or R_2) and R_1 found is approximately $R_{1\rho}/R_1=4$. This result is expected for dipolar relaxation at paramagnetic centers when spin-3/2 nuclei are considered, see Refs. [61,5]. Furthermore, the ratio $R_1({}^7\text{Li})/R_1({}^6\text{Li}) \approx 2$, which has been measured at comparable Larmor frequencies ω_0 , also suggests a dipolar rather than a quadrupolar NMR relaxation mechanism in the garnet studied. The corresponding ratio in the case of quadrupolar NMR spin-lattice relaxation is expected to be much larger, see, e.g., the study of Pietrass et al. on Li_xSnS_2 [62].

The suggestion that dipolar relaxation at paramagnetic centers is the relevant relaxation mechanism, is corroborated by analyzing the different NMR SLR rates with a global-fit procedure as described in [11]. A satisfying joint fit, by which the SLR rates are linked with each other, is only obtained if $\omega_1 = \omega_{\text{lock}}$ is replaced by an effective locking field $\omega_{1\text{eff}} = \omega_{\text{lock}} + \omega_{\text{local}}$. By comparing the rates R_1 and R_2 , a local field ω_{local} can be estimated which is larger than the pulsed one. Therefore, relaxation events taking place in the vicinity of paramagnetic impurities, characterized by their large magnetic moments, dominate the relaxation rates measured. For comparison, in Fig. 3 the corresponding Li jump rate associated with the $R_{1\rho}(1/T)$ -peak is estimated using $\omega_1\tau \approx 0.5$ as well as $\omega_{1\text{eff}}\tau \approx 0.5$ (see the unfilled square in Fig. 3). Here, it turned out that $\omega_{1\text{eff}} \approx 3\omega_1$, see Ref. [11]. The global fit is represented by solid lines in Fig. 3(A). It takes into account a stretched exponential correlation function $g(t)$ and yields $E_A \approx 0.5$ eV, $\tau_0 \approx 1 \times 10^{-14}$ s $^{-1}$, and $\alpha \approx 0.5$. Relaxation of spin-3/2 nuclei at paramagnetic impurities, i.e., $R_2/R_1 = 4$ in the limit $\omega_0\tau \ll 1$, was taken into account by multiplying the spectral density terms in ω_0 and $2\omega_0$ by the factor of four. As mentioned above, the local field was estimated from the interaction strength obtained from fitting the R_1 and R_2 data only.

For comparison, in Fig. 3(B) Li jump rates deduced from both NMR rate maxima ($R_1(1/T)$, $R_{1\rho}(1/T)$) and dc-conductivity measurements (see Ref. [11]) are shown. The Arrhenius line drawn, reflects the result obtained from the NMR global fit. The good agreement of the rates deduced from quite different methods suggests that NMR and conductivity measurements are sensitive to the same long-range Li diffusion process in tetragonal $\text{Li}_7\text{La}_3\text{Zr}_2\text{O}_{12}$.

3.2. Investigation of Li dynamics in $\text{Li}_{12}\text{Si}_7$ by NMR spin-lattice relaxation solely induced by distinct diffusion processes

Polycrystalline $\text{Li}_{12}\text{Si}_7$ serves as an interesting model substance to study fast Li dynamics in Zintl phase anode materials having a complex crystal structure. Fig. 4(A) shows the ${}^7\text{Li}$ NMR SLR rates R_1 and $R_{1\rho}$ of crystalline $\text{Li}_{12}\text{Si}_7$ measured at two Larmor frequencies ω_0 as well as two locking frequencies ω_1 . Remarkably, the data, which were recorded over a wide temperature range, reveal at least three diffusion-induced NMR rate peaks. As described above, from the NMR SLR rate maxima, lithium jump rates can be deduced in a rather straightforward way. The corresponding jump rates are shown in the Arrhenius diagram in Fig. 4(B). First, let us consider the diffusion process which belongs to the maxima in $R_{1\rho}$ as well as to the corresponding maxima in R_1 , showing up at the lowest temperatures.

Here, four Li jump rates are obtained from the four maxima (see the lines connecting Fig. 4(A) with (B)). An Arrhenius fit yields an activation energy of approximately 0.18 eV. However, the slope of the high-temperature flank leads to 0.09 eV only, as visible from the $R_{1\rho}$ data [63]. Additionally, the rates in the limits $\omega_0\tau \ll 1$ and $\omega_1\tau \ll 1$ measured at different frequencies do not coincide, i.e., they show a frequency dependence. As pointed out recently, see Ref. [63], these are indications for a spatially confined diffusion process. While the extraction of jump rates from NMR SLR rate peaks is rather independent of a diffusion

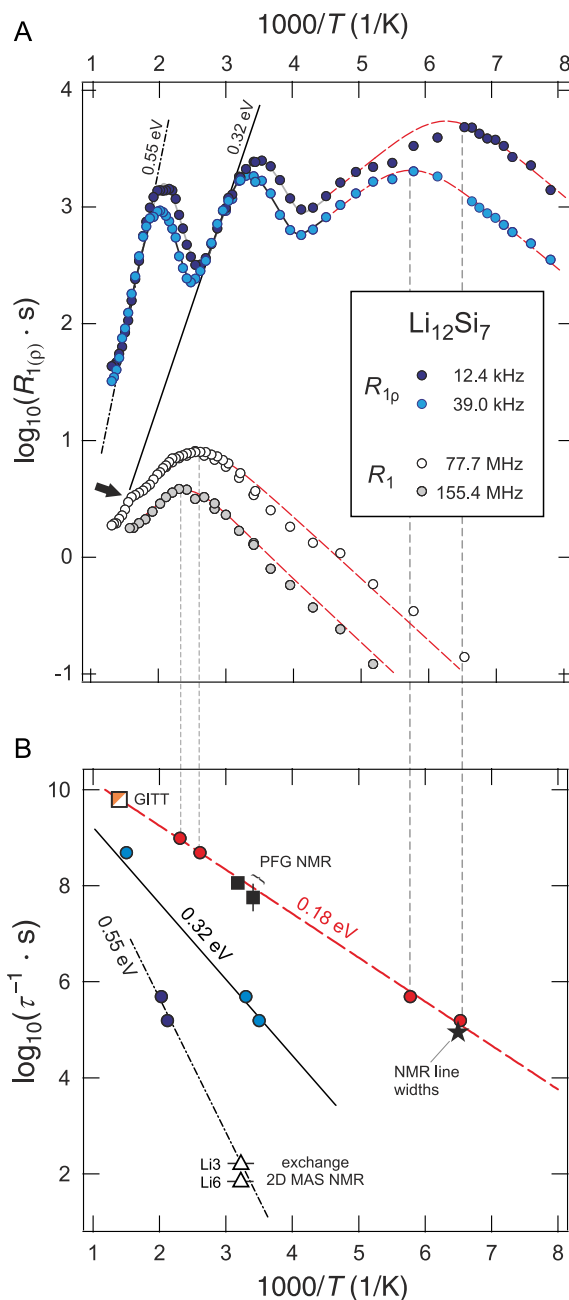


Fig. 4. (A) Arrhenius plot of the ${}^7\text{Li}$ NMR SLR rates R_1 and R_{1p} of polycrystalline $\text{Li}_{12}\text{Si}_7$. Data were recorded at the frequencies indicated. Dashed lines mark the diffusion-induced NMR rate peaks which belong to the same (extremely fast) Li diffusion process in $\text{Li}_{12}\text{Si}_7$. The dashed-dotted and solid line represent Arrhenius fits in the limit $\omega_1\tau \ll 1$ in order to determine the activation energy E_A of the slower diffusion processes showing up at higher T . (B) Li jump rates extracted from the diffusion-induced NMR SLR data shown in (A). For comparison, the Li jump rates which can be extracted from static ${}^7\text{Li}$ NMR line narrowing (\star) as well as from preliminary 2D exchange MAS NMR (Δ) and PFG MR measurements (\blacksquare) are also included [64,65]. While the dashed line represents an Arrhenius fit yielding 0.18 eV for the fastest process (see text for further details), the other Arrhenius lines were drawn using the activation energies deduced from the high-temperature flanks of the NMR SLR rate peaks shown in (A). Data were partly taken from Ref. [63].

model, information on the exact dimensionality of the hopping process (1D or 2D), however, can be extracted only with a suitable hopping model. Certainly, the behavior of the NMR SLR rates found here might also be explained by assuming several additional diffusion processes.

Additionally, Li NMR line narrowing of the dipolarly broadened central transition of $\text{Li}_{12}\text{Si}_7$ can be used to roughly estimate a Li jump rate τ^{-1} . As shown in Ref. [63], motional narrowing of the ${}^7\text{Li}$ NMR line yields $\tau^{-1} \approx 1 \times 10^5 \text{ s}^{-1}$ at 150 K (see Fig. 4). This is in good agreement with the fast diffusion process probed by NMR SLR measurements.

Wen and Huggins [66] reported a value for the self-diffusion coefficient of Li in $\text{Li}_{12}\text{Si}_7$ measured at 688 K using the galvanostatic intermittent titration technique (GITT). Additionally, we carried out preliminary pulsed field gradient (PFG) NMR measurements at 298 and 313 K from which diffusion coefficients D have been deduced [64]. Interestingly, the data from GITT and PFG NMR, after conversion into jump rates, are in good agreement with those obtained from NMR relaxometry corroborating the small activation energy of approximately 0.2 eV found. Since (macroscopic) tracer-like diffusion coefficients are available from GITT and PFG NMR the consistency found serves as a good indication that the very fast diffusion process probed by NMR SLR measurements is indeed of long-range nature.

Certainly, it is worth noting that the conversion of tracer-like diffusion coefficients used here is based on several simplifications. Here, we assumed a correlation factor $f=1$ connecting the macroscopic diffusion coefficient D from GITT and PFG NMR with the microscopic Einstein–Smoluchowski diffusion coefficient D_{sd} available by NMR spin–lattice relaxation, $D=fD_{sd}$. Note that D_{sd} depends on the dimensionality d of the diffusion process and is given by $D=a^2/(3d\tau)$ where a represents the jump distance. However, even if good agreement between D_{sd} and D is found, this does not allow a clear conclusion on the dimensionality of the dynamic process. Some uncertainties may easily give rise to a factor of two describing the difference of the jump rates estimated from the various methods. For example, the effective jump distance used for the estimate might be different from that than one simply deduces from the crystal structure. Such a false estimation might be easily rationalized by considering a diffusion pathway where the jumping ion transitionally occupies interstitial positions. Moreover, the NMR correlation rate might differ from the exact (mean) Li jump rate.

Going back to Fig. 4, at least two additional jump processes in $\text{Li}_{12}\text{Si}_7$ can be extracted from the NMR relaxation data. These are clearly characterized by the features expected for 3D diffusion [4]. In particular, the NMR SLR rates in the limit $\omega_{0(1)}\tau \ll 1$ turn out to be independent of frequency [63]. As illustrated in Fig. 4 the activation energies (*viz.* 0.32 eV and 0.55 eV) obtained from the Arrhenius plot $\tau^{-1}(1/T)$ are very similar to those which can be obtained from the respective high-temperature NMR flanks $R_{1p}(1/T)$. Note that for the faster of the 3D processes the R_1 maximum is also visible as a slight shoulder (see the NMR SLR rates measured at 77.7 MHz, arrow in Fig. 4(A)). Due to temperature limitations, for the slower 3D process the NMR SLR rate maxima are only visible in the R_{1p} data.

For comparison, in Fig. 4(B), Li jump rates obtained from preliminary 2D (magic angle spinning) MAS exchange NMR measurements are also included [65]. Based on the assignments of the NMR lines to the crystallographic positions in $\text{Li}_{12}\text{Si}_7$, see Refs. [67–69], the rates deduced from 2D MAS NMR, carried out at ambient bearing gas temperature, reflect Li exchange processes in which the Li6 and the Li3 sites are involved. The Li6 ions are located between the Si_5^{6-} rings in $\text{Li}_{12}\text{Si}_7$; the Li3 ions reside in the direct neighborhood of the Li6 ion. Expectedly, the Li6 ions are more tightly bound as compared to other Li ions in $\text{Li}_{12}\text{Si}_7$. Hence,

this easily rationalizes the low exchange rate and the higher activation energy found.

Finally, let us comment on the SLR relaxation mechanism in $\text{Li}_{12}\text{Si}_7$. In contrast to the situation in $\text{Li}_7\text{La}_3\text{Zr}_2\text{O}_{12}$, the ratio $R_1(^7\text{Li})/R_1(^6\text{Li}) \approx 40$ suggests that ^7Li NMR relaxation is dominated by a quadrupolar mechanism. $R_{1\rho}(\omega_{\text{lock}})$ reveals that local fields are much smaller than in the case of $\text{Li}_7\text{La}_3\text{Zr}_2\text{O}_{12}$. An analysis of the interaction strength is not as clear-cut as in the case of the garnet studied. An estimation shows that the apparent interaction strength, which can be obtained from a global-fit procedure, is highest for the fastest process and diminishes for the slower processes. Note, not all of the ions take part in the respective jump processes at the same time. Finally, by fitting the data with the modified BPP expression (see above), also the stretching exponents α of the underlying motional correlation function can be obtained. Interestingly, the three diffusion processes seem to be governed by non-exponential correlation functions characterized by $\alpha = 0.7$, $\alpha = 0.5$, and $\alpha = 0.6$. This shows that Li diffusion in the silicide $\text{Li}_{12}\text{Si}_7$ is considerably influenced by correlation effects [54] due to Coulomb interactions, for example. In particular, the observed deviation from random motion for the slower diffusion processes found might be explained by preferences of backward jumps of those ions which are more tightly bound than others (see above).

4. Conclusions

^7Li NMR spin relaxometry is a reliable – though sometimes time-consuming – tool for profound investigations of Li dynamics in solids. Certainly, the method is highly applicable provided the samples under study do not undergo significant structural changes. Exemplarily, two recent NMR studies of our group have been presented highlighting the capabilities of NMR SLR rate measurements to study Li jump rates and activation energies. In the ideal case, an NMR SLR study includes both R_1 and $R_{1\rho}$ measurements preferentially carried out over a wide temperature and frequency range. In such cases, the data are expected to contain comprehensive information on the dynamic processes present. While variable-temperature NMR spin-relaxometry gives access to dynamic parameters, frequency-dependent measurements may help clarify the dimensionality of a diffusion process. Moreover the detailed analysis of the shape of diffusion-induced NMR rate peaks offers the possibility to obtain valuable information on the underlying motional correlation functions determining the dynamic process. These information, as exemplarily outlined for $\text{Li}_7\text{La}_3\text{Zr}_2\text{O}_{12}$ and $\text{Li}_{12}\text{Si}_7$, might be of great help to characterize further (non-paramagnetic) materials being relevant as components for battery applications.

Acknowledgments

We thank Martin Winter and Stefano Passerini (University of Münster) for access to the PFG NMR equipment. Financial support by the Bundesministerium für Bildung und Forschung (BMBF, HE-Lion), the Deutsche Forschungsgemeinschaft (DFG) in the frame of the research unit 1277, the Leibniz University Hannover (“Wege in die Forschung II”), and by the Studienstiftung des deutschen Volkes e.V. are gratefully acknowledged.

References

- [1] R.A. Huggins, *Electrochim. Acta* 22 (1977) 773.
- [2] V. Thangadurai, W. Weppner, *Ionics* 12 (2006) 81.
- [3] P. Knauth, *Solid State Ionics* 180 (2009) 911.
- [4] P. Heitjans, A. Schirmer, S. Indris, in: P. Heitjans, J. Kärger (Eds.), *Diffusion in Condensed Matter: Methods, Materials, Models* Springer, Berlin, 2005, p. 369. (Chapter 9).
- [5] P.M. Richards, *Top. Curr. Phys.* 25 (1979) 1019.
- [6] D. Brinkmann, *Prog. Nucl. Magn. Reson. Spectrosc.* 24 (1992) 527.
- [7] M. Grüne, W. Müller-Warmuth, P. zum Hebel, B. Krebs, *Solid State Ionics* 78 (1995) 305.
- [8] R. Bertermann, W. Müller-Warmuth, *Z. Naturforsch.* A 53 (1998) 863.
- [9] J. Emery, O. Bohnke, J.L. Fourquet, J.-Y. Buzare, P. Florian, D. Massiot, *J. Phys.: Condens. Matter* 14 (2002) 523.
- [10] M. Wilkening, W. Kuchler, P. Heitjans, *Phys. Rev. Lett.* 97 (2006) 065901.
- [11] A. Kuhn, S. Narayanan, L. Spencer, G. Goward, V. Thangadurai, M. Wilkening, *Phys. Rev. B* 83 (2011) 094302.
- [12] F. Qi, T. Jörg, R. Böhmer, *Solid State Nucl. Magn. Reson.* 22 (2002) 484.
- [13] R. Böhmer, T. Jörg, F. Qi, A. Titze, *Chem. Phys. Lett.* 316 (2000) 419.
- [14] M. Wilkening, P. Heitjans, *Phys. Rev. B* 77 (2008) 024311.
- [15] M. Wilkening, A. Kuhn, P. Heitjans, *Phys. Rev. B* 78 (2008) 054303.
- [16] M. Wilkening, R. Amade, W. Iwaniak, P. Heitjans, *Phys. Chem. Chem. Phys.* 9 (2006) 1239.
- [17] R. Böhmer, K. Jeffrey, M. Vogel, *Prog. Nucl. Magn. Reson. Spectrosc.* 50 (2007) 87.
- [18] M. Wilkening, P. Heitjans, *J. Phys.: Condens. Matter* 18 (2006) 9849.
- [19] M. Wilkening, P. Heitjans, *Solid State Ionics* 177 (2006) 3031.
- [20] N. Bloembergen, E. Purcell, R. Pound, *Phys. Rev.* 73 (1948) 679.
- [21] A. Abragam, *The Principles of Nuclear Magnetism*, Oxford University Press, 1961.
- [22] C.A. Sholl, *J. Phys. C: Solid State Phys.* 14 (1981) 447.
- [23] T.K. Halstead, K. Metcalfe, T.C. Jones, *J. Magn. Reson.* 47 (1982) 292.
- [24] O. Kanert, *Phys. Rep.* 91 (1982) 183.
- [25] W. Kuchler, P. Heitjans, A. Payer, R. Schöllhorn, *Solid State Ionics* 70/71 (1994) 434.
- [26] V. Epp, M. Wilkening, *Phys. Rev. B* 82 (2010) 020301.
- [27] R. Kimmich, *NMR Tomography, Diffusiometry, Relaxometry*, Springer, Berlin, 1997.
- [28] R. Kimmich, E. Anardo, *Prog. Nucl. Magn. Reson. Spectrosc.* 44 (2004) 257.
- [29] H. Ackermann, P. Heitjans, H.-J. Stöckmann, *Top. Curr. Phys.* 31 (1983) 291.
- [30] P. Heitjans, *Solid State Ionics* 18/19 (1986) 50.
- [31] P. Heitjans, W. Faber, A. Schirmer, *J. Non-Cryst. Solids* 131–133 (1991) 1053.
- [32] P. Freiländer, P. Heitjans, H. Ackermann, B. Bader, G. Kiese, A. Schirmer, H.-J. Stöckmann, C. van der Marel, A. Magerl, H. Zabel, *Z. Phys. Chem. NF* 151 (1987) 93.
- [33] H. Estrade, J. Conrad, P. Lauginie, P. Heitjans, F. Fujara, W. Buttler, G. Kiese, H. Ackermann, D. Guerard, *Physica* 99B (1980) 531.
- [34] A. Schirmer, P. Heitjans, W. Faber, J.E. Fischer, *Mater. Sci. Forum* 91–93 (1992) 589.
- [35] A. Schirmer, P. Heitjans, W. Faber, D. Clausen, *Solid State Ionics* 53–56 (1992) 426.
- [36] A. Körblein, P. Heitjans, H.-J. Stöckmann, F. Fujara, H. Ackermann, W. Buttler, K. Dürr, H. Grupp, *J. Phys. F: Met. Phys.* 15 (1985) 561.
- [37] P. Heitjans, A. Körblein, H. Ackermann, D. Dubbers, F. Fujara, H.-J. Stöckmann, *J. Phys. F: Met. Phys.* 15 (1985) 41.
- [38] D. Ailion, C.P. Slichter, *Phys. Rev. Lett.* 12 (1964) 168–171.
- [39] C.P. Slichter, D.C. Ailion, *Phys. Rev.* 135 (1964) A1099.
- [40] D.C. Ailion, C.P. Slichter, *Phys. Rev.* 137 (1965) A235.
- [41] D.C. Look, I.J. Lowe, *J. Chem. Phys.* 44 (1966) 2995.
- [42] T.J. Rowland, F.Y. Fradin, *Phys. Rev.* 182 (1969) 760.
- [43] D. Wolf, *Phys. Rev. B* 10 (1974) 2724.
- [44] H.W. Spiess, *NMR – Basic Principles and Progress*, vol. 15, 1978, p. 169.
- [45] J.H. van Vleck, *Phys. Rev.* 74 (1948) 1168.
- [46] L.S. Brown, *IBM J. Res. Div.* 6 (1962) 338.
- [47] P.S. Hubbard, *J. Chem. Phys.* 53 (1970) 985.
- [48] P.M. Richards, *Phys. Rev. B* 18 (1978) 6358.
- [49] M. Grüne, W. Müller-Warmuth, *Solid State Nucl. Magn. Reson.* 5 (1995) 145.
- [50] J.L. Björkstam, L. Listerud, M. Villa, *Solid State Ionics* 18 (1986) 117.
- [51] E. Göbel, W. Müller-Warmuth, H. Olyschläger, H. Dutz, *J. Magn. Reson.* 36 (1979) 371.
- [52] K. Ngai, O. Kanert, *Solid State Ionics* 53 (1992) 936.
- [53] K. Funke, *Prog. Solid State Chem.* 22 (1993) 111.
- [54] M. Meyer, P. Maass, A. Bunde, *Phys. Rev. Lett.* 71 (1993) 573.
- [55] M. Wilkening, W. Iwaniak, J. Heine, V. Epp, A. Kleinert, M. Behrens, G. Nussli, W. Bensch, P. Heitjans, *Phys. Chem. Chem. Phys.* 9 (2007) 6199.
- [56] S. Indris, P. Heitjans, *J. Non-Cryst. Solids* 307 (2002) 555.
- [57] M. Wilkening, S. Indris, P. Heitjans, *Phys. Chem. Chem. Phys.* 5 (2003) 2225.
- [58] D. Tse, S.R. Hartmann, *Phys. Rev. Lett.* 21 (1968) 511.
- [59] H.-J. Stöckmann, P. Heitjans, *J. Non-Cryst. Solids* 66 (1984) 501.
- [60] J. Awaka, N. Kijima, H. Hayakawa, J. Akimoto, *J. Solid State Chem.* 182 (2009) 2046.
- [61] R.E. Walstedt, *Phys. Rev. Lett.* 19 (1967) 146.
- [62] T. Pietrass, F. Taulelle, P. Lavelle, J. Olivier-Fourcade, J. Jumas, S. Steuernagel, *J. Phys. Chem. B* 101 (1997) 6715.
- [63] A. Kuhn, P. Sreeraj, R. Pöttgen, H.-D. Wiemhöfer, M. Wilkening, P. Heitjans, *J. Am. Chem. Soc.* 133 (2011) 11018.
- [64] A. Kuhn, M. Kunze, M. Wilkening, P. Heitjans, to be published.
- [65] A. Kuhn, M. Wilkening, P. Heitjans, to be published.
- [66] C.J. Wen, R.A. Huggins, *J. Solid State Chem.* 37 (1981) 271.
- [67] A. Kuhn, P. Sreeraj, R. Pöttgen, H.-D. Wiemhöfer, M. Wilkening, P. Heitjans, *Angew. Chem. Int. Ed.* 50 (2011) 12099.
- [68] T.K.-J. Köster, E. Salager, A.J. Morris, B. Key, V. Seznec, M. Morcrette, C.J. Pickard, C.P. Grey, *Angew. Chem. Int. Ed.* 50 (2011) 12591–12594.
- [69] S. Dupke, T. Langer, R. Pöttgen, M. Winter, H. Eckert, *Solid State Nucl. Magn. Reson.* doi:10.1016/j.ssnmr.2011.09.002, in press.

Chapter 3

Li Ion Dynamics in Garnet-type Li Electrolytes $\text{Li}_7\text{La}_3\text{Zr}_2\text{O}_{12}$

3.1 Garnet-type Li electrolytes and LLZ

In the recent years, garnet-type Li electrolytes - first introduced by the Weppner group - have attracted a lot of attention due to their high ionic conductivity combined with a large electrochemical window. [115–136] In 2007, Murugan *et al.* [18, 137] reported on the garnet-type electrolyte of the composition $\text{Li}_7\text{La}_3\text{Zr}_2\text{O}_{12}$ (LLZ) crystallizing with cubic symmetry (space group $Ia\bar{3}d$). Cubic LLZ was found to exhibit a RT conductivity of 3×10^{-4} S/cm, an activation energy as low as 0.34 eV, and chemical stability of the material against molten Li. These promising results can be considered as a breakthrough towards all-solid-state Li secondary batteries. Eversince this publication, LLZ has been in the focus of many research group and corporates. [20, 21, 27–31, 33, 34, 138–152] However, it took the community more than 4 years to reproduce the high conductivity of Murugan *et al.* and to begin to understand its origin. This chapter can be understood as contribution of this scientific process.

3.2 LLZ crystallizing with tetragonal symmetry \leftrightarrow LLZ crystallizing with cubic symmetry

In 2009 Awaka *et al.* published a consistent study on $\text{Li}_7\text{La}_3\text{Zr}_2\text{O}_{12}$ (LLZ) containing single crystal diffraction data, Rietveld analysis with a structural model, and impedance spectroscopy data. Most probably, the authors were attempting to reproduce the results published by Murugan *et al.* earlier. In contrast to the LLZ sample published by Murugan *et al.*, the LLZ sample obtained by Awaka *et al.* crystallized with tetragonal symmetry (space group $I4_1/acd$ (142), see Fig. 3.1). The RT conductivity of this tetragonal LLZ sample was about 2 orders of magnitude lower than the one reported for the cubic modification. The activation energy was roughly 0.5 eV. Thus, the conductivity of the tetragonal LLZ is in the range typical of oxide Li superionic conductors (*cf.* section 2.1.3). Clearly, the behavior of this LLZ sample was rather expected than the extraordinary-

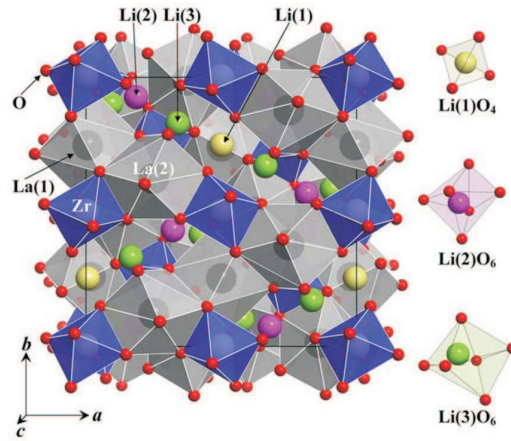


Figure 3.1: The structure model of tetragonal LLZ $\text{Li}_7\text{La}_3\text{Zr}_2\text{O}_{12}$ (space group $I4_1/acd$ (142)). The picture is taken from Ref. [20].

ily high conductivity of the cubic LLZ. The differences between these two modifications are rather small, *i. e.* - most prominently - a slight distortion of the lattice parameters below 2% leading to the lower tetragonal symmetry. Already at this point, it can be assumed that some additional structural changes must be the reason for the high conductivity in the cubic sample of.

Clearly, before attempts should be made to understand the unusual situation of cubic LLZ, the exact characterization of the usual situation found in tetragonal LLZ should be considered. This was done here for a tetragonal LLZ sample provided by V. Thangadurai by means of impedance spectroscopy, ^7Li NMR relaxometry/line shape analysis, and ^7Li SAE NMR was part of this thesis. The results are already published [21, 26]; the papers are presented below (pages 50-68). The results of Awaka *et al.* were corroborated, a single isotropic diffusion process was observed. More recent results on this LLZ sample (SFG NMR, re-evaluation of all measurements) follow the two papers presented below.

In 2011, Geiger *et al.* reported that tetragonal LLZ undergoes a gradual phase transition to cubic LLZ at temperatures above 400 K. [28] Indeed, this phase transition was also observed for our tetragonal LLZ sample, see Fig. 3.2. Interestingly, this phase transition did not lead to any observable changes in the Li mobility, neither in conductivity nor in relaxometry - a first hint that the cubic modification *alone* is not the reason for the high conductivity of some cubic LLZ samples. A second LLZ sample provided by V. Thangadurai was a mixture of cubic LLZ and two tetragonal LLZ phases with slightly different lattice constants. This sample showed exactly the same diffusivity as the tetragonal sample.

In the same study, Geiger *et al.* emphasized that small amounts of Al stabilize the cubic modification at room temperature. The same result was also suggested by Japanese researchers in a US patent [139]. Indeed, the samples provided by V. Thangadurai were free of Al as corroborated by ^{27}Al MAS NMR.

In the framework of the BMBF project KVN, F. Tietz (FZ Jülich, Germany) provided a cubic LLZ sample. The XRD pattern is in very good agreement with those reported in the literature [18, 28]. The ^{27}Al MAS NMR spectrum showed the same lines as reported in Ref. [28] for the Al-doped LLZ. The Li diffusivity as measured by impedance spectroscopy and NMR relaxometry, however,

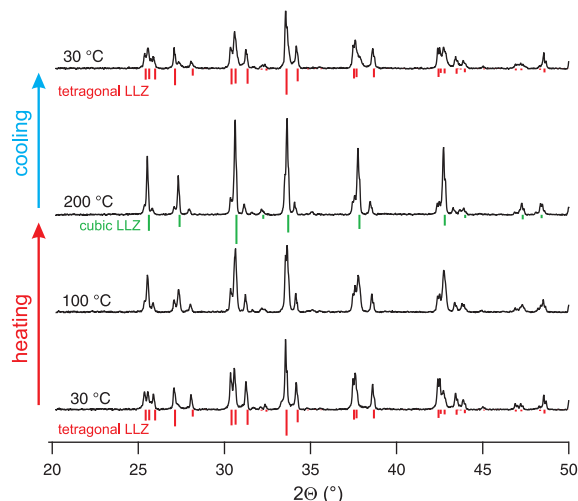


Figure 3.2: Temperature-dependent XRD patterns of the LLZ sample provided by V. Thangadurai that is tetragonal at RT. The sample undergoes a gradual and reversible phase transition to the cubic modification. The measurement was performed with a Bruker D8 Advance X-ray diffractometer and a high-temperature cell (HTK-1200N, Anton-Paar).

was hardly distinguishable from that found for the tetragonal LLZ sample. The results of this study are summarized in the paper shown below (pages 71-83). At least now, it was clear that the cubic modification is not a sufficient condition for the high Li diffusivity.

As a next step a Al-doped cubic LLZ sample which indeed showed the high conductivity as reported in Ref. [18] was examined. The sample was provided by H. Buschmann (group of Prof. Dr. J. Janek, University of Gießen). The high Li mobility could be corroborated by means of ^7Li NMR relaxometry and true dc conductivity measurements. The results have been published and the paper is shown below (page 84-98). For the LLZ prepared by H. Buschmann, after the publication of this first paper, a complete ^6Li NMR relaxometry study, an impedance spectroscopy study, and an SFG NMR study were performed in order to get more insight into the dynamics occurring in the Al-doped cubic LLZ. The global fit analyses of all data point to a intragrain diffusivity characterized by roughly 0.3 eV. These results directly follow the mentioned paper (Buschmann *et al.*, Ref. [19] and pages 84-98).

Trying to understanding why one of the Al-doped LLZ samples showed the high Li ion conductivity and the other did not, led to a cooperation project with A. Düvel (a PhD student in the same group) who focused on mechanochemical synthesis during his PhD. A. Düvel developed a mechanochemical synthesis route for the cubic LLZ which includes a milling step and a low-temperature reaction step. The mechanochemical synthesis allows the exact adjustment of the cationic ratios which is not possible for the high-temperature necessary in conventional synthesis. This allows a systematic study of the effect of Al on structure and dynamics. From the XRD and ^{27}Al results I concluded that Al does not only replace Li - as assumed in the literature before - but also Zr and La. Thus, Al doping affects the garnet network of LLZ and most probably goes along with strong local distortions of the lattice. The Li dynamics was studied by means of NMR line narrowing for all samples (more than 30) and, for selected samples, by means of additional techniques. The manuscript (submitted to J. Phys. Chem. C) of this study is added below (pages 105-115).

Li self-diffusion in garnet-type $\text{Li}_7\text{La}_3\text{Zr}_2\text{O}_{12}$ as probed directly by diffusion-induced ^7Li spin-lattice relaxation NMR spectroscopy

A. Kuhn,¹ S. Narayanan,² L. Spencer,³ G. Goward,³ V. Thangadurai,² and M. Wilkening^{1,*}

¹*Institute of Physical Chemistry and Electrochemistry, Leibniz University Hannover, Callinstr. 3a, D-30167 Hannover, Germany*

²*Department of Chemistry, University of Calgary, 2500 University Drive NW, Calgary, Alberta, Canada T2N 1N4*

³*Department of Chemistry, McMaster University, 1280 Main Street W, Hamilton, Ontario, Canada L8S 4M1*

(Received 18 November 2010; published 15 March 2011)

Li self-diffusion in garnet-type $\text{Li}_7\text{La}_3\text{Zr}_2\text{O}_{12}$, crystallizing with tetragonal symmetry at room temperature, is measured by temperature-variable ^7Li spin-spin as well as spin-lattice relaxation (SLR) nuclear magnetic resonance (NMR) spectroscopy. The SLR NMR rates which were recorded in both the laboratory and the rotating frame of reference pass through characteristic diffusion-induced rate peaks allowing for the direct determination of Li jump rates τ^{-1} , which can be directly converted into self-diffusion coefficients D_{sd} . The NMR results are compared with those obtained from electrical impedance spectroscopy measurements carried out in a large temperature and wide frequency range. Taken together, the long-range diffusion process, being mainly responsible for ionic conduction at ambient temperature, is characterized by an activation energy of approximately 0.5 eV, with $\tau_0^{-1} \approx 1 \times 10^{14} \text{ s}^{-1}$ being the pre-exponential factor of the underlying Arrhenius relation.

DOI: 10.1103/PhysRevB.83.094302

PACS number(s): 66.30.-h, 76.60.-k, 82.56.-b, 82.47.Aa

I. INTRODUCTION

Crystalline solids with a high Li-ion conductivity¹⁻⁵ but a vanishing electronic conductivity are of great importance in current developments of new chemically resistant electrolytes. Such materials are urgently needed in the field of clean and safe energy storage systems such as powerful supercapacitors as well as advanced high-energy density lithium-ion batteries.⁶⁻¹⁰ Recently, garnet-type $\text{Li}_7\text{La}_3\text{Zr}_2\text{O}_{12}$ crystallizing with cubic symmetry¹¹ has attracted great attention^{9,10,12} because of its high ionic conductivity.¹¹ At room temperature the bulk conductivity of a sample with cubic symmetry is reported to be high enough to make the development of all-solid-state Li-ion batteries feasible.^{11,12} The tetragonal phase of $\text{Li}_7\text{La}_3\text{Zr}_2\text{O}_{12}$ shows an Li-ion conductivity in the order of $10^{-6} \text{ S cm}^{-1}$ at ambient temperature.¹³ This value is comparable to that of most oxide ceramics belonging to the group of good Li-ion-conducting solids, which includes also those of the large family of structurally complex garnet-type compounds studied during the past years.^{2,9,10,14-19}

So far, Li transport properties in garnets of the composition $\text{Li}_7\text{La}_3\text{Zr}_2\text{O}_{12}$, as well as others,⁹ have been exclusively studied by (alternating-current) impedance spectroscopy.¹¹⁻¹³ Alternatively, Li nuclear magnetic resonance (NMR) techniques²⁰⁻²⁸ can be used to provide direct insights into Li dynamics and to quantify the ion diffusivity in solids precisely over a large dynamic range.²⁹⁻³² NMR is a non-destructive and noncontact method, making it advantageous over other techniques capable of studying ion dynamics. For example, no elaborate postpreparation of the samples including sintering procedures to minimize influences of, for example, blocking grain boundaries, or the application of electrodes, as in the case of impedance spectroscopy, are necessary when NMR techniques are used.

Although a huge number of NMR studies have been published dealing with Li diffusion properties in solids, to our knowledge, only few studies³³⁻³⁶ employing NMR spectroscopy to probe structural as well as diffusion parameters in Li-containing garnets can be found in the

literature. While Koch and Vogel³⁴ used ^7Li stimulated-echo NMR spectroscopy to trace slow Li dynamics in garnet-type $\text{Li}_5\text{La}_3\text{Nb}_2\text{O}_{12}$, van Wüllen *et al.*³³ took advantage of ^6Li 2D exchange NMR spectroscopy to reveal details on the migration mechanism in the same sample. Such investigations are indispensable in order to determine local Li environments, as well as to enlighten the origins of fast Li dynamics in solids. Additionally, the reliable measurement of Li self-diffusion parameters from a microscopic point of view, as it is possible in the case of most of the NMR techniques,²¹ provides valuable information to help identify as well as purposefully modify those candidates having the potential to be used as solid electrolytes.

In the case of $\text{Li}_7\text{La}_3\text{Zr}_2\text{O}_{12}$ [space group $I4_1/acd$ (tetragonal phase),¹³ $Ia\bar{3}d$ (cubic phase)³⁷], Li spin-lattice relaxation (SLR) NMR relaxation experiments (see, e.g., Refs. 20,21 and 38-45) are ideally suited to probe Li jump rates which can be directly converted into Li self-diffusion coefficients by applying the Einstein-Smoluchowski equation.^{21,32,46-48} In the present contribution, purely diffusion-induced ^7Li SLR NMR rates of $\text{Li}_7\text{La}_3\text{Zr}_2\text{O}_{12}$ in both the laboratory and rotating frame of reference were recorded over a large temperature range. The sample studied shows tetragonal symmetry at room temperature. The NMR results are comprehensively compared with those obtained from electrical impedance spectroscopy measurements, leading to a consistent picture of Li dynamics in highly pure $\text{Li}_7\text{La}_3\text{Zr}_2\text{O}_{12}$.

II. EXPERIMENT

Tetragonal $\text{Li}_7\text{La}_3\text{Zr}_2\text{O}_{12}$ was prepared by conventional solid-state reaction. Stoichiometric amounts of the starting materials (Li_2CO_3 , La_2O_3 , and ZrO_2) were mixed, put in an alumina crucible, and heated at 1173 K in air for 24 h. An excess (10 wt%) of Li_2CO_3 was added to compensate for any loss of lithium due to volatilization. After that, the mixture was air-quenched and analyzed by x-ray powder diffraction (XRPD) using a D8 Advance diffractometer (Bruker) operating

with Cu K_α radiation at 40 kV and 40 mA (see Fig. 1). Some XRPD patterns were recorded *in situ* using a high-temperature cell HTK-1200N (Anton-Paar) at elevated temperatures. For the NMR measurements performed under static conditions the polycrystalline sample was fire-sealed in quartz tubes under vacuum.

^6Li magic angle spinning (MAS) NMR spectra (Fig. 2) as a function of delay time were recorded with a single-pulse experiment. For that purpose an Avance III NMR spectrometer (Bruker) connected to a precisely shimmed cryomagnet with a magnetic field of 14.1 T was used. The field strength corresponds to a resonance frequency of approximately 88 MHz. A standard MAS NMR probe (2.3-mm rotors) was employed. The spinning frequency ν_{rot} was 30 kHz. As in the case of the ^7Li NMR data, a single room-temperature ^6Li NMR SLR rate was estimated with the help of a saturation recovery experiment.^{21,49} For comparison, some ^6Li MAS NMR spectra were recorded at 73 MHz and $\nu_{\text{rot}} = 39$ kHz. The spectra shown in Fig. 2 were referenced to 1 M LiCl.

^7Li SLR NMR rates in both the laboratory as well as the rotating frame of Refs. 21 and 49 were recorded with an MSL 100 spectrometer (Bruker) which is connected to an Oxford cryomagnet with a magnetic field of 4.7 T. This corresponds to a ^7Li resonance frequency of 77 MHz. A standard probe as well as a home-built high-temperature probe were used for the ^7Li SLR NMR measurement. The temperature in the sample chamber was monitored by an Oxford ITC4 with an accuracy of about ± 0.5 K. The ITC controls the output of a heater placed inside the probe and its interplay with a stream of either freshly evaporated nitrogen or ambient air. Additional ^7Li SLR NMR measurements were carried out using an MSL 400 spectrometer with the same setup and at a resonance frequency of 155 MHz (9.4 T). ^7Li SLR times (T_1) were recorded using the saturation recovery pulse sequence.^{21,49} Analogous measurements in the rotating frame of reference (T_{1e}) were acquired with the spin-lock technique⁴⁹ at a locking frequency of $\omega_1/2\pi \approx 30$ kHz. The recycle delay was at least $5T_1$. In both cases the transients were fitted with stretched exponentials. Presumably, such a time behavior is an indication of coupling

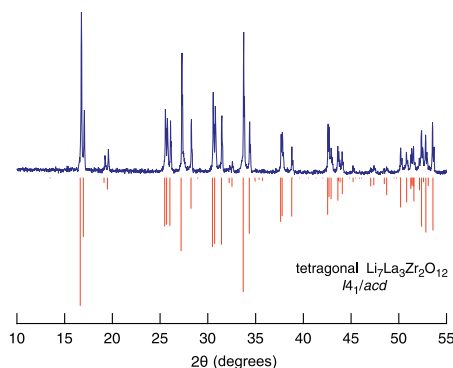


FIG. 1. (Color online) XRPD of $\text{Li}_7\text{La}_3\text{Zr}_2\text{O}_{12}$ proving its tetragonal symmetry at room temperature. Vertical lines indicate intensities and diffraction angles calculated on the basis of the neutron diffraction study of Awaka *et al.* (Ref. 13).

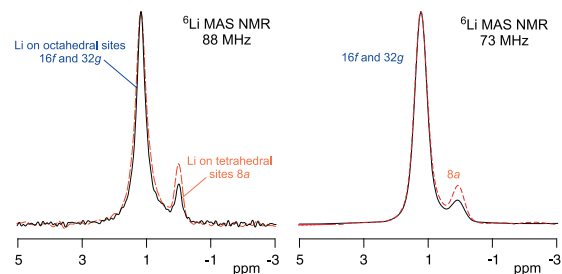


FIG. 2. (Color online) (Left) ^6Li MAS NMR spectrum of garnet-type $\text{Li}_7\text{La}_3\text{Zr}_2\text{O}_{12}$ recorded at $\nu_{\text{rot}} = 30$ kHz and a resonance frequency of 88 MHz. The solid line shows a spectrum obtained from 16 scans which were accumulated at an interval of 2400 s; for the second spectrum (dashed line) 12 scans were accumulated and the delay time was set to 9000 s so that full ^6Li NMR SLR is ensured (see text). The main signal can be attributed to Li ions occupying the distorted octahedral sites 16*f* and 32*g*. The signal with much lower intensity reflects Li ions residing in the tetrahedral interstices. (Right) ^6Li MAS NMR recorded with the same relaxation delays but at 73 MHz and $\nu_{\text{rot}} = 39$ kHz. Up to 64 scans were accumulated.

of the hopping Li ions with paramagnetic impurities. ^7Li NMR spectra (155 MHz) were obtained by Fourier transformation of the free induction decays (FIDs) measured with a 90° pulse applying the quadrature detection technique.⁴⁹ Additionally, (fully relaxed) ^7Li -stimulated echo (here spin-alignment echo) NMR spectra were recorded at the same frequency with the Jeener-Broekaert pulse sequence^{20,24,50–52} in order to enhance the NMR signal of satellite intensities. Up to 512 scans were accumulated to obtain a satisfying signal-to-noise ratio. Mixing and preparation time were chosen as short as possible.⁵³

Li-ion conductivities were measured with a Novocontrol impedance spectrometer which is equipped with a BDS 1200-sample cell and a Beta analyzer (Novocontrol). The latter is capable of measuring impedances down to 10^{-14} S at frequencies ranging from a few μHz to 20 MHz. Temperature regulation and controlling within an accuracy of about 0.5 K was carried out with a Quattro cryosystem (Novocontrol) using dry nitrogen gas. The root-mean-square ac voltage was typically 0.1 to 1.0 V. Prior to the measurements the powder samples were uniaxially cold pressed at 1 GPa to cylindrical pellets (8 mm in diameter and ca. 1 mm in thickness). The thickness of each pellet was measured with a vernier caliper. Electrodes were applied either by Au evaporation using an Edwards 306 or by pressing the uncoated pellet between Pt powder according to a sandwich configuration.

III. RESULTS AND DISCUSSION

A. Characterization of the sample by ^6Li MAS NMR

Prior to the temperature-variable NMR measurements, the as-prepared sample was characterized by XRPD as well as (high-resolution) ^6Li MAS NMR spectroscopy carried out at ambient bearing gas pressure corresponding to approximately 308 K. It shows the typical XRPD pattern of phase-pure tetragonal $\text{Li}_7\text{La}_3\text{Zr}_2\text{O}_{12}$ (Fig. 1), as shown in Ref. 13. Similar to a very recently published study³⁷ on $\text{Li}_7\text{La}_3\text{Zr}_2\text{O}_{12}$, which motivated us to carry out some additional *in situ* XRPD

measurements, the crystal structure slightly changes and the symmetry gradually increases from tetragonal to cubic at elevated temperatures. Whereas in Ref. 37 the transformation starts at approximately 400 K, in the present study it is shifted by almost 200 K toward higher T . Presumably, this reflects the higher purity of the sample investigated here. $\text{Li}_7\text{La}_3\text{Zr}_2\text{O}_{12}$ showing purely cubic symmetry is expected to be formed at temperatures larger than 623 K in the present case. However, as we show below, these gradual changes in local structure seem to have almost no effect on the Li jump rates measured, which strictly follow Arrhenius behavior over a wide dynamic range.

The room-temperature ^6Li MAS NMR spectra shown in Fig. 2 are dominated by a signal which can be attributed to Li ions on the distorted octahedral interstices $16f$ and $32g$ in the garnet-related-type structure of tetragonal $\text{Li}_7\text{La}_3\text{Zr}_2\text{O}_{12}$. Only at sufficiently long delay times does a second component show up which is shifted to negative ppm values by about 1.2 ppm (see Fig. 2). The signal with low intensity can be attributed to Li ions occupying the tetrahedral $8a$ sites in the tetragonal garnet. In the case of a fully relaxed spectrum recorded at a delay time of 9000 s, the corresponding area fraction is approximately 14(1)% of that of the total area. This is in perfect agreement with the crystal structure proposed by Awaka *et al.*¹³ The $8a$ sites are fully occupied by Li ions; i.e., 14.3% of the Li ions reside on tetrahedral interstices.¹³ The assignment of the two signals is also consistent with that reported by van Wüllen *et al.*³³ who observed two ^6Li NMR signals for $\text{Li}_5\text{La}_3\text{Nb}_2\text{O}_{12}$ having a related structure to tetragonal $\text{Li}_7\text{La}_3\text{Zr}_2\text{O}_{12}$. Since the two components are well separated, two individual ^6Li SLR times T_1 can be measured. Interestingly, T_1 of the main component is approximately 5 s at 88 MHz, whereas that of the other component is on the order of at least 1200 s at 308 K. Thus, from a dynamic point of view the two spin reservoirs are also well separated (cf. Refs. 33 and 36). At room temperature the Li ions representing the minor component are much less mobile than those residing on the octahedral sites. This is in good agreement with the result of van Wüllen *et al.* who analyzed ^6Li 2D exchange NMR spectra.³³ Provided these features do not change much with increasing temperature,⁵⁴ in the case of the ^7Li NMR SLR rate measurements presented below, the rates are exclusively determined by the fast Li ions on the octahedral positions. This is due to the circumstance that the rates were recorded using delay times of up to $5T_1 = 200$ s (at 230 K; see below). For comparison, at 77 MHz the ^7Li SLR NMR time turned out to be 2.4 s (308 K), indicating that the diffusion-controlled relaxation mechanism, when probed at ambient temperature, is mainly of dipolar nature for which $T_1(^7\text{Li})/T_1(^6\text{Li}) \approx 1/2$ is expected (see, e.g., Ref. 55 for an analogous estimation).

B. Temperature-variable (static) ^7Li NMR spectra

Simultaneously with the measurements of ^7Li SLR NMR rates (see below) we have recorded ^7Li NMR spectra (Fig. 3) under static conditions and over a wide temperature range. They provide rough information on the diffusion parameters controlling Li hopping at low temperatures in phase-pure $\text{Li}_7\text{La}_3\text{Zr}_2\text{O}_{12}$. Moreover, when a larger temperature range is

regarded they might provide information on possible structural changes upon heating. The complete ^7Li (spin-quantum number $I = 3/2$) NMR line of a powdered sample consists of two components, viz. a first-order quadrupole distributed satellite contribution ($\pm 3/2 \leftrightarrow \pm 1/2$) and the central one ($1/2 \leftrightarrow -1/2$), which is only broadened by nuclear dipole interactions of the spins. At first, the focus is directed toward the central transition of the Li NMR spectra. Satellite intensities, are expected if the ^7Li nuclei are placed in sites with a nonvanishing electric field gradient. Such contributions, if they span a wide range of frequencies corresponding to a large quadrupole coupling constant, can be made visible by using suitable NMR echo techniques (see the spectra labeled (a), (b) and (c) shown in the insets of Fig. 3). Satellite intensities are difficult to detect when the spectra are simply obtained by Fourier transformation of the free induction decays (main spectra of Fig. 3). These difficulties are simply caused by receiver dead time effects cutting off sharply decaying components at the initial part of the FID.

1. ^7Li NMR spectra: Central lines

Below 260 K the shape of the dipolarly broadened ^7Li NMR central line is Gaussian-like and shows a width (full width at half maximum) of approximately 8.6 kHz. This value represents the so-called rigid lattice line width δ_0 ; in this regime Li motions are characterized by jump rates much smaller than 10^3 s^{-1} . With increasing Li motions ^7Li - ^7Li dipole-dipole interactions are increasingly averaged, resulting in a narrowing of the width δ which is already decreased to 1.2 kHz when T reaches 333 K. As expected, the narrowing process is accompanied by a change of the line shape from a Gaussian to a Lorentzian. At approximately 400 K the regime of extreme narrowing ($T \rightarrow \infty$) is reached where $\delta = \delta_\infty$ is solely determined by inhomogeneities of the external magnetic field. In that region, dipole-dipole interactions are completely averaged due to sufficiently fast Li diffusion, indicating an average jump rate on the order some tens of kHz in this temperature range.

In Fig. 4 the NMR line width δ is plotted as a function of temperature, exhibiting a typical motional narrowing (MN) curve. A few approaches can be found in the literature aiming at the analysis of $\delta(T)$ curves in order to estimate the activation energy of the underlying Li diffusion process. If the full $\delta(T)$ curve cannot be determined, the activation energy of the underlying Li hopping process can be estimated by using the empirical expression of Waugh and Fedin,⁵⁶

$$E_a^{\text{WF}} = 1.617 \times 10^{-3} \cdot T_c / \text{K}, \quad (1)$$

where T_c , denotes the so-called onset temperature of MN. With $T_c \approx 290$ K, E_a^{WF} amounts to be approximately 0.47 eV, which is here in good agreement with the value probed by SLR NMR, as shown below. The dashed line in Fig. 4 shows a fit according to the *ad hoc* formalism introduced by Abragam⁵⁷ for motional averaging of dipole-dipole interactions:

$$\delta(T) = \sqrt{\delta_0^2 \frac{2}{\pi} \arctan \left[\zeta \delta(T) \tau_{0\text{MN}} \exp \left(\frac{E_a^{\text{MN}}}{k_B T} \right) \right] + \delta_\infty^2}, \quad (2)$$

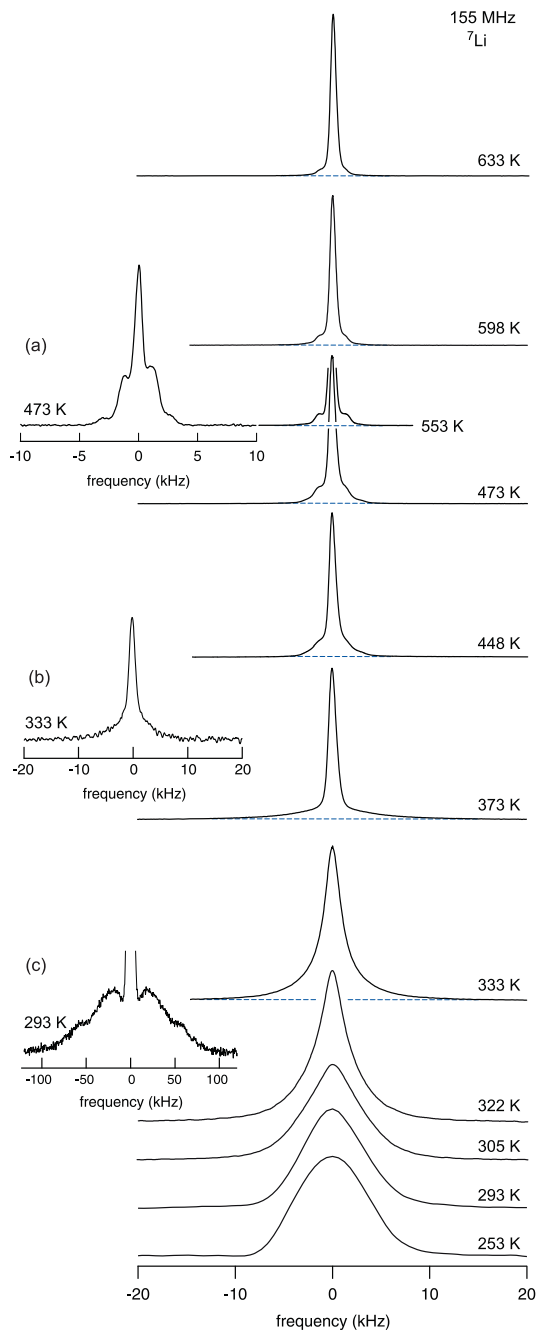


FIG. 3. Temperature-variable ${}^7\text{Li}$ NMR spectra of polycrystalline garnet-type $\text{Li}_7\text{La}_3\text{Zr}_2\text{O}_{12}$ recorded at a resonance frequency of 155 MHz. The spectra were obtained directly from the FIDs of the ${}^7\text{Li}$ SLR NMR measurements in the laboratory frame of reference. The insets (a), (b), and (c) represent NMR spectra obtained after Fourier transformation of ${}^7\text{Li}$ NMR spin-alignment echoes beginning from their top. See text for further details.

where ζ is a fit parameter here chosen to be one. k_B denotes Boltzmann's constant and τ_0^{MN} represents the pre-exponential factor of the corresponding correlation time τ_c^{MN} . The activation energy E_a^{MN} turned out to be approximately 0.43 eV, thus underestimating the precise value E_a obtained from SLR NMR by approximately 10% (see below). The same activation energy is obtained when $\tau_c^{\text{MN}}(\delta)$ values are calculated and plotted vs the inverse temperature $1/T$ (see the inset of Fig. 4). However, analyzing the data according to the phenomenological equation of Hendrickson and Bray, which is given in Ref. 58, yields a much higher activation energy, although the resulting fit, which is not shown for the sake of clarity here, nearly coincides with that shown in Fig. 4. This difference clearly indicates that in some cases the extraction of quantitative information from temperature-variable line widths measurements is fraught with large difficulties. Even within a given approach these difficulties appear; the solid line in Fig. 4 represents an alternative fit according to Eq. (2), however, with the fit parameter E_a^{MN} being fixed at 0.5 eV. This is roughly the activation energy probed by impedance spectroscopy (see below). The very small differences of the two fits reveal that irrespective of the validity of these models for spin-3/2 nuclei, highly precise line width measurements are required to give accurate results. Obviously, small errors in measurement could have a large impact on the resulting parameters of interest.

Nevertheless, line-shape measurements are highly valuable for a rough estimate of diffusion parameters in ionically conducting solids.^{32,33,59–63} Here, the results indicate that the maximum of the diffusion-induced ${}^7\text{Li}$ SLR NMR rate peak [$R_l(\omega_1/2\pi)$], when recorded at a locking frequency $\omega_1/2\pi$ in the kHz range, should show up between 300 K and 400 K. Indeed, this is exactly found for the garnet-type oxide studied here (see below).

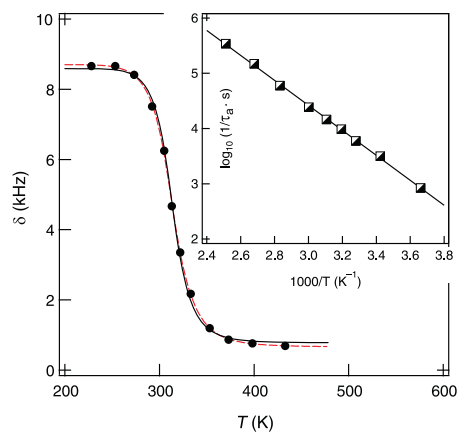


FIG. 4. (Color online) ${}^7\text{Li}$ NMR line widths δ of the central line versus temperature. The dashed line represents a fit according to Eq. (2) with no restrictions for the adjustable parameters. The solid line shows the same fit, however, with E_a being fixed at 0.5 eV. (Inset) Arrhenius plot of the correlation rates τ_a^{-1} of Eq. (2). The solid line shows a fit according to the corresponding Arrhenius relation and yields $E_a \approx 0.43$ eV.

2. ^7Li NMR spectra: Quadrupole intensities

In order to study the temperature behavior of the quadrupole intensities (see above), complete NMR spectra were recorded by using the stimulated echo technique. Exemplarily, in the insets of Fig. 3 ^7Li spin-alignment echo NMR spectra are shown which were acquired with the Jeener-Broekaert pulse sequence. Besides its central line, the room temperature ^7Li NMR spectrum of tetragonal $\text{Li}_7\text{La}_3\text{Zr}_2\text{O}_{12}$ exhibits a powder pattern of satellite intensities. In the tetragonal phase of $\text{Li}_7\text{La}_3\text{Zr}_2\text{O}_{12}$ the Li ions occupy distinct crystallographic sites being characterized by different electric field gradients. Most likely, the quadrupole intensity is composed of distinct patterns belonging to the Li ions residing on the distorted octahedral sites¹³ (see above). However, distinct patterns are difficult to resolve because of dipole-dipole interactions broadening the spectrum. From the outer wings an average coupling constant C_q of approximately 108 kHz can be estimated.

At a sufficiently large Li jump rate, on the order of $\tau^{-1} \approx 10^5 \text{ s}^{-1}$, quadrupole interactions are expected to be averaged to a great extent provided an isotropic diffusion process is present in which all Li sites participate equally. In fact, in the NMR spectrum recorded at 333 K (see inset (b) of Fig. 3) any significant contributions from quadrupole interactions are absent. However, as can be seen from the Fourier transforms of the FIDs in Fig. 3, a new quadrupole powder pattern emerges characterized by a much smaller coupling constant of $C'_q \approx 4.6 \text{ kHz}$. This is more apparent in the stimulated echo NMR spectrum (inset (a) of Fig. 3). In general, in single-phase materials this reflects incomplete averaging of quadrupole couplings and indicates an anisotropic diffusion process; for comparison, see also Ref. 39. Here the change from tetragonal to cubic symmetry (see Ref. 37) might also be related to this observation. When the temperature is increased to 663 K the intensity of these residual satellite contributions finally decreases. At even higher temperatures a single NMR resonance is expected due to complete averaging. Most likely, besides the main diffusion process causing line narrowing, averaging of quadrupole interactions governing the spectrum at room temperature (inset (c) of Fig. 3) as well as NMR SLR (see below), the ions seem to get access to further diffusion pathways if the temperature is sufficiently high. However, owing to the small value of C'_q this additional process has to be characterized by a very small exchange rate since full averaging is not reached at 663 K yet. It might reflect Li exchange between the two spin reservoirs made visible in Fig. 2, which are also present in $\text{Li}_7\text{La}_3\text{Zr}_2\text{O}_{12}$ with cubic symmetry. While the majority of the Li ions in the octahedral interstices govern the diffusion properties of $\text{Li}_7\text{La}_3\text{Zr}_2\text{O}_{12}$, Li ions occupying tetrahedral sites take part in the diffusion process at higher temperatures only. However, the latter has a negligible influence on the overall jump rates measured below.

C. ^7Li NMR spin-lattice relaxation rates

1. Basics of ^7Li NMR spin-lattice relaxation

Within an NMR relaxation experiment the equilibrium state of a spin system exposed to an external magnetic field B_0 is perturbed in a specific way by a short external radio frequency

pulse. Immediately after excitation the spin system will start to return to its state of thermal equilibrium. The recovery of longitudinal magnetization M_z , that is, the magnetization aligned with the external magnetic field, is called spin-lattice relaxation. This process can be recorded when the recovery of M_z along the axis z defined by the magnetic field B_0 is monitored as a function of waiting (or delay) time t . Usually, the transient $M_z(t)$ follows an exponential containing the temperature-dependent SLR NMR rate $R_1 = 1/T_1$ (or $R_{1\varrho} = 1/T_{1\varrho}$), being a measure of the transition probability of the spins between distinct Zeeman levels.

In general, if SLR is solely induced by diffusion processes, the rate $R_{1(\varrho)}$ is proportional to the spectral density function $J(\omega)$, which is the Fourier transform of the correlation function $G(t)$. $G(t)$ contains the temporal information of the atomic diffusion. It describes the internal fluctuating dipolar magnetic or quadrupolar electric fields due to the motion of the ions. Transitions between the energy levels of the spin system will be induced and SLR becomes effective, when $J(\omega)$ has components at the transition frequencies $\omega = \omega_0$ and $\omega = \omega_1$, respectively. The SLR NMR rates may be expressed in terms of the Lorentzian-shaped spectral density functions $J^{(q)}(\omega_{0(1)})$ given in, for example, Refs. 57 and 64:

$$R_1 \propto J^{(1)}(\omega_0) + J^{(2)}(2\omega_0), \quad (3)$$

$$R_{1\varrho} \propto J^{(0)}(2\omega_1) + 10J^{(1)}(\omega_0) + J^{(2)}(2\omega_0). \quad (4)$$

$J^{(q)}(\omega_{0(1)})$ with $q = 0, 1, 2$ denote spectral densities which result in transitions of spin pairs where the combined angular momentum changes by $q\hbar$. \hbar is Planck's constant divided by 2π . The phenomenological SLR NMR model introduced by Bloembergen, Purcell, and Pound (BPP) considers random jump diffusion. The correlation function is assumed to be an exponential,⁶⁵

$$G(t)^{(q)} = G^{(q)}(t=0) \exp(-|t|/\tau_c), \quad (5)$$

leading to a Lorentzian-shaped spectral density function,

$$J^{(q)}(\omega) = G^{(q)}(t=0) \frac{2\tau_c}{1 + (\omega\tau_c)^\beta} \quad \text{with } \beta = 2 \text{ (BPP)}. \quad (6)$$

The temperature dependence of the correlation time τ_c or the corresponding rate can be described by an Arrhenius relation,

$$\tau_c^{-1} = \tau_{c,0}^{-1} \exp[-E_a/(k_B T)]. \quad (7)$$

Altogether, the diffusion-induced relaxation rate R_1 , measured at $\omega = \omega_0$ (or $\omega = \omega_1$), first increases with increasing T (low- T range, $\omega_0\tau \gg 1$), passes through a maximum at a specific temperature T_{max} , and then decreases [high- T range, $\omega_0\tau \ll 1$]. Taking into account the frequency dependence of $R_1(\omega_{0(\varrho)}, T)$, the behavior can be summarized as follows:

$$R_{1(\varrho)} \propto \begin{cases} \exp[E_{a\text{low}}/(k_B T)], & \text{if } T \gg T_{\text{max}}, \\ \omega_{0(1)}^\beta \exp[-E_{a\text{high}}/(k_B T)], & \text{if } T \ll T_{\text{max}}. \end{cases} \quad (8)$$

$T_{\text{max}} = f(\omega_{0(\varrho)})$ decreases with decreasing Larmor and locking frequency, respectively. The absolute value of ω_0 is linked to the external homogenous magnetic field B_0 via $\omega_0 = \gamma B_0$, where γ is the magnetogyric ratio of the probe nucleus.

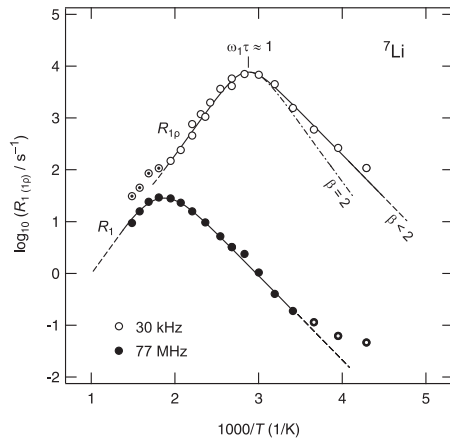


FIG. 5. ${}^7\text{Li}$ NMR SLR rates of garnet-type $\text{Li}_7\text{La}_3\text{Zr}_2\text{O}_{12}$ recorded in both the laboratory (\bullet) and the rotating frame of reference (\circ). The solid lines show fits according to Eqs. (3) and (4). Data points marked with a dot were excluded from the fit (see text for further details). The dashed-dotted line illustrates the deviation of the rate peak $R_{1e}(1/T)$ from simple BPP-type behavior characterized by $\beta = 2$.

Usually B_0 has a value of several teslas so that $\omega_0/2\pi$ is of the order of 100 MHz. At the temperature $T_{\text{max}}(\omega_0)$ where the rate maximum appears, the correlation rate τ_c^{-1} , which is within a factor of two identical with the mean Li jump rate τ^{-1} , is of the order of ω_0 meaning $\omega_0\tau_c \approx 1$. The temperature dependence of τ^{-1} is given by an Arrhenius relation being analogous to that of the correlation rate: $\tau^{-1} = \tau_0^{-1} \exp(-E_a/k_B T)$. Thus, SLR NMR measurements allow for the determination of extremely fast Li jump processes characterized by rates on the order of 10^9 s^{-1} . If the diffusion-induced maximum is recorded, $\tau^{-1}(1/T_{\text{max}})$ can be directly determined. Regarding SLR NMR measurements performed in the rotating frame of reference,^{49,66} ω_0 has to be replaced with the locking frequency ω_1 and B_0 with the radio-frequency magnetic field B_1 . The locking field B_1 corresponds to $\omega_1/2\pi$ values in the kHz range, making the method ideal for the detection of slower Li motions with jump rates on the order of 10^5 s^{-1} .

2. Arrhenius plot of the ${}^7\text{Li}$ SLR NMR data and analysis of the diffusion-induced rate peaks

${}^7\text{Li}$ SLR NMR rates of $\text{Li}_7\text{La}_3\text{Zr}_2\text{O}_{12}$ measured at $\omega_1/2\pi = 30 \text{ kHz}$ as well as $\omega_0/2\pi = 77.8 \text{ MHz}$ are plotted in the Arrhenius diagram of Fig. 5. As indicated by the line widths analysis (see above), the rate maximum shows up at approximately $T_{\text{max}} = 325 \text{ K}$ and 530 K , respectively. The mean Li jump rates at these two temperatures turn out to be $1.9 \times 10^5 \text{ s}^{-1}$ and $4.9 \times 10^8 \text{ s}^{-1}$, respectively. As expected, the SLR NMR rate peak recorded at $\omega_0/2\pi = 155.5 \text{ MHz}$ is slightly shifted to higher temperatures. While its shape equals that of the peak recorded at the lower field, the maximum shows up at 570 K . The jump rate can be easily converted into the self-diffusion coefficient D_{sd} by means of the Einstein-Smoluchowski equation. In the case of 3D

diffusion D_{sd} is expressed by $D_{\text{sd}} = a^2/(6\tau)$, where a is the jump distance which can be identified with the average Li-Li distance.¹³ With a being of the order of 2 \AA the diffusion coefficient at $T_{\text{max}} = 325 \text{ K}$ amounts to $1.3 \times 10^{-17} \text{ m}^2 \text{ s}^{-1}$ and increases to $3.3 \times 10^{-14} \text{ m}^2 \text{ s}^{-1}$ when T is raised to 530 K .

Interestingly, an asymmetric rate peak $R_{1e}(1/T)$ is obtained; that is, the slope of the low-temperature flank ($T < 330 \text{ K}$) is lower than that of the high-temperature side, leading to $E_{a,\text{low}} < E_{a,\text{high}}$. Analyzing just the data points on the flanks of this peak, the corresponding activation energies are $E_{a,\text{low}} = 0.32(3) \text{ eV}$ [the same value is found for the $R_1(1/T)$ peak] and $E_{a,\text{high}} = 0.48(3) \text{ eV}$, respectively. Asymmetric rate peaks are predicted by several BPP-based relaxation models taking into account correlation effects such as Coulomb interactions and/or structural disorder.²¹ In particular, this holds for amorphous (glassy) ion conductors with an irregularly formed, time-dependent potential landscape the ions are exposed to while diffusing. Li diffusion in such materials is governed by nonexponential correlation functions reflecting a distribution of jump rates (as well as activation barriers).^{32,67,68} In general, in the regime $\tau_c\omega_1 \gg 1$, i.e., on the low-temperature side of $R_{1e}(1/T)$, only few Li jumps are sampled in the time interval set by ω_1 . Therefore, Li motions taking place on a shorter length scale mainly cause SLR in this temperature regime. This is in contrast to the situation on the high-temperature flank, where $\tau_c\omega_1 \ll 1$ holds (see above) and long-range Li diffusion parameters are probed, which reasonably implies $E_{a,\text{low}} < E_{a,\text{high}}$.

The asymmetry of a SLR NMR rate peak is taken into account in Eq. (6) when the exponent β is allowed to adopt values in the interval $1 < \beta \leq 2$.²¹ The original BPP model, which has been developed for uncorrelated jump diffusion, contains a quadratic dependence of the SLR NMR rate on frequency [$\beta = 2$; see Eq. (6)], leading to symmetric rate peaks; that is, $E_{a,\text{low}} = E_{a,\text{high}} = E_a$. Solid lines in Fig. 5 represent fits according to Eqs. (3) and (4) for R_1 and R_{1e} , respectively. The angular frequencies ω_0 and ω_1 were kept constant. The spectral density functions $J^{(q)}(\omega_{0(1)})$ are defined in Ref. 64 considering exponential correlation functions. The functions $J^{(q)}(\omega_{0(1)})$ are of the form of Eq. (6) taking into account $1 < \beta \leq 2$ leading to $R_{1(\beta)} \propto \omega^\beta$ in the limit $\omega_{0(1)}\tau_c \ll 1$. On the high-temperature flank of the diffusion-induced rate peak the SLR rate is independent of frequency. In the case of R_{1e} NMR measurements the fit shown in Fig. 5 yields $E_a = 0.47(2) \text{ eV}$ and $\beta = 1.7(1)$. The same parameters can be used to describe the R_1 peak. The results fulfill the relation $E_{a,\text{low}} = (\beta - 1) \cdot E_{a,\text{high}}$ given in Ref. 21. As an illustration the dashed-dotted line of Fig. 5 indicates the shape of $R_{1e}(1/T)$ for uncorrelated motion. This means that it represents the behavior for $\beta = 2$ leading to a symmetric rate peak.

Let us mention that the data points marked by dots were excluded from the fits shown. The R_1 rates recorded below approximately 260 K are increasingly governed by nondiffusive background effects caused, for example, by lattice vibrations or coupling of the spins with paramagnetic impurities. Above 530 K the R_{1e} rates are already influenced by R_1 [see Eqs. (3) and (4)]. Hence, the measured rate turned out to be larger than expected without this contribution. It is roughly taken into account in the global fit shown below.

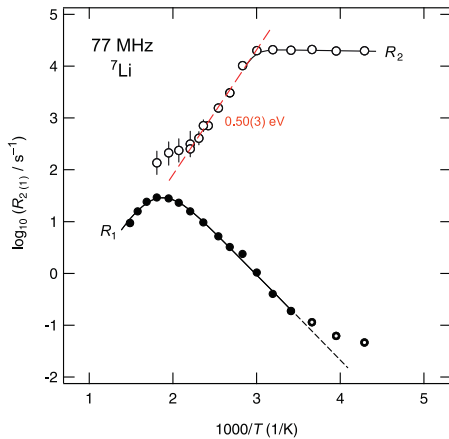


FIG. 6. (Color online) Temperature dependence of the ${}^7\text{Li}$ NMR SLR rates R_2 of $\text{Li}_7\text{La}_3\text{Zr}_2\text{O}_{12}$. The dashed line represents a fit according to an Arrhenius law yielding an activation energy of $0.50(3)$ eV. For comparison, the rates R_1 of Fig. 5 are shown, too.

3. Brief analysis of ${}^7\text{Li}$ spin-spin relaxation NMR rates

Compared with $E_a = 0.47(2)$ eV obtained from SLR NMR performed in the rotating frame of reference, a very similar activation energy can be deduced from temperature-variable spin-spin relaxation (SSR) NMR rate measurements when the temperature regime of MN is analyzed. SSR NMR rates R_2 , which were recorded at a resonance frequency of 77 MHz, are plotted in the Arrhenius diagram of Fig. 6. For comparison, the corresponding rates R_1 are shown, too. In terms of spectral densities $J^{(q)}$ the rate R_2 , when governed by homonuclear dipole-dipole interactions, reads²¹

$$R_2 \propto J^{(0)}(0) + 10J^{(1)}(\omega_0) + J^{(2)}(2\omega_0). \quad (9)$$

If the Li jump rate τ^{-1} is much smaller than ω_0 , the rate R_2 is approximately given by

$$R_2 \propto J^{(0)}(0) \propto \tau, \quad (10)$$

which holds for $J^{(0)}\tau \ll 1$ or $G^{(0)}\tau^2 \ll 1$ (MN regime; see above). This condition is violated at very low temperatures where $\tau^{-1} \ll R_2$ (rigid lattice), that is, in the limit $G^{(0)}\tau^2 \gg 1$. As mentioned above, the spins experience slightly different dipolar interactions, leading to a Gaussian distribution of frequencies around the mean value ω_0 . The rigid-lattice result is given by $R_{20} = \sqrt{G^{(0)}} = \text{const}$. Here, $1/R_{20} = T_{20}$ turns out to be about $45 \mu\text{s}$. In the present case Eq. (10) is valid in the temperature range from 300 K to 430 K. From the dashed line in Fig. 6 an activation energy of approximately 0.5 eV can be deduced, which is in good agreement with that probed by impedance spectroscopy (see below). As in the case of R_{1e} , at much higher temperatures, that is, in the so-called extreme narrowing regime, $J^{(1)}(\omega_0)$ and $J^{(2)}(2\omega_0)$ increasingly start to contribute to transverse relaxation (see the deviations of the data points in Fig. 6 with respect to the dashed line).

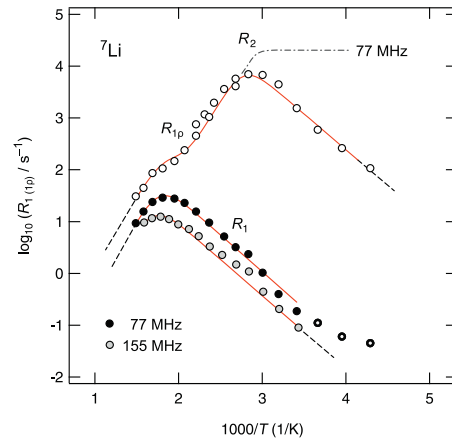


FIG. 7. (Color online) ${}^7\text{Li}$ NMR SLR rates R_1 as well as R_{1e} recorded at $\omega_1/2\pi = 30$ kHz and at 77 and 155 MHz. The solid lines represent a global fit according to Eqs. (3) and (4). The dashed-dotted line indicates the position of the SSR rates R_2 shown in Fig. 6. At higher T the R_2 rates follow the behavior of R_{1e} . Note that the fitting functions were modified such that dipolar relaxation is taken into account (see text for further details). Furthermore, ω_1 was replaced by an effective locking frequency ω_{eff} taking into account the coupling of the Li spins with paramagnetic centers. The data points marked by dots were excluded from the fit.

4. Global analysis of the NMR relaxation rates

Careful inspection of the NMR rates shows that at the highest temperature, i.e., in the limit $\omega_0\tau \gg 1$, the ratio R_2/R_1 is approximately given by $R_2/R_1 \approx 4$. This is in good agreement with the prediction $R_2/R_1 = (I + 1/2)^2$ for (magnetic dipolar) coupling to paramagnetic impurities which is obtained for half-integer spins ($I > 1/2$) when only the central transition is regarded.⁶⁹ Such couplings are taken into account by the so-called global fit shown in Fig. 7, where all the fitting parameters of the three curves, that is, E_a , τ_0^{-1} , β , as well as the other prefactors, are linked to each other. In other words, a single diffusion process with a set of temperature-independent parameters is assumed.

The R_2/R_1 ratio is implemented in the fit by multiplying the respective $J^{(i)}(\omega_0)$ terms in Eq. (4) with a factor of four. It is important to note that a successful joint fit can only be obtained when ω_1 is replaced by an effective locking frequency ω_{eff} taking into account local magnetic fields caused by paramagnetic impurities. Comparing the prefactor of Eq. (3) with that one deduced from the second moment yields $\omega_{\text{eff}} \approx 2\omega_1$. The corresponding jump rate (see the above estimation using ω_1 instead of ω_{eff}) increases accordingly.

Taken together, the joint fit of Fig. 7, which also makes use of an exponent β with $1 < \beta \leq 2$ (see above), yields an activation energy of $0.54(4)$ which is slightly larger than that obtained by analyzing the rate peaks independently of each other (see Fig. 6). From the global fit a β value of $1.5(1)$ is obtained which might indicate that a nonexponential correlation function governs Li diffusion in the garnet. The

pre-exponential factor amounts to approximately $\tau_0^{-1} = 1.4 \times 10^{14} \text{ s}^{-1}$, which is in the typical range of phonon frequencies.

D. Comparison with results from impedance spectroscopy

For the comparison of Li jump rates deduced from SLR NMR with results from impedance data (presented in Fig. 8), the measured conductivity values σ' characterizing the bulk response of $\text{Li}_7\text{La}_3\text{Zr}_2\text{O}_{12}$ have been converted into jump rates τ^{-1} .

This has been done by means of the Nernst-Einstein and Einstein-Smoluchowski equations. The first one connects $\sigma' = f(T)$, which is the real part of the complex conductivity $\hat{\sigma}$, with the tracer diffusion coefficient D_{tr} via the Haven ratio H_R ,

$$D_{\text{tr}} = H_R \frac{\sigma' k_B T}{N q^2}. \quad (11)$$

Here we have assumed $H_R = 1$. q in Eq. (11) represents the charge of the Li ions and N denotes the number density of charge carriers in the garnet. The macroscopic diffusion coefficient D_{tr} is related via the correlation factor f to the microscopic self-diffusion coefficient, $D_{\text{tr}} = f D_{\text{sd}}$. The correlation factor f reflects the degree of correlated motion of the charge carriers. It ranges between 0 and 1. $f = 1$ is obtained for uncorrelated motion. Using $D_{\text{sd}} = a^2/(6\tau)$ (see above) τ^{-1} and σ' are connected to each other according to the following expression:

$$\tau^{-1} = H_R f \frac{6k_B T}{N q^2 a^2} \cdot \sigma'. \quad (12)$$

Here σ' equals the so-called dc conductivity σ'_{dc} which is obtained when the conductivity, which is measured as a function frequency ν , is extrapolated to $\nu \rightarrow 0$. Figure 8(a) shows some typical impedance spectra $\sigma'(\nu)$, illustrating the difficulty to determine σ'_{dc} characterizing Li transport in the bulk of polycrystalline $\text{Li}_7\text{La}_3\text{Zr}_2\text{O}_{12}$ prepared as a powder sample. These difficulties arise from the presence of very pronounced blocking effects being caused by grain boundaries as well as metallic electrodes [Fig. 8(a)]. In the case of cold-pressed and nonsintered pellets these contributions dominate the impedance spectra at high temperatures and (or) low frequencies, in particular. Determination of ion conductivities using Cole-Cole plots is fraught with the same uncertainties. The different contributions of the electrical response can also be distinguished by plotting the real part of the capacity as a function of frequency. The bulk response is characterized by a capacitance of approximately 4 pF while those associated with grain boundary processes and electrode effects are in the order of 100 and 10^7 pF, respectively. In Fig. 9 the τ^{-1} rates calculated from the bulk σ'_{dc} values which were read out from the ac-conductivity isotherms shown in Fig. 8(a) (nonsintered pellet) are plotted versus the inverse temperature. For this estimation, we have simply assumed $f = 1$.

For a direct comparison with NMR results, the Li jump rates obtained from the diffusion-induced rate peaks are also included in Fig. 9. Note that in the case of $R_{1\theta}$ the upper value is calculated using ω_{eff} while the other one simply by the use of ω_1 . The data point labeled by MN corresponds to a Li jump rate estimated from the inflexion point of the MN curve shown

in Fig. 4. At the corresponding temperature the jump rate can be estimated according to the relation $\tau^{-1} \approx 2\pi\delta_0$. The consistency of the absolute values shows that both methods obviously probe the same Li dynamics in $\text{Li}_7\text{La}_3\text{Zr}_2\text{O}_{12}$. While conductivity measurements can be regarded as a tool probing transport in a macroscopic way, SLR NMR spectroscopy is capable of measuring the same parameters from a microscopic, that is, atomic-scale point of view. It takes advantage of internal dipolar-magnetic as well as quadrupolar-electric field fluctuations caused by the diffusive motion of the spins. While NMR is sensitive to Li motions characterized by residence times of the order of the inverse Larmor or locking frequency given by $\omega_0^{-1} \approx 1 \text{ ns}$ and $\omega_1^{-1} \approx 1 \mu\text{s}$, respectively, σ'_{dc} values were measured in the frequency range from 0.1 s to 1 μs . Thus, SLR NMR performed in the rotating frame of reference as well as impedance spectroscopy probe Li jump rates on the same time scale, however, in a quite different manner. The solid line shown in Fig. 9 represents an Arrhenius fit using all the data points shown except the one at the lowest temperature. The so-called long-range activation energy, being relevant for the application of the material in lithium-ion batteries, turned out to be $E_a = 0.52(2) \text{ eV}$ and the pre-exponential factor τ_0^{-1} is on the order of $1 \times 10^{14} \text{ s}^{-1}$. The activation energy deduced is in good agreement with that one probed by analyzing the diffusion-controlled NMR relaxation rate peaks as well as temperature-variable NMR SSR rates. From the fit of Fig. 9 the room-temperature diffusion coefficient D_{sd} turned out to be $1.8 \times 10^{-18} \text{ m}^2 \text{ s}^{-1}$. Interestingly, the gradual transition from a tetragonal to a cubic phase³⁷ (see above) is hardly reflected by the data. Thus, slight local changes in the structure do not show a significant influence on the dynamic parameters governing Li hopping in highly pure garnet-type $\text{Li}_7\text{La}_3\text{Zr}_2\text{O}_{12}$.

In order to prove in another way the low-frequency part of the impedance spectra shown in Fig. 8(a) is not related to bulk processes, the impedance pellet was annealed in air at high temperatures. Sintering the pellet at 1098 K (or 1148 K) leads to impedance spectra which are, particularly at low temperatures, increasingly dominated by the electrical response of the bulk material. Hence, σ'_{dc} can be easier read out from the ac-conductivity isotherms shown in Fig. 8(b). As expected, the bulk response remains nearly unaffected by this annealing process. Presumably, small differences might be explained by slight structural changes (see above), as well as a possible loss of lithium after the material was exposed to very high temperatures. Here the corresponding rates (or σ'_{dc} values) of the sintered material nearly coincide with those of the as-prepared sample. The results obtained from the latter, which was investigated by NMR, are shown in Fig. 9. At high frequencies and low temperatures the σ'_{dc} plateau reflecting bulk conductivity merges into the (frequency-dependent) dispersive regime of $\sigma'(\nu)$. Below approximately 135 K $\sigma'(\nu)$ becomes independent of temperature and tends to follow the power law $\sigma'(\nu) \propto \nu^s$. For structurally disordered materials the fractional exponent s takes values in the range from 0.5 to 0.8 in most cases (universal dynamic response).⁷⁰ Here, s turned out to be 0.77 at $T = 135 \text{ K}$.

Finally, in the Arrhenius plot of Fig. 8(c) bulk ion conductivities of $\text{Li}_7\text{La}_3\text{Zr}_2\text{O}_{12}$ are shown. For comparison, the corresponding conductivity values of the low-frequency plateau of Fig. 8(a) are also included. At ambient temperature

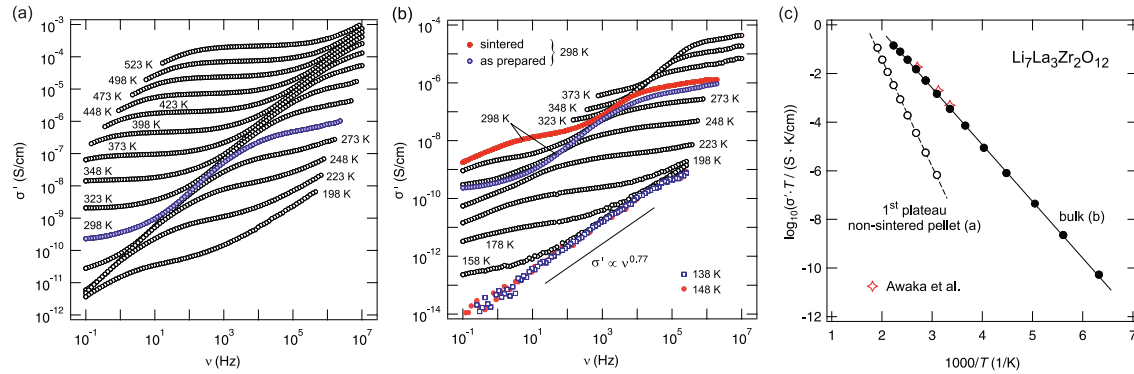


FIG. 8. (Color online) (a) Impedance spectra $\sigma'(\nu)$ of $\text{Li}_7\text{La}_3\text{Zr}_2\text{O}_{12}$ recorded at the temperatures indicated. The spectra are composed of different contributions reflecting electrode polarization, grain boundary, and bulk response (see, e.g., the highlighted spectra recorded at 298 K). The latter becomes most evident at low temperatures and merges into a dispersive regime at higher frequencies. σ'_{dc} of the bulk response is read out at the corresponding inflexion points. The uncertainty is somewhat less than half an order of magnitude (see also Fig. 9). At the lowest frequencies and highest temperatures, polarization effects showing up being characteristic for metallic electrodes blocking Li-ion transport. (b) Impedance spectra $\sigma'(\nu)$ of $\text{Li}_7\text{La}_3\text{Zr}_2\text{O}_{12}$ obtained after sintering the pellet at 1148 K. For comparison, the spectrum recorded at 298 K recorded before annealing is also shown. (c) σ'_{dc} (plotted as $\sigma'_{\text{dc}}T$ vs $1/T$) of the bulk response [see (b), sintered sample] as well as of the low-frequency conductivity plateau of the nonsintered sample [cf. panel (a)]. The solid line shows a fit according to $\sigma'_{\text{dc}}T \propto \exp[-E_a/(k_B T)]$, yielding $E_a = 0.47(2)$ eV (bulk). The dashed line corresponds to $E_a = 0.87(2)$ eV. For comparison, the data published recently by Awaka *et al.* are also shown (Ref. 13).

the lithium-ion dc conductivity of the bulk process is about $1.2 \times 10^{-6} \text{ S cm}^{-1}$. This is in very good agreement with that one reported by Awaka *et al.*¹³ The data follow an Arrhenius law characterized by an activation energy of approximately 0.46 eV. Almost the same value is probed by diffusion-induced ^7Li NMR SLR when the high-temperature flank of the diffusion-induced rate peak $R_{1\rho}(1/T)$ is analyzed.

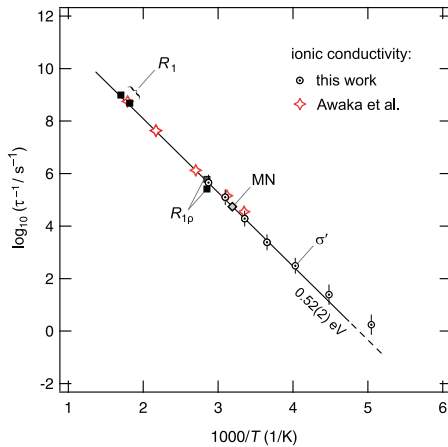


FIG. 9. (Color online) Temperature dependence of the Li jump rate in garnet-type $\text{Li}_7\text{La}_3\text{Zr}_2\text{O}_{12}$ as obtained from various NMR methods as well as ionic conductivity measurements. The jump rates deduced from R_1 NMR measurements were obtained at two different Larmor frequencies (see Sec. III C 1). For comparison, the conductivity data of Awaka *et al.* (Ref. 13), which were converted into Li jump rates according to Eq. (12), are also included. See Ref. 13 for details concerning these data points.

IV. CONCLUSIONS AND OUTLOOK

Polycrystalline garnet-type $\text{Li}_7\text{La}_3\text{Zr}_2\text{O}_{12}$, which was prepared by conventional solid-state synthesis, was investigated by temperature-variable NMR relaxation techniques particularly by monitoring purely diffusion-induced NMR SLR rate peaks in both the laboratory and the rotating frame of reference. While NMR line-shape measurements provide first insights into the Li dynamics in $\text{Li}_7\text{La}_3\text{Zr}_2\text{O}_{12}$, the fully recorded rate peak at a locking frequency of 30 kHz allowed, besides the observation of correlation effects, the precise and direct determination of Li self-diffusion parameters around ambient temperature. Altogether, the parameters characterizing Li dynamics, viz. jump rates and activation energies obtained by NMR, are in good agreement with those deduced from macroscopic conductivity measurements carried out in this study, as well as those reported in the literature quite recently. Let us note that the latter are often fraught with difficulties due to the unavoidable postpreparation of the sample specimens. In contrast, NMR is a noncontact method. Taken together, at ambient temperature the Li self-diffusion coefficient is in the order of $10^{-18} \text{ m}^2 \text{ s}^{-1}$. Li hopping in the garnet structure is thermally activated characterized by $E_a \approx 0.5$ eV. Interestingly, when the tetragonal garnet is used as starting material, the smooth transformation to a cubic phase, whose structure is very similar to that of the tetragonal phase, has negligible influence on the Li jump rates deduced (see Fig. 9); their temperature behavior can be described by a single diffusion process. Thus, from a dynamic point of view the highly pure garnet-type $\text{Li}_7\text{La}_3\text{Zr}_2\text{O}_{12}$ investigated here acts like a single-phase material.

This is corroborated by recent NMR measurements in our laboratory. Ongoing NMR experiments of a monoclinic distorted $\text{Li}_7\text{La}_3\text{Zr}_2\text{O}_{12}$ does not show any significant

differences compared to the sample studied here. SLR NMR as well as frequency-dependent conductivity measurements on a sample, which was prepared such that it shows cubic symmetry at ambient temperature, are in progress in our laboratory. First results indicate that NMR SLR rates of a relatively pure, nonannealed sample are very similar to those presented in this work. Thus, slight structural changes seem to have no measurable influences on ion conductivity in the pure three-component system $\text{Li}_2\text{O}:\text{La}_2\text{O}_3:\text{ZrO}_2$. It has to be checked in detail what the origins are for the large increase in ion conductivity observed for a cubic sample of $\text{Li}_7\text{La}_3\text{Zr}_2\text{O}_{12}$ previously.¹¹ At least partially, it might be due to the incorporation of impurities such as Al cations, as proposed quite recently.³⁷

ACKNOWLEDGMENTS

We thank Paul Heitjans (Hannover) for stimulating discussions as well as for access to his NMR laboratory in Hannover. We greatly acknowledge Konstantin Efimov and Armin Feldhoff (Hannover) for the *in situ* XRPD measurements carried out (at the last minute). We thank Frank Tietz (Forschungszentrum Jülich) for valuable discussions. Financial support by the Deutsche Forschungsgemeinschaft (DFG) in the framework of the Research unit FOR 1277 (Grant No. WI3600/2-1 and 4-1) as well as the Leibniz University Hannover (“Wege in die Forschung II”) are highly appreciated.

*Author to whom correspondence should be addressed: wilkening@pci.uni-hannover.de

¹A. V. Chadwick, *Phys. Status Solidi A* **204**, 631 (2007).

²P. Knauth and J. Schoonman (editors), *Nanocomposites—Ionic Conducting Materials and Structural Spectroscopies* (Springer, New York, 2007).

³H. L. Tuller, in *Springer Handbook of Electronic and Photonic Materials*, edited by S. Kasap and P. Capper (Springer, Berlin, 2006), Chap. 11, p. 213.

⁴S. Hull, *Rep. Prog. Phys.* **67**, 1233 (2004).

⁵E. Kendrick and P. Slater, *Annu. Rep. Prog. Chem., Sect. A: Inorg. Chem.* **106**, 429 (2010).

⁶A. S. Aricó, P. G. Bruce, B. Scrosati, J.-M. Tarascon, and W. V. Schalkwijk, *Nature (London)* **4**, 366 (2005).

⁷P. G. Bruce, B. Scrosati, and J.-M. Tarascon, *Angew. Chem. Int. Ed. Engl.* **47**, 2930 (2008).

⁸M. Whittingham, *Chem. Rev.* **104**, 4271 (2004).

⁹E. J. Cussen, *J. Mater. Chem.* **20**, 5167 (2010).

¹⁰A. Ramzy and V. Thangadurai, *ACS Appl. Mater. Interfaces* **2**, 385 (2010).

¹¹R. Murugan, V. Thangadurai, and W. Weppner, *Angew. Chem. Intern. Ed.* **46**, 7778 (2007).

¹²M. Kotobuki, H. Munakata, K. Kanamura, Y. Sato, and T. Yoshida, *J. Electrochem. Soc.* **157**, A1076 (2010).

¹³J. Awaka, N. Kijima, H. Hayakawa, and J. Akimoto, *J. Solid State Chem.* **182**, 2046 (2009).

¹⁴V. Thangadurai, S. Adams, and W. Weppner, *Chem. Mater.* **16**, 2998 (2004).

¹⁵V. Thangadurai and W. Weppner, *J. Am. Ceram. Soc.* **88**, 411 (2005).

¹⁶V. Thangadurai and W. Weppner, *Adv. Funct. Mater.* **15**, 107 (2005).

¹⁷R. Murugan, W. Weppner, P. Schmid-Beurmann, and V. Thangadurai, *Mater. Res. Bull.* **43**, 2579 (2008).

¹⁸V. Thangadurai and W. Weppner, *J. Power Sources* **142**, 339 (2005).

¹⁹V. Thangadurai, H. Kaack, and W. Weppner, *J. Am. Ceram. Soc.* **86**, 437 (2003).

²⁰R. Böhmer, K. Jeffrey, and M. Vogel, *Prog. Nucl. Magn. Reson. Spectrosc.* **50**, 87 (2007).

²¹P. Heitjans, A. Schirmer, and S. Indris, in *Diffusion in Condensed Matter—Methods, Materials, Models*, edited by P. Heitjans and J. Kärger (Springer, Berlin, 2005), Chap. 9, p. 369.

²²L. S. Cahill, R. Chapman, J. Britten, and G. Goward, *J. Phys. Chem. B* **110**, 7171 (2006).

²³L. J. M. Davis, I. Heinmaa, and G. R. Goward, *Chem. Mater.* **22**, 769 (2010).

²⁴M. Wilkening and P. Heitjans, *J. Phys. Condens. Matter* **18**, 9849 (2006).

²⁵M. Wilkening and P. Heitjans, *Solid State Ionics* **177**, 3031 (2006).

²⁶Z. Xu and J. F. Stebbins, *Science* **270**, 1332 (1995).

²⁷V. W. J. Verhoeven, I. M. de Schepper, G. Nachttegaal, A. P. M. Kentgens, E. M. Kelder, J. Schoonman, and F. M. Mulder, *Phys. Rev. Lett.* **86**, 4314 (2001).

²⁸J. Cabana, N. Dupré, G. Rousse, C. P. Grey, and M. R. Palacin, *Solid State Ion.* **176**, 2205 (2005).

²⁹M. Wilkening, W. Küchler, and P. Heitjans, *Phys. Rev. Lett.* **97**, 065901 (2006).

³⁰M. Wilkening and P. Heitjans, *Phys. Rev. B* **77**, 024311 (2008).

³¹M. Wilkening, D. Gebauer, and P. Heitjans, *J. Phys. Condens. Matter* **20**, 022201 (2008).

³²M. Wilkening, A. Kuhn, and P. Heitjans, *Phys. Rev. B* **78**, 054303 (2008).

³³L. van Wüllen, T. Echelmeyer, H.-W. Meyer, and D. Wilmer, *Phys. Chem. Chem. Phys.* **9**, 3298 (2007).

³⁴B. Koch and M. Vogel, *Solid State Nucl. Magn. Reson.* **34**, 37 (2008).

³⁵M. Nyman, T. M. Alam, S. K. McIntyre, G. C. Bleier, and D. Ingersoll, *Chem. Mater.* **22**, 5401 (2010).

³⁶M. P. O’Callaghan, A. S. Powell, J. J. Titman, G. Z. Chen, and E. J. Cussen, *Chem. Mater.* **20**, 2360 (2008).

³⁷C. A. Geiger, E. Alekseev, B. Lazic, M. Fisch, T. Armbruster, R. Langner, M. Fechtelkord, N. Kim, T. Pettke, and W. Weppner, *Inorg. Chem.* **50**, 1089 (2011).

³⁸D. Brinkmann, *Prog. Nucl. Magn. Reson. Spectrosc.* **24**, 527 (1992).

³⁹R. Bertermann and W. Müller-Wahrmuth, *Z. Naturforsch.* **53a**, 863 (1998).

⁴⁰J. Emery, J. Buzare, O. Bohnke, and J. Fourquet, *Solid State Ionics* **99**, 41 (1997).

⁴¹A. Rivera and J. Sanz, *Phys. Rev. B* **70**, 094301 (2004).

⁴²C. León, M. L. Lucía, J. Santamaría, M. A. París, J. Sanz, and A. Várez, *Phys. Rev. B* **54**, 184 (1996).

⁴³V. Epp and M. Wilkening, *Phys. Rev. B* **82**, 020301 (2010).

⁴⁴M. Wilkening, W. Iwaniak, J. Heine, V. Epp, A. Kleinert, M. Behrens, G. Nussli, W. Bensch, and P. Heitjans, *Phys. Chem. Chem. Phys.* **9**, 6199 (2007).

⁴⁵D. Bork and P. Heitjans, *J. Phys. Chem. B* **105**, 9162 (2001).

⁴⁶A. R. Allnatt and A. B. Lidiard, *Atomic Transport in Solids* (Cambridge University Press, Cambridge, 1993).

- ⁴⁷H. Mehrer, *Diffusion in Solids* (Springer, Berlin, 2006).
- ⁴⁸M. Wilkening, C. Mühle, M. Jansen, and P. Heitjans, *J. Phys. Chem. B* **111**, 8691 (2007).
- ⁴⁹E. Fukushima and S. Roeder, *Experimental Pulse NMR* (Addison-Wesley, Reading, 1981).
- ⁵⁰F. Qi, T. Jörg, and R. Böhmer, *Solid State Nucl. Magn. Reson.* **22**, 484 (2002).
- ⁵¹R. Böhmer, T. Jörg, F. Qi, and A. Titze, *Chem. Phys. Lett.* **316**, 419 (2000).
- ⁵²F. Qi, C. Rier, R. Böhmer, W. Franke, and P. Heitjans, *Phys. Rev. B* **72**, 104301 (2005).
- ⁵³X.-P. Tang and Y. Wu, *J. Magn. Res.* **133**, 155 (1998).
- ⁵⁴Let us note that $\text{Li}_7\text{La}_3\text{Zr}_2\text{O}_{12}$, which was prepared such that it crystallizes with cubic symmetry already at room temperature, shows the same NMR spectral features as observed for the tetragonal modification here.
- ⁵⁵T. Pietrass, F. Taulelle, P. Lavela, J. OlivierFourcade, J. Jumas, and S. Steuernagel, *J. Phys. Chem. B* **101**, 6715 (1997).
- ⁵⁶J. Waugh and E. Fedin, *Sov. Phys. Solid State* **4**, 1633 (1963).
- ⁵⁷A. Abragam, *The Principles of Nuclear Magnetism* (Clarendon, Oxford, 1961).
- ⁵⁸J. Hendrickson and P. Bray, *J. Magn. Res.* **9**, 341 (1973).
- ⁵⁹P. Heitjans, M. Masoud, A. Feldhoff, and M. Wilkening, *Faraday Discuss.* **134**, 67 (2007).
- ⁶⁰K. Nakamura, H. Ohno, K. Okamura, Y. Michihiro, T. Moriga, I. Nakabayashi, and T. Kanashiro, *Solid State Ionics* **177**, 821 (2006).
- ⁶¹T. Matsuo, M. Shibasaki, and T. Katsumata, *Solid State Ionics* **154**, 759 (2002).
- ⁶²H. Mattfeld, G. Balzer-Jöllenbeck, G. Meyer, and P. Heitjans, *Solid State Ionics* **62**, 265 (1993).
- ⁶³Y. Xia, N. Machida, X. Wu, C. Lakeman, L. vanWullen, F. Lange, C. Levi, and H. Eckert, *J. Phys. Chem. B* **101**, 9180 (1997).
- ⁶⁴C. A. Sholl, *J. Phys. C: Solid State Phys.* **14**, 447 (1981).
- ⁶⁵N. Bloembergen, E. Purcell, and R. Pound, *Phys. Rev.* **73**, 679 (1948).
- ⁶⁶D. C. Ailion and C. P. Slichter, *Phys. Rev.* **137**, A235 (1965).
- ⁶⁷S. Faske, H. Eckert, and M. Vogel, *Phys. Rev. B* **77**, 104301 (2008).
- ⁶⁸C. Brinkmann, S. Faske, B. Koch, and M. Vogel, *Z. Phys. Chem.* **224**, 1535 (2010).
- ⁶⁹P. M. Richards, in *Topics in Current Physics*, edited by M. B. Salamon (Springer, Berlin, 1979), Vol. 15.
- ⁷⁰K. Funke, C. Cramer, and D. Wilmer, in *Diffusion in Condensed Matter—Methods, Materials, Models*, edited by P. Heitjans and J. Kärger (Springer, Berlin, 2005), Chap. 9, p. 857.

Spin-alignment echo NMR: probing Li^+ hopping motion in the solid electrolyte $\text{Li}_7\text{La}_3\text{Zr}_2\text{O}_{12}$ with garnet-type tetragonal structure*

A Kuhn¹, V Epp¹, G Schmidt², S Narayanan³, V Thangadurai³ and M Wilkening^{1,4,5}

¹ Institute of Physical Chemistry and Electrochemistry, and Centre for Solid State Chemistry and New Materials (ZFM), Gottfried Wilhelm Leibniz University Hannover, Callinstraße 3a, D-30167 Hannover, Germany

² Bruker BioSpin GmbH, Silberstreifen, D-76287 Rheinstetten, Germany

³ Department of Chemistry, University of Calgary, 2500 University Drive NW, Calgary, Alberta, T2N 1N4, Canada

⁴ Institute for Chemistry and Technology of Materials, Graz University of Technology, A-8010 Graz, Austria

E-mail: epp@pci.uni-hannover.de, wilkening@pci.uni-hannover.de and wilkening@tugraz.at

Received 19 July 2011, in final form 14 November 2011

Published 19 December 2011

Online at stacks.iop.org/JPhysCM/24/035901

Abstract

⁷Li spin-alignment echo (SAE) nuclear magnetic resonance (NMR) spectroscopy has been used to measure single-spin hopping correlation functions of polycrystalline $\text{Li}_7\text{La}_3\text{Zr}_2\text{O}_{12}$. Damping of the echo amplitude $S_2(t_m, t_p)$, recorded at variable mixing time t_m but fixed preparation time t_p , turns out to be solely controlled by slow Li jump processes taking place in the garnet-like structure. The decay rates τ_{SAE}^{-1} directly obtained by parametrizing the curves $S_2(t_m, t_p)$ with stretched exponential functions show Arrhenius behaviour pointing to an activation energy of approximately 0.5 eV. This value, probed by employing an atomic-scale NMR method, is in very good agreement with that deduced from impedance spectroscopy used to measure macroscopic Li transport parameters. Most likely, the two methods are sensitive to the same hopping correlation function although Li dynamics are probed in a quite different manner.

(Some figures may appear in colour only in the online journal)

1. Introduction

The precise microscopic measurement of Li jump rates, which can be directly transformed into self-diffusion coefficients via the Einstein–Smoluchowski equation (see below), increasingly attracts materials scientists working in the field of clean energy storage systems [1–7]. In

rechargeable batteries, Li ion conductors serve as anodes and cathodes as well as (solid) electrolytes [2–6, 8]. Besides chemical resistance, guaranteeing the safety of an all-solid-state battery, the prerequisites of a promising electrolyte are a high Li ion conductivity and a vanishing electronic one. Among a large number of pure ion conductors, garnet-type oxides [9–13], in particular, have attracted great attention during the past few years. Due to their structural complexity a number of possibilities are offered to control the influence on their ion transport properties, e.g. by changing the overall chemical composition (full replacement of a cation

* Dedicated to Professor Dr Paul Heitjans on the occasion of his 65th birthday.

⁵ www.wilkening.pci.uni-hannover.de.

species), by knowledge-based doping with isovalent and non-isovalent cations as well as by manipulating the lithium or oxygen stoichiometry. In particular, the latter might be greatly affected by the preparation route chosen to synthesize an oxidic garnet. A thorough understanding of the impact of these changes on Li dynamics requires deep insights into the Li jump processes present in the undoped garnets serving as internal reference materials.

Solid-state nuclear magnetic resonance (NMR) spectroscopy offers a rich portfolio of highly sophisticated techniques which can be used to measure Li jump processes on quite different timescales and length scales [14–28], respectively. In particular, the analysis of stimulated (spin-alignment) echoes [15, 16, 18, 29–42] turned out to be well suited to trace slow motions of spin-1 and spin-3/2 probes such as ${}^6\text{Li}$ and ${}^7\text{Li}$ (as well as ${}^9\text{Be}$ [43–45]) in a rather straightforward way which is comparable to that of magic angle spinning (MAS) NMR exchange spectroscopy [20–24, 27, 46–48]. While exchange spectroscopy requires well-resolved NMR spectra, NMR spin-alignment echoes (SAE) are recorded under static conditions. This makes the technique an attractive alternative when amorphous materials have to be investigated [31, 33, 38].

${}^7\text{Li}$ as well as ${}^6\text{Li}$ SAE NMR [15], using the three-pulse sequence of Jeener and Broekaert [49] (see section 2), takes advantage of temporal fluctuations of the electric field gradients (EFGs) the jumping ions experience during diffusing. The interaction of the quadrupole moment of the Li nucleus with an EFG, which is caused by the electric charge distribution in its neighborhood, leads to the well-known alteration of the Zeeman frequency [15, 18, 35, 50]. The corresponding orientation-dependent (angular) quadrupole frequency ω_q , which is determined by the quadrupole coupling constant δ_q as well as the asymmetry parameter of the interaction η_q , is used to label the electrically inequivalent Li sites. The diffusive jump process of the ions is coded in terms of a change in ω_q . Thus, the spin-alignment technique allows the measurement of a single-spin correlation function [15, 16]. The intensity of the spin-alignment echo is given by [15, 51]

$$S_2(t_p, t_m) = \frac{9}{20} \langle \sin[\omega_q(t_m = 0)t_p] \sin[\omega_q(t_m)t_p] \rangle. \quad (1)$$

Here, t_m denotes the mixing time and t_p the preparation time while $\langle \dots \rangle$ means powder average. In order to obtain dynamic information of the jump process, $S_2(t_p, t_m)$ is recorded for fixed t_p and variable t_m . The decay curve can be approximated with stretched exponential functions containing a decay rate τ_{SAE}^{-1} which, in the ideal case, might be identified with the mean jump rate τ^{-1} of the ion [18, 33, 38, 40]. In the case of three-dimensional diffusion, τ^{-1} is related via the well-known Einstein–Smoluchowski equation with the self-diffusion coefficient D according to $D = a^2/6\tau$, see, e.g., [28, 52] for an introduction into solid-state diffusion phenomena. a is the (mean) jump distance which can be easily deduced from the crystallographic structure of the material [53]. Certainly, in analogy to ${}^2\text{H}$ as well as ${}^9\text{Be}$ SAE NMR, the technique is applicable if a non-selective excitation of the Li NMR spectrum is possible. For the two stable

Li isotopes, ${}^6\text{Li}$ (spin-1) and ${}^7\text{Li}$, the quadrupole moments are small enough, resulting in quadrupole coupling constants in the kHz range so that this pre-requirement is perfectly fulfilled [33, 41].

Quite recently, we have investigated Li dynamics in a polycrystalline sample of $\text{Li}_7\text{La}_3\text{Zr}_2\text{O}_{12}$, crystallizing with tetragonal symmetry at room temperature, complementarily by diffusion-induced NMR spin–lattice relaxation and electrical impedance spectroscopy [54]. In good agreement with previous impedance spectroscopy results reported by Awaka *et al* [53], slightly above room temperature the Li jump rate amounts to approximately 10^4 s^{-1} pointing to an Li self-diffusion coefficient in the order of $10^{-16} \text{ m}^2 \text{ s}^{-1}$. Therefore, the material is suitable to be studied with Li-stimulated echo NMR which has proven to be a tool giving direct access to Li motions with rates smaller than 10^5 s^{-1} [16, 37, 40, 45, 55]. The upper and lower limits of SAE NMR are given by the spin–spin and spin–lattice relaxation NMR rates of the Li ion conductor under investigation [15].

2. Experimental details

${}^7\text{Li}$ NMR spin-alignment echoes (see figure 1) were recorded using an Avance III NMR spectrometer (Bruker BioSpin, Rheinstetten (Germany)) in connection with a shimmed cryomagnet (Bruker) operating at a fixed field of 7 T. The corresponding resonance frequency was 116 MHz. Additionally, some measurements were also carried out at 77 MHz using a Bruker MSL 100 spectrometer in combination with an unshimmed cryomagnet. NMR echoes were acquired with the Jeener–Broekaert pulse sequence [49] which is

$$\beta_{1\phi_1} - t_p - \beta_{2\phi_2} - t_m - \beta_{3\phi_3} - t_{\text{acq}}. \quad (2)$$

where $\beta_1 = 90^\circ$ and $\beta_2 = \beta_3 = 45^\circ$. ϕ_i denotes the phases of the rf pulses β_i . A suitable phase cycling with 32 entries ensures the elimination of unwanted coherences so that dipolar contributions to the echo are, as far as possible, suppressed. The 90° pulse length was $2.4(1) \mu\text{s}$. If not stated otherwise the preparation time t_p was chosen to be $10 \mu\text{s}$ and the mixing time t_m was varied from $10 \mu\text{s}$ to 10 s . t_{acq} denotes the acquisition time. The temperature in the sample chamber was controlled with an accuracy of $\pm 0.5 \text{ K}$.

The recycle delay t_d between each scan was chosen to be sufficiently long so that any influence on the echo amplitudes due to short repetition times can be excluded. For this purpose the temperature- and frequency-dependent ${}^7\text{Li}$ NMR spin–lattice relaxation time T_1 was measured independently by the use of the saturation recovery pulse sequence, see, e.g., [28, 56], before each SAE NMR experiment. T_1 measurements were carried out at various temperatures ranging from 283 to 333 K with a commercial solid-state NMR probe (Bruker). Let us note that the corresponding NMR spin–lattice relaxation transients, which can be represented by a stretched exponential, reveal a two-component behaviour. The amplitude of the main component, which is characterized by the rate T_1^{-1} , is about 85%. In the T range covered here T_1 is of the order of 10 s . The

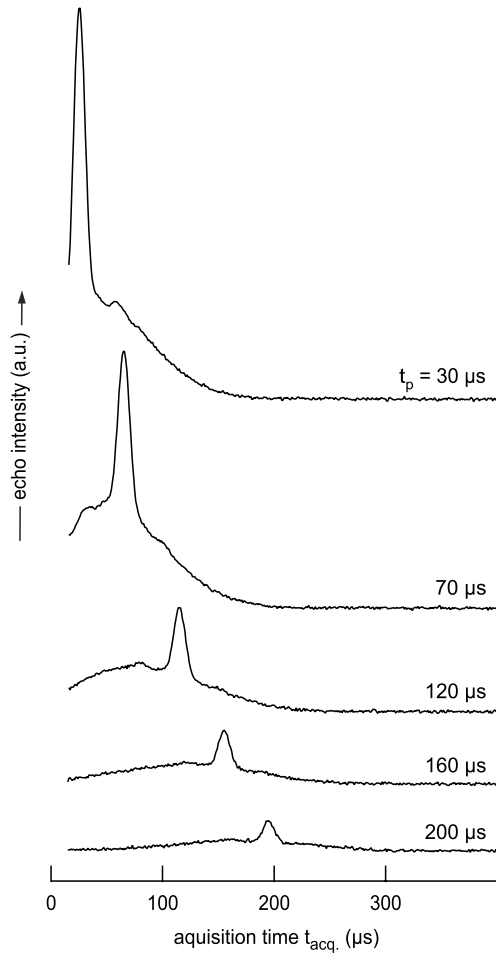


Figure 1. ${}^7\text{Li}$ NMR spin-alignment echoes of tetragonal $\text{Li}_7\text{La}_3\text{Zr}_2\text{O}_{12}$ recorded at 116 MHz and 294 K with the Jeener–Broekaert pulse sequence. The mixing time was chosen as short as possible to ensure that the echoes are not affected by Li motions. Each echo is composed of a sharply decaying quadrupole intensity and a broad dipolar echo.

second contribution does show up only at much larger delay times. It is characterized by an NMR spin–lattice relaxation time T_{1s} , which is of the order of a few hundreds seconds. As will be shown below, the relevant part of the SAE decay curves from which the Li diffusion parameters have been deduced is measured at mixing times t_m ranging from 10 μs to 0.1 s. Thus, from a dynamic point of view the slowly relaxing component has a negligible effect on the echo amplitudes analysed.

The powder sample was fire-sealed in a quartz tube with a diameter of 4 mm and a length of 3 cm. The details of sample preparation and characterization can be found in [54]. X-ray powder diffraction (XRPD) measurements reveal the typical powder pattern of phase-pure $\text{Li}_7\text{La}_3\text{Zr}_2\text{O}_{12}$ crystallizing with tetragonal symmetry. *In situ* XRPD shows that up to 353 K no phase transformation of the sample occurs. Note that at higher

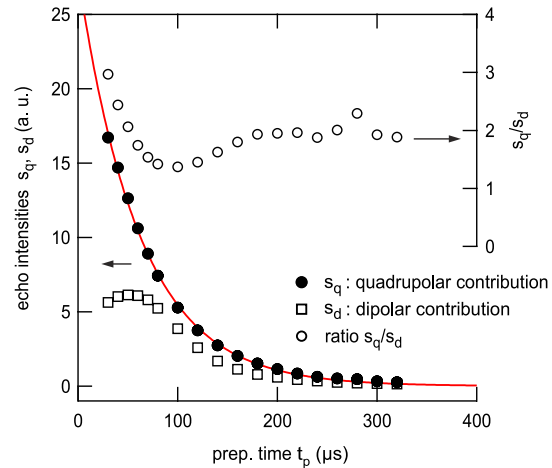


Figure 2. Echo intensities s_q and s_d versus preparation time, i.e. evolution of the two contributions to the ${}^7\text{Li}$ spin-alignment echoes in figure 1 with increasing t_p which is the delay time between the first two pulses of the Jeener–Broekaert echo sequence. The solid line represents a fit using an exponential function $s_q \propto \exp(-t_{\text{acq}}/T_{2,q})$. For comparison, the ratio s_q/s_d is also shown.

temperatures the space group reversibly changes towards cubic symmetry. However, as is shown in detail in [54], these slight structural changes have no impact on the Li diffusion parameters probed by impedance as well as NMR spin–lattice relaxation measurements.

3. Results

In figure 1 a set of typical ${}^7\text{Li}$ SAE NMR echoes, which have been recorded at ambient temperature using preparation times ranging from 10 to 325 μs , is shown. The recycle delay used was $5T_1$. The echoes are composed of two contributions. The sharp echo appearing at $t_{\text{acq}} = t_p$ refers to the spin-alignment (quadrupolar) echo whose intensity, when recorded as a function of t_m , leads to a single spin hopping correlation function (see below). It superimposes a broad echo most likely owing to strong ${}^7\text{Li}$ homonuclear dipole–dipole interactions [30]. In the ideal case these interactions are completely absent, because for symmetry reasons this contribution should not show up in sin–sin quadrupolar spin-alignment echoes [15].

As expected, owing to transverse dephasing effects, the intensities of the two contributions, s_q and s_d , change individually with increasing preparation time (see figure 2). The transverse decay rate of the ${}^7\text{Li}$ spin-alignment echo, referring to the quadrupolar information stored during t_p , turns out to be of the order of $T_{2,q}^{-1} = 62(3) \mu\text{s}$ (see the solid line in figure 2 representing a fit according to a single exponential function). The broad echo representing the weaker dipolar contribution reaches its maximum intensity at $t_p \approx 50 \mu\text{s}$. At preparation times larger than $t_p \approx 80 \mu\text{s}$ it starts to decay exponentially with a decay rate $T_{2,d}^{-1} \approx 55 \mu\text{s}$

being very similar to $T_{2,q}^{-1}$. The ratio s_q/s_d tends to two at a sufficiently long preparation time. This is in agreement with the calculations presented by Tang and Wu [44]. They analysed the possibility to separate dipolar from quadrupolar contributions to the spin-alignment echo of spin-3/2 nuclei by proper choosing of the interpulse delay t_p .

Note that in the range $10 \mu\text{s} < t_p < 300 \mu\text{s}$ the spin-alignment echo precisely appears at $t' = t_p + t_a$ with $t_a = 5.5 \mu\text{s}$ reflecting receiver dead time effects as well as the influence of the rf pulses with lengths of a few μs . This behaviour is in contrast to the broader dipolar echo showing up at $t' < t_p$ when preparation times $t_p > 50 \mu\text{s}$ are regarded. The corresponding shift t_a turns out to be larger and to depend slightly on t_p .

Fourier transformation starting from the top of the alignment echoes shown in figure 1 yields NMR spectra certainly being composed of two contributions (see figure 3). In a sample with various electrically inequivalent Li sites, which is the case here, the quadrupolar spin-alignment contribution is a superposition of distinct site-specific quadrupole powder patterns. At short t_p a substructure of the powder pattern can be recognized. From the outer wings a mean quadrupole coupling constant δ_q is estimated to be approximately 108 kHz. Note that, due to phase errors, in some cases distorted spin-alignment spectra are obtained. Possible origins of undershoots near the central intensities are explicitly worked out and discussed in [57]. It is beyond the scope of the present paper to analyse the shape of the echoes in detail. Additional echoes and anti-echoes with low intensity and appearing at $t = t_p \pm t_e$ might contribute to the total echo signal. In the following we will restrict the analysis on the mixing-time-dependent evolution of the intensity of the quadrupolar alignment echo showing up at $t = t_p$.

In general, damping of the stimulated echo as a function of mixing time but constant preparation time, that is, recording the curve $S_2(t_m, t_p)$, is caused by Li motional processes as well as NMR spin–lattice relaxation effects [15, 32]. Moreover, spin diffusion might influence the echo intensity S_2 , particularly at sufficiently low temperatures where jump rates of the order of 1 s^{-1} are expected. Thus, the single-spin correlation function $S_2'(t_m, t_p)$, which in many cases can be parametrized with a stretched exponential $S_2'(t_m, t_p) \propto \exp(-(t_m/\tau_{\text{SAE}})^\gamma)$ with $0 < \gamma \leq 1$, is additionally damped by the terms $\exp(-(t_m/T_{1,q})^{\gamma_q})$ and $\exp(-(t_m/T_{1,\text{sd}})^{\gamma_{\text{sd}}})$, respectively. Here, $T_{1,q}^{-1}$ denotes the quadrupolar spin–lattice relaxation rate (see [32]) and $T_{1,\text{sd}}^{-1}$ the corresponding decay rate of spin diffusion which is temperature-independent. While the latter decay terms lead to $S_2 \rightarrow 0$ for $t_m \rightarrow \infty$, the single-particle correlation function S_2' , containing the dynamic information of the diffusion process, generally shows a so-called final-state amplitude S_∞ . Thus, the complete decay curve $S_2(t_m, t_p)$ can be written as

$$S_2(t_m, t_p) \propto S_2' \exp(-(t_m/T_{1,q})^{\gamma_q}) \exp(-(t_m/T_{1,\text{sd}})^{\gamma_{\text{sd}}}) \quad (3)$$

with

$$S_2'(t_m, t_p) = (A \exp(-(t_m/\tau_{\text{SAE}})^\gamma) + B) \quad (4)$$

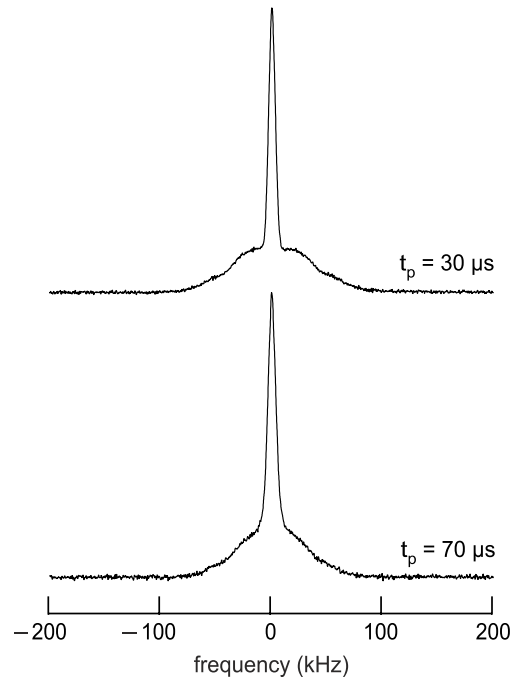


Figure 3. ${}^7\text{Li}$ SAE NMR spectra obtained by Fourier transformation of the echoes shown in figure 1. The spectra are composed of a spin-alignment powder pattern and central intensities due to homonuclear dipole–dipole couplings.

and $S_\infty = B/(A + B)$. In the case of normalized curves, meaning the echo intensity ranges from 1 to 0, $S_\infty = B$ because $A = 1 - B$. If $S_\infty \neq 0$ usually a two-step decay behaviour is observed and the second decay step is characterized by an effective decay rate $T_{1,\text{eff}}^{-1}$ replacing the product $\exp(-(t_m/T_{1,q})^{\gamma_q}) \exp(-(t_m/T_{1,\text{sd}})^{\gamma_{\text{sd}}})$ by a single damping term $\exp(-(t_m/T_{1,\text{eff}})^{\gamma_{\text{eff}}})$.

In figure 4 normalized echo decay curves S_2 are shown which have been recorded at $t_p = 12 \mu\text{s}$ and a resonance frequency of 116 MHz. Solid lines show fits according to a stretched exponential function. The stretching exponent γ turns out to be difficult to determine at temperatures higher than 300 K because the decay curves are only partly accessible. This is due to the increase of the Li jump rate τ^{-1} being responsible for the shift of the inflection points towards shorter mixing times. Satisfactory results are obtained at lower temperatures. As an example, at 273 K the decay rate $\tau_{\text{SAE}}^{-1}(T)$, which might be comparable with the Li jump rate, turned out to be approximately $1.4 \times 10^3 \text{ s}^{-1}$ and the stretching exponent γ is 0.52(3).

The SAE NMR decay curves in figure 4 were recorded using a recycle delay t_d of $5T_1$. In that case the amplitude S_∞ , which slightly depends on temperature, is approximately 0.05 ($300 \text{ K} < T < 333 \text{ K}$). Interestingly, S_∞ increases if t_d is increased to a few hundred seconds. As an example, in figure 5 an echo decay curve is shown which was recorded at 294 K and a delay time $t_d = 400 \text{ s}$. The curve clearly reflects

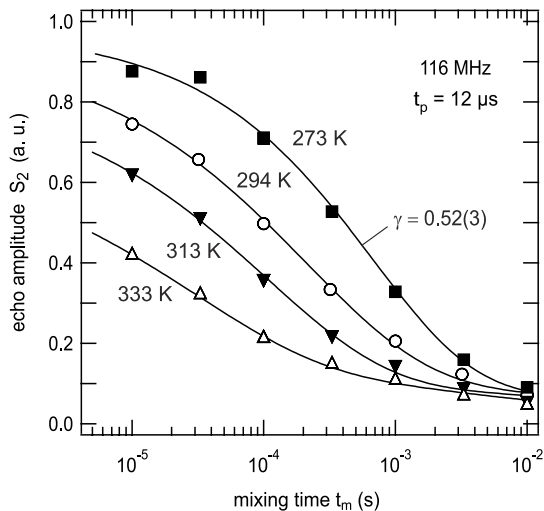


Figure 4. Two-time spin-alignment echo NMR correlation functions reflecting diffusive Li motions in the tetragonal garnet-like oxide $\text{Li}_7\text{La}_3\text{Zr}_2\text{O}_{12}$. Data points have been recorded at 116 MHz. The recycle delay t_d was $5T_1$. Solid lines show fits according to equation (4) which has been combined with an additional damping term $\exp(-t_m/T_{1,\text{eff}})^{\gamma_{\text{eff}}}$ taking into account the echo intensities at $t_p > 10$ ms.

the two-step behaviour of the spin-alignment echo decay. For comparison, at $t_d = 400$ s the corresponding effective rate characterizing the second decay step is of the order of 1 s^{-1} . It is worth mentioning that the first S_2 -decay step, which proceeds on a much shorter timescale ($t_m \ll 0.1$ s), is unaffected by the additional increase of t_d . Thus, for a reliable determination of τ_{SAE}^{-1} the condition $t_d \approx 5T_1$ is absolutely sufficient.

Usually the residual correlation S_∞ directly reflects the inverse number of Li sites equivalently participating in the diffusion process. Certainly, this interpretation holds only if these Li sites are equally populated. Assuming that T_1 is of the order of $T_{1,q}$, the residual amplitude $S_\infty = 0.05$ obtained at $t_d = 5T_1$ might be interpreted in such a way. However, ${}^7\text{Li}$ dipole-dipole couplings generally lead to an additional decrease of S_∞ than expected from the crystallographic structure. However, the fact that S_∞ largely increases with increasing t_d might be interpreted differently. Presumably, the additional echo intensity originates from a separate spin ensemble characterized by a much slower diffusivity, see also [13, 35]. The same ensemble does also show up in the corresponding ${}^7\text{Li}$ NMR spin-lattice relaxation transients (see figure 6) as already mentioned in section 2, see also [35] for a very similar observation in the case of the garnet $\text{Li}_5\text{La}_3\text{Nb}_2\text{O}_{12}$. The echo amplitude measured at $t_m = 0.1$ s (cf figure 5) shows that approximately 15% of the Li ions present in the sample turn out to be much less mobile than those being responsible for the first SAE NMR decay step. This value is in good agreement with that obtained from a brief analysis of the NMR spin-lattice relaxation transients also recorded

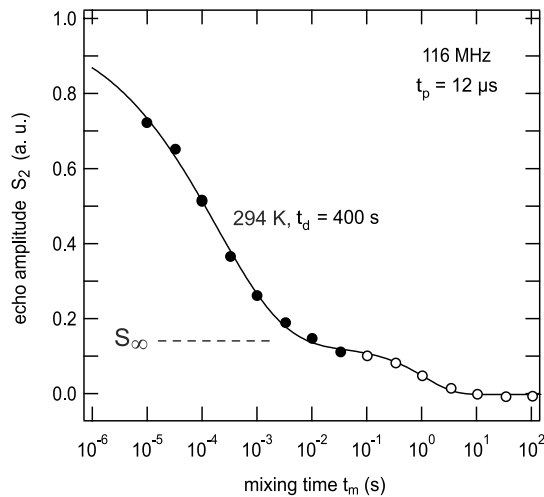


Figure 5. ${}^7\text{Li}$ SAE NMR two-time correlation function (116 MHz) of tetragonal $\text{Li}_7\text{La}_3\text{Zr}_2\text{O}_{12}$ which has been recorded at 294 K, $t_p = 12 \mu\text{s}$ and a recycle delay of 400 s. The first decay step (filled symbols) reflects extremely slow Li motions in the garnet structure. A fit similar to those shown in figure 4 yields $6.3 \times 10^3 \text{ s}^{-1}$. See text for further details.

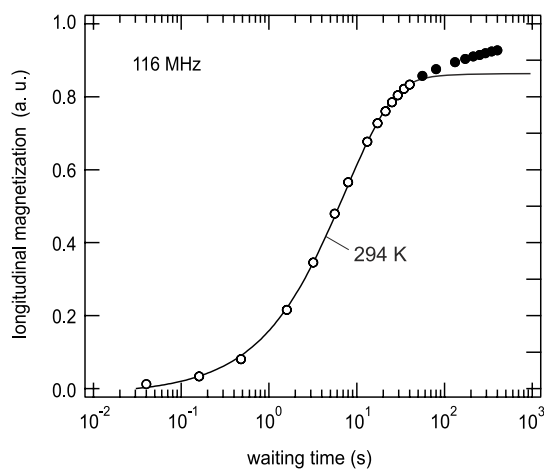


Figure 6. ${}^7\text{Li}$ spin-lattice relaxation NMR transient of a powder sample of $\text{Li}_7\text{La}_3\text{Zr}_2\text{O}_{12}$ crystallizing with tetragonal symmetry. Data have been measured at 116 MHz and 294 K. The largest waiting time used in the saturation recovery experiment was 400 s. The solid line shows a fit to the main component of the transient (\circ) using a stretched exponential. The fit yields $T_1 \approx 7.1$ s and a stretching factor of approximately 0.79. At larger delay times a second contribution shows up (\bullet) which is characterized by a much larger spin-lattice relaxation time T_1 . This component reflects extremely slow Li spins which presumably lead to the second decay step of the corresponding S_2 curve shown in figure 5.

at $t_d = 400$ s. It is worth noting that, in the present case, it cannot be excluded that the slower spin reservoir stems from a spatially separated second phase which is

a priori characterized by its individual ${}^7\text{Li}$ NMR spin–lattice relaxation rates T_1^{-1} and $T_{1,\text{eff}}^{-1}$, respectively.

Judging from the x-ray powder diffraction pattern of the present sample, already presented in [54], such a minor phase, coexisting with the highly pure garnet one, ought to be x-ray amorphous to a great extent. Recent investigations on other garnet-type oxides have indeed revealed that the presence of a small amount of lithium carbonate cannot be excluded [58]. Its amount might be reduced by post-treatment of the sample with acids as well as by subsequent thermal treatment. It might also be expected that it affects Li transport across grain boundaries. These turned out to block through-going Li transport as compared to long-range transport taking place solely in the bulk of $\text{Li}_7\text{La}_3\text{Zr}_2\text{O}_{12}$ [54]. Along with these considerations one might think about (re-)interpreting the ${}^6\text{Li}$ MAS NMR spectra of the garnets, which have been presented in the literature so far, in an alternative way. In the present case, cf [54], the ${}^6\text{Li}$ MAS NMR spectrum reveals two well-separated spectral components: a fast relaxing main signal appears at a chemical shift of 1 ppm and a slowly relaxing minor intensity shows up at 0 ppm. The latter does only emerge at an extraordinarily large recycle delay time. Thus, when compared with that of the main signal, it is characterized by a very large ${}^6\text{Li}$ NMR spin–lattice relaxation time. This observation is in agreement with the two-component shape of the ${}^7\text{Li}$ magnetization transient shown in figure 6. The difference in NMR spin–lattice relaxation rates of the two spectral components might be diagnostic for two magnetically decoupled spin reservoirs. Hence, this could also serve as an argument that the two spin ensembles are also spatially greatly divided. Certainly, further measurements are needed to answer the question whether the minor ${}^6\text{Li}$ NMR signal, as well as the residual correlation measured here, simply reflects a small amount of a second Li-containing phase (for comparison, see also [59]) rather than much less mobile Li ions in the garnet. Recently, the latter, i.e. the presence of an Li sub-ensemble with very low diffusivity, has been reported on the basis of ${}^6\text{Li}$ 2D exchange NMR spectroscopy for similar garnet-like oxides [13, 24].

Irrespective of the nature of the two spin ensembles, from a dynamic point of view the two spin reservoirs are well separated. Hence, the dynamic parameters of the Li ions in phase-pure $\text{Li}_7\text{La}_3\text{Zr}_2\text{O}_{12}$ can be studied very well. The first decay step of the measured S_2 curves clearly reflects successful translational Li jumps between electrically inequivalent sites in the garnet structure. The corresponding decay rates τ_{SAE}^{-1} are shown in the Arrhenius plot of figure 7. As an example, the rate deduced from the curve at 294 K is approximately $6.3 \times 10^3 \text{ s}^{-1}$. Using $D = a^2/6\tau$ and $a \approx 2 \text{ \AA}$, which is a good approximation for the jump distance, a room-temperature Li self-diffusion coefficient $D \approx 7 \times 10^{-17} \text{ m}^2 \text{ s}^{-1}$ is obtained.

The ${}^7\text{Li}$ SAE NMR decay rates shown in figure 7 are in agreement with the Li jump rates estimated from impedance spectroscopy as well as diffusion-induced ${}^7\text{Li}$ spin–lattice relaxation NMR measurements performed in the rotating frame of reference, see [54]. These rates are indicated in

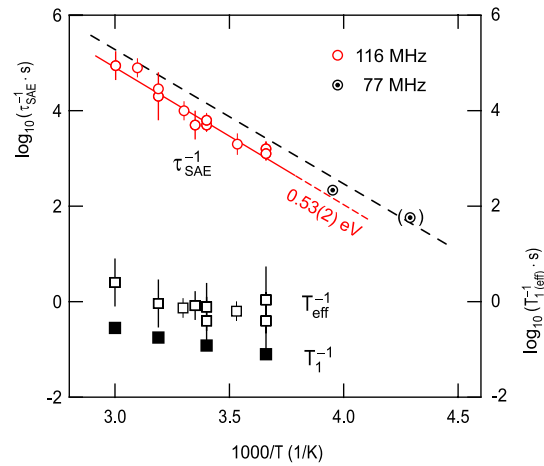


Figure 7. Arrhenius plot of the decay rates τ_{SAE}^{-1} obtained from the $S_2(t_m, t_p)$ curves (partly) shown in figures 4 and 5. The solid line is a fit according to $\tau_{\text{SAE}}^{-1} \propto \exp(-E_a/(k_B T))$ yielding $E_a \approx 0.53 \text{ eV}$. For comparison, the rates T_1^{-1} and $T_{1,\text{eff}}^{-1}$ are also shown. The dashed line indicates the temperature dependence of Li jump rates estimated from conductivity as well as temperature- and frequency-variable ${}^7\text{Li}$ NMR spin–lattice relaxation rate measurements [54].

figure 7 by the dashed line. In general, the ionic conductivity σ is related via

$$\tau^{-1} = (H_R/f) \frac{2dk_B T}{Nq^2 a^2} \sigma. \quad (5)$$

with the hopping correlation rate τ^{-1} . Equation (5) is a combination of the Einstein–Smoluchowski and the Nernst–Einstein equations, see, e.g., [52]. It takes into account that the self-diffusion coefficient D (see above) is related to the Nernst–Einstein diffusion coefficient D_σ via $D = H_R/fD_\sigma$. The small differences between the rates measured by SAE NMR here and by spin–lattice relaxation in [54] might be explained by the uncertainty of the product $H_R f$, which is anticipated to be of the order of unity.

The solid line in figure 7 represents a linear fit also taking into account an SAE NMR decay rate which has been recorded at a lower magnetic field and a slightly larger preparation time. The corresponding S_2 curves are shown in figure 8. For comparison, the one recorded at 116 MHz and 273 K (see figure 7) is also shown. The decay curve recorded at 233 K yields a decay rate τ_{SAE}^{-1} which is slightly larger than expected from the measurements carried out at higher T (see figure 7). This behaviour is even more pronounced when S_2 -curves measured at 116 MHz are regarded. For the sake of brevity, these are not shown here. Therefore, we excluded data points below 260 K from the Arrhenius fit shown (solid line). Presumably, the correlation functions recorded at lower temperatures start to be increasingly affected by (temperature-independent) spin-diffusion effects. According to the method described by Vogel *et al* [35, 36] the SAE NMR data can be corrected for spin-diffusion effects, see also [42, 50]. Here, however, it turned out that the correction procedure

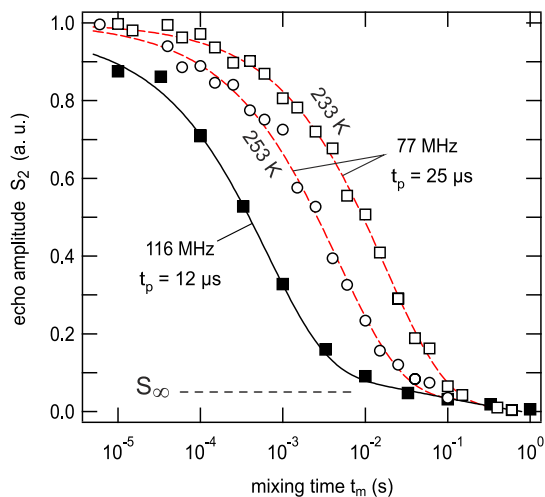


Figure 8. Low-temperature ${}^7\text{Li}$ SAE NMR correlation functions of polycrystalline $\text{Li}_7\text{La}_3\text{Zr}_2\text{O}_{12}$ recorded at 77 MHz and $t_p = 25 \mu\text{s}$. Echo intensities have been measured at 253 and 233 K. For comparison, the curve shown in figure 5 which has been recorded at 273 K and 116 MHz is also shown. The lines represent fits according to equation (4) which have been combined with an additional damping term, see caption of figure 5. Interestingly, the shape of $S_2(t_m, t_p)$, that is the first decay step, turns out to depend only slightly on T . The corresponding stretching factor is approximately 0.54 at 253 K. See text for further explanation.

has no significant influence on the decay rates recorded above room temperature. The Arrhenius fit shown in figure 7 yields an activation energy of $E_a = 0.53(2)$ eV. This value is in good agreement with that probed by impedance spectroscopy, quite recently [53, 54]. This similarity shows that stimulated echo NMR is able to probe long-range Li diffusion from an atomic-scale point of view, that is, taking advantage of the fluctuations of site-specific electric field gradients the mobile Li spins are exposed to. Similar observations have been made for other Li ion conductors studied by both impedance and stimulated echo NMR spectroscopy so far [31, 33, 40, 41, 60, 61].

At sufficiently low temperatures the complete S_2 decay is accessible. In particular, the curves recorded at 294 and 273 K (see figure 8) are of interest although the influence of spin-diffusion effects might play an increasing role. Starting from $\gamma = 0.52(3)$ (see the S_2 curve recorded at 273 K and 116 MHz, cf figure 8), the stretching exponent decreases to $\gamma = 0.48(2)$ (294 K). For comparison, at lower temperatures (233 K) it turns out to be 0.57(2). Thus, most likely the underlying dynamic correlation function probed by ${}^7\text{Li}$ stimulated echo NMR near ambient temperature is characterized by an exponent γ which is approximately 1/2. Interestingly, impedance as well as ${}^7\text{Li}$ NMR spin-lattice relaxation measurements, see [54], also indicate a non-exponential hopping correlation function. The corresponding stretching factor deduced from impedance spectroscopy is very similar to the value deduced from SAE NMR. Together with the good agreement of the activation energies probed, this observation indicates that the methods, which *a priori*

probe Li dynamics in different ways, are sensitive to very similar motional correlation functions. Quite recently, the same similarity has also been observed for polycrystalline Li_2C_2 complementarily investigated by both impedance as well as SAE NMR spectroscopy by Ruprecht *et al* [60].

4. Conclusions

Alignment echoes of ${}^7\text{Li}$ spins have been used to trace Li jump processes in the tetragonal modification of $\text{Li}_7\text{La}_3\text{Zr}_2\text{O}_{12}$. The method is sensitive to successful translational ionic motions on a relatively long timescale which might be compared with that of dc conductivity measurements. From the diffusion-controlled two-time correlation functions decay rates have been extracted which favourably agree with those probed by impedance spectroscopy and spin-lattice relaxation NMR techniques. Thus, the changes of the site-specific quadrupole frequencies due to diffusive motions of the Li spins result in an echo damping from which the associated jump rate can be deduced in a rather direct way. In the present case this enables the determination of the Li self-diffusion coefficient D at ambient temperature. The shape of the SAE NMR decay functions probed at room temperature indicates that the underlying motional correlation function can be represented by the term $\exp(-(t'/\tau)^\gamma)$ with $\gamma \approx 0.5$. Finally, we discussed possible origins of a second spin reservoir characterized by much smaller motional correlation rates as reflected by NMR spin-lattice relaxation transients as well as NMR spin-alignment data.

In summary, the example studied here shows once more that spin-alignment echo NMR spectroscopy turns out to be a versatile tool for the investigation of Li jump processes in lithium ion conductors. The information gained from temperature-variable SAE NMR might be helpful to characterize new solid electrolytes urgently needed to develop powerful energy storage systems.

Acknowledgments

We thank the Deutsche Forschungsgemeinschaft (DFG) within the research unit 1277 (Mobility of Li ions in solids, projects WI-3600 4-1 and 2-1) as well as the Leibniz University Hannover (Wege in die Forschung II, Dynama) for financial support. AK gratefully acknowledges a grant of the Studienstiftung des Deutschen Volkes eV.

References

- [1] Kang K S, Meng Y S, Breger J, Grey C P and Ceder G 2006 *Science* **311** 977
- [2] Winter M and Besenhard J O 1999 *Electrochem. Acta* **45** 31
- [3] Whittingham M S 2004 *Chem. Rev.* **104** 4271
- [4] Poizot P, Laruelle S, Grugeon S, Dupont L and Tarascon J M 2000 *Nature* **407** 496
- [5] Tarascon J M and Armand M 2001 *Nature* **414** 359
- [6] Bruce P G, Scrosati B and Tarascon J-M 2008 *Angew. Chem. Int. Edn* **47** 2930
- [7] Kavan L, Kalbác M, Zúkalová M, Exnar I, Lorenzen V, Nesper R and Grätzel M 2004 *Chem. Mater.* **16** 477

- [8] Aricó A S, Bruce P, Scrosati B, Tarascon J -M and Van Schalkwijk W 2005 *Nature Mater.* **4** 366
- [9] Ramzy A and Thangadurai V 2010 *ACS Appl. Mater. Interfaces* **2** 385
- [10] Murugan R, Weppner W, Schmid-Beurmann P and Thangadurai V 2008 *Mater. Res. Bull.* **43** 2579
- [11] Thangadurai V and Weppner W 2005 *J. Power Sources* **142** 339
- [12] Cussen E J 2010 *J. Mater. Chem.* **20** 5167
- [13] O'Callaghan M P, Powell A S, Titman J, Chen G Z and Cussen E 2008 *Chem. Mater.* **20** 2360
- [14] Brinkmann D 1992 *Prog. Nucl. Magn. Reson. Spectrosc.* **24** 527
- [15] Böhmer R, Jeffrey K and Vogel M 2007 *Prog. Nucl. Magn. Reson. Spectrosc.* **50** 87
- [16] Böhmer R, Jörg T, Qi F and Titze A 2000 *Chem. Phys. Lett.* **316** 419
- [17] Epp V and Wilkening M 2010 *Phys. Rev. B* **82** 020301
- [18] Wilkening M and Heitjans P 2008 *Phys. Rev. B* **77** 024311
- [19] Kuhn A, Sreeraj P, Pöttgen R, Wiemhöfer H-D, Wilkening M and Heitjans P 2011 *J. Am. Chem. Soc.* **133** 11018
- [20] Xu Z and Stebbins J F 1995 *Science* **270** 1332
- [21] Cahill L S, Chapman R P, Britten J F and Goward G R 2006 *J. Phys. Chem. B* **110** 7171
- [22] Verhoeven V W J, de Scheper I M, Nachtegaal G, Kentgens A P M, Kelder E M and Mulder F M 2001 *Phys. Rev. Lett.* **86** 4314
- [23] Cabana J, Dupré N, Rousse G, Grey C P and Palacin M R 2005 *Solid State Ion.* **176** 2205
- [24] van Wüllen L, Echelmeyer T, Meyer H-W and Wilmer D 2007 *Phys. Chem. Chem. Phys.* **9** 3298
- [25] Bräunling D, Pecher O, Trots D M, Senyshyn A, Zherebtsov D A, Haarmann F and Niewa R 2010 *Z. Anorg. Allg. Chem.* **636** 936
- [26] Aatiq A, Ménétrier M, Croguennec L, Suard E and Delmas C 2002 *J. Mater. Chem.* **12** 2971
- [27] Wilkening M, Romanova E E, Nakhla S, Weber D, Lerch M and Heitjans P 2010 *J. Phys. Chem. C* **114** 19083
- [28] Heitjans P, Schirmer A and Indris S 2005 *Diffusion in Condensed Matter—Methods, Materials, Models* 2nd edn, ed P Heitjans and J Kärger (Berlin: Springer) chapter 9, pp 369–415
- [29] Qi F, Jörg T and Böhmer R 2002 *Solid State Nucl. Magn. Reson.* **22** 484
- [30] Qi F, Diezemann G, Böhm H, Lambert J and Böhmer R 2004 *J. Magn. Reson.* **169** 225
- [31] Qi F, Rier C, Böhmer R, Franke W and Heitjans P 2005 *Phys. Rev. B* **72** 104301
- [32] Böhmer R and Qi F 2007 *Solid State Nucl. Magn. Reson.* **31** 28
- [33] Faske S, Eckert H and Vogel M 2008 *Phys. Rev. B* **77** 104301
- [34] Brinkmann C, Faske S, Koch B and Vogel M 2010 *Z. Phys. Chem.* **224** 1535
- [35] Koch B and Vogel M 2008 *Solid State Nucl. Magn. Reson.* **34** 37
- [36] Faske S, Koch B, Murawski S, Kuechler R, Boehmer R, Melchior J and Vogel M 2011 *Phys. Rev. B* **84** 024202
- [37] Wilkening M, Kuechler W and Heitjans P 2006 *Phys. Rev. Lett.* **97** 065901
- [38] Wilkening M, Kuhn A and Heitjans P 2008 *Phys. Rev. B* **78** 054303
- [39] Wilkening M, Lyness C, Armstrong A R and Bruce P G 2009 *J. Phys. Chem. C* **113** 4741
- [40] Wilkening M, Mühle C, Jansen M and Heitjans P 2007 *J. Phys. Chem. B* **111** 8691
- [41] Wilkening M, Gebauer D and Heitjans P 2008 *J. Phys.: Condens. Matter* **20** 022201
- [42] Wilkening M, Lyness C, Armstrong A R and Bruce P G 2009 *J. Phys. Chem. C* **113** 4741
- [43] Tang X -P, Geyer U, Busch R, Johnson W L and Wu Y 1999 *Nature* **402** 160
- [44] Tang X -P and Wu Y 1998 *J. Magn. Reson.* **133** 155
- [45] Tang X -P, Busch R, Johnson W L and Wu Y 1998 *Phys. Rev. Lett.* **81** 5358
- [46] Davis L J M, Heinmaa I and Goward G R 2010 *Chem. Mater.* **22** 769
- [47] Cahill L S, Iriyama Y, Nazar L F and Goward G R 2010 *J. Mater. Chem.* **20** 4340
- [48] Carlier D, Ménétrier M and Delmas C 2001 *J. Mater. Chem.* **11** 594
- [49] Jeener J and Broekaert P 1967 *Phys. Rev.* **157** 232
- [50] Wilkening M, Heine J, Lyness C, Armstrong A R and Bruce P G 2009 *Phys. Rev. B* **80** 064302
- [51] Böhmer R 2000 *J. Magn. Reson.* **147** 78
- [52] Mehrer H 2006 *Diffusion in Solids* (Berlin: Springer)
- [53] Awaka J, Kijima N, Hayakawa H and Akimoto J 2009 *J. Solid State Chem.* **182** 2046
- [54] Kuhn A, Narayanan S, Spencer L, Goward G, Thangadurai V and Wilkening M 2011 *Phys. Rev. B* **83**
- [55] Wilkening M and Heitjans P 2006 *J. Phys.: Condens. Matter* **18** 9849
- [56] Fukushima E and Roeder S B W 1981 *Experimental Pulse NMR* (Reading, MA: Addison-Wesley)
- [57] Böhmer R, Faske S and Geil B 2008 *Solid State Nucl. Magn. Reson.* **34** 32
- [58] Galven C, Fourquet J-L, Crosnier-Lopez M-P and Le Berre F 2011 *Chem. Mater.* **23** 1892
- [59] Boulant A, Bardeau J F, Jouanneaux A, Emery J, Buzare J Y and Bohnke O 2010 *Dalton Trans.* **39** 3968
- [60] Ruprecht B, Billetter H, Ruschewitz U and Wilkening M 2010 *J. Phys.: Condens. Matter* **22** 245901
- [61] Wilkening M, Amade R, Iwaniak W and Heitjans P 2006 *Phys. Chem. Chem. Phys.* **9** 1239

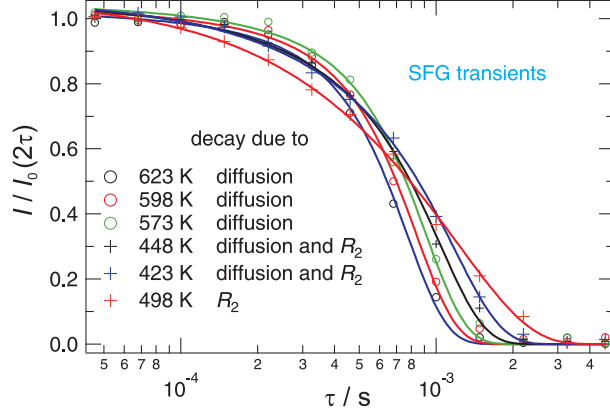


Figure 3.3: ${}^7\text{Li}$ SFG NMR transients of the tetragonal LLZ sample. At the five highest temperatures, diffusion coefficients could be deduced from the data.

3.3 SFG NMR on the tetragonal LLZ

3.3.1 Results

${}^7\text{Li}$ static-field-gradient NMR measurements were performed in the static field gradient of a 14.1-T cryomagnet ($B_0=9.4$ T, $g=69$ T/m, quadrupolar echo pulse sequence). The SFG echo transients of the tetragonal LLZ sample (provided by V. Thangadurai) are shown in Fig. 3.3. The solid lines represent regressions according to Eqn. 3.1

$$I/I_0(2\tau) = \exp\left(-2\tau R_2 - \frac{2}{3}D\gamma^2 g^2 \tau^3\right) \quad (3.1)$$

with the pulse separation τ , the spin-spin relaxation time R_2 , the diffusion coefficient D , the gyromagnetic ratio γ and the magnetic field gradient g . Note that the decay due to diffusion follows a different time dependence (cubic exponential) than that due to relaxation (single exponential). Therefore, it is easy to distinguish between both cases. In the present case, above 423, it is possible to extract diffusion coefficients from the data.

The tracer-diffusion coefficients obtained from the regression of the transients were translated into jump rates ($\tau^{-1} = 6D/a^2$) assuming a jump distance a of 3 \AA (in contrast to Ref. [21] where $a = 2 \text{ \AA}$ was assumed), see turquoise diamonds in Fig 3.4. Hereby, the error bars of the SFG rates marked by the horizontal lines are the errors of the regression, the vertical ones the maximum uncertainty of the method (uncertainty of the field gradient). The original graphic shown in Fig. 3.4 was taken from Ref. [21] and the new results were added. The conductivity data (red squares) was shifted according to the new assumption of the jump distance $a = 3 \text{ \AA}$. The purple line represents the global fit of the NMR relaxometry data. Additionally, the correlation rates obtained from SAE NMR (see Ref. [26] and pages 61-68) are included. SAE rates measured at a field of 77 MHz are also added. These were recorded with two different evolution times τ_e ($12 \mu\text{s}$ and $25 \mu\text{s}$). For both evolution times, the same SAE rates were obtained. Therefore, the points represent both evolution times.

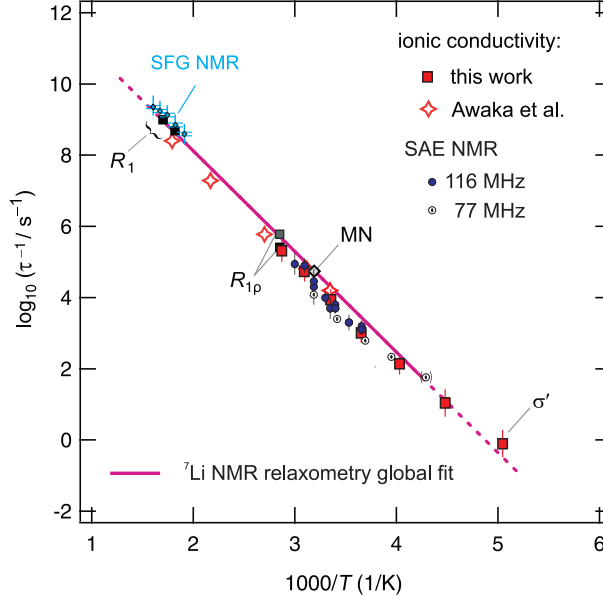


Figure 3.4: Arrhenius plot of the Li jump rates obtained from various methods under the assumption of a jump distance $a = 3 \text{ \AA}$. purple line: NMR relaxometry global presented in Ref. [21]). Red squares: conductivity ($a = 3 \text{ \AA}$, $H_R = 1$, $f=1$). Turquoise diamonds: calculated from SFG NMR tracer diffusion coefficients ($a = 3 \text{ \AA}$, $f = 1$) obtained from the transients shown in Fig. 3.3. Points: SAE correlation rates measured at 116 MHz and 77 MHz. The figure was taken from [21] and modified accordingly.

3.3.2 Concluding remarks

Comparing the nuclear microscopic method NMR relaxometry (purple line) and SFG NMR, clearly, the Li jump process seen in NMR relaxometry and SAE NMR is of long-range nature. The activation energy and absolute values (under the assumption of $a = 3 \text{ \AA}$) are in good accordance for these long-range and short-range nuclear methods. Under the assumption of $a = 3 \text{ \AA}$, $H_R = 1$, $f=1$, the non-nuclear long-range technique dc-conductivity yields jump rates that are in good agreement with the jump rates obtained from the nuclear methods. The conductivity seems to be due to a single, well-defined, Arrhenius-activated Li hopping diffusion process. With the methods available, no anisotropy in the diffusivity could be observed.

Z. Phys. Chem. **226** (2012) 525–537 / DOI 10.1524/zpch.2012.0250
© by Oldenbourg Wissenschaftsverlag, München

Li Ion Dynamics in Al-Doped Garnet-Type $\text{Li}_7\text{La}_3\text{Zr}_2\text{O}_{12}$ Crystallizing with Cubic Symmetry

By Alexander Kuhn^{1,*}, Joon-Yong Choi², Lars Robben³, Frank Tietz²,
Martin Wilkening⁴, and Paul Heitjans¹

¹ Leibniz University Hannover, Institute of Physical Chemistry and Electrochemistry, and ZFM – Center for Solid State Chemistry and New Materials, Callinstr. 3a, 30167 Hannover, Germany

² Institute of Energy and Climate Research (IEK-1), Forschungszentrum Jülich GmbH, 52425 Jülich, Germany

³ Leibniz University Hannover, Institute of Mineralogy, Callinstr. 3, 39167 Hannover, Germany

⁴ Graz University of Technology, Institute for Chemistry and Technology of Materials, Stremayrgasse 9, 8010 Graz, Austria

(Received April 13, 2012; accepted in revised form May 18, 2012)

(Published online June 18, 2012)

Solid Electrolytes / Garnets / Lithium Ion Dynamics / NMR / Spin-Lattice Relaxation

Lithium-ion dynamics in the garnet-type solid electrolyte “ $\text{Li}_7\text{La}_3\text{Zr}_2\text{O}_{12}$ ” (LLZ) crystallizing with cubic symmetry was probed by means of variable-temperature ^7Li NMR spectroscopy and ac impedance measurements. Li jump rates of an Al-containing sample follow Arrhenius behavior being characterized by a relatively high activation energy of 0.54(3) eV and a pre-exponential factor of $2.2(5) \times 10^{13} \text{ s}^{-1}$. The results resemble those which were quite recently obtained for an Al-free LLZ sample crystallizing, however, with tetragonal symmetry. Hence, most likely, the significantly higher Li conductivity previously reported for a cubic LLZ sample cannot be ascribed solely to the slight structural distortions accompanying the change of the crystal symmetry. Here, even Al impurities, acting as stabilizer for the cubic polymorph at room temperature, do not lead to the high ion conductivity reported previously.

1. Introduction

In recent years, Li containing garnets have attracted large interest due to their potential usage as electrolytes in all-solid-state Li secondary batteries [1–8]. The high lithium-ion conductivity of such ceramics showing good electrochemical stability to lithium metal makes them promising candidates to be used, for example, in thin-film batteries [9].

* Corresponding author. E-mail: kuhn@pci.uni-hannover.de

In particular, garnet-type $\text{Li}_7\text{La}_3\text{Zr}_2\text{O}_{12}$ (LLZ) crystallizing with cubic symmetry has captured the attention of the materials science community due to its extraordinarily high room-temperature lithium-ion conductivity which is $3 \times 10^{-4} \text{ S cm}^{-1}$ [10]. Interestingly, the corresponding Li conductivity of the tetragonal modification [11] is only $1.6 \times 10^{-6} \text{ S cm}^{-1}$. However, the structural differences of the two modifications are rather small with respect to the garnet-type network $[\text{La}_3\text{Zr}_2\text{O}_{12}]^{-7}$ [11,12]. This raises the question whether the distortion of the lattice, which amounts to less than 2%, is solely responsible for the large difference in ion conductivity observed. Quite recently, Geiger *et al.* assumed that traces of Al ions incorporated during the high-temperature synthesis of cubic LLZ play an important role in the enhancement of the conductivity observed [12]. Note that an Al-containing sample of cubic LLZ, which was complementarily investigated by some of us using impedance measurements and NMR spectroscopy [13], indeed showed the extremely high lithium-ion conductivity mentioned above. Doping with Al might create additional vacancies at the regularly occupied Li sites, for example. However, in view of the large fraction of unoccupied Li sites already present in (phase-pure) cubic LLZ [12], the effect of additionally generated Li vacancies on the Li ion conductivity might be too small to solely account for the enhancement found.

Irrespective of such an effect, evidences have been found that the Al^{3+} ions incorporated do stabilize the cubic modification relative to the tetragonal one [12]. Whereas an Al-free sample with cubic symmetry is reported to be the non-quenchable high-temperature form [12], the tetragonal modification can be obtained at much lower synthesis temperatures [11,14] or, alternatively, by the use of Pt crucibles, for example [12]. In agreement with these observations, Al-free tetragonal LLZ reversibly transforms into the cubic polymorph at elevated temperatures as reported recently [12,14]. However, as has been shown by some of us [14], no change in ion conductivity is associated with this phase transformation. This indicates that the slight structural changes coming along with the increase of the symmetry do not alter the Li transport parameters significantly. These readily follow a single Arrhenius line over a large dynamic range of several orders of magnitudes [14].

Whereas the studies available so far give evidences that incorporation of Al is beneficial to stabilize the cubic modification at room temperature as mentioned above, the corresponding influence on lithium ion dynamics is still unclear. The investigations published until now bring up the question whether the increased ion conductivity observed can solely be ascribed to Al doping. In the present study, lithium-ion dynamics of an LLZ sample, which is slightly contaminated with Al ions, is comprehensively studied by both time-domain ^7Li NMR measurements and ac impedance spectroscopy, *i. e.*, from a microscopic and macroscopic point of view [15–17]. The results are compared with those of an Al-free sample crystallizing with tetragonal symmetry [11,14]. Surprisingly, although the sample studied here expectedly shows the typical X-ray powder pattern of a garnet crystallizing with cubic symmetry, the lithium-ion conductivity turns out to be rather low and is very similar to that of the (Al-free) tetragonal modification [11,14]. Thus, stabilization of the cubic modification by appropriate doping with a trivalent cation such as Al might be not the only reason of the enhanced conductivity found in some of the LLZ samples studied so far.

2. Experimental

$\text{Li}_7\text{La}_3\text{Zr}_2\text{O}_{12}$ crystallizing with cubic symmetry was prepared by a conventional solid-state reaction. Highly pure Li_2CO_3 , ZrO_2 and La_2O_3 were used as starting materials. With regard to the stoichiometric mixture, an excess of 10 wt. % of Li_2CO_3 was used to compensate for any Li loss expected at high temperatures. After grinding, the materials were placed in an alumina crucible and calcined at 1253 K for several hours and, following a second grinding step, heated at 1500 K for 1 h once again. The amount of Al introduced into the sample during this procedure has been determined by inductively coupled plasma optical emission spectroscopy (ICP-OES 750, Varian) to be 1.1 wt. %.

X-ray powder diffraction (XRPD) data were recorded on a Bruker D4 Endeavor diffractometer using a reflection geometry, $\text{Cu } K_{\alpha 1,2}$ radiation and a secondary Ni filter. 4000 data points were collected with a step width of 0.02° in the 2θ range from 10 to 90° . XRPD data were analyzed by TOPAS 4.2 (Bruker AXS) software. During refinements, the general parameters such as scale factors, background parameters and zero point errors were optimized. Profile shape calculations were carried out on the basis of standard instrumental parameters using the fundamental parameter approach implemented in the program, also varying the average crystal size (integral breadth) of the reflections. The phases have been considered in the total pattern calculations either as crystal structures or hkl phases. Energy-dispersive X-ray (EDX) mapping was performed with a Jeol 6390 scanning electron microscope equipped with a JEOL JED-2300 Analysis Station in order to get insight into the elemental distribution in different crystallites.

Static ^7Li NMR line shape and spin-lattice relaxation (SLR) rate measurements were performed with a modified Bruker MSL 100 and an MSL 400 spectrometer each connected to an Oxford cryomagnet with nominal fields of 4.7 T and 9.4 T, respectively. Both commercial and home-built probes (designed for high temperatures) were used. ^7Li SLR NMR rates were recorded with the standard saturation recovery pulse sequence, $10 \times \pi/2 - t_{\text{delay}} - \pi/2 - \text{acquisition}$, using 14 different delay times t_{delay} . The magnetization transients were in satisfying agreement with single-exponential relaxation. Alternatively, the transients were fitted with stretched exponentials in order to account for small deviations from single-exponential behavior. The rates obtained from the two fits yielded comparable results.

High-resolution, *i. e.*, magic angle spinning (MAS), ^{27}Al and ^6Li NMR measurements were performed on an Avance III spectrometer (Bruker) connected to a Bruker cryomagnet with a nominal field of 14.1 T. A commercial 2.5 mm-MAS probe (Bruker) was employed which allowed spinning speeds of up to 30 kHz. NMR spectra were referenced to an 1N aqueous solution of $\text{Al}(\text{NO}_3)_3$.

Ac impedance measurements were performed with a Novocontrol impedance spectrometer Concept 80 equipped with a BDS 1200 sample cell and an Alpha analyzer (Novocontrol) in the frequency range from 0.1 Hz to 10 MHz. Impedance spectra were recorded at temperatures ranging from 198 K to 523 K. Pt electrodes were applied to the non-sintered pellets which were 8 mm in diameter and approximately 1 mm in thickness. The measurements were performed under a stream of heated nitrogen. Prior to the first measurement, the sample was dried at 523 K for 30 min in order to remove any moisture.

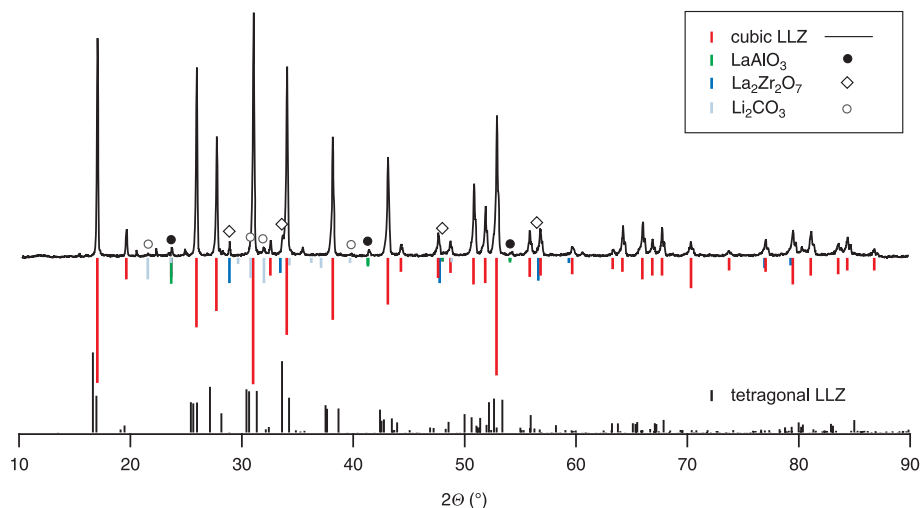


Fig. 1. XRD pattern of the cubic LLZ sample investigated which contains a small amount of Al. The main peaks of the impurities detected (LaAlO_3 , $\text{Li}_2\text{Zr}_2\text{O}_7$, Li_2CO_3) are additionally highlighted (see legend). Note that these do overlap with some of the peaks of LLZ. For comparison, the XRD pattern of tetragonal LLZ according to Ref. [11] is shown.

3. Results and discussion

3.1 Sample characterization

3.1.1 X-ray powder diffraction

Analysis of the XRPD pattern of the prepared LLZ sample (Fig. 1) reveals the cubic modification as described by Geiger *et al.* [12] to be the main phase with a content of approximately 97 wt. %. Some additional peaks with low intensity point to impurities such as $\text{La}_2\text{Zr}_2\text{O}_7$, LaAlO_3 , and Li_2CO_3 . The actual amount of Li_2CO_3 determined by Rietveld analysis is uncertain due to the low crystallinity of the sample which leads to rather broad peak widths.

3.1.2 ^{27}Al and ^6Li MAS NMR spectra

In order to further characterize the prepared sample and to study its structure from an atomic-scale point of view, ^{27}Al and ^6Li MAS NMR spectra were recorded at ambient bearing gas temperature. In Fig. 2, ^{27}Al MAS NMR spectra of cubic LLZ with about 1.1 wt. % Al and the Al-free tetragonal LLZ studied recently [14] are shown. While the latter does not reveal any ^{27}Al NMR intensities, the first is composed of at least three different lines showing up at 12 ppm, 64 ppm, and 80 ppm. The signal with an isotropic chemical shift of $\delta = 12$ ppm indicates Al ions residing in octahedral sites. Thus, most likely, it can be attributed to LaAlO_3 which has also been detected by XRPD (see above and the study by Geiger *et al.* [12]) The NMR intensities showing up at approximately 65 ppm and 80 ppm point to tetrahedrally coordinated Al ions [18] in the LLZ structure. Most probably, the broad signal at 65 ppm reflects Al ions on the Li(1) site in cubic

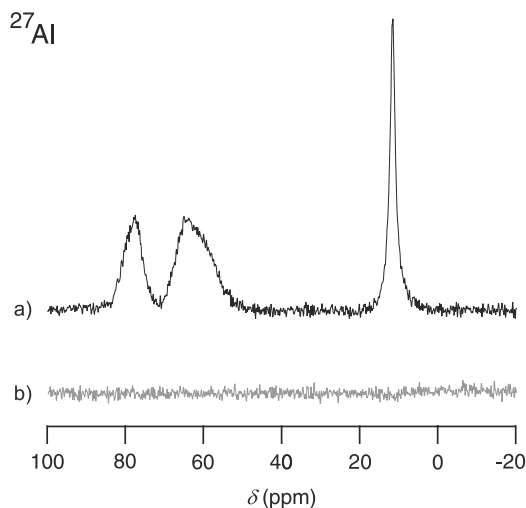


Fig. 2. a) ^{27}Al MAS NMR spectrum of the (Al-doped) cubic LLZ sample investigated. The spectrum was recorded at 14.1 T using an MAS spinning speed of 30 kHz. While the line at 12 ppm might be attributed to LaAlO_3 , the intensities showing up in the range from 50 to 90 ppm indicate Al ions incorporated into LLZ. b) For comparison, the ^{27}Al MAS NMR spectrum of the Al-free tetragonal LLZ sample [14] is also presented.

LLZ [12] while the line with a larger chemical shift value might be related to the replacement of La and Zr by Al [19]. Most likely, Al resides on a tetrahedral site near a La or Zr vacancy. In order to further check the distribution of Al in the different phases occurring in the sample, an EDX elemental mapping was performed using a SEM microscope equipped with a JEOL JED-2300 Analysis Station. The results are shown in Fig. 3. The large particle contains La, Zr and traces of Al and most probably is the LLZ phase. Smaller particles show higher amounts of Al and La and probably resemble the LaAlO_3 minor phase.

The ^6Li MAS NMR spectrum of cubic LLZ (not shown here) is composed of two lines which are characterized by quite different NMR SLR rates. The main line at 1.1 ppm (referenced to 1 N aqueous LiCl), comprising approximately 90% of the total integral, presumably reflects the Li ions in LLZ while the minor component at -0.1 ppm might be attributed to a separate phase such as Li_2CO_3 , as detected by XRPD (see above). Additionally, carbonate modes are also seen in the corresponding transmission infrared (IR) spectra recorded. At room temperature the corresponding ^6Li NMR spin-lattice relaxation time is in the order of 1000 s whereas that of the main component is less than 10 s. Li_2CO_3 might either stem from the preparation route chosen or from the reaction with ambient air as also found in the case of lithium lanthanum titanate (LLT) [20]. Note that the replacement of Li^+ by H^+ , which is the key reaction for the formation of Li_2CO_3 in the case of LLT, was reported at least for the related garnet-type electrolytes $\text{Li}_5\text{La}_3\text{Nb}_2\text{O}_{12}$ and $\text{Li}_5\text{La}_3\text{Ta}_2\text{O}_{12}$ [21]. IR spectra in the mentioned work revealed the characteristic bands of carbonate ions. Interestingly, Nyman *et al.* [21] showed that the ^6Li MAS NMR line in question, which shows up at approxi-

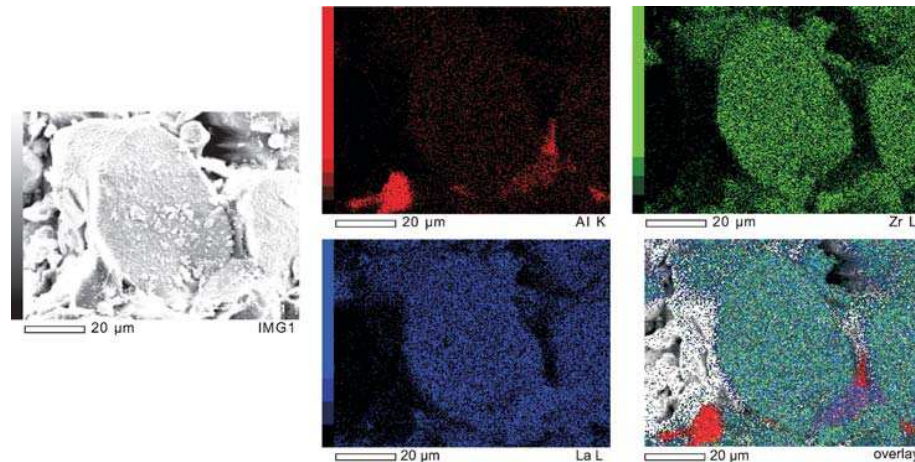


Fig. 3. Left: SEM micrograph of the cubic LLZ sample. Right: EDX mapping (JEOL JED-2300 Analysis Station) of the same image section for the elements Al, La, and Zr. The overlay of the elemental distribution is also included.

mately 0.2 ppm, disappears when the sample is treated with acids. Concomitantly, the IR bands reflecting the carbonate modes disappear.

3.2 Bulk ion conductivity

Unlike the case of NMR SLR measurements, small amounts of impurities such as Li_2CO_3 , when located on the surface of the grains, might affect the resistance attributed to the grain boundary regions. However, the respective impact on the bulk conductivities might be less significant as long as the grains are large enough and the volume fraction of the insulating impurities is low. Here, bulk conductivities (see Fig. 4) of the cubic sample were read out from the frequency-independent plateau showing up at higher frequencies in the corresponding conductivity isotherms [14].

The conductivity spectra were constructed by plotting the real part of the conductivity σ' vs. frequency f . The plateau analyzed here is related to the process with the lowest capacity; it reflects the electrical response of the bulk. In Fig. 4 the corresponding bulk conductivities of cubic LLZ are shown (red dots). At room temperature the ion conductivity amounts to $3(1) \times 10^{-7}$ S/cm. The activation energy derived from the Arrhenius plot shown turns out to be 0.53(2) eV.

For comparison, literature data of cubic and Al-free tetragonal LLZ [14] are also included in Fig. 4. The conductivities probed here are in very good agreement with those of the tetragonal sample studied by Awaka *et al.* [11]. However, significant differences become apparent when the present data are compared with the results reported by Murugan *et al.* [10] for cubic LLZ. Thus, although the sample investigated crystallizes with cubic symmetry, no enhancement is found compared to the tetragonal form. Even more important, the incorporated Al ions seem to have no effect on the Li mobility.

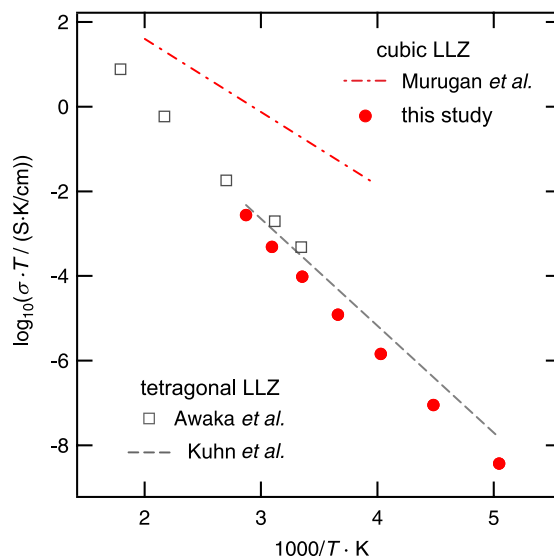


Fig. 4. Temperature dependence of the bulk lithium-ion conductivities of Al-doped, cubic LLZ (plotted as $\log_{10} \sigma T$ vs. temperature). For comparison, literature data for cubic [10] and tetragonal LLZ [11,14] are also shown.

3.3 Variable-temperature ^7Li NMR line shapes

In addition to impedance spectroscopy, static ^7Li NMR lines (see Fig. 5a) were recorded to study the Li diffusivity in the cubic sample prepared. At low temperatures, the lines are dipolarly broadened and show a Gaussian shape. With rising temperature the Li jump rate τ^{-1} increases. At a given temperature, here at approximately 290 K, τ^{-1} becomes comparable to the dipolar coupling constant. Dipolar interactions are then increasingly averaged resulting in the so-called motional narrowing (MN) of the NMR line. At high temperatures, *i. e.*, in the regime of extreme narrowing, the line width simply reflects the inhomogeneity of the external magnetic field used. The two-component line shape showing up in the intermediate T range might indicate heterogeneous dynamics taking place in the cubic sample. Alternatively such effects might be explained by coupling of the spins with paramagnetic impurities leading in some cases to a slight line broadening [23]. As expected for cubic symmetry, the NMR line recorded at high temperatures (533 K) does not reveal any indications for satellite transitions (see Fig. 5a). Note that this is in contrast to the tetragonal sample studied recently [14]. In general, at high temperatures the fast diffusing Li ions are exposed to a mean electric field gradient (EFG) of all visited sites. This leads to a vanishing mean EFG in the case of cubic LLZ and a non-vanishing one in tetragonal LLZ. Incorporation of isotropically distributed dopant atoms such as Al is expected not to change this situation.

As pointed out above, the temperature-dependent narrowing of the NMR (central) transition line can be used to roughly estimate the Li diffusivity. In Fig. 5b the resulting MN curve is shown, which is obtained by plotting the line width (full width at half maximum *fwhm*) vs. temperature. Obviously, the data points are very similar to those of

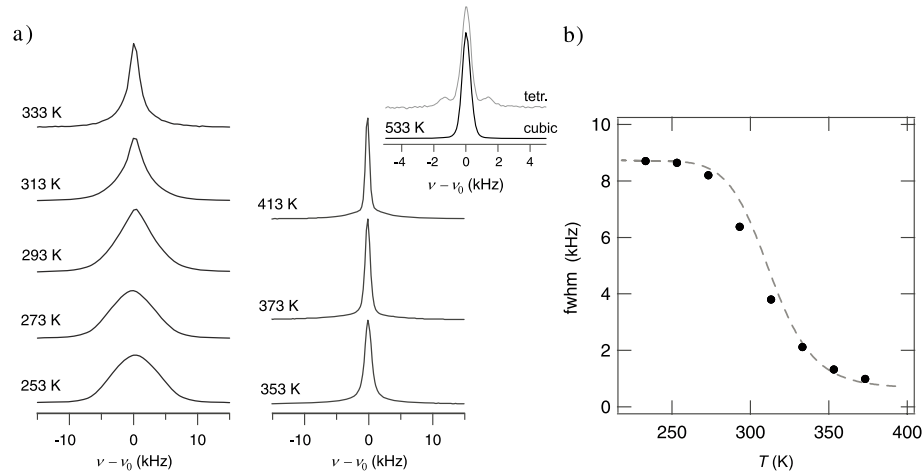


Fig. 5. a) Temperature-dependent static ${}^7\text{Li}$ NMR lines of the Al-doped, cubic sample of LLZ. Inset: The spectrum recorded at 553 K does not reveal any quadrupole satellites as expected for a material with cubic symmetry. For comparison, the spectrum of tetragonal LLZ (533 K) which shows quadrupole satellites is included (grey line) [14]. See text for further explanation. b) Motional narrowing (MN) of the central transition of the ${}^7\text{Li}$ NMR line of cubic LLZ (black dots). The dashed line, shown for comparison, represents a fit [22] through the MN data of the tetragonal modification of LLZ studied recently [14].

the Al-free sample crystallizing with tetragonal symmetry. This result corroborates the similarity of the two samples found by impedance spectroscopy presented above. At the temperature of the inflection point the mean Li jump rate is given by $\Delta\omega_{\text{rigid lattice}} \approx \tau^{-1}$ where $\Delta\omega_{\text{rigid lattice}}/2\pi$ refers to the line width in the rigid lattice regime. Here, τ^{-1} amounts to approximately $5.5 \times 10^4 \text{ s}^{-1}$ at 300 K.

3.4 ${}^7\text{Li}$ NMR relaxometry

A more detailed insight into the Li ion dynamics in solid electrolytes can be obtained by variable-temperature NMR relaxometry [14,24–28]. Provided the jump rates follow a single Arrhenius law

$$\tau^{-1} = \tau_0^{-1} \cdot \exp\left(-\frac{E_A}{k_B T}\right) \quad (1)$$

then the same diffusion process can be studied over a wide dynamic range being tantamount to a wide temperature range. Here, k_B denotes Boltzmann's constant. Whereas NMR SLR rate (R_1) measurements performed in the laboratory frame are sensitive to jump rates in the order of $\tau^{-1} \approx 10^9 \text{ s}^{-1}$, lower values of τ^{-1} (approximately 10^5 s^{-1}) can be probed by SLR rate measurements carried out in the rotating frame of reference ($R_{1\rho}$). Typical locking frequencies of the latter are of the order of some tens of kHz. Here, the combination of the two methods [14,29] yields a comprehensive picture of the Li dynamics taking place in cubic LLZ.

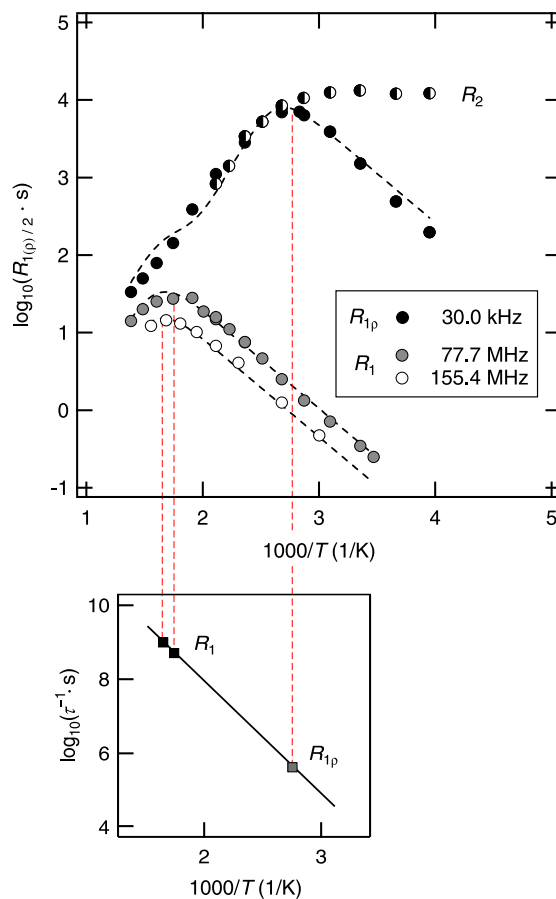


Fig. 6. Top: Arrhenius plot of the ^7Li NMR SLR rates of Al-doped LLZ. The rates were probed in both the laboratory frame (R_1) and in the rotating frame R_{1p} of reference. For comparison, ^7Li NMR spin-spin relaxation rates (R_2) are shown, too. Bottom: Arrhenius plot of the Li jump rates extracted solely from the SLR rate maxima.

In Fig. 6, ^7Li NMR SLR rates R_1 measured at two different Larmor frequencies ($\omega_0/2\pi = 77.7$ MHz and $\omega_0/2\pi = 155.4$ MHz) are shown in an Arrhenius plot. The corresponding SLR rates R_{1p} , measured in the rotating frame of reference at a locking frequency $\omega_{\text{lock}}/2\pi$ of 30.0 kHz, are also included in Fig. 6. The R_1 rates pass through a maximum at rather elevated temperatures, *i. e.*, slightly above 570 K. From each rate maximum, an absolute Li jump rate can be calculated using the maximum condition $\tau^{-1} \approx \omega_0$ [24]. For the R_{1p} rate peak, the maximum condition $\tau^{-1} \approx 2\omega_{\text{lock}}$ holds [30]. The so obtained Li jump rates are shown in the Arrhenius plot of Fig. 6 (bottom). The solid line represents a fit according to Eq. 1 and yields $E_A = 0.59(4)$ eV. Here, the error given is estimated from the uncertainty of the exact positions of the diffusion-

induced rate maxima. The value is in fair agreement with that probed by impedance spectroscopy (*vide supra*).

A more detailed analysis of the NMR relaxometry data collected includes a joint fit requiring a suitable relaxation model. According to the model of Bloembergen, Purcell and Pound [24] developed for 3D isotropic diffusion (of spin-1/2 nuclei), in the case of homonuclear dipolar relaxation the SLR rates R_1 and $R_{1\rho}$ are given by [23,31]

$$R_1 = M_2 \cdot \left[\frac{1}{3} j(\omega_0) + \frac{4}{3} j(2\omega_0) \right], \quad (2)$$

$$R_{1\rho} = M_2 \cdot \left[\frac{1}{2} j(2\omega_1) + \frac{5}{6} j(\omega_0) + \frac{1}{3} j(2\omega_0) \right]. \quad (3)$$

Here, M_2 is the second moment of the interaction in the rigid lattice and

$$\omega_1 = \sqrt{\omega_{\text{lock}}^2 + \omega_{\text{local}}^2}$$

denotes the effective locking frequency where ω_{local} represents the frequency corresponding to the local internal field. $j(\omega)$ is the Fourier transform of the normalized NMR correlation function $g(t)$ which decays from 1 to 0. $g(t)$ describes the random fluctuations of an interaction due to motional processes of the spins. If the motional process is a Brownian one, *i. e.*, assuming the jump process is uncorrelated, the correlation function can be represented by a single exponential decay function

$$g(t) = \exp[-t/\tau_c] \quad (4)$$

where τ_c is the motional correlation time. Deviations from uncorrelated motion can often be sufficiently well described by replacing the single exponential by a stretched exponential one. This is independent of the assumed nature of the microscopic reason of the correlation such as structural disorder, Coulomb interactions or the presence of cooperative motion. Hereby, the stretching parameter $0 < \beta \leq 1$ is introduced.

$$g(t) = \exp[-(t/\tau^*)^\beta] \quad (5)$$

There is no general analytical expression for the Fourier transform of the stretched exponential function but the following expression is a good approximation (with τ and $\langle \tau_c \rangle = \frac{\tau^*}{\beta} \cdot \Gamma\left(\frac{1}{\beta}\right)$ being of the same order of magnitude):

$$j(\omega) = \frac{2\tau}{1 + (\omega\tau)^{1+\beta}}. \quad (6)$$

Equations 1, 2 and 6 can be used to fit the NMR relaxometry data with the only fit parameters being (i) those describing the Arrhenius-activated jump process τ_0 and E_A , (ii) the stretching exponent β , and (iii) the external and internal experimental parameters. The latter include the NMR frequencies used, the local field ω_{local} , and the interaction strength M_2 of the fluctuating interaction which is responsible for the relaxation process.

Here, the obtained ratio $R_1(^7\text{Li})/R_1(^6\text{Li}) \approx 2$ points to a dipolar relaxation mechanism. Interestingly, the interaction strength for dipolar interaction between ^7Li nuclei,

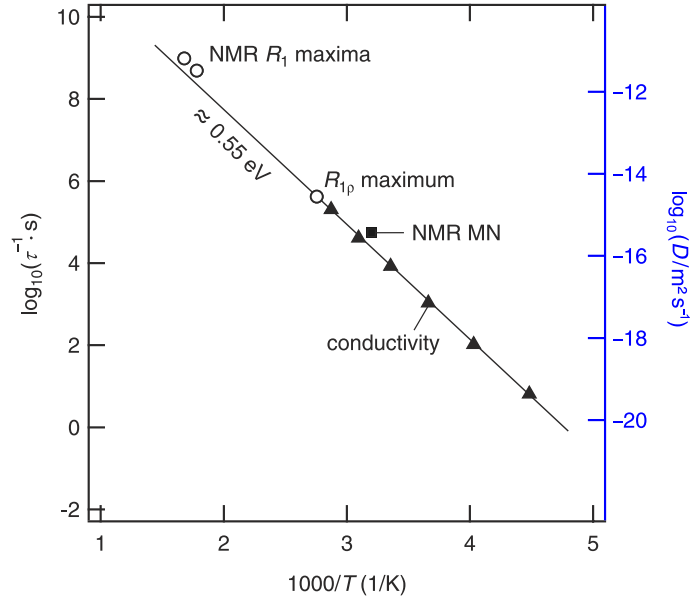


Fig. 7. Li jump rates (left axis) and diffusion coefficients (right axis) of Al-doped cubic LLZ. The rates were obtained from bulk conductivity and ^7Li NMR measurements as indicated. The solid line shows an Arrhenius fit yielding an activation energy of approximately 0.55 eV and a pre-exponential factor of $2 \times 10^{13} \text{ s}^{-1}$.

which is obtained from spin-spin relaxation rate (R_2) measurements (see Fig. 6) carried out in the rigid lattice regime, is too low to explain the absolute value of the rates. This difference might be ascribed to a relaxation mechanism governed by dipolar interactions of the diffusing ^7Li spins with immobile paramagnetic impurities [23]. The corresponding interaction strength is expected to be higher due to the much larger magnetic moment of the relaxation center. Besides this difference observed, the diffusion-induced ^7Li NMR SLR rates recorded in the laboratory and rotating frames of reference do not seem to coincide at high temperatures. Here, the found ratio of $R_{1\rho}/R_1 = 4$ also points to the assumed relaxation mechanism taking into account the spin-quantum number $I = 3/2$ of ^7Li , see [23,32].

The assumption of relaxation at paramagnetic centers is also in agreement with the observation that the $R_{1\rho}(1/T)$ rate peak cannot be satisfactorily well fitted with $\omega_1 = (\omega_{\text{lock}}^2 + \omega_{\text{local}}^2)^{1/2}$, *i. e.*, when solely homonuclear ^7Li - ^7Li dipole interactions are considered. Replacing ω_1 with $\omega_{1\text{eff}}$, corresponding to an effective field, does yield a reasonable fit. Here, $\omega_{1\text{eff}}$ can be estimated from a comparison of the R_1 and R_2 rates (Fig. 6), and it turned out that it is of the same order of magnitude as the pulsed locking field.

Taking these parameters, a joint fit can be performed with only three free variables being τ_0 , E_A and β which fully describe the motional process. In Fig. 6, the joint fit is indicated as dashed lines yielding $E_A = 0.55 \text{ eV}$, $\tau_0 = 2.2 \times 10^{13} \text{ s}^{-1}$ and $\beta = 0.45$.

3.5 Comparison of conductivity data and NMR results

Finally, in order to compare conductivity data with those deduced from NMR, the conductivity values probed have to be converted into jump rates using both the Nernst-Einstein equation and the Einstein-Smoluchowski equation. A combination of the two yields

$$\tau^{-1} = H_R/f \cdot \frac{6\sigma_{DC}k_B T}{Nq^2 a^2}. \quad (7)$$

H_R is the Haven ratio and f denotes the correlation factor, see *e.g.* Ref. [17]. Here, H_R/f is assumed to be 1. N is the charge carrier density and q is the charge of the Li ions. a denotes the jump distance estimated from the crystal structure. In Fig. 7, the so obtained jump rates τ^{-1} are shown in an Arrhenius plot together with those deduced from NMR. Obviously, the two methods are sensitive to the same motional process. Taken together, Li diffusion in cubic LLZ turned out to be characterized by $E_A \approx 0.54(3)$ eV and $\tau_0^{-1} \approx 2.2(5) \times 10^{13} \text{ s}^{-1}$. Interestingly, these values are very similar to those recently reported for the tetragonal modification of LLZ [14].

4. Conclusions

Dynamic parameters of Li dynamics in $\text{Li}_7\text{La}_3\text{Zr}_2\text{O}_{12}$ crystallizing with cubic symmetry were studied by both impedance spectroscopy and ^7Li NMR relaxometry. The sample was prepared in alumina crucibles at high temperatures; it contains a small amount of aluminium which has been detected by ^{27}Al MAS NMR. Presumably, the incorporated Al stabilizes the *cubic* modification. Impedance data and NMR SLR rates point to the same Arrhenius-type transport process being characterized by $E_A \approx 0.54(3)$ eV and a pre-exponential factor of $\tau_0^{-1} \approx 2.2(5) \times 10^{13} \text{ s}^{-1}$. Interestingly, the same result was obtained for phase-pure (Al-free) LLZ crystallizing with *tetragonal* symmetry. Therefore, in the present case neither the change in crystal symmetry nor the fact that Al has been incorporated leads to the enhancement of the Li ion conductivity as found for other (Al-doped) samples, recently. This indicates that the reasons for the enhancement in ionic conductivity observed in some cases are still unclear. Presumably, the oxygen stoichiometry might also influence the ion conductivity which has to be taken into account in further experimental studies to elucidate Li dynamics in garnet-type LLZ.

Acknowledgement

We thank Marc Krey for the ICP-OES analysis. Financial support by the Federal Ministry of Education and Science (BMBF) within the framework of the ‘‘Kompetenzverbund Nord’’ and by the Deutsche Forschungsgemeinschaft (DFG) *via* the Research Unit 1277 (molife) is gratefully acknowledged. A. K. acknowledges support by the Studienstiftung des deutschen Volkes e.V.

References

1. V. Thangadurai, H. Kaack, and W. Weppner, *J. Am. Chem. Soc.* **86** (2003) 437.
2. V. Thangadurai and W. Weppner, *Adv. Funct. Mater.* **15** (2005) 107.
3. V. Thangadurai and W. Weppner, *J. Power Sources* **142** (2005) 339.
4. A. Ramzy and V. Thangadurai, *Appl. Mater. Interfaces* **2** (2010) 385.
5. L. v. Wüllen, T. Echelmeyer, H.-W. Meyer, and D. Wilmer, *Phys. Chem. Chem. Phys.* **9** (2007) 3298.
6. B. Koch and M. Vogel, *Solid State Nucl. Magn.* **34** (2008) 37.
7. E. J. Cussen, *Chem. Commun.* (2006) 412.
8. E. J. Cussen, *J. Mater. Chem.* **20** (2010) 5167.
9. M. Kotobuki, H. Munakata, K. Kanamura, Y. Sato, and T. Yoshida, *J. Electrochem. Soc.* **157** (2010) A1076.
10. R. Murugan, V. Thangadurai, and W. Weppner, *Angew. Chem. Int. Edit.* **46** (2007) 7778.
11. J. Awaka, N. Kijima, H. Hayakawa, and J. Akimoto, *J. Solid State Chem.* **182** (2009) 2046.
12. C. A. Geiger, E. Alekseev, B. Lazic, M. Fisch, T. Armbruster, R. Langner, M. Fechtelkord, N. Kim, T. Pettke, and W. Weppner, *Inorg. Chem.* **50** (2011) 1089.
13. H. Buschmann, J. Dölle, S. Berendts, A. Kuhn, P. Bottke, M. Wilkening, P. Heitjans, A. Senyshyn, H. Ehrenberg, A. Lottnyk, V. Duppel, L. Kienle, and J. Janek, *Phys. Chem. Chem. Phys.* **13** (2011) 19378.
14. A. Kuhn, S. Narayanan, L. Spencer, G. Goward, V. Thangadurai, and M. Wilkening, *Phys. Rev. B* **83** (2011) 094302.
15. S. Narayanan, V. Epp, M. Wilkening, and V. Thangadurai, *RSC Adv.* **2** (2012) 2553.
16. M. Wilkening and P. Heitjans, *Chem. Phys. Chem.* **13** (2012) 53.
17. P. Heitjans and S. Indris, *J. Phys.-Condens. Mat.* **15** (2003) R1257.
18. K. J. D. MacKenzie and M. E. Smith, *Multinuclear Solid-State NMR of Inorganic Materials*, Elsevier, Oxford (2002).
19. A. Düvel, A. Kuhn, L. Robben, M. Wilkening, and P. Heitjans, *J. Phys. Chem. C* submitted (2011).
20. A. Boulant, J. F. Bardeau, A. Jouanneaux, J. Emery, J.-Y. Buzare, and O. Bohnke, *Dalton T.* **39** (2010) 3968.
21. M. Nyman, T. M. Alam, S. K. McIntyre, G. C. Bleier, and D. Ingersoll, *Chem. Mater.* **22** (2010) 5401.
22. J. Hendrickson and P. Bray, *J. Magn. Reson.* **9** (1973) 341.
23. P. M. Richards, *Top. Curr. Phys.* **25** (1979) 1019.
24. N. Bloembergen, E. Purcell, and R. Pound, *Phys. Rev.* **73** (1948) 679.
25. D. Ailion and C. P. Slichter, *Phys. Rev. Lett.* **12** (1964) 168.
26. A. Kuhn, M. Kunze, P. Sreeraj, H.-D. Wiemhöfer, V. Thangadurai, M. Wilkening, and P. Heitjans, *Solid State Nucl. Magn. Reson.* **42** (2012) 2.
27. M. Wilkening and P. Heitjans, *Phys. Rev. B* **77** (2008) 024311.
28. V. Epp and M. Wilkening, *Phys. Rev. B* **82** (2010) 020301.
29. A. Kuhn, P. Sreeraj, R. Pöttgen, H.-D. Wiemhöfer, M. Wilkening, and P. Heitjans, *J. Am. Chem. Soc.* **133** (2011) 11018.
30. D. C. Look and I. J. Lowe, *J. Chem. Phys.* **44** (1966) 2995.
31. C. A. Sholl, *J. Phys. C Solid State* **14** (1981) 447.
32. R. E. Walstedt, *Phys. Rev. Lett.* **19** (1967) 146.

Cite this: *Phys. Chem. Chem. Phys.*, 2011, **13**, 19378–19392

www.rsc.org/pccp

Structure and dynamics of the fast lithium ion conductor “Li₇La₃Zr₂O₁₂”[†]

Henrik Buschmann,^a Janis Dölle,^a Stefan Berendts,^a Alexander Kuhn,^b Patrick Bottke,^b Martin Wilkening,^b Paul Heitjans,^b Anatoliy Senyshyn,^c Helmut Ehrenberg,^d Andriy Lotnyk,^e Viola Duppel,^f Lorenz Kienle^e and Jürgen Janek^{*a}

Received 28th June 2011, Accepted 30th August 2011

DOI: 10.1039/c1cp22108f

The solid lithium-ion electrolyte “Li₇La₃Zr₂O₁₂” (LLZO) with a garnet-type structure has been prepared in the cubic and tetragonal modification following conventional ceramic syntheses routes. Without aluminium doping tetragonal LLZO was obtained, which shows a two orders of magnitude lower room temperature conductivity than the cubic modification. Small concentrations of Al in the order of 1 wt% were sufficient to stabilize the cubic phase, which is known as a fast lithium-ion conductor. The structure and ion dynamics of Al-doped cubic LLZO were studied by impedance spectroscopy, dc conductivity measurements, ⁶Li and ⁷Li NMR, XRD, neutron powder diffraction, and TEM precession electron diffraction. From the results we conclude that aluminium is incorporated in the garnet lattice on the tetrahedral 24d Li site, thus stabilizing the cubic LLZO modification. Simulations based on diffraction data show that even at the low temperature of 4 K the Li ions are blurred over various crystallographic sites. This strong Li ion disorder in cubic Al-stabilized LLZO contributes to the high conductivity observed. The Li jump rates and the activation energy probed by NMR are in very good agreement with the transport parameters obtained from electrical conductivity measurements. The activation energy E_a characterizing long-range ion transport in the Al-stabilized cubic LLZO amounts to 0.34 eV. Total electric conductivities determined by ac impedance and a four point dc technique also agree very well and range from $1 \times 10^{-4} \text{ Scm}^{-1}$ to $4 \times 10^{-4} \text{ Scm}^{-1}$ depending on the Al content of the samples. The room temperature conductivity of Al-free tetragonal LLZO is about two orders of magnitude lower ($2 \times 10^{-6} \text{ Scm}^{-1}$, $E_a = 0.49 \text{ eV}$ activation energy). The electronic partial conductivity of cubic LLZO was measured using the Hebb–Wagner polarization technique. The electronic transference number t_{e-} is of the order of 10^{-7} . Thus, cubic LLZO is an almost exclusive lithium ion conductor at ambient temperature.

^a *Physikalisch-Chemisches Institut, Justus Liebig Universität Giessen, Heinrich-Buff-Ring 58, 35392 Giessen, Germany.*

E-mail: juergen.janek@phys.chemie.uni-giessen.de

^b *Institut für Physikalische Chemie und Elektrochemie, Leibniz Universität Hannover, Callinstr. 3a, 30167 Hannover, Germany*

^c *Forschungsneutronenquelle Heinz Maier-Leibnitz (FRM II), Technische Universität München, Lichtenbergstrasse 1, 85747 Garching, Germany*

^d *Institute for Applied Materials (IAM), Karlsruhe Institute of Technology (KIT), Hermann-von-Helmholtz-Platz 1, 76344 Eggenstein-Leopoldshafen, Germany*

^e *Faculty of Engineering, Institute for Material Science, Synthesis and Real Structure, Christian Albrechts Universität zu Kiel, Kaiserstr. 2, D-24143 Kiel, Germany*

^f *Max Planck Institute for Solid State Research, Heisenbergstr. 1, D-70569 Stuttgart, Germany*

[†] Electronic supplementary information (ESI) available: TEM pictures, CCDC reference numbers 833727. For ESI and crystallographic data in CIF or other electronic format see DOI: 10.1039/c1cp22108f

Introduction

Today, state-of-the-art electrolytes in lithium (ion) batteries are composed of organic solvents or polymers with a dissolved Li-salt.¹ These are combustible in case of abuse, and they often react with electrode materials to form passivating films in the best case.^{2,3} This is on the one hand necessary and favourable, on the other hand proceeding film growth and electrolyte decomposition at elevated temperatures lead to degradation of the battery and shorter battery life times.⁴ In particular, new cell concepts based on high voltage cathodes or mobile non-metal cathode systems based on sulfur or oxygen require improved electrolytes, and it may well be that ion-conducting membranes become indispensable. Therefore, the search for stable and incombustible inorganic solid electrolytes with high lithium ion conductivity is currently an important issue in battery research.

Recently Li ion conducting garnet-type oxides are considered as promising electrolytes because of their high conductivity and stability vs. Li metal. Thangadurai *et al.* first reported about Li ion mobility in $\text{Li}_5\text{La}_3\text{M}_2\text{O}_{12}$ ($M = \text{Nb}, \text{Ta}$).⁵ After the report on cubic $\text{Li}_7\text{La}_3\text{Zr}_2\text{O}_{12}$ (LLZO) with the so far highest room temperature conductivity⁶ in 2007 these materials have attracted a lot of interest, but it was often found to be difficult to obtain highly conductive LLZO. Later Awaka *et al.* showed that the reason for this is the existence of a second, tetragonally distorted modification⁷ with a much lower conductivity than cubic LLZO. Although some groups reported about the successful preparation of cubic LLZO it is impossible to judge about the quality of the reported materials, due to missing experimental data like conductivities and/or X-ray diffractograms (XRD).^{8,9} Recently, some groups reported on aluminium impurities and the formation of cubic LLZO in combination with Al impurities or Al doping.^{10–13} None of these groups could clarify the exact effect of Al on the formation of cubic LLZO and the changes of the crystal structure caused by Al incorporation except the suggestion that Al might substitute Li in the garnet lattice. In order to indicate that it is in fact not pure $\text{Li}_7\text{La}_3\text{Zr}_2\text{O}_{12}$ which shows high Li ion conductivity, we will use the abbreviation LLZO or the formula in quotation marks throughout the paper.

Despite attempts to clarify the crystal structure of cubic LLZO by single crystal XRD^{8,10} not much is known about the lithium distribution in cubic LLZO, owing to the small scattering factors of lithium ions. It is the aim of this study to gain deeper insight into the structure and ion dynamics of cubic LLZO in order to better judge its potential as a battery electrolyte. In particular, we made a systematic study of the effect of aluminium doping on the formation of the tetragonal and the cubic LLZO modification. In order to obtain maximal structural information we combined XRD, neutron powder diffraction as well as transmission electron microscopy/precession electron diffraction (TEM-PED) and nuclear magnetic resonance (NMR) spectroscopy. We propose a structure model which takes the lithium ions properly into account as well as the aluminium dopant. In order to also obtain comprehensive information on the lithium ion dynamics we combined electrochemical measurements and ⁷Li NMR spin–spin as well as spin–lattice relaxation techniques. Very good agreement of the different results was found. Finally, we used the Hebb–Wagner method to determine the electronic transference number of cubic LLZO which has not been reported before so far.

Experimental

Synthesis

LLZO was prepared by a high temperature route using LiOH (Chempur, 99%, anhydrous), ZrO_2 (Chempur, 99.9%) and La_2O_3 (Chempur 99.99%, dried at 900 °C for 12 h). The starting materials were mixed in stoichiometric amounts (10 wt%–20 wt% LiOH excess was used) and milled for 8 h–12 h in 2-propanol in a planetary ball mill (Fritsch, Pulverisette 7 premium line or Fritsch, Pulverisette 5 classic line)

with zirconia balls and grinding bowls. We made use of three different procedures to prepare Al-free and Al-containing LLZO samples. Interestingly, although we followed the preparation route described in the literature⁶ to synthesize cubic LLZO, the second calcination step at 1130 °C led to the formation of the tetragonal modification⁷ of LLZO. The successful preparation of cubic LLZO turned out to depend on the number of calcination steps and the kind of crucibles used. The cubic phase of LLZO only formed when alumina crucibles were used and when the powder was annealed several times at 1130 °C for about 12 h with milling steps in between. As a result of the reaction between the crucible and the powder a thinning of the crucible after some preparation steps was observed. Several batches of cubic LLZO were prepared according to this procedure and investigated by ICP-OES (inductively coupled plasma optical emission spectroscopy). All of the cubic LLZO samples prepared showed an Al content of about 0.9 wt% (28 mol% Al per mol $\text{Li}_7\text{La}_3\text{Zr}_2\text{O}_{12}$). To verify the hypothesis that Al stabilizes the cubic modification we prepared LLZO samples intentionally doped with Al as well as free of Al. For this purpose crucibles free of any Al traces have been used. A small amount (corresponding to 0.5 wt% and 0.9 wt% in LLZO) of $\gamma\text{-Al}_2\text{O}_3$ (Merck, anhydrous) was added to the mixture of the starting materials. The Al-doped samples were otherwise prepared according to the procedure described above. After calcination at 900 °C and 1130 °C the powder was pressed to pellets, covered with mother powder, and sintered at 1230 °C for 30 h. For comparison, Al-free LLZO has been prepared without addition of $\gamma\text{-Al}_2\text{O}_3$ powder.

Phase characterization

Phase analysis along synthesis was carried out on a Siemens D500 Siemens AG, now Bruker AXS in Bragg-Bretano geometry with $\text{CuK}\alpha$ -radiation. Phase analysis and determination of cell parameters at room temperature in cubic LLZO were carried out using X-ray powder diffraction (XPD) with a STOE STADI P diffractometer either by using $\text{MoK}\alpha_1$ -radiation, $\lambda = 0.7093 \text{ \AA}$ or $\text{CoK}\alpha_1$ -radiation, $\lambda = 1.78897 \text{ \AA}$.

Elastic coherent neutron scattering experiments were performed on the high-resolution powder diffractometer SPODI at the research reactor FRM-II (Garching, Germany).¹⁴ Monochromatic neutrons ($\lambda = 1.5482 \text{ \AA}$) were obtained at a 155° take-off angle using the (551) reflection of a vertically-focused composite Ge monochromator. The vertical position-sensitive multidetector (300 mm effective height) consisting of 80 ³He tubes and covering an angular range of 160°. 2θ was used for data collection. Measurements were performed in Debye–Scherrer geometry. The powder sample was filled into a thin-wall (0.15 mm) vanadium can of 13 mm in diameter and then mounted in the top-loading closed-cycle refrigerator. Helium 4 was used as a heat transmitter. The instantaneous temperature was measured using two thin film resistance cryogenic temperature sensors Cernox and controlled by a temperature controller from LakeShore. Two-dimensional powder diffraction data were collected at 4 K and 300 K using two wavelengths and then corrected for geometrical aberrations and curvature of Debye–Scherrer rings.

The analysis of powder diffraction data was carried out using the Rietveld technique implemented into the software package FullProf.¹⁵ The peak profile was described by a modified pseudo-Voigt function (*Thompson–Cox–Hastings*). The background of the diffraction patterns was fitted using a linear interpolation between selected data points in non-overlapping regions. Cylindrical absorption correction with $\mu R = 0.7072$ has been applied to obtain neutron intensities. The scale factor, lattice parameter, fractional coordinates of atoms and their iso-/anisotropic displacement parameters, zero angular shift, profile shape parameters and half width (Caglioti) parameters were varied during the fitting. Prior to the Rietveld refinement route the lattice parameters, background and profile shape parameters were estimated using the full profile decomposition (Le-Bail) technique.

The maximum entropy method (MEM) implemented in the program PRIMA¹⁶ was used to determine the nuclear densities. MEM deals with the 3D densities in the way giving the maximum variance of structure factors $F_c(\text{MEM})$ within standard deviation of observed structure factors F_o , where structural information can effectively be extracted from the diffraction data and reflected on the resulting three-dimensional distribution of electron/nuclear densities. MEM analysis was conducted using either 189 (at 4 K) or 192 (at 300 K) structure factors obtained from the Rietveld analysis, with the unit cell divided into $128 \times 128 \times 128$ pixels.

TEM investigations

Transmission electron microscopy (TEM) was performed in a Philips CM 30 STwin microscope ($C_s = 1.15$ mm, 300 kV, LaB₆) equipped with a Spinning Star precession module (Nanomegas) and an EDX detector (Fa. Noran). Energy dispersive X-ray (EDX) analyses were performed in a Tecnai F30 STwin microscope ($C_s = 1.2$ mm, 300 kV, FEG) equipped with a Si/Li detector (EDAX system). The analyses were carried out in scanning transmission electron microscope (STEM) mode using the HAADF detector for image acquisition. The samples for TEM investigations were grinded and suspended in n-butanol. One drop of each suspension was placed on a TEM support (a lacey carbon film on a copper grid). All images were recorded with a Gatan Multiscan CCD camera ($1 \text{ k} \times 1 \text{ k}$) and evaluated with a program Digital Micrograph (Gatan, Inc.). Identification of the crystal modification of LLZO was performed by comparing the diffracted intensities of simulated and experimental precession electron diffraction (PED) images. The precession angle was set to 3° for the PED experiments. The selected area electron diffraction (SAED) and PED patterns were recorded along different zone axes. Several zone axes were examined, however, in the present work we are focusing on [001] since this direction represents the most significant one for phase distinction. The software JEMS¹⁷ was used for the simulations of SAED and PED patterns (including multiple scattering events (dynamical calculations)) as well as for simulations of high-resolution TEM (HRTEM) images (using the multislice approach). The Weickenmeier–Kohl atomic form factor was used for the simulations. For PED calculations the sample thickness was set to 10 nm. For HRTEM simulations the

following microscope parameters were used: $C_s = 1.15$ mm, defocus spread 7 nm and illumination semiangle of 0.8 mrad. In order to reduce noise, all HRTEM images were filtered after Fast Fourier transformation using a band-pass mask, with no loss of essential structural information in the following. The structural data for PED simulations of tetragonal LLZO were taken from ref. 7.

NMR measurements

⁷Li (spin-quantum number $I = 3/2$) NMR spin–spin- and spin–lattice relaxation rates in both the laboratory and rotating frame of reference were recorded using a modified MSL 100 spectrometer and an MSL 400 spectrometer operating at 4.7 T (77.8 MHz) and 9.4 T (155.5 MHz), respectively. The spectrometers were connected to Oxford cryomagnets. Standard broadband probes (Bruker) as well as home-built high temperature probes were used for data acquisition. 90° pulse lengths ranged from 4 μs to 6 μs . The temperature in the sample chamber was monitored with the help of an Oxford ITC4 using Ni–CrNi thermocouples to within ± 2 K. Temperatures below room temperature were adjusted with the help of a flow of freshly evaporated nitrogen. Above 290 K the temperature in the sample chamber was controlled with a stream of heated air. ⁷Li NMR spin–lattice relaxation rates ($1/T_1 = R_1$) in the laboratory frame of reference were recorded using a saturation recovery pulse sequence: a 90° detection pulse is sent after a comb of closely spaced saturation pulses of the same duration. The corresponding transients $M_z(t)$ describing the recovery of longitudinal magnetization follow single exponential time behaviour. This is in contrast to the analogous measurements of $1/T_{1\rho} = R_{1\rho}$ in the rotating frame of reference performed using the spin-lock technique at frequencies of 11.5 kHz and 33.1 kHz. The transients $M_{(xy)}(t)$ can be well parameterized by stretched exponentials $M_{(xy)}(t) \propto \exp(-(t/T_{1\rho})^\gamma)$ with $0.4 < \gamma < 1$.

High-resolution ⁶Li and ²⁷Al NMR spectra under fast sample rotation were recorded using an Avance III spectrometer (Bruker) in combination with a shimmed cryomagnet of 14.1 T. Magic angle spinning (MAS) spectra were recorded with a 2.5-mm-probe at 88.4 MHz and 156.5 MHz, respectively. The spinning speed was 30 kHz.

Electrochemical characterization

Pellets of sintered LLZO samples were cut into pieces of different lengths and vacuum dried at 100 °C for at least 6 h. The dried pellets were then exclusively handled in an argon filled glove box (MBraun, Labmaster) with less than 0.1 ppm H₂O and O₂ in the gas. Lithium foil (Chemetall) was used as electrode material for conductivity measurements by two electrode ac impedance spectroscopy and four electrode dc techniques. The lithium foil was pressed on the sides of the LLZO pellets (Fig. 1a) and then annealed at 170 °C for some minutes on a heating plate to improve the contact between Li and LLZO. For the dc measurements two additional electrodes were placed in the flank of the pellet. Therefore, two 0.5 mm wide grooves were cut in the flank and filled with Li metal (Fig. 1b). For both ac and dc measurements the Li

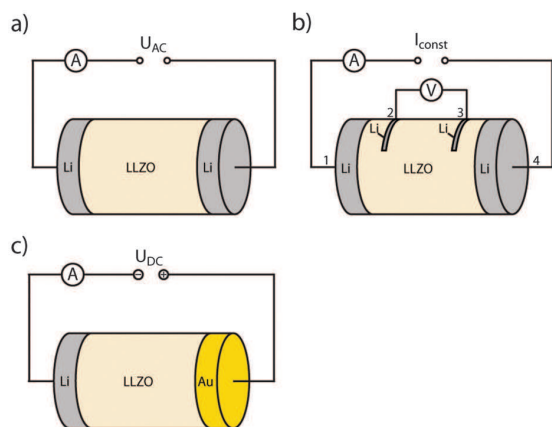


Fig. 1 Scheme of different electrode arrangements (a) for ac conductivity measurements with two lithium electrodes, (b) for dc conductivity measurements with four lithium electrodes and (c) for Hebb–Wagner type electronic conductivity measurements with one lithium and one Li ion blocking gold electrode.

electrodes were contacted with a silver or copper wire. These cells were sealed in gas-tight pouches of aluminized compound foil. Temperature dependent conductivity measurements were carried out in a temperature chamber (WTL 64 Weiss Technik) in the temperature range from $-40\text{ }^{\circ}\text{C}$ to $100\text{ }^{\circ}\text{C}$. A potentiostat/galvanostat (model SP-300 from Biologic Science Instruments) was employed for electrochemical characterization. The software package EC-Lab V10.02 was used for data acquisition and impedance data fitting. Impedance spectroscopy was carried out in the frequency range from 7 MHz to 1 Hz (amplitude of 20 mV).

Additionally, low-temperature impedance spectra down to $-148\text{ }^{\circ}\text{C}$ were recorded by employing a Novocontrol Concept 80 broadband dielectric spectrometer which is equipped with a BDS 1200 sample cell and a BETA analyzer. The latter is capable to measure impedances down to $10^{-14}\ \Omega$ at frequencies ranging from a few μHz to 20 MHz. Temperature regulation and controlling within an accuracy of about 0.5 K was carried out with a Quattro cryosystem (Novocontrol) using dry nitrogen gas. The root mean square ac voltage was typically 0.1 V to 1.0 V. These data were mainly used to extract electrical relaxation rates from the corresponding modulus spectra.

The dc conductivity was measured by applying a constant current in the range from $1\ \mu\text{A}$ – $100\ \mu\text{A}$ between the electrodes 1 and 4 (Fig. 1b) and measuring the resulting voltage drop over the distance of the potential probes 2 and 3 (Fig. 1b). At each temperature a constant dc current was applied for 90 s. The voltage drop was simultaneously measured and remained constant over the measured time period.

The electronic partial conductivity of cubic LLZO was measured using the Hebb–Wagner technique.^{18,19} A gold blocking electrode of approximately $1\ \mu\text{m}$ thickness was deposited on one of the pellets surfaces by thermal Au evaporation. As mentioned above, Li foil was attached on the opposing surface as a reversible electrode for Li ions (Fig. 1c). Measurements were performed in potentiostatic

mode (Keithley 6430) in a home-built cell in the range from 2.5 V and 4.5 V vs. Li/Li^+ in an argon filled glove box with the Li electrode connected as cathode. Steady-state was assumed when the current remained constant within 10% over a period of several hours.

Results and discussion

Synthesis

Synthesis of cubic LLZO was only successful when an aluminium source was present during synthesis. Thus cubic LLZO formed either by working in Al_2O_3 crucibles, where the LLZO starting materials react with the crucible, or when intentionally using $\gamma\text{-Al}_2\text{O}_3$ powder as a dopant in the LLZO synthesis. Preparation of cubic LLZO in Al_2O_3 crucibles without further doping takes more than two calcination and milling steps due to the stepwise reaction of the powder at the crucible walls only. When the formation of phase pure cubic LLZO (by reaction with the wall) was completed the aluminium content of these samples was typically about 0.9 wt% as determined by ICP-OES. The Al free synthesis did not lead to pure cubic LLZO but rather to the tetragonal modification or a mixture of the cubic and tetragonal modifications of LLZO (Fig. 2a–b). Synthesis with 0.5 wt% Al_2O_3 led mainly to cubic LLZO, however, the corresponding reflexes are somewhat broader indicating that there might be some tetragonal LLZO present as well (Fig. 2c). Doping with 0.9 wt% Al_2O_3 in Al free crucibles as well as synthesis without doping but using Al_2O_3 crucibles led to cubic LLZO (Fig. 2d and e). These results clearly prove that the aluminium content plays a crucial role for the formation of phase pure cubic LLZO.

Structural information from MAS NMR

Structural features of Al-doped cubic LLZO were elucidated by ^{27}Al MAS NMR spectroscopy. In Fig. 3 the NMR spectra

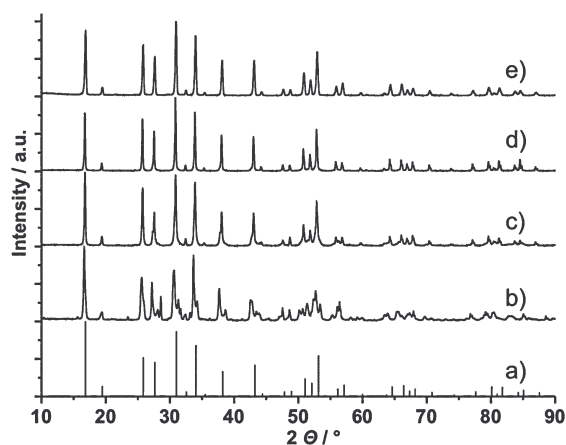


Fig. 2 XRD patterns of LLZO after the final calcination step (a) simulated pattern (JCPDS 80-0457), (b) Al-free synthesis in Al free crucible, (c) doping with 0.5 wt% $\gamma\text{-Al}_2\text{O}_3$ in Al free crucible, (d) doping with 0.9 wt% $\gamma\text{-Al}_2\text{O}_3$ in Al free crucible, (e) undoped sample prepared in Al_2O_3 crucible (0.9 wt% Al content measured by ICP-OES).

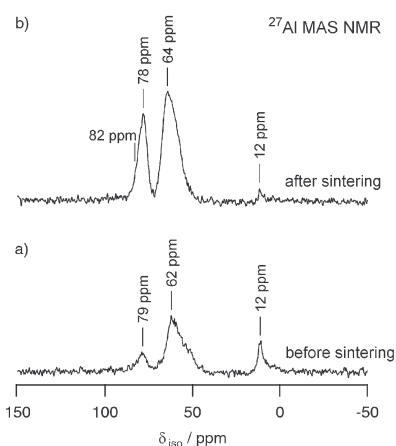


Fig. 3 ^{27}Al MAS NMR spectra of cubic LLZO before (a) and after sintering (b). The spectra were recorded at a magnetic field of 14.1 T and referenced to aqueous $\text{Al}(\text{NO}_3)_3$. The rotation frequency was 30 kHz.

of cubic LLZO before and after sintering at elevated temperatures (see above) are shown. The spectrum obtained after the sintering step is similar to that in ref. 10. Geiger *et al.* suggest that the signal showing up at a chemical shift of $\delta_{\text{iso}} = 12$ ppm reflects octahedrally coordinated Al in LaAlO_3 being an impurity phase.¹⁰ The δ_{iso} value of 64 ppm (see Fig. 3b) is characteristic of Al ions residing on lattice sites with tetrahedral coordination. Most probably the Al ions occupy the Li site $24d$ in the garnet structure according to the aliovalent doping mechanism $3\text{Li}^+ \rightarrow \text{Al}^{3+}$. Multiple-quantum magic angle spinning (MQ-MAS) measurements of Geiger *et al.* have shown that the asymmetry parameter η of the corresponding electric field gradient EFG tensor is close to zero indicating axial symmetry.¹⁰ Preliminary ^{27}Al MAS measurements on samples with varying Li, La and Al contents indicate that the signal near 80 ppm in fact represents at least two NMR lines.²⁰ Obviously, at a sufficiently large Al content, Al^{3+} ions occupy various magnetically inequivalent sites in the cubic LLZO structure. NMR lines near 80 ppm, which most likely reflect Al ions also occupying sites with tetrahedral coordination, show up for samples of cubic LLZO which are characterized either by a deficit of La and/or Zr.²⁰

It is worth mentioning that the cubic LLZO sample obtained before the sintering step (see the ^{27}Al MAS NMR spectrum in Fig. 3a) is characterized by a Li ion conductivity which is by about two orders of magnitude lower than that reported for cubic LLZO. The low Li conductivity of the non-sintered sample, which is comparable to that of LLZO crystallizing in tetragonal symmetry, has been confirmed by ^7Li NMR spin–lattice relaxation measurements revealing a rather low Li diffusivity.²¹ Comparison of the two spectra reveals distinct differences which might help explain the high ion conductivity (see below) of the sintered material from an atomic-scale point of view. Firstly, the sintering step clearly enhances the Al content within LLZO. Secondly, the NMR line intensity at 12 ppm has decreased after the sintering step. Thus, LaAlO_3 seems to act as a kind of precursor for the incorporation of Al into LLZO.

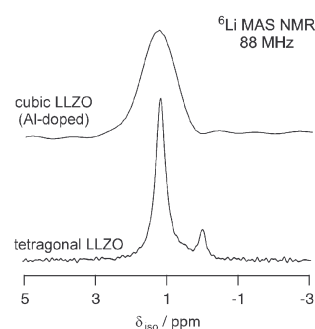


Fig. 4 ^6Li MAS NMR spectra of cubic and tetragonal LLZO. The latter was taken from ref. 21. A 1 M aqueous solution of LiCl served as reference. The spectrum of cubic LLZO refers to the sample which has been sintered at elevated temperatures; the corresponding ^{27}Al MAS NMR spectrum is shown in Fig. 8b. Note that the tetragonal Al-free sample and its Li dynamics have been investigated in detail by NMR spectroscopy in ref. 21.

Finally, in Fig. 4 (top) the ^6Li MAS spectrum of Al-doped cubic LLZO is shown. Even under MAS conditions with a spinning rate of 30 kHz, the ^6Li NMR line is comparably broad showing a line width (full width at half maximum, fwhm) of 1.1 ppm. This value should be compared with that one of the tetragonal Al-free counterparts (space group $I4_1/acd$)²¹ (see Fig. 4, bottom).

Crystal structure from neutron and X-ray diffraction

Our XRD results do not indicate any tetragonal distortion, but show some weak reflections, which can be attributed to a residue of lithium carbonate. These reflexes are more pronounced in the neutron data (Fig. 5) and the content of lithium carbonate can be quantified as 1.8(4) wt%. The comparison of neutron powder diffraction patterns collected at 4 K and 300 K indicates the isostructurality of LLZO at both temperatures. All reflexes originate either from cubic LLZO as the main phase or lithium carbonate as the residual phase. Different structure models were considered and simulated^{7,10,22} which, however, did not reveal a satisfactory description of the Bragg intensities mainly due to underestimated isotropic displacement parameters and differences in lithium occupations. After the adjustment of the models, the best results have been obtained with the model proposed by Geiger *et al.*¹⁰ Aluminium was not taken into account in their structure model, as its position in the lattice cannot easily be determined by X-ray diffraction. In fact, in the presence of relatively heavy lanthanum and zirconium atoms the location of “light” lithium and aluminium atoms is cumbersome. Moreover, the neutron scattering length b for aluminium is rather low and therefore small concentrations can be hardly quantified using neutron powder diffraction. However, the ^{27}Al MAS NMR spectra show that about 70% of the aluminium is located on the lithium sites with $24d$ symmetry which was included into our structure simulation. Placing Al on the $24d$ position did not improve the residual intensities in the difference between observed and calculated diffraction patterns, but affects the lithium occupation on the $24d$ site. Without aluminium $g_{\text{Li}(24d)}$ has been found to be 42(2)%, whilst $g_{\text{Li}(24d)} = 52(2)\%$ was

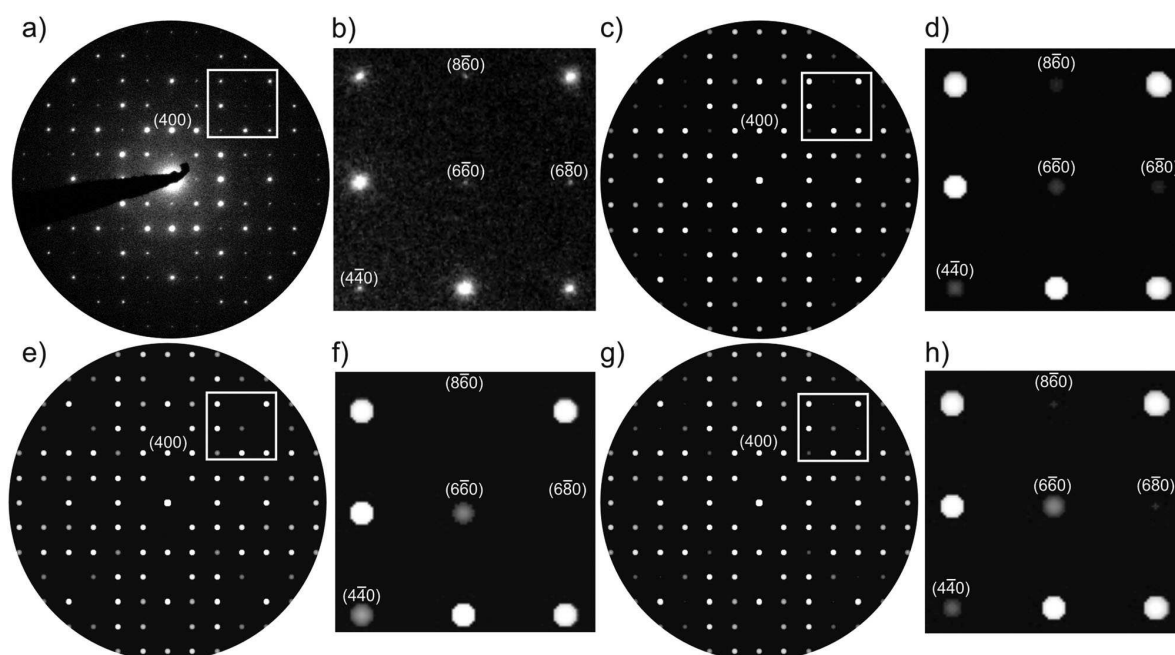


Fig. 5 (a) Experimental and (c) simulated PED patterns of LLZO along [001] assuming the cubic structural model from Table 1. (e) Simulated PED pattern of cubic LLZO according to ref. 9. (g) Simulated PED images of cubic LLZO using the structural model from ref. 10. (b), (d), (f) and (h) Enlarged areas of the marked regions in (a), (c), (e) and (g). The differences between the simulated and experimental PED patterns are clearly seen, with the experimental pattern most convincingly agreeing with the simulated image in (c) (our structure model from Table 1).

determined assuming the presence of Al with $g_{\text{Al}(24d)} = 6.53\%$. In the latter case the overall lithium content x in $\text{Li}_x\text{La}_3\text{Zr}_2\text{O}_{12}$ has been determined to be 6.05 ± 0.25 , which agrees with the proposed heterovalent substitution mechanism $3\text{Li}^+ \leftrightarrow \text{Al}^{3+}$ (see above).¹⁰ The best fits to the neutron diffraction data collected at 4 K and 300 K were obtained with the parameters listed in Table 1 and the results of the Rietveld refinements are shown in Fig. 5. Anomalously large isotropic displacement parameters have been noticed for both lithium sites in LLZO already at low temperatures, which might be attributed to static lithium disorder. An application of the split site model to Li on the 24d atomic site did neither lead to a stable fit nor a significant improvement of the fit residuals. The comparison of results obtained at 4 K and 300 K indicates a minor influence of the temperature on the crystal structure of LLZO which is quite typical for garnet-like structures.^{23,24} Heating from 4 K to 300 K results in the elongation of the lattice parameter a by 0.223% with very small atomic movements involved. This means that only a small shift of Li2 in the a_1 direction of the cubic lattice takes place, whereas the coordinates for the other atoms in LLZO remain almost unchanged within the limits of their estimated standard deviations. Temperature increase causes a pronounced rise of displacement parameters on all atomic sites, but the major increase (*ca.* 50%) was observed for Li on the 96h atomic site and (*ca.* 30%) for Li on 24d. A strong increase of the displacement parameter indicates a development of dynamic lithium disorder on the background of the static one. The analysis of the temperature evolution of the anisotropic displacement parameters for lanthanum, zirconium and oxygen indicates their evolution from elliptic

towards spherical shape with nearly unchanged spatial orientation. This might correspond to a temperature stability of the framework built by these elements. A closer look on the disorder details by examination of differential Fourier maps indicates the presence of quite broad minima around Li (24d) with a stripe-like shape penetrating the garnet lattice. This anomaly can be related to the observed very high displacement parameters. However, details of such stripes with negative densities were sufficiently smeared out due to termination effects. Therefore, further examinations of the disorder have been performed using the maximum entropy method (MEM),²⁶ which can estimate non-zero structure factors for high-Q reflections (typically excluded in the analysis of the powder diffraction data). This feature makes the termination effect in MEM analysis less pronounced in comparison to Fourier synthesis, thus yielding less noisy three-dimensional distributions of electron/nuclear densities. Therefore, the MEM technique has been successfully used to a diversity of scientific problems either concerning disorder in $\text{Sr}_{9,3}\text{Ni}_{1,2}(\text{PO}_4)_7$ ²⁷ and in $\text{Rb}_4\text{Cu}_{16}\text{I}_{7,2}\text{Cl}_{12,8}$ ²⁸ or experimental visualization of lithium diffusion in Li_xFePO_4 ²⁹ and $\text{La}_{9,69}(\text{Si}_{5,70}\text{Mg}_{0,30})\text{O}_{26,24}$.³⁰

The negative nuclear densities obtained after the MEM analysis of datasets collected at 4 K and 300 K are shown in Fig. 6. They correspond to stripes observed in differential Fourier maps and might be related to the lithium diffusion pathway (as lithium is the only negative neutron scatterer in LLZO), where all lithium atoms take part in the diffusion process. Rise of the temperature from 4 K to 300 K unambiguously indicates an enhancement of Li-ion diffusivity, which corresponds to the increase of the ionic conductivity.

Table 1 Refined structural parameters of cubic LLZO at $T = 4$ K and $T = 300$ K as deduced from Rietveld refinement with FullProf. The space group is $Ia\bar{3}d$ (No. 230). Displacement parameters for lithium were modelled in isotropic approximation. Numbers in parentheses give the statistical deviations of the last significant digit

$T = 4$ K, Lattice parameter: $a = 12.9438(2)$ Å						
Atom site	x/a_1	y/a_2	z/a_3	$u_{\text{iso}} = u_{\text{eq}}/\text{Å}^2$	$u_{11}, u_{22}, u_{33}, u_{12}, u_{13}, u_{23}/\text{Å}^2$	Occ. g
Li1, 24 <i>d</i>	1/8	0	1/4	0.041(6)	—	0.54(2)
Al1, 24 <i>d</i>	1/8	0	1/4	0.041(6)	—	0.0653 ^a
Li2, 96 <i>h</i>	0.0980(7)	0.6859(7)	0.5764(7)	0.020(4)	—	0.37(1)
La, 24 <i>c</i>	0	1/4	1/8	0.0074(6)	0.0065(5), 0.0065(5), 0.0091(10), 0.0039(6), 0.00000, 0.00000	1.0
Zr, 16 <i>a</i>	0	0	0	0.0067(3)	0.0067(3), 0.0067(3), 0.0067(3), 0.0006(5), 0.0006(5), 0.0006(5)	1.0
O, 96 <i>h</i>	-0.03173(8)	0.05463(9)	0.14951(8)	0.0105(6)	0.0120(6), 0.0137(7), 0.0058(5), 0.0017(5), -0.0013(4), -0.0037(5)	1.0
Fit residuals: $R_p = 2.53\%$, $R_{\text{wp}} = 3.22\%$, $R_{\text{exp}} = 0.93\%$						
$T = 300$ K, Lattice parameter: $a = 12.9727(2)$ Å						
Atom site	x/a_1	y/a_2	z/a_3	$u_{\text{iso}} = u_{\text{eq}}/\text{Å}^2$	$u_{11}, u_{22}, u_{33}, u_{12}, u_{13}, u_{23}/\text{Å}^2$	Occ. g
Li1, 24 <i>d</i>	1/8	0	1/4	0.054(5)	—	0.54 ^b
Al1, 24 <i>d</i>	1/8	0	1/4	0.054(5)	—	0.0653
Li2, 96 <i>h</i>	0.1004(8)	0.6853(8)	0.5769(8)	0.031(3)	—	0.37 ^b
La, 24 <i>c</i>	0	1/4	1/8	0.0106(6)	0.0095(4), 0.0095(4), 0.0128(9), 0.0035(6), 0.00000, 0.00000	1.0
Zr, 16 <i>a</i>	0	0	0	0.0095(3)	0.0095(3), 0.0095(3), 0.0095(3), 0.0005(5), 0.0005(5), 0.0005(5)	1.0
O, 96 <i>h</i>	-0.03161(8)	0.05454(9)	0.14940(8)	0.0148(6)	0.0170(6), 0.0179(6), 0.0094(5), 0.0018(5), -0.0006(4), -0.0026(5)	1.0
Fit residuals: $R_p = 2.22\%$, $R_{\text{wp}} = 2.79\%$, $R_{\text{exp}} = 0.94\%$						
^a Taken from NMR experiments. ^b Fixed to the value obtained at 4 K.						

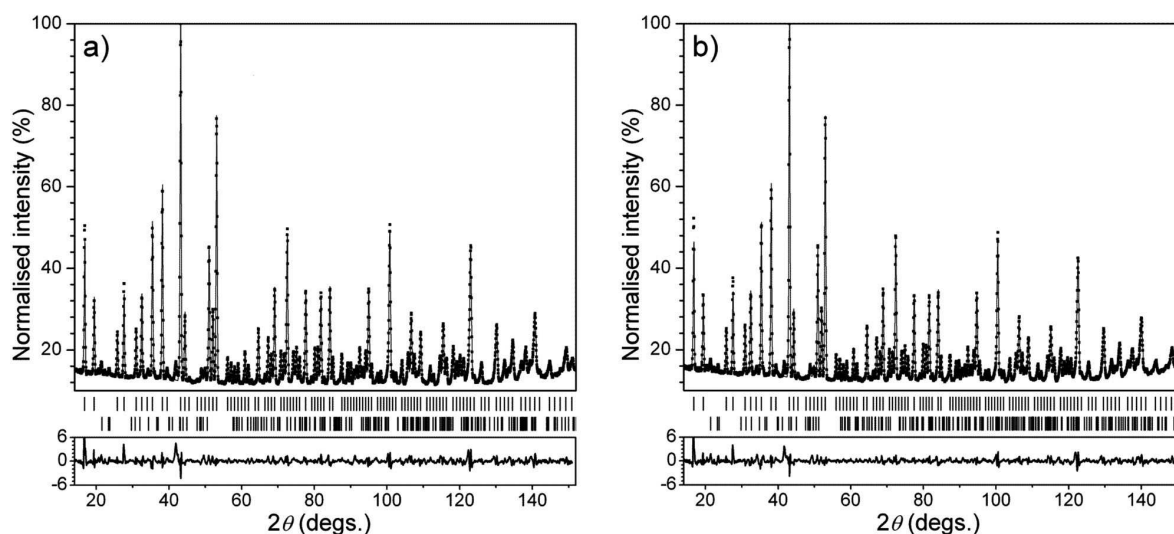


Fig. 6 Results of Rietveld refinements for neutron powder diffraction data at 4 K (a) and 300 K (b) for LLZO ($\lambda = 1.5482$ Å). Calculated positions of Bragg reflections are shown by vertical tick marks, where the top row of the tick marks corresponds to LLZO, whilst the lower ones describe the peak positions for lithium carbonate. Differences between observed and calculated pattern are shown below.

It is noteworthy that the structural investigations were carried out on the LLZO powder before sintering. Although the ²⁷Al NMR results show changes of the Al distribution on different crystallographic sites during sintering which seems to have a significant effect on the Li diffusivity we do not believe that this significantly changes the results of the diffraction investigations. As already mentioned it is quite cumbersome to

refine Al and Li positions with a high level of reliability. Therefore, from a crystallographic point of view, the small structural changes detected by NMR after sintering might only lead to an increase of the Li displacement parameters. The small changes in the occupations of La and Zr positions by Al will hardly be detectable by diffraction methods. As the disorder of Li atoms is already quite high, an additional

increase will be within the limit of reasonably refineable displacement parameters. Nevertheless, this will be a subject for further investigations.

PED and HRTEM results

In the last decade, PED has become a powerful technique for the advanced characterization of materials. The superior advantage of the PED method over the SAED technique is its ability to reduce dynamical effects arising due to multiple scattering in the transmission electron microscope. Dynamical effects in SAED patterns make the distinction between two phases difficult, particularly, if the phases are structurally and chemically related, as it is the case for cubic and tetragonal LLZO (see ESI†, Fig. SX1). In this case, the diffraction patterns differ only by the absolute values of diffracted intensity. Recently, PED was successfully applied for the distinction of polymorphs occurring in bulk materials and thin films, *e.g.* of quartz³¹ and Ag₂Se,³² respectively. In the present work, we compare our results from PED examinations on single microcrystals with those from neutron powder diffraction. Fig. 7a displays the experimental PED pattern of a LLZO sample containing 0.9 wt% of Al and the simulated PED patterns based on the cubic and tetragonal LLZO along zone axis [001] (Fig. 7b and c, respectively). The differences in the simulated intensities of the reflections $h00$ with $h = 2n$ are obvious.

For the cubic phase, the $h00$ reflections with $h \neq 4n$ are kinematically forbidden (Fig. 7b). However, since the PED only reduces dynamical effects, the serial reflection conditions based on the 4₁ screw axis can be violated by residual dynamical effects. Thus, the significant intensity of the (200) reflection in the experimental PED pattern (Fig. 7a) can be rationalized, even for the cubic structure. The dynamical effects decrease with increasing h , thus, the intensity of the reflections (600) and (10 0 0) are zero in the experimental and simulated patterns (Fig. 7a and b). In the case of the tetragonal LLZO, the integral reflection condition $h00$ with $h = 2n$ is consistent with the occurrence of strong reflections (600) and (10 0 0), *cf.* the simulated pattern in Fig. 7c. Simulated patterns based on the tetragonal and cubic polymorphs also

indicate differences in the intensities of (440) and (660) reflections, *cf.* line profiles in Fig. 7. Thus, the experimental PED pattern is better described by the cubic structure of LLZO. It should be noted that we have tested different structural models for PED simulations obtained from neutron powder diffraction. We found that calculated PED patterns using the structural model in Table 1 show the best match with our experimental PED data. In addition, the calculated PED patterns using the structural model for LLZO of Table 1 match even better as the PED images calculated based on the models for the cubic LLZO^{8,10} (see *e.g.* Fig. 8).

Even when adjusting low dose settings, the LLZO sample was extremely unstable under the imaging conditions used for HRTEM. Thus, a complete series of images with variable focus values could not be recorded without initiating considerable loss of structural ordering. Fig. 9a and b show experimental and Fourier-filtered HRTEM micrographs for the first overfocused image of a focus series, zone axis [111]. The simulated micrograph of Fig. 9c convincingly agrees confirming again our assignment to the cubic structure given in Table 1. However, after a few seconds the structure is completely amorphized, just leaving crystalline islands embedded within an amorphous matrix, *cf.* complete focus series in ESI†, Fig. SX2.

EDX investigations showed a homogeneous distribution of Al in the LLZO sample within the experimental errors. Particularly, no Al-rich regions were found in the LLZO specimen (see ESI†, Fig. SX3).

Electrochemical results

Electrochemical measurements were performed to determine the ionic and electronic conductivity of the cubic LLZO. The total conductivity was measured both by ac impedance spectroscopy and four electrode dc measurements. The electronic conductivity was determined by the Hebb–Wagner technique.^{18,19} Impedance measurements with Au electrodes on LLZO known from the literature show two semicircles and a low frequency tail. These were interpreted to be corresponding to the bulk, grain boundary and electrode contributions, respectively.⁶ Our impedance measurements performed with

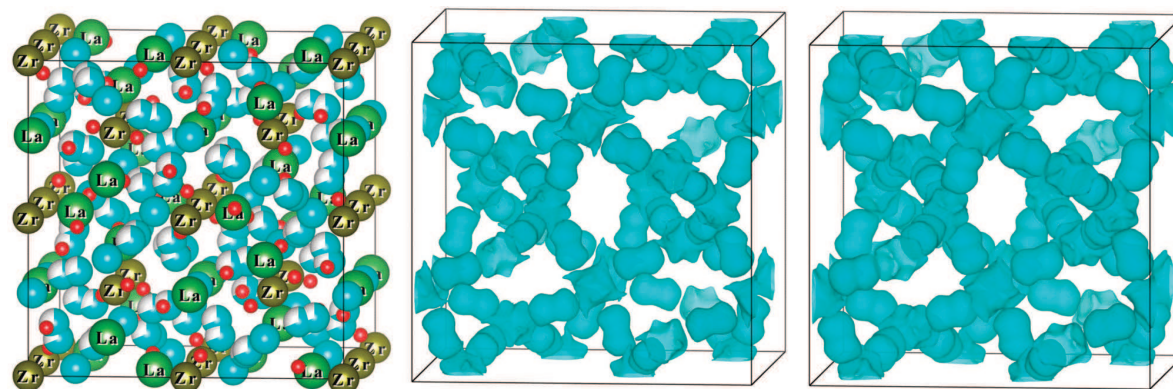


Fig. 7 Structural model of cubic LLZO (left, atoms shown by cyan and red correspond to lithium and oxygen, respectively) and negative scattering neutron density maps determined at 4 K (middle) and 300 K (right) by MEM. Negative scattering neutron density maps are shown with a equidensity level of $0.035 \text{ fm } \text{\AA}^{-3}$. Data visualization has been performed using the program VESTA.²⁵

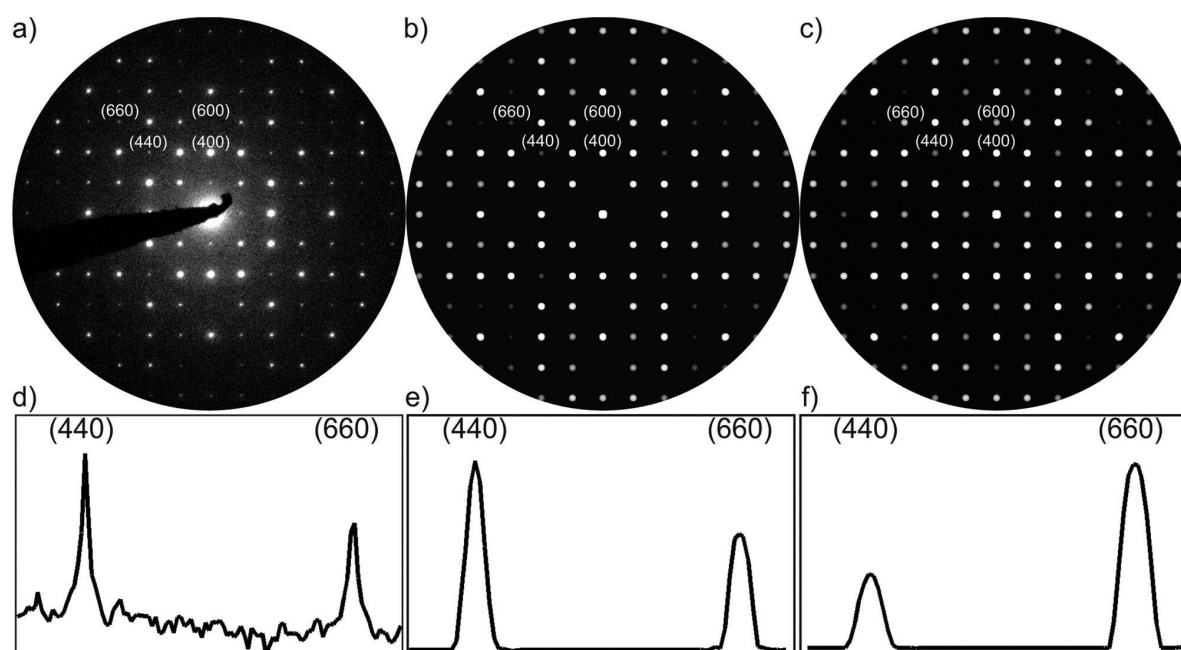


Fig. 8 (a) Experimental and (b) simulated PED patterns of LLZO along [001]. For the simulation of (b) we used the cubic structure model presented in Table 1. (c) Simulated PED images of tetragonal LLZO based on the structure model from ref. 7. (d)–(f) Line profiles taken from (440) and (660) reflections in (a)–(c). The differences in the intensities of (600), (440) and (660) reflections are clearly seen. The experimental pattern fits better to the cubic LLZO.

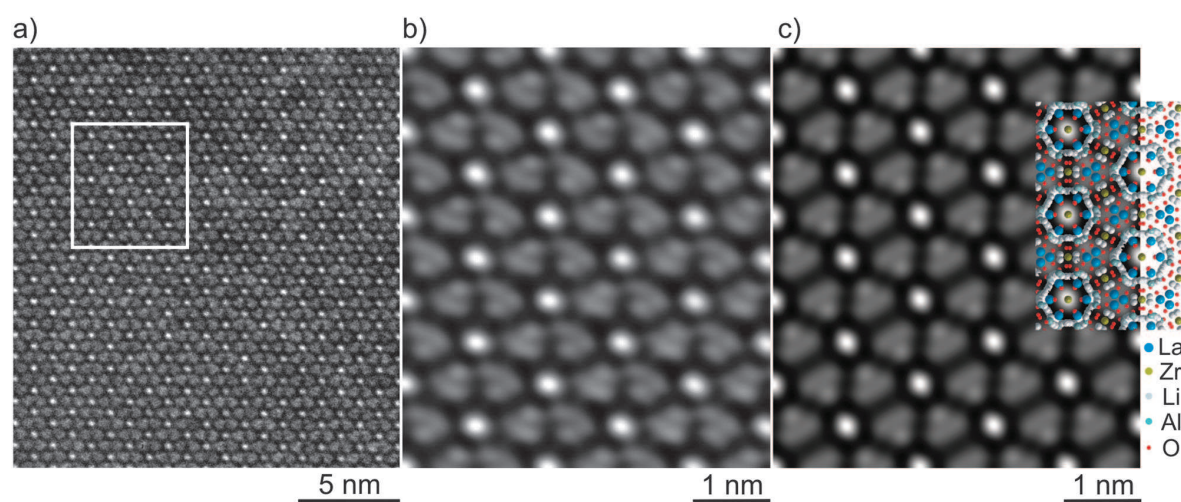


Fig. 9 (a) Experimental HRTEM micrograph of LLZO along [111] viewing direction. (b) Fourier-filtered HRTEM image of the region marked in (a). (c) Simulated HRTEM image (defocus 90 nm, $t = 9$ nm, 2-fold astigmatism estimated to 10 nm) based on the crystal structure model of LLZO from Table 1 (inserted).

Li electrodes show only one semicircle for the total resistivity of the LLZO pellet and a second semicircle instead of the tail. The appearance of an additional semicircle when using Li electrodes can be expected since Li electrodes can reversibly incorporate Li ions from the LLZO, so the charge transfer resistance and the electrode capacity should give rise to an additional semicircle in the impedance measurements explaining the appearance of a second semicircle instead of the low

frequency tail. Still it was surprising that our samples only showed one semicircle for the LLZO contribution so we took a detailed look into the impedance data to be sure that there was no misinterpretation. Fig. 10a shows an example of a typical Nyquist plot measured on a LLZO pellet between Li electrodes. Impedance data were fitted with an equivalent circuit (RC)(RQ) or (RQ)(RQ) depending on whether the respective sample showed a depressed high frequency semicircle or not.

From the fit to this measurement the first high frequency semicircle resistance and capacity were determined to be 20.4 k Ω and 0.38 nF, respectively. The second low frequency semicircle resistance and capacity result in 13.3 k Ω and 0.15 μ F, respectively. These relatively high capacity values are typical for grain boundaries or electrodes of polycrystalline ceramics.³³ As both semicircles yield to comparable resistances as supposed for the bulk and grain boundary contributions in cubic LLZO,⁶ some additional experiments were carried out to clarify the origin of the impedance contributions when using Li electrodes. Fig. 10b shows a Nyquist plot of a sample measured once with Au and once with reversible Li electrodes. The Au electrodes were gas phase deposited by thermal evaporation, whereas the Li electrodes were pressed

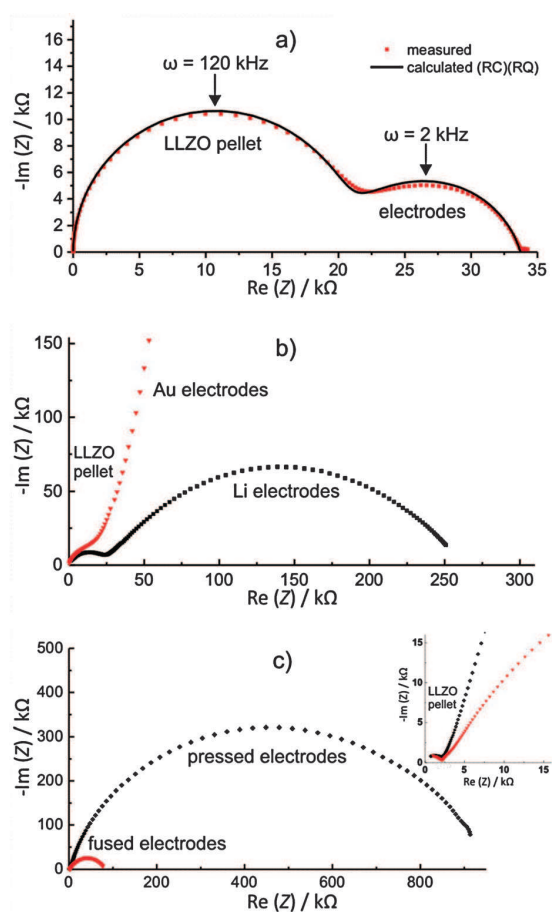


Fig. 10 Room temperature impedance spectra of different LLZO samples with various electrodes (a) impedance spectrum of a LLZO pellet doped with 0.9 wt% Al. The pellet size was 5.3 mm diameter and 16.2 mm length. The pellet was sandwiched between two Li electrodes (frequency range from 7 MHz to 50 mHz at 20 mV amplitude). An equivalent circuit (RC)(RQ) was used to fit the impedance data. (b) Impedance spectra of a LLZO pellet doped with 0.9 wt% Al measured with blocking Au and reversible Li electrodes in a frequency range 7 MHz to 1 Hz at 20 mV. (c) Impedance spectra of a LLZO pellet doped with 0.9 wt% Al measured with Li electrodes pressed and fused on the pellet (frequency range 7 MHz to 1 Hz at 20 mV).

mechanically on the pellet. The measurement with the Au electrodes shows a semicircle merging into a low frequency tail. The low frequency tail is caused by an almost solely capacitive behaviour of the Au electrodes indicating their blocking nature under the given experimental conditions. The measurement with Li electrodes leads to two semicircles proving that the second semicircle corresponds to the Li electrodes charge transfer resistance and capacity. This also clarifies that our samples only show one semicircle representing the total resistivity of the LLZO pellet. Murugan *et al.* reported that bulk and grain boundary contributions could only be resolved at low temperatures,⁶ *i.e.*, in their case room temperature and slightly above. In the present case even at -40 $^{\circ}$ C only one semicircle representing the total resistivity of the sample is observed. As shown in Fig. 10c the charge transfer resistance of the Li electrodes depends strongly on the preparation method of the Li electrodes. Two impedance measurements of the same sample, in one case with Li electrodes gently pressed on the pellet and in the second case with Li electrodes fused on the pellet, were performed. The different preparation methods change the charge transfer resistance almost by one order of magnitude while the pellet resistance remains unchanged as seen in the inset. We did not find any evidence for a reaction of the LLZO with Li metal which might have shown up as an additional impedance during our measurements. It has to be noted that the charge transfer resistance is not negligible and may play a role when LLZO is applied as a solid electrolyte in battery cells with Li metal electrodes. The total voltage drop across a cell is the sum of the charge transfer resistances at the electrode interfaces and the voltage drop along the electrolyte bulk itself. Therefore further investigations on the charge transfer resistances between different electrode materials and preparation procedures are in progress.

In addition to ac impedance we used four electrode dc measurements to determine the conductivity of the samples under continuous current load. By using the four electrode dc technique the bulk resistance of the sample (as a sum of grain and grain boundary contributions) can be determined without electrode overvoltages. The results of the dc conductivities are shown together with ac data in Fig. 11. Comparing the conductivities of samples with different aluminium contents it is clearly visible that the conductivity depends on the aluminium content in the samples. The highest conductivity of 3×10^{-4} Scm^{-1} to 4×10^{-4} Scm^{-1} at 25 $^{\circ}$ C were found for samples containing 0.9 wt% Al prepared either by synthesis in Al_2O_3 crucibles or by intentional $\gamma\text{-Al}_2\text{O}_3$ doping. The Arrhenius activation energy is determined to be 0.34 eV. The conductivity and activation energy data agree well with results from Murugan *et al.*⁶ who did not report on any aluminium in their samples and did not give information on the impurity level at all. The 0.5 wt% Al containing sample ($\gamma\text{-Al}_2\text{O}_3$ doped) shows a slightly lower conductivity of 1×10^{-4} Scm^{-1} but the same activation energy of $E_a = 0.34$ eV. The Al-free sample with tetragonal crystal structure is characterized by a two orders of magnitude lower conductivity of 2×10^{-6} Scm^{-1} at 25 $^{\circ}$ C and an activation energy $E_a = 0.49$ eV. The latter value is in good agreement with that reported for a tetragonal sample which has recently been

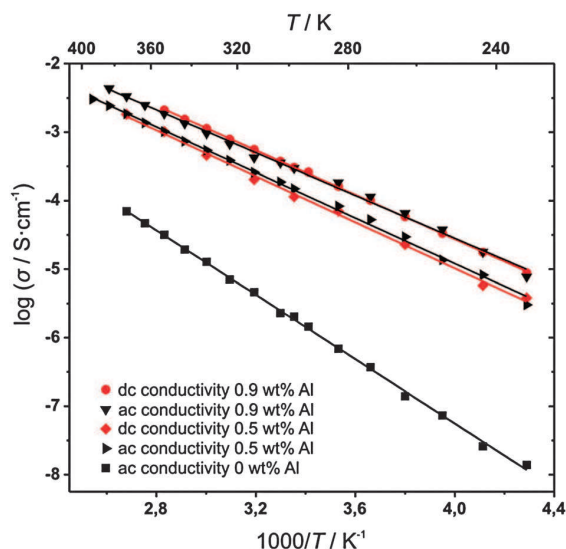


Fig. 11 Temperature dependence of the conductivity of LLZO samples with different Al contents. Al-containing samples have been studied by two electrode ac (impedance) as well as four electrode dc techniques. Note, for the sake of readability $\log \sigma$ vs. $1000/T$ is shown. The activation energies given in the text were calculated from the slope of $\ln(\sigma T)$ vs. $1000/T$ remembering that $\ln(\sigma T) = \ln \sigma_0 - E_a/RT$.

investigated by NMR spectroscopy.²¹ The electronic conductivity of cubic LLZO, which controls the self-discharge of a lithium battery and therefore is of great interest, was measured with a Hebb–Wagner type cell arrangement with one reversible and one blocking electrode (Fig. 1c). In optimal cases Hebb–Wagner measurements can be used to determine the individual electron hole and electron partial conductivities as a function of the Fermi level (*i.e.* as a function of the lithium metal content in the present case).

When the cell is polarized, as can be seen in Fig. 1c, a high mixed ionic and electronic transient current is rapidly decreasing and finally reaching a steady state electronic current. The steady state current under ion-blocking conditions can only be due to electron and hole conduction in the material as no Li ions can be delivered from the blocking gold electrode. Prior to the polarization experiments the open circuit voltage of the cell shown in Fig. 1c was approximately 2 V which is probably due to formation of a lithium gold alloy at the LLZO Au interface³⁴ prior to the measurement. Lithium activity gradients in the sample may also be a reason as well as capacitive effects of the high resistance cell. (Note that the low electronic conductivity leads to an electronic resistance in the order of $10^{10} \Omega$). Fig. 12 shows the potential dependent mean conductivities measured in the range of typical battery operating voltage. As described in detail in the literature on the Wagner–Hebb technique, the increasing voltage leads to a corresponding decrease of the chemical potential of Li at the Au electrode. This changes the electron and hole concentrations in LLZO. Therefore, the overall electronic partial conductivity increases with increasing polarization voltages. Over the potential range of 2.5 V–4.5 V the electronic conductivity takes values in the range from

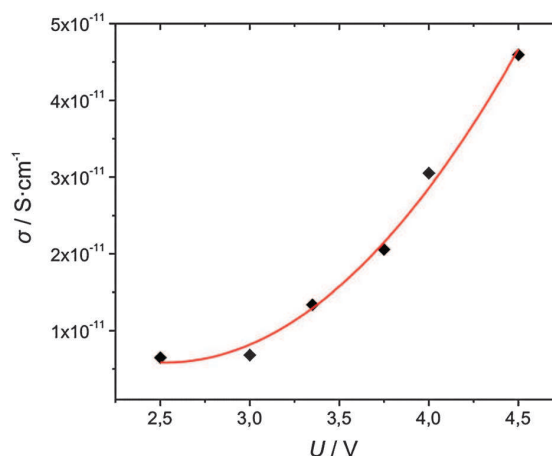


Fig. 12 Partial electronic conductivity of a cubic LLZO pellet vs. Hebb–Wagner cell voltage at room temperature. The solid line is only a guide to the eye.

$5 \times 10^{-12} \text{ Scm}^{-1}$ to $5 \times 10^{-11} \text{ Scm}^{-1}$. With the total conductivity of $3 \times 10^{-4} \text{ Scm}^{-1}$ the electronic and ionic transference numbers

$$t_{e^-} = \frac{\sigma_{e^-}}{\sigma_{\text{total}}} \quad \text{and} \quad t_{\text{Li}^+} = \frac{\sigma_{\text{Li}^+}}{\sigma_{\text{total}}} \quad (1)$$

result in values between 2×10^{-8} – 2×10^{-7} and 0.99999998–0.99999998, respectively. This clearly shows that cubic Al-doped LLZO is an almost exclusive Li ion conducting material having great potential as an electrolyte for lithium-ion batteries. We note that the increase of the electronic conductivity with increasing potential is due to growing hole conduction.

Solid-state NMR measurements

In addition to impedance spectroscopy we used various NMR techniques to probe Li dynamics in a sintered sample of garnet-like LLZO crystallizing with cubic symmetry. In Fig. 13 the central transitions (see below) of a typical set of ^7Li NMR spectra of cubic LLZO doped with 0.9 wt% Al are shown. The corresponding ^{27}Al MAS NMR spectrum is shown in Fig. 3b. The ^7Li NMR spectra were recorded at various temperatures at a resonance frequency of 155.5 MHz. The broad NMR line, which is observed at the very low temperatures, can be well represented by a Gaussian reflecting the distribution of resonance frequencies due to non-averaged dipole–dipole interactions of the Li nuclei. Here, the associated line width δ (full width at half maximum) of this so-called rigid lattice regime is given by $\delta_{\text{rl}} = 9.7(2) \text{ kHz}$. In this temperature range the mean Li jump rate $1/\tau$ is much smaller than the spectral width δ_{rl} , *i.e.*, $1/\tau \ll 10^3 \text{ s}^{-1}$. With rising temperature $1/\tau$ increases resulting in an averaging of homonuclear dipolar interactions. Consequently, the NMR line increasingly narrows, finally reaching the width δ_{en} which is solely governed by inhomogeneities of the external magnetic field used (regime of extreme narrowing). Interestingly, in the case of cubic LLZO doped with Al a heterogeneous motional narrowing (MN) is observed. At intermediate temperatures

the NMR line partially narrows resulting in a two-component line shape, *i.e.*, the broad rigid-lattice line (see above) is superimposed by a motionally narrowed Lorentzian-shaped component.³⁵ Recently, the same behaviour has been observed by Koch *et al.* who studied the Li dynamics in the garnet $\text{Li}_5\text{La}_3\text{Nb}_2\text{O}_{12}$.³⁶ It is worth mentioning that the spectra shown in Fig. 13 were simply obtained by Fourier transformation of a free induction decay recorded after excitation with a 90° pulse. Thus, quadrupole intensities arising from the interaction of the spin-3/2 probe nucleus with electric field gradients produced by the electric charge distribution in the neighbourhood of the Li nuclei are largely suppressed. These can be made visible by using appropriate echo pulse sequences.^{35,37} Usually, when low temperatures are regarded, such interactions are represented by a broad Gaussian line of low intensity characterized by a width of some tens of kHz.^{21,36} As an example, a stimulated echo NMR spectrum is shown in Fig. 13e which has been recorded using the Jeener–Broekaert echo sequence.³⁸ In the present case, we will exclusively focus on the ^7Li NMR central transition of LLZO. In contrast to other garnet-like oxides, in the case of cubic LLZO two-phase NMR spectra show up at

temperatures as low as 200 K indicating a spin ensemble of rapidly diffusing Li ions (see Fig. 13). As an example, at 220 K the narrow Lorentzian-shaped component shows a line width of approximately 1.9 kHz while the broad one is characterized by $\delta = 8.7$ kHz. The area fraction A_f of the narrow line, which reflects the number fraction of fast Li ions with jump rates larger than about 10^4 s^{-1} , amounts to approximately 19% at this temperature. Values of A_f have been estimated by fitting the spectra with a combination of two Voigt functions. Interestingly, A_f steadily increases with increasing T reaching 28% at 233 K, 35% at 243 K, and 41% at 253 K. At a temperature of 263 K nearly 50% of the total number of Li ions participate in a very fast Li diffusion process. The corresponding line width of the sharp component became smaller than 1 kHz. Thus, with rising temperature the fractional amount of Li ions being highly mobile on the NMR time scale increase in an almost linear fashion (Fig. 13c), a similar behaviour has been found for nanocrystalline LiNbO_3 .³⁸ Let us note that at higher temperatures a separation of the two spin reservoirs with their distinct dynamics turns out to be difficult. This is due to the fact that the broad spectral component, representing rather

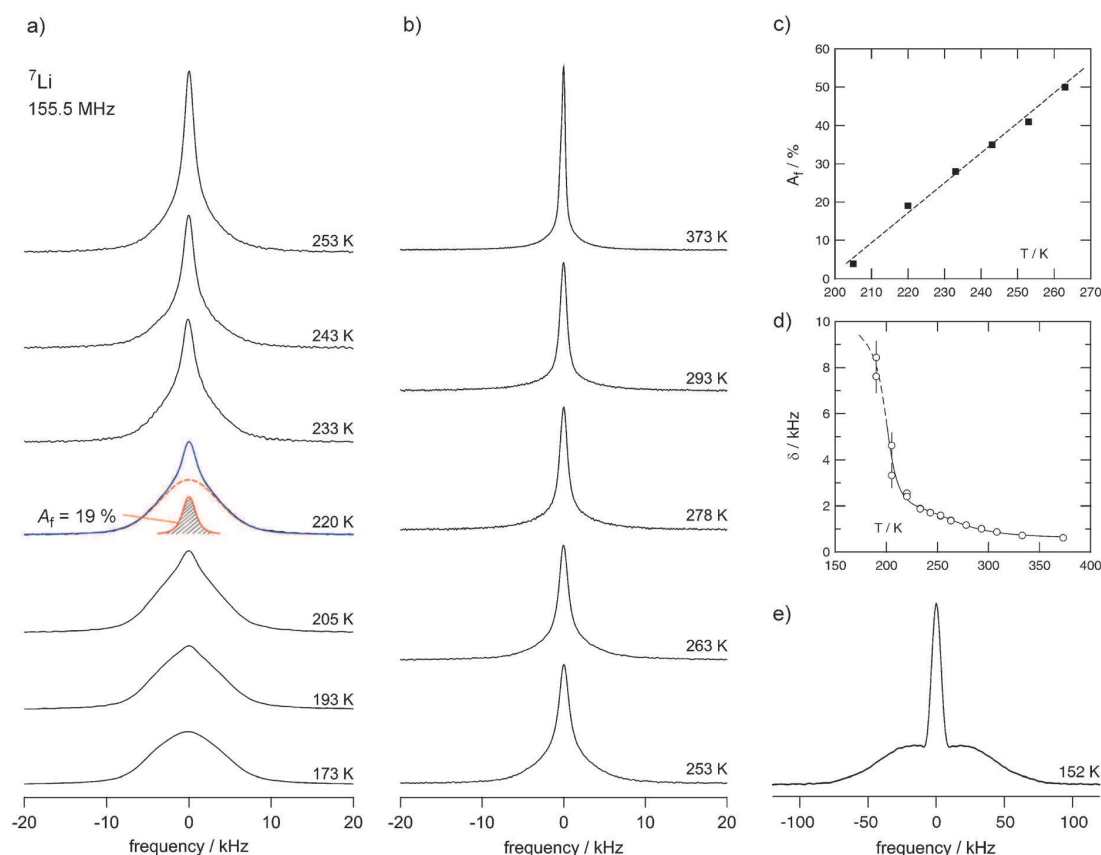


Fig. 13 (a) and (b) ^7Li NMR spectra of a non-rotating sample of cubic LLZO (0.9 wt% Al) recorded at 155.5 MHz in the temperature range from 173 K to 373 K. As an example, the two-component NMR line at 220 K is represented by a superposition of two Voigt functions, that is, a combination of a Gaussian and a Lorentzian. The area fraction $A_f = f(T)$ of the narrow contribution (solid line), representing very fast Li ions in LLZO, amounts to approximately 19%. The dashed line shows the dipolarly broadened component which reflects slow Li ions. See text for further details. (c) Temperature dependence of A_f , (d) NMR line width d of the narrow component highlighted in (a), (e) ^7Li stimulated echo NMR spectrum recorded at 152 K in order to reveal quadrupole intensities next to the Gaussian-shaped central transition.

slow Li ions in LLZO, steadily decreases in intensity. The heterogeneous MN observed at low T might reflect a large distribution of Li jump rates. Such a distribution is expected to be preserved even at temperatures larger than 300 K. Interestingly, even the line width of the sharp component reveals a stepwise narrowing reflecting a transition from partial to full averaging of dipolar interactions. Starting from 2 kHz at 263 K the line width is further decreased with increasing T finally reaching 800 Hz in the regime of extreme narrowing (see Fig. 13d). This is very similar to the behaviour observed by ^7Li NMR spin-spin-relaxation measurements discussed below (see Fig. 14).

In addition to NMR line shapes, ^7Li NMR spin-lattice relaxation (SLR) rates have been recorded in both, the laboratory and rotating frames of reference, see ref. 21, 37, and 39 for an introduction into these NMR techniques. It is worth mentioning that the two components of the NMR line are characterized by the same ^7Li SLR NMR rates R_1 and $R_{1\rho}$. Thus, a separation of the two, dynamically different spin reservoirs according to that shown previously for the nanocrystalline two-phase Li conductor $\text{Li}_2\text{O}:\text{Al}_2\text{O}_3$,^{35,40} is not possible. In contrast to the present work, in the previous study two spin ensembles, which seem to be unaffected by spin-diffusion effects, were anticipated to be also spatially separated.²⁹ The temperature dependence of the rates of the sintered sample of cubic LLZO, which have been recorded at different frequencies, are shown in Fig. 14 in an Arrhenius plot. Below 180 K, *i.e.*, in the rigid-lattice regime (see above), the rates are governed by non-diffusive background relaxation and reveal a weaker-than-activated temperature dependence. Presumably, the SLR NMR rates in this temperature range are influenced by lattice vibrations, interactions between the spins and paramagnetic impurities and/or by strictly localized, *i.e.*, caged ion dynamics which do not reflect translational jump processes. However, at higher temperatures the SLR

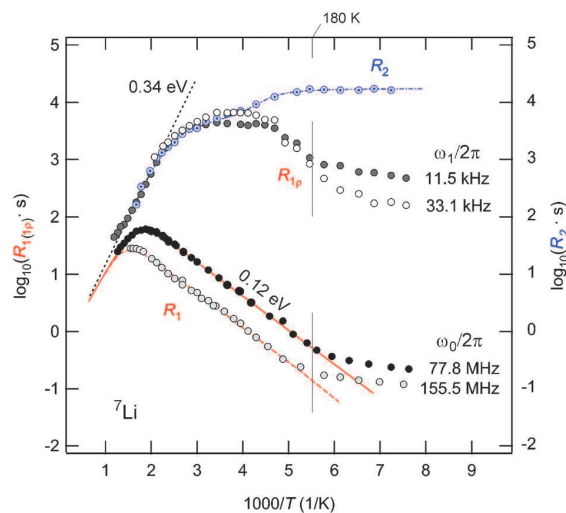


Fig. 14 Temperature dependence of the ^7Li NMR spin-spin (R_2) as well as spin-lattice relaxation rates (R_1 and $R_{1\rho}$) of cubic LLZO. The NMR spin-lattice relaxation rates were measured at the frequencies indicated. Spin-spin relaxation rates were recorded at a resonance frequency of 77.8 MHz. See text for further details.

NMR rates pass through characteristic diffusion-induced rate peaks from which Li jump rates $1/\tau$ and activation energies $E_{a,\text{NMR}}$ can be deduced. Interestingly, the rates recorded at 77.8 MHz reveal an asymmetric diffusion-induced peak $R_1(1/T)$. In general, the low-temperature flank, for which $\omega_0\tau \gg 1$ holds, is influenced by short-range Li motions which might be affected by correlation effects (see below).^{21,37,39,40} Compared with this, on the high-temperature side of the rate peak, *i.e.*, in the limit $\omega_0\tau \ll 1$, the SLR rate is governed by long-range Li transport.^{21,37,39,40}

The mean diffusion parameters characterizing the latter are directly comparable with the results obtained from dc conductivity measurements (see above). The solid line in Fig. 14 represents a fit according to the model introduced by Bloembergen, Purcell and Pound⁴¹ which was originally developed for isotropic uncorrelated diffusion: $R_1 \propto \tau/[1 + (\omega_0\tau)^\beta]$. Here, the asymmetry of the rate peak is taken into account by the parameter β , which can adopt values ranging from 1 to 2. $\beta = 2$, the so-called BPP-behaviour, is obtained for uncorrelated motion. $\beta < 2$ indicates that the underlying hopping correlation function $G(t)$ is represented by a non-exponential rather than an exponential function. Correlation effects such as structural disorder and/or Coulomb interactions are considered to be responsible for the deviation from exponential time behaviour of $G(t)$. In the present case, β amounts to about 1.4; the activation energy $E_{a,\text{NMR}}$ turns out to be approximately 0.31 eV. This value is in good agreement with that probed by impedance spectroscopy (see above). For comparison with $E_{a,\text{NMR}}$, the corresponding activation energy in the limit $\omega_0\tau \gg 1$ turns out to be about $E'_{a,\text{NMR}} = 0.12$ eV. In general, $E'_{a,\text{NMR}}$ and $E_{a,\text{NMR}}$ are linked with each other *via* $E'_{a,\text{NMR}} = (\beta - 1) E_{a,\text{NMR}}$.³⁷ In addition, β determines the frequency dependence of R_1 in the limit $\omega_0\tau \gg 1$ according to $R_1 \propto \omega_0^{-\beta}$. No frequency dependence is expected in the limit $\omega_0\tau \ll 1$ when 3D diffusion is regarded.³⁷ This is in contrast to ion conductors showing low-dimensional Li diffusion.^{37,42–44}

Owing to technical limitations of our NMR setup, temperatures higher than 800 K could not be reached. Thus, the high-temperature flank of the R_1 rate peak recorded at 77.8 MHz was only partly accessible. However, with the help of SLR NMR measurements performed in the rotating frame of reference and carried out at locking frequencies $\omega_1/2\pi$ in the kHz the complete high-temperature flank of the corresponding diffusion-induced rate peak can be probed. The dotted line in Fig. 14 represents an Arrhenius fit of some of the data points of the high- T flank of the $R_{1\rho}$ data recorded at $\omega_1/2\pi = 11.5$ kHz. The fit yields an activation energy of approximately 0.34 eV and is in good agreement with the trend of the ^7Li NMR spin-spin relaxation rates R_2 which are also included in Fig. 13. The $R_{1\rho}$ measurements are limited by R_2 leading to an apparently broad rate peak whose top is cut off. Nevertheless the temperature at which the rate maximum appears can be estimated to be approximately 300 K. In general, the diffusion-induced SLR rate maximum shows up when the Li correlation rate $1/\tau'$ reaches the order of the angular frequencies ω_0 and ω_1 , respectively.³⁷ $1/\tau'$ is expected to be identical with the mean jump rate $1/\tau$ within a factor of two. In Fig. 15 the Li

jump rates $1/\tau_{\text{NMR}}$ directly deduced from the rate maxima according to $\omega_0\tau_{\text{NMR}} = 1$ and $\omega_1\tau_{\text{NMR}} = 0.5$, see ref. 39, respectively, are shown in an Arrhenius plot. The additional vertical axis in Fig. 15 converts the rates $1/\tau_{\text{NMR}}$ into self-diffusion coefficients according to the Einstein–Smoluchowski equation: $D_{\text{NMR}} = a_j^2/(6\tau_{\text{NMR}})$. The mean jump distance a_j was estimated to be approximately 0.2 nm. In analogy to previous studies^{21,45,46} comparing results obtained from NMR with those from impedance spectroscopy, dc conductivity values σ_{DC} (Fig. 11) have been roughly converted into Li jump rates using both the Nernst–Einstein and Einstein–Smoluchowski equations. As is well-known, the combination of the two relations yields

$$\tau_{\sigma}^{-1} = H_{\text{R}}f_{\text{c}} \frac{6k_{\text{B}}T}{Nq^2a_j^2} \sigma_{\text{DC}} \quad (2)$$

where N denotes the number density of charge carriers and q the charge of the Li ions. The product of Haven ratio H_{R} and correlation factor f_{c} was assumed to be 1. Additionally, in Fig. 15 electrical relaxation rates $1/\tau_{\text{M}}$ are included which were obtained from the imaginary part of the electrical modulus M'' which has been analyzed as a function of frequency ν . Modulus spectra $M''(\nu)$ were recorded at various temperatures T (not shown here for the sake of brevity). The characteristic maxima show up when $1/\tau_{\text{M}}$ is of the order of the angular frequency $\nu 2\pi$. The solid line in Fig. 15 represents a fit taking into account $1/\tau_{\text{M}}$ and $1/\tau_{\sigma}$ yielding 0.34 eV (see above).

The jump rates $1/\tau_{\text{NMR}}$ obtained from NMR R_1 measurements are in fair agreement with the conductivity results. The agreement between $1/\tau_{\sigma}$ and $1/\tau_{\text{NMR}}$ probed via $R_{1\rho}$ turns out to be somewhat better which might be due to the fact that the two methods probe Li dynamics on a very similar time scale. For the sake of completeness, a Li jump rate is included in Fig. 15 which has been estimated from NMR line narrowing (Fig. 8). Slightly above 200 K the narrow

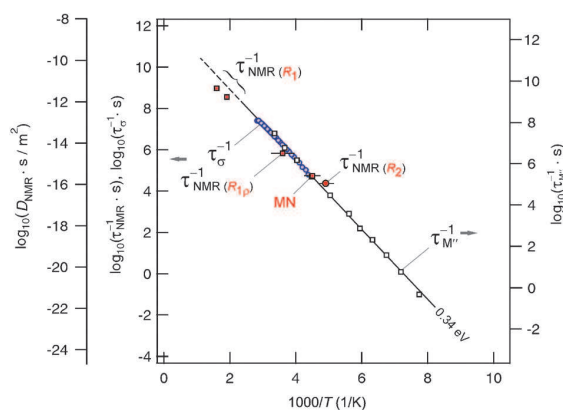


Fig. 15 Temperature dependence of the Li jump rates of cubic LLZO (0.9 wt% Al) obtained from NMR $1/\tau_{\text{NMR}}$ and impedance spectroscopy $1/\tau_{\sigma}$. For comparison, electrical relaxation rates $1/\tau_{\text{M}}$ deduced from the peaks of various modulus spectra $M''(\nu)$ are also included. The solid line shows an Arrhenius fit yielding 0.34 eV. The jump rate marked with MN denotes a value deduced from NMR line narrowing. See text for further details.

component shows up. At 225 K the corresponding line width is reduced to $\delta_{\text{rl}}/2$ and the associated jump rate is given by $1/\tau_{\text{NMR}} = \delta_{\text{rl}}2\pi$. For comparison, at 205 K the rates R_2 start to deviate from their rigid-lattice value $R_{20} = 60 \mu\text{s}$ leading to $1/\tau_{\text{NMR}} \approx R_{20}$ at this temperature. This jump rate is also included in Fig. 15. Taken together, the jump rates probed by NMR spectroscopy corroborate the transport parameters of a sintered sample of cubic LLZO obtained from impedance spectroscopy. In agreement with line widths measurements (Fig. 13d), R_2 shows a two-step decrease with increasing temperature indicating that the Li ions get access to further diffusion pathways at elevated temperatures.

Conclusions

We have synthesized the two different structural modifications of LLZO and found a certain Al content to be necessary for the formation of cubic LLZO. One already could speculate from the patent by Yoshida⁴⁷ that Al is a necessary ingredient for the formation of cubic LLZO. As in the present work, the recently published papers^{10–13} state that cubic LLZO only forms when Al is present during synthesis but there was no definite knowledge about the role of Al. With the combination of XRD, TEM-PED and neutron scattering we are able to propose a structure model which takes both Al and Li ions into account. Neutron diffraction measurements show a high degree of Li disorder even at 4 K which becomes even more pronounced at 300 K. We regard this disorder as the reason for the high mobility of the Li ions in the cubic garnet-type lattice. As proved by ²⁷Al MAS NMR spectroscopy most of the Al ions are located on the 24d site. With the results of phase transformation during synthesis we regard the Al ions on the 24d site to stabilize the cubic garnet structure.

NMR was found to be a very sensitive probe for small structural changes in the garnet-type lattice. NMR shows that minor changes of the Al distribution during the sintering process cause the Li disorder to become even more pronounced than in the powder before sintering. The TEM-PED patterns agree very well with our proposed structure model and the corresponding pattern simulation; other structure models fit less well. The simulated structure image also fits well with the HRTEM image, confirming our cubic structure model.

Electrochemical measurements performed with different LLZO samples confirm that the conductivity depends on the Al content, *i.e.*, the degree of transformation from the tetragonal to the cubic crystal structure. Ac and dc conductivities show almost identical values approving the high conductivity also under current load. Li jump rates deduced from NMR spin-lattice relaxation measurements agree well with those calculated from electrical conductivity data. Moreover, the activation energies determined by both techniques agree very well. The electronic conductivity and the corresponding electronic transference number are very small, and LLZO was found to be stable against reaction with Li metal over the measured period of several days. Therefore, we suppose that Al-stabilized cubic LLZO is a suitable Li solid electrolyte. Tests of the compatibility of LLZO with various cathode materials and measurements of the overvoltages occurring

in contact with these as well as Li metal under current load are in progress and will help further clarify the applicability of cubic LLZO as a solid state electrolyte for Li ion batteries.

Acknowledgements

We acknowledge financial support by the German Research Foundation (DFG) within the project “High performance lithium batteries” (DFG JA 648/15-1 and 15-2). We also acknowledge helpful discussion within the BASF research network for Batteries and Electrochemistry. Furthermore financial support by the Federal Ministry of Education and Research (BMBF) within the projects “Competence in Electrochemistry for Electromobility” and “Lithium Ion Batteries LIB 2015” both for the Gießen and the Hannover teams is gratefully acknowledged.

The authors benefitted from discussions with Alan Logéat, Thomas Köhler and Ulrich Eisele from Robert Bosch GmbH and thank Christoph Essig for the ICP-OES analysis of the garnet samples.

Notes and references

- 1 K. Xu, *Chem. Rev.*, 2004, **104**, 4303–4417.
- 2 D. Aurbach, *J. Power Sources*, 2000, **89**, 206–218.
- 3 D. Aurbach, B. Markovsky, G. Salitra, E. Markevich, Y. Talyossef, M. Koltypin, L. Nazar, B. Ellis and D. Kovacheva, *J. Power Sources*, 2007, **165**, 491–499.
- 4 J. Vetter, P. Novak, M. R. Wagner, C. Veit, K. C. Moller, J. O. Besenhard, M. Winter, M. Wohlfahrt-Mehrens, C. Vogler and A. Hammouche, *J. Power Sources*, 2005, **147**, 269–281.
- 5 V. Thangadurai, H. Kaack and W. J. F. Weppner, *J. Am. Ceram. Soc.*, 2003, **86**, 437–440.
- 6 R. Murugan, V. Thangadurai and W. Weppner, *Angew. Chem., Int. Ed.*, 2007, **46**, 7778–7781.
- 7 J. Awaka, N. Kijima, H. Hayakawa and J. Akimoto, *J. Solid State Chem.*, 2009, **182**, 2046–2052.
- 8 J. Awaka, A. Takashima, K. Kataoka, N. Kijima, Y. Idemoto and J. Akimoto, *Chem. Lett.*, 2011, 60–62.
- 9 K. H. Kim, Y. Iriyama, K. Yamamoto, S. Kumazaki, T. Asaka, K. Tanabe, C. A. J. Fisher, T. Hirayama, R. Murugan and Z. Ogumi, *J. Power Sources*, 2011, **196**, 764–767.
- 10 C. A. Geiger, E. Alekseev, B. Lasic, M. Fisch, T. Armbruster, R. Langner, M. Fechtelkord, N. Kim, T. Pettke and W. Weppner, *Inorg. Chem.*, 2011, **50**, 1089–1097.
- 11 S. Kumazaki, Y. Iriyama, K.-H. Kim, R. Murugan, K. Tanabe, K. Yamamoto, T. Hirayama and Z. Ogumi, *Electrochem. Commun.*, 2011, **13**, 509–512.
- 12 Y. Jin and P. J. McGinn, *J. Power Sources*, 2011, DOI: 10.1016/j.jpowsour.2011.05.065.
- 13 M. Kotobuki, K. Kanamura, Y. Sato and T. Yoshida, *J. Power Sources*, 2011, **196**, 7750–7754.
- 14 M. Hoelzel, A. Senyshyn, R. Gilles, H. Boysen and H. Fuess, *Neutron News*, 2008, **18**.
- 15 J. Rodriguez-Carvajal, *Commission on Powder Diffraction Newsletter*, 2001, **26**, 12–19.
- 16 F. Izumi and R. A. Dilanian, *Recent Research Developments in Physics*, Transworld Research Network, 2002.
- 17 P. A. Stadelmann, *Ultramicroscopy*, 1987, **21**, 131–145.
- 18 M. H. Hebb, *J. Chem. Phys.*, 1952, **20**, 185–190.
- 19 C. Wagner, *J. Chem. Phys.*, 1953, **21**, 1819–1827.
- 20 A. Kuhn, A. Düvel and P. Heitjans, 2011, unpublished results.
- 21 A. Kuhn, S. Narayanan, L. Spencer, G. Goward, V. Thangadurai and M. Wilkening, *Phys. Rev. B: Condens. Matter Mater. Phys.*, 2011, **83**, 094302.
- 22 E. J. Cussen, T. W. S. Yip, G. O'Neill and M. P. O'Callaghan, *J. Solid State Chem.*, 2011, **184**, 470–475.
- 23 L. Thieblot, J. Roux and P. Richet, *Eur. J. Mineral.*, 1998, **10**, 7–15.
- 24 A. Grzechnik, H. Kruger, V. Kahlenberg and K. Friese, *J. Phys.: Condens. Matter*, 2006, **18**, 8925–8934.
- 25 K. Momma and F. Izumi, *J. Appl. Crystallogr.*, 2008, **41**, 653–658.
- 26 F. Izumi, *Solid State Ionics*, 2004, **172**, 1–6.
- 27 A. A. Belik, F. Izumi, T. Ikeda, V. A. Morozov, R. A. Dilanian, S. Torii, E. M. Kopnin, O. I. Lebedev, G. Van Tendeloo and B. I. Lazoryak, *Chem. Mater.*, 2002, **14**, 4464–4472.
- 28 K. Oikawa, T. Kamiyama, R. Kanno, F. Izumi, T. Ikeda and B. C. Chakoumakos, *Mater. Sci. Forum*, 2004, **443–444**, 337.
- 29 K. Takada, H. Sakurai, E. Takayama-Muromachi, F. Izumi, R. A. Dilanian and T. Sasaki, *Nature*, 2003, **422**, 53–55.
- 30 M. Yashima, *J. Ceram. Soc. Jpn.*, 2009, **117**, 1055–1059.
- 31 D. Jacob and P. Cordier, *Ultramicroscopy*, 2010, **110**, 1166–1177.
- 32 L. Kienle, V. Duppel, B. Mogwitz, J. Janek, M. v. Kreutzbruck, A. Leineweber and A. Simon, *Cryst. Growth Des.*, 2011, **11**, 2412–2421.
- 33 I. M. Hodge, M. D. Ingram and A. R. West, *J. Electroanal. Chem.*, 1976, **74**, 125–143.
- 34 A. D. Pelton, *Bull. Alloy Phase Diagrams*, 1986, **7**, 228–231.
- 35 M. Wilkening, S. Indris and P. Heitjans, *Phys. Chem. Chem. Phys.*, 2003, **5**, 2225–2231.
- 36 B. Koch and M. Vogel, *Solid State Nucl. Magn. Reson.*, 2008, **34**, 37–43.
- 37 P. Heitjans and J. Kärger, *Diffusion in Condensed Matter—Methods, Materials, Models*. Springer, Berlin, 2005.
- 38 P. Heitjans, M. Masoud, A. Feldhoff and M. Wilkening, *Faraday Discuss.*, 2007, **134**, 67–82.
- 39 W. Bensch, T. Bredow, H. Ebert, P. Heitjans, S. Indris, S. Mankovsky and M. Wilkening, *Prog. Solid State Chem.*, 2009, **37**, 206–225.
- 40 M. Wilkening and P. Heitjans, *Phys. Rev. B: Condens. Matter Mater. Phys.*, 2008, **77**, 024311.
- 41 N. Bloembergen, E. M. Purcell and R. V. Pound, *Phys. Rev.*, 1948, **73**, 679–712.
- 42 V. Epp and M. Wilkening, *Phys. Rev. B: Condens. Matter Mater. Phys.*, 2010, **82**, 020301.
- 43 W. Küchler, P. Heitjans, A. Payer and R. Schöllhorn, *Solid State Ionics*, 1994, **70**, 434–438.
- 44 A. Kuhn, P. Sreeraj, R. Pöttgen, H. D. Wiemhofer, M. Wilkening and P. Heitjans, *J. Am. Chem. Soc.*, 2011, **133**, 11018.
- 45 M. Wilkening, C. Mühle, M. Jansen and P. Heitjans, *J. Phys. Chem. B*, 2007, **111**, 8691–8694.
- 46 M. Wilkening, A. Kuhn and P. Heitjans, *Phys. Rev. B: Condens. Matter Mater. Phys.*, 2008, **78**, 054303.
- 47 *United States Pat.*, US 2010/0047696 A1, 2010.

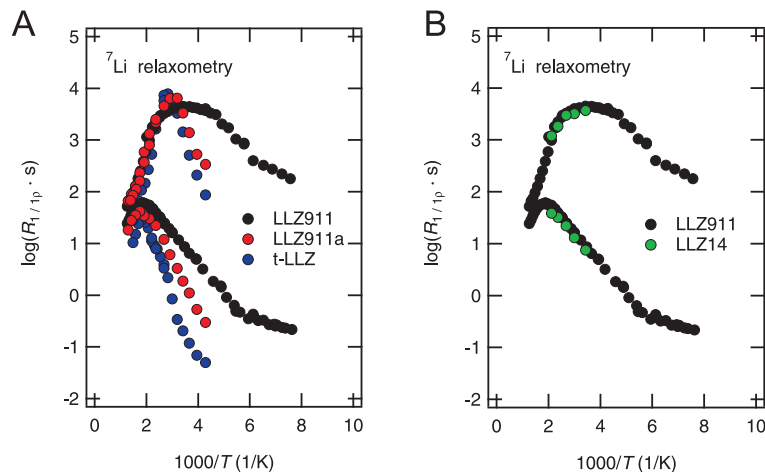


Figure 3.5: Comparison of ${}^7\text{Li}$ NMR relaxometry results (R_1 measured at 77.7 MHz and R_1 measured at approx. 30 kHz) A: LLZ911, LLZ911a and tetragonal LLZ of Ref. [21]. Non-sintered LLZ911a shows a similar Li diffusivity like the tetragonal LLZ. B: LLZ911 and LLZ14 show nearly identical behavior.

3.4 Recent results on cubic LLZ

3.4.1 Samples

Altogether, three samples provided by H. Buschmann were studied. The sample LLZ911 has been thoroughly studied in the above-shown paper with ${}^7\text{Li}$ NMR relaxometry. This sample was obtained by sintering a pellet of the powder LLZ911a which showed a lower diffusivity comparable to that of the tetragonal modification although from XRD it was not distinguishable from LLZ911. The sample LLZ911a is also mentioned in Ref. [19] (see also pages 84-98), where the ${}^{27}\text{Al}$ spectrum of LLZ911a is shown (page 88). The NMR relaxometry results of LLZ911, LLZ911a are shown in Fig. 3.5A together with the NMR relaxometry results from the tetragonal LLZ (Ref. [21] and pages 50-60). Obviously, the cubic LLZ911a is characterized by a similar diffusivity like the tetragonal LLZ.

The third sample studied was LLZ14. This sample was prepared in the same way as LLZ911 but originates from another batch. This sample was studied thoroughly by means of ${}^6\text{Li}$ NMR relaxometry, ${}^7\text{Li}$ SFG NMR, and impedance spectroscopy. A complete ${}^7\text{Li}$ NMR relaxometry study was omitted since it showed the same behavior as LLZ911 in test measurements (shown in Fig. 3.5B). Therefore, I assume that the ${}^7\text{Li}$ NMR relaxometry results of LLZ911 can be compared with the ${}^6\text{Li}$ NMR relaxometry results of LLZ14 - at least in the temperature range above room temperature.

3.4.2 Impedance spectroscopy on LLZ14

Impedance spectroscopy measurements were performed on two pellets of sintered LLZ14. One pellet had a thickness of 3 mm, the other one of 0.6 mm. The crystallite diameter in the sintered LLZ14 was typically around 1-2 mm. The crystallites showed slightly different colors ranging from transparent colorless to slightly yellowish opaque ones. For the thin pellet, mostly one-grain pro-

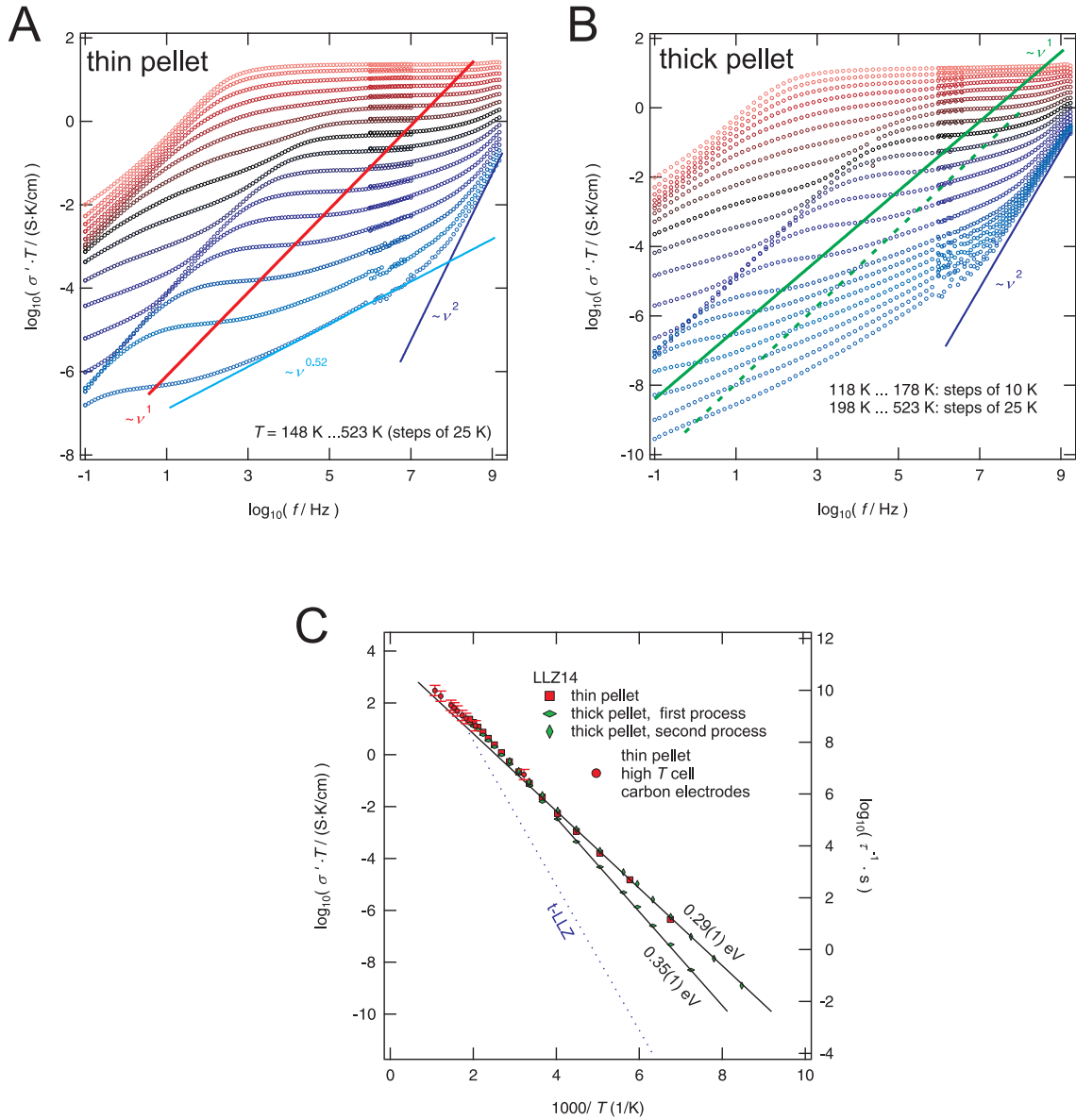


Figure 3.6: A: log-log plot of conductivity isotherms of the thin LLZ14 sample. The Jonscher power exponent amounts to approx. $n = 0.5$. At high frequencies, a transition to a ν^2 -frequency dependence is observed. B: log-log plot of conductivity isotherms of the thick LLZ14 sample. C: Arrhenius plot of the conductivities read out from the respective plateaus. Red squares: thin pellet, bulk plateau (from red line in graph A), green diamonds: thick pellet, long-range plateau (from green line in graph B) and short-range plateau (from green dashed line in graph B), red points: high-temperature conductivities of the thin pellet obtained with a different experimental setup, see text for details. The right axis represents jump rates calculated under the assumption of a jump length of $a = 3 \text{ \AA}$ and $H_R = f = 1$. The dashed blue line represents the conductivity of tetragonal LLZ. [20, 21]

cesses play a role. The situation is different for the thick sample where Li ions have to surpass at least 2-3 crystallites and the respective grain boundaries to give rise to a true dc conductivity.

For the measurements, Au electrodes were evaporated on the surfaces of the samples. The measurements were performed with a Novocontrol impedance spectrometer. For the usual impedance frequency range from (0.1 Hz . . . 10 MHz), a BDMS1200 cell and a Alpha AN Analyzer (Novocontrol) were used. For frequencies from 1 MHz to 3 GHz, a RF analyzer (Agilent 4991) and a RF extension line (Agilent) were used. In both cases, the measurements were performed under a flow of heated nitrogen. The temperature was controlled by a QUATRO cryosystem. Additionally, for the thin pellet, high-temperature measurements were performed using a HP 4192A Impedance analyzer, a Loba oven, and an Eurotherm 818 Temperature Controller with a home-built impedance cell under a constant flow of nitrogen. At high temperatures, evaporated Au electrodes did not adhere to the sample. Therefore, as an alternative, carbon electrodes (carbon paste) were used. This slightly changed the shape of the conductivity spectra for frequencies lower than the bulk plateau but had no effect on the bulk conductivity.

Fig. 3.6A and B show the conductivity isotherms of the LLZ14 samples (A: thin, B: thick) in a log-log plot (Au electrodes, Novocontrol spectrometer; see above). At low frequencies, in both cases, a plateau is observed which one might assign to a grain-boundary process. However, true dc conductivity measurements using Li electrodes on the same sample yielded conductivities related to the bulk process marked by the lines. [19] Therefore, the first plateau already represents an electrode-related process. This is discussed in detail below but first, I will concentrate on the bulk response.

At high frequencies and low temperatures, in both cases, the conductivity appears to be proportional to the square of the frequency $\sigma' \propto \nu^2$. This is typical of any localized process occurring on a much faster time scale. Here, (if the observed behavior is not an artifact), it probably represents the low-frequency flank of vibrational conductivity. Interestingly, LLZ14 does show Jonscher behavior but no NCL behavior. There is a direct transition from a strongly sub-linear power law ($n \approx 0.5$) characterizing correlated hopping dynamics to the ν^2 -dependence.

But let us focus on the bulk hopping processes, first: For the thin pellet (Fig. 3.6A), reading out the bulk plateau leads to the red squares shown in Fig. 3.6C (and to the red circles for the high-temperature measurements). Hereby, the left axis shows the conductivities, and the right axis shows the jump rates calculated via the Nernst-Einstein relation and Einstein-Smoluchowski relation: $\tau^{-1} = \frac{6\sigma_0 k_B T}{Nq^2 a^2}$ ($a = 3 \text{ \AA}$, $H_R = 1$, $f = 1$). At low temperatures, the conductivity is characterized by an activation energy of 0.29(1) eV. At higher temperatures, there is a slight threshold but the activation energy at high T , is again roughly 0.30 eV. The threshold can be explained as follows: at low T , some grains do not surpass the pellet but there are blocking grain boundaries. These regions of the sample do not contribute significantly to the dc conductivity at low T and therefore can be considered "dead" volume. As the blocking effect diminishes at high T , these regions also contribute to the overall dc conductivity.

In Fig. 3.6B, for the thick pellet, two bulk-related plateaus are visible. Reading out the two plateaus leads to two Arrhenius-activated processes marked by the green diamonds. The process connected to the first plateau is activated with 0.35(1) eV while the second process appears to be identical to the one found in the thin pellet. Thus, this process probably represents intragrain conductivity while the one activated with 0.35 eV marks the intergranular (=grain boundary) re-

sistance. In the thin sample, the bulk processes and the grain boundary processes are parallel. In thick sample, however, the processes are in series, and therefore, the slowest process dominates the true dc conductivity. At high frequencies (representing a shorter time-scale and a shorter length scale), the intragrain properties are visible again as the second slight plateau. For comparison, the dashed blue line represents the data for the (tetragonal) LLZ sample provided by V. Thangadurai. [20,21]

3.4.3 ${}^6\text{Li}$, ${}^7\text{Li}$ NMR relaxometry and ${}^7\text{Li}$ SFG NMR on LLZ14/LLZ911

Fig. 3.7A and B shows the ${}^6\text{Li}$ NMR relaxometry results of the LLZ14 sample and LLZ911 sample, respectively. From Fig. 3.5B, it was assumed that LLZ14 shows the same behavior as LLZ911 and the whole time-consuming ${}^7\text{Li}$ relaxometry study was omitted. From hereon, we will treat the data as if they resulted from LLZ14. The blue lines in the graph represent a global fit according to Eqns. 2.173¹ with the parameters determining long-range Li hopping dynamics $E_A = 0.30(1)$ eV and $\tau_0^{-1} = 1.7(5) \cdot 10^{11} \text{ s}^{-1}$. The Jonscher exponent was $n = 0.52$ for ${}^6\text{Li}$ and $n = 0.56$ for ${}^7\text{Li}$, in good accordance with the value found in the conductivity spectra.

Clearly, the rotating-frame SLR rates and the SSR rates show significant deviations from the fit at temperatures above the maximum pointing to the presence of a second jump process present. Looking at Fig. 3.5B gives an idea what that process might be: higher-activated jump processes as those that occur in tetragonal LLZ or cubic Al-doped LLZ with low Al concentration. Obviously, in LLZ14, these jump processes don't give rise to long-range conduction paths but they still occur as localized jump processes in the structurally disordered Al-doped LLZ.

It has to be noted that the appearance of the rates point to well-separated spin reservoirs. The rates shown here, were all determined from the magnetization transients using stretched-exponential regression. Especially for the ${}^7\text{Li}$ rotating-frame SLR rates for $T < T_{\text{max}}$, the stretching exponents were as low as 0.5-0.6 which is not expected in that temperature range from theory for a single process. Probably, a double-exponential regression would have been more suitable, here.²

Fig. 3.7C shows the ${}^6\text{Li}$ and ${}^7\text{Li}$ relaxometry global fit together with the jump rates obtained from dc conductivity already shown in Fig. 3.6C. The latter ones have been calculated from the conductivity under the assumption of $a = 3 \text{ \AA}$ and $H_R = f = 1$. Clearly, the short-range nuclear method NMR relaxometry and the long-range non-nuclear method dc conductivity probe the same bulk Li ion hopping process.

Fig. 3.7D shows the ${}^7\text{Li}$ SFG NMR measurements ($B = 9.4 \text{ T}$, $g = 69 \text{ T/m}$, quadrupolar echo pulse sequence). ${}^7\text{Li}$ SFG NMR allows the determination of Li tracer diffusion coefficients from the diffusion-related echo decay. The procedure of the measurement and the analysis is described above for the tetragonal LLZ and will not be reiterated here. The diffusion coefficients obtained from the regressions are given in the graph. These were transformed into jump rates assuming a jump distance of $a = 3 \text{ \AA}$ and a correlation factor of $f = 1$ and included into Fig. 3.7C. The

¹Fitting procedure: 1) from the low-temperature flanks of the ${}^6\text{Li}$ relaxometry data, the local field was determined. 2) With this information, the effective fields for ${}^6\text{Li}$ and ${}^7\text{Li}$ were determined. 3) With these parameters, the global fit with only diffusion-relevant parameters was performed.

²Therefore, new experiments with delay-times covering several orders of magnitude would be required to ensure reasonable fitting of both processes.

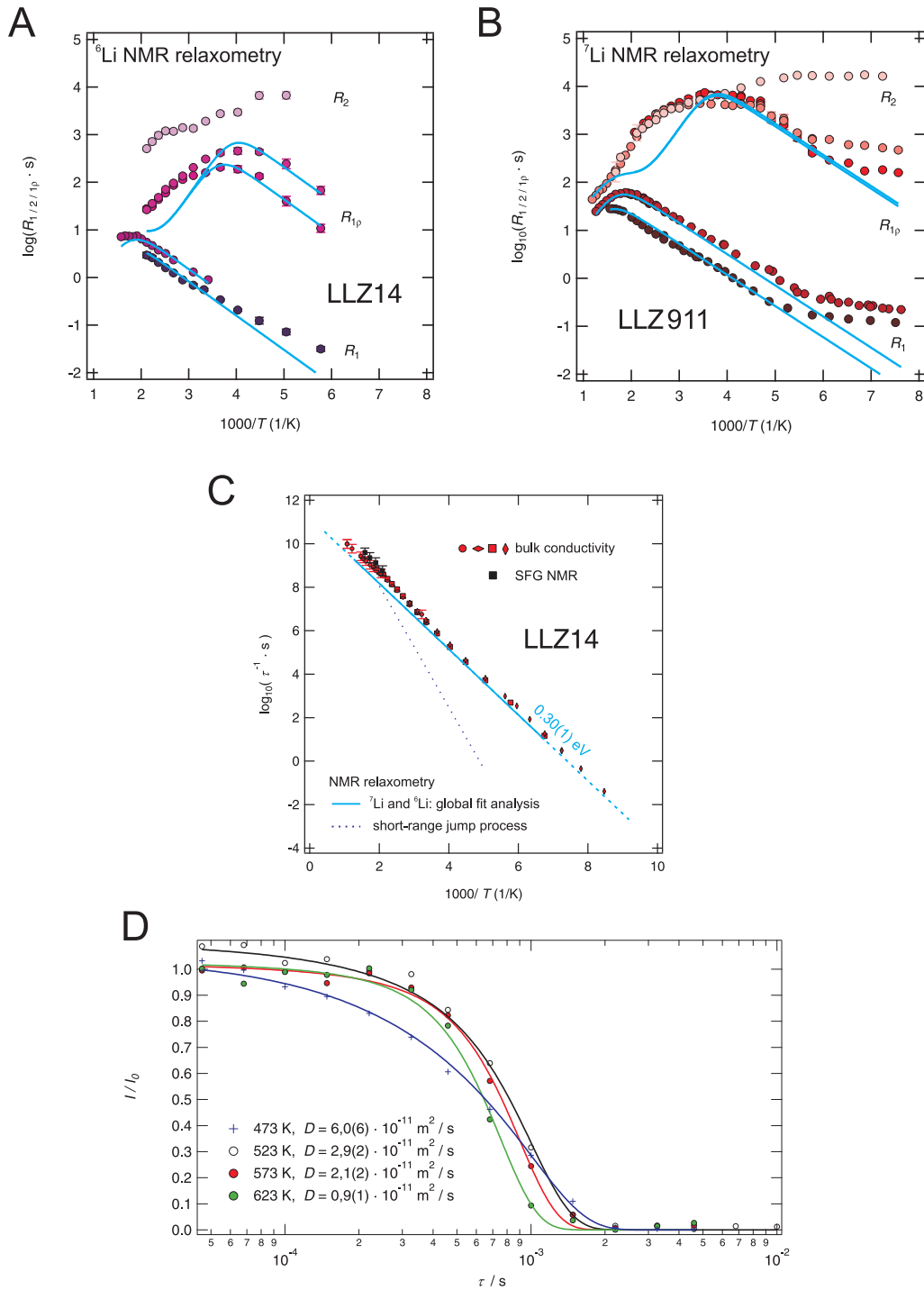


Figure 3.7: A: ${}^6\text{Li}$ NMR relaxometry results of the LLZ14 sample (ω_0 : 59 MHz and 88 MHz, $\omega_1 = 6.6 \text{ kHz}$ and 88.4 kHz). B: ${}^6\text{Li}$ NMR relaxometry results of the LLZ911 sample as already published in Ref. [19] (LLZ14 shows the same results at least in the diffusion-induced regime, *cf.* Fig. 3.5B). In graph A and B, the blue lines represent a global fit with $E_A = 0.30(1) \text{ eV}$, $\tau_0^{-1} = 1.7(5) \cdot 10^{11} \text{ s}^{-1}$. For ${}^6\text{Li}$ the Jonscher exponent amounts to $n = 0.52$, for ${}^7\text{Li}$ a better fit is obtained with $n = 0.56$. C: Arrhenius plot of the bulk process jump rates obtained from conductivity, ${}^6\text{Li}$ and ${}^7\text{Li}$ NMR relaxometry, and ${}^7\text{Li}$ SFG NMR from graph D. D: ${}^7\text{Li}$ SFG NMR echo decays with the respective fits yielding the displayed diffusion coefficients and the jump rates in graph C. For all calculations, $a = 3 \text{ \AA}$ and $H_R = f = 1$ were assumed.

long-range nuclear method ^7Li SFG NMR ultimately clarifies that all techniques are sensitive to the same Li dynamics.

3.4.4 Conclusion

The Li dynamics in the bulk of LLZ14 is traced back to a strongly correlated Li hopping process being characterized by an activation energy of 0.29(1) eV and a preexponential factor τ^{-1} in the order of 10^{11} s^{-1} . The Jonscher exponent which describes the deviation from uncorrelated motion amounts to $n \approx 0.5$. The hopping process was characterized over a dynamic range of 12 orders of magnitude in a temperature range from 118 K to 920 K by long-range non-nuclear methods, long-range nuclear methods, and atomic-scale nuclear methods. The measurements point to a Haven ratio and correlation factor in the order of unity. The hopping barrier over grain boundaries of the sintered pellets of LLZ14 amounts to 0.35(1) eV.

Mechanosynthesis of Solid Electrolytes: Preparation, Characterization, and Li Ion Transport Properties of Garnet-Type Al-Doped $\text{Li}_7\text{La}_3\text{Zr}_2\text{O}_{12}$ Crystallizing with Cubic Symmetry

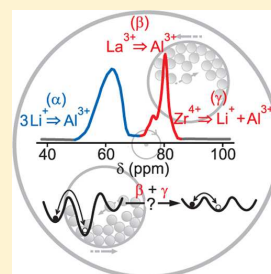
Andre Düvel,^{*,†} Alexander Kuhn,^{*,†,‡} Lars Robben,^{‡,§} Martin Wilkening,^{†,||} and Paul Heitjans[†]

[†]Institute of Physical Chemistry and Electrochemistry, and ZFM – Center for Solid State Chemistry and New Materials, Leibniz University Hannover, Callinstr. 3a, D-30167 Hannover, Germany

[‡]Institute of Mineralogy, Leibniz University Hannover, Callinstr. 3, D-30167 Hannover, Germany

Supporting Information

ABSTRACT: Various polycrystalline samples of Al-doped garnet-like $\text{Li}_7\text{La}_3\text{Zr}_2\text{O}_{12}$ crystallizing with cubic symmetry were synthesized from the binary oxides Li_2O , ZrO_2 , Al_2O_3 , and La_2O_3 . The synthesis of phase pure samples was carried out following a two-step preparation route. It consists of an activation step by high-energy ball milling and a subsequent annealing step at elevated temperatures. The synthesis route chosen allows the precise adjustment of the cationic ratios, leading to a garnet which is best described by the formula $\text{Li}_{7-3x+z}\text{Al}_{x+y+z}\text{La}_{3-y}\text{Zr}_{2-z}\text{O}_{12}$. As confirmed by X-ray powder diffraction and ^{27}Al magic angle spinning nuclear magnetic resonance (NMR), at low Al concentrations the incorporated Al^{3+} ions act as an aliovalent dopant by replacing three Li^+ ions. However, with increasing Al content, La^{3+} and Zr^{4+} ions are progressively replaced by Al ions. It turned out that, in particular, the substitution of La^{3+} and Zr^{4+} with Al^{3+} ions stabilizes the cubic modification of the garnet and greatly affects the corresponding Li ion dynamics. The latter has been probed by both impedance and ^7Li NMR spectroscopy. The high ion conductivity ($10^{-4} \text{ S cm}^{-1}$ at 293 K) found does not only depend on the stoichiometry and the annealing conditions chosen but also on the exact kind of Al distribution on the different sites in $\text{Li}_7\text{La}_3\text{Zr}_2\text{O}_{12}$.



1. INTRODUCTION

Li-containing garnet-type oxides are considered to act as promising fast ion-conducting electrolytes in, e.g., all-solid-state lithium-ion batteries. These are expected to be one of the key technologies to store electrical energy in the next years.^{1–7} Hence, previously a number of studies have been published which are concerned with profound investigations of the structure–property relations of crystalline garnet-type oxides (see, e.g., refs 6 and 8–14). In particular, the garnet with the nominal composition “ $\text{Li}_7\text{La}_3\text{Zr}_2\text{O}_{12}$ ” (LLZ) crystallizing with cubic symmetry attracted large interest. In contrast to the tetragonal counterpart, which is characterized by an ionic bulk conductivity in the order of $10^{-6} \text{ S cm}^{-1}$ (300 K),^{16,22} some of the samples with cubic symmetry investigated so far show an extraordinarily high Li^+ conductivity in the order of $10^{-4} \text{ S cm}^{-1}$ (300 K).^{1,7,14–21} Currently, much work is in progress to identify the origins causing the high lithium ion conductivity.

The results of recently published studies provide strong evidence that Al^{3+} ions, which were unintentionally incorporated into LLZ during the high-temperature synthesis procedure using alumina crucibles, at least stabilize the cubic modification against the tetragonal one.^{14,17,20,23} For comparison, the preparation of Al-free LLZ usually leads to the formation of the tetragonally distorted garnet.^{17,19,23} It is worth noting that Al-free tetragonal LLZ transforms into the cubic modification at elevated temperatures.²³ However, as some of

us showed quite recently, the phase transformation is not accompanied by a significant enhancement of the ionic conductivity.¹⁶ Obviously, merely increasing the symmetry does not lead to the enhancement of the Li^+ conductivity observed for some of the samples studied (see also ref 24). As already discussed by Geiger et al., at low dopant levels the incorporation of Al may influence the number fraction of Li vacancies and, thus, the Li ion conductivity. Further investigations focusing on the role Al plays in influencing the Li ion dynamics parameters might be useful to understand and, in the best case, to improve Li ion transport in LLZ.

Here, we present a systematic study addressing in depth the effects of Al incorporation on both structural and dynamic properties of LLZ. For this purpose we developed a soft synthesis route avoiding high temperatures and enabling the precise adjustment of the contents of all cations in LLZ. Alternatively, sol–gel procedures^{25–28} may certainly be used for similar investigations. However, the necessary temperatures for the latter procedures are still higher than the temperatures needed for the synthesis routine described here.

In the present study, various polycrystalline samples of cubic LLZ with different amounts of Al were prepared from mixtures

Received: February 6, 2012

Revised: June 18, 2012

Published: June 25, 2012

of the binary oxides Li_2O , ZrO_2 , La_2O_3 , and Al_2O_3 by high-energy ball milling^{29–32} and subsequent annealing of the mechanically activated mixtures. While the final composition of the samples can easily be controlled by precisely adjusting the amounts of the starting materials used, a low annealing temperature prevents Li loss usually taking place when LLZ is prepared according to high-temperature ceramic synthesis routes. Sample characterization was carried out by X-ray powder diffraction (XRPD) and ^{27}Al magic angle spinning (MAS) nuclear magnetic resonance (NMR) spectroscopy. In particular, ^{27}Al NMR spectroscopy has been used to roughly correlate the distinct NMR lines of Al-doped LLZ^{17,23} with the doping mechanisms identified. Ion transport properties were probed by variable-temperature ^7Li NMR line shape measurements as well as impedance spectroscopy. The latter take advantage of measurements carried out at frequencies up to the gigahertz range.

II. EXPERIMENTAL DETAILS

A series of polycrystalline samples with the nominal composition $\text{Li}_{7-3x+z}\text{Al}_x\text{La}_3\text{Zr}_{2-y}\text{O}_{12}$ were prepared by high-energy ball milling from the corresponding binary oxides, viz. dry Li_2O (99.5%, Sigma-Aldrich), $\gamma\text{-Al}_2\text{O}_3$ (99.997%, Alfa Aesar), La_2O_3 (99.99%, Fluka), and ZrO_2 (99.99%, Sigma-Aldrich).

For the conventional solid-state synthesis routines reported in the literature an excess of Li is used (*vide supra*). To elucidate the effect of the Li_2O ratio on the structure as well as on the ion dynamics, three series of samples with different Li_2O ratios were prepared. The first one, labeled series A, has the nominal stoichiometry $\text{Li}_{7-3x}\text{Al}_x\text{La}_3\text{Zr}_2\text{O}_{12}$. Series B, which is $\text{Li}_{7-3x}\text{Al}_x\text{La}_3\text{Zr}_2\text{O}_{12} + 0.75x(\text{Li}_2\text{O})$ and series C ($\text{Li}_{7-3x}\text{Al}_x\text{La}_3\text{Zr}_2\text{O}_{12} + 1.25x(\text{Li}_2\text{O})$) were prepared with a slight excess of Li_2O .

Here, mixtures with a total mass of 2 g were high-energy ball milled in an argon atmosphere using a planetary mill P7 premium line (Fritsch) in combination with a vial set made of tungsten carbide (45 mL beaker, 100 balls with a diameter of 5 mm each). The mixtures were milled at a rotational speed of 600 rpm for 8 h at ambient temperature. Afterward, a pellet (8 mm in diameter and ~ 1 mm in thickness) was prepared from each of the milled powders by cold-pressing at ~ 1 GPa. The pellet and the residual powder were placed in quartz shuttles and annealed at 873 K using a constant flow of synthetic air (Linde). After 6 h, the samples were cooled down to a temperature of about 773 K. After that, the shuttles were removed from the oven and quenched to ambient temperature by putting them on a fire brick. For comparison, for one of the samples the annealing step was replaced by a reaction step; i.e., the powder was kept for 15 h at 1500 K in a corundum crucible.

The obtained powders were characterized by XRPD using a D8 Advance diffractometer (Bruker) operating with $\text{Cu K}\alpha$ radiation at 40 kV. Further characterization was carried out by ^{27}Al MAS NMR spectroscopy using a Bruker Avance III spectrometer connected to an Ultrashield Plus 600 MHz magnet (Bruker) with a nominal field of 14.1 T. NMR spectra were acquired with a Bruker 2.5 mm double-resonance MAS probe using a single excitation pulse with a length of ~ 2 μs . The spinning rate ν_{rot} was set to 30 kHz using room-temperature bearing gas. Chemical shift values δ_{iso} were referenced to an aqueous solution of aluminum nitrate.

Variable-temperature ^7Li NMR measurements, including the acquisition of (i) line shapes under nonrotating, i.e., static

conditions, and (ii) spin–lattice relaxation (SLR) rates, were performed with an MSL 400 spectrometer (Bruker) in combination with a 9.4 T cryomagnet (Oxford). Prior to these measurements the samples were dried at 373 K for at least 12 h in vacuum and then heat-sealed in glass ampulla. The resonance frequency was 155.4 MHz. For the measurements presented a standard high-temperature probe (Bruker) was used. The $\pi/2$ pulse length was 2 μs . SLR NMR rates were measured with the saturation recovery pulse sequence where a comb of closely spaced $\pi/2$ pulses was used to destroy any longitudinal magnetization $M(t)$.^{33,34} The subsequent recovery of $M(t)$ was probed with a single $\pi/2$ pulse as a function of waiting time. Additionally, some preliminary solid echo NMR measurements were recorded by taking advantage of the static field-gradient of a cryomagnet (14.1 T of an Avance III spectrometer (Bruker)). Macroscopic lithium diffusion coefficients were estimated from the obtained echo decay curves.

Additionally, ac impedance spectra (0.05 Hz to 20 MHz) were measured with a Novocontrol Concept 80 broadband dielectric spectrometer which is equipped with an Alpha-AN analyzer in connection with a ZGS active sample cell test interface (Novocontrol). The sample temperature was controlled (± 0.1 K) with a Novocontrol QUATRO using a gas-flow of heated nitrogen which was freshly evaporated. After annealing the impedance pellets as mentioned above electrodes were applied by Au evaporation using an Edwards 306 evaporator. In order to remove any residual moisture, prior to the measurements all pellets were kept several hours inside the sample cell at 390 K under a constant flow of nitrogen gas. The ac impedance data, recorded at frequencies up to 3 GHz, were measured using a (microwave) rf extension line (Novocontrol) connected to an Agilent 4991 rf analyzer.

For selected samples the amount of Al and Li was measured by inductive coupled plasma (ICP) optical emission spectroscopy (OES) using a Varian 715 spectrometer. Here, 25 mg of the samples was mixed with an equimolar solution of 3 mL of concentrated nitric acid and concentrated phosphoric acid. The mixture was placed in a Teflon autoclave which was heated inside a microwave oven at 523 K for about 25 min. Calibration curves were measured using LiOH and Al_2O_3 . It turned out that the losses of Li and Al, occurring during annealing at 873 K for 6 h after mechanical activation, were as low as ca. 1 and 2 wt %, respectively.

III. RESULTS AND DISCUSSION

A. Mechanosynthesis of Al-Doped $\text{Li}_7\text{La}_3\text{Zr}_2\text{O}_{12}$

Exemplarily, in Figure 1 the XRPD patterns of mechano-synthesized Al-doped LLZ with $x = 0.3$ (series B) before and after the annealing step are shown. Judging from XRPD the two-step synthesis route yields phase-pure LLZ crystallizing with cubic symmetry. Directly after high-energy ball milling, the polycrystalline powder is composed of nanometer-sized crystallites of LLZ as well as ZrO_2 . The XRPD pattern of ZrO_2 (Joint Committee on Powder Diffraction Standards (JCPDS) number 37-1484) is indicated in Figure 1a by vertical bars. The broad humps detected point to amorphous milling products. Thermal annealing of the activated powder for 6 h at 873 K completes the mechanically initiated reaction. The pattern obtained for the final product (Figure 1b) is in perfect agreement with the data reported by Geiger et al.²³

Without the assistance of thermal annealing, merely by increasing the milling time (up to 48 h) no complete conversion of the starting materials has been observed. Thus,

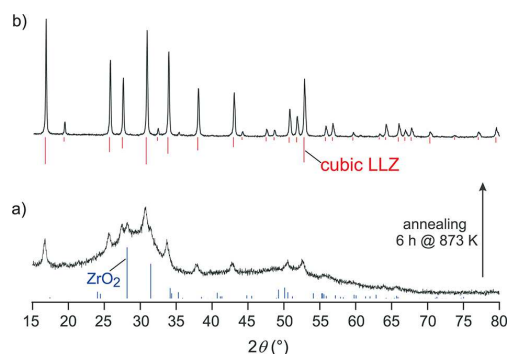


Figure 1. XRPD patterns of a mechano-synthesised sample of LLZ with $x = 0.30$ (series B, see text for further details): (a) XRPD directly recorded after 8 h of mechanical treatment in a high-energy ball mill; (b) final XRPD pattern of phase-pure cubic LLZ which was obtained after annealing the material for 6 h at 873 K.

soft annealing is a necessary preparation step in the synthesis of cubic LLZ. Here, the complete transformation of a mechanically activated mixture advantageously occurs at a significantly lower temperature as compared to conventional synthesis routes (see also ref 29).

B. Aliovalent Doping: Replacement of 3Li^+ with Al^{3+} .

It is assumed that a replacement of Li with Al according to $3\text{Li}^+ \Rightarrow \text{Al}^{3+}$, which leads to LLZ with the composition $\text{Li}_{7-3x}\text{Al}_x\text{La}_3\text{Zr}_2\text{O}_{12}$, takes place. This doping mechanism, in the following denoted by (α), was already discussed by Geiger et al.²³ (*vide supra*). At first glance, one might assume that the substitution of Al^{3+} for 3Li^+ could explain the enhanced

conductivity usually observed for cubic “ $\text{Li}_7\text{La}_3\text{Zr}_2\text{O}_{12}$ ”. However, it seems questionable whether the associated formation of additional vacancies on the lithium sites further facilitates Li transport since, from the outset, the regular Li sites are only partially occupied in cubic LLZ.

In order to get further insight into the role that Al plays, in a first approach we prepared aliovalently exchanged LLZ samples with the nominal composition of $\text{Li}_{7-3x}\text{Al}_x\text{La}_3\text{Zr}_2\text{O}_{12}$ ($0 \leq x \leq 1.2$) by using the exact stoichiometric ratios of the starting materials (series A, *vide supra*). Figure 2a shows the corresponding XRPD patterns recorded with the Al contents x as indicated. For all values of x , LLZ is obtained as a major phase. Up to an Al amount of $x = 0.25$, the products are phase-pure on the XRD level, and the aliovalent exchange turns out to be successful.

For $x < 0.20$ the obtained powders do not crystallize well with cubic symmetry. This is in good agreement with the results of Rangasamy et al.¹⁴ The patterns show broad and asymmetric peaks presumably caused by very small crystallites and/or increased lattice strain. Moreover, a partial reduction of the crystal symmetry might be responsible for the broadening observed. In Figure 5, the width of the most intense XRPD peak, showing up at $2\theta \approx 17^\circ$, of the three series is shown as a function of x . Except for a few samples (notably the ones with $x = 0.60$ of series A and C), the peak width almost continuously decreases with increasing Al content. Obviously, the relevant substitution processes taking place (see below) stabilize the cubic crystal structure.

The aliovalent exchange goes along with the emergence of a ^{27}Al MAS NMR line around 64 ppm (see Figure 2b). With increasing Al content several impurity phases such as $\text{La}_2\text{Zr}_2\text{O}_7$ (JCPDS 17-450), LaAlO_3 (JCPDS 31-22), $\gamma\text{-LiAlO}_2$ (JCPDS

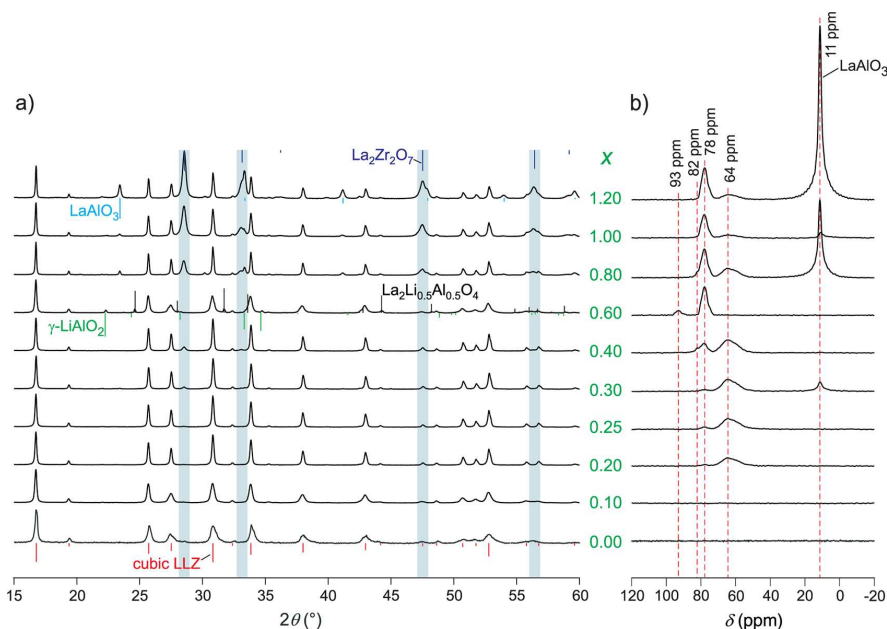


Figure 2. (a) XRPD patterns of a series of $\text{Li}_{7-3x}\text{Al}_x\text{La}_3\text{Zr}_2\text{O}_{12}$ samples (series A) with the nominal Al contents x as indicated. (b) Corresponding ^{27}Al MAS NMR spectra which were recorded at a magnetic field of 14.1 T and an MAS spinning rate of 30 kHz. See text for further explanation.

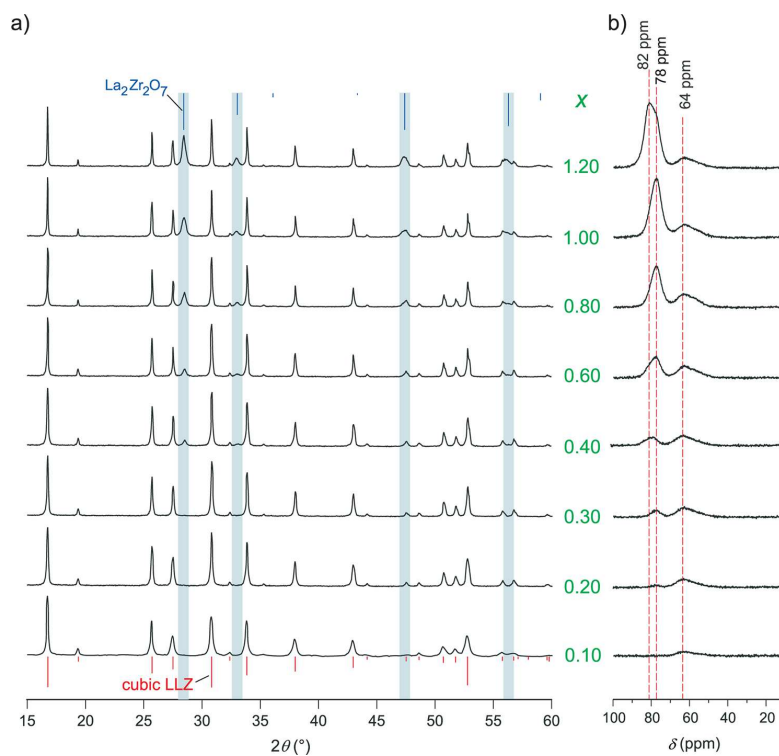


Figure 3. (a) XRPD patterns of a series of $\text{Li}_{7-3x}\text{Al}_x\text{La}_3\text{Zr}_2\text{O}_{12} + 0.75x(\text{Li}_2\text{O})$ samples (series B) with the nominal Al contents x as indicated. (b) Corresponding ^{27}Al MAS NMR spectra which were recorded at a magnetic field of 14.1 T and an MAS spinning rate of 30 kHz. See text for further explanation.

38-1464) and $\text{La}_2\text{Li}_{0.5}\text{Al}_{0.5}\text{O}_4$ (JCPDS 40-1167) show up. However, no clear trend in the formation of these phases is observed. At least for $x > 0.6$, $\text{La}_2\text{Zr}_2\text{O}_7$ seems to be the main side product formed. An important consequence is that the stoichiometry of the LLZ phase is altered. For example, when $\text{La}_2\text{Zr}_2\text{O}_7$ is formed, the garnet phase contains less La and Zr. Accordingly, when LaAlO_3 shows up, LLZ is reduced in Al and La. Obviously, Al replaces not only Li but also La and Zr.

The corresponding ^{27}Al MAS NMR spectra of the samples (Figure 2b) comprise several lines viz. at 11, 64, 78, 82, and 93 ppm. The signal at 11 ppm shows up when LaAlO_3 is formed. The associated isotropic chemical shift value δ_{iso} is in accordance with literature data for pure LaAlO_3 .^{23,35} The corresponding chemical shift of $\gamma\text{-LiAlO}_2$ can be calculated from the quadrupolar and isotropic shift values given in the literature.³⁹ It turns out to be ~ 75 ppm at 14.1 T. Here, a slight shoulder is indeed observed at 75 ppm when LiAlO_2 is formed. However, it is covered by the intense NMR line at 78 ppm which represents Al in the LLZ phase. Interestingly, the line at 78 ppm is observed in La or Zr deficient LLZ. Therefore, it might represent Al residing on the La and/or Zr sites in the garnet. This assumption will be checked in detail below. Interestingly, some of the samples investigated by ^{27}Al MAS NMR reveal a slight shoulder at 82 ppm. Probably, this NMR line also represents Al in LLZ (see also below).

The NMR line at 93 ppm is only observed for $x = 0.6$. At first glance it might be assigned to Al ions in $\text{La}_2\text{Li}_{0.5}\text{Al}_{0.5}\text{O}_4$ wherein

Al is assumed to be coordinated by oxygen forming an elongated octahedron.³⁶ Because there are no NMR data in the literature available, we prepared almost phase pure $\text{La}_2\text{Li}_{0.5}\text{Al}_{0.5}\text{O}_4$ by mechano-synthesis. The corresponding ^{27}Al MAS NMR spectrum of an annealed sample (6 h at 873 K) is composed of a single line at 12 ppm which shows a relatively low intensity. This might explain the absence of such an NMR line with this chemical shift in the ^{27}Al MAS NMR spectrum of the LLZ sample with $x = 0.60$ (see Figure S1, Supporting Information). Thus, the NMR intensity located at 93 ppm seems to represent Al on an unknown site in the garnet (see also ref 37).

The effect that incorporated Al does stabilize the cubic modification over the tetragonal one has already been discussed in refs 17 and 23. In the present study, this effect can also be monitored via the change of the XRPD peak widths with increasing x . The peak widths are significantly reduced with the incorporation of Al (see Figure 5). Certainly, when impurity phases are present (series A), the trend is less clearly visible. The samples of series B and C, which were prepared with an excess of Li_2O , proved to be more suitable to show the effect. The additional amount of Li_2O seems to provide a reaction medium where the growth of the LLZ phase is favored. For example, this might be due to an improved contact between crystallites in the ball-milled precursor material. However, in the case of series B and C, the only significant minority phase found is $\text{La}_2\text{Zr}_2\text{O}_7$.

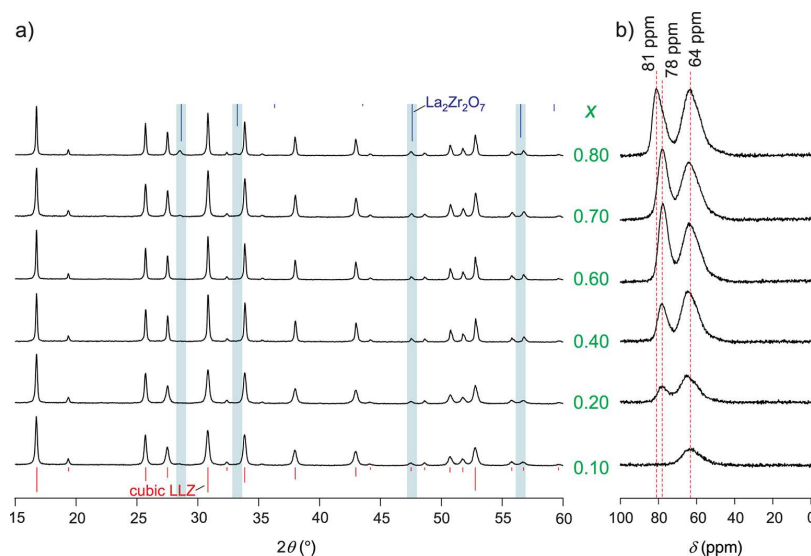


Figure 4. (a) XRPD patterns of a series of $\text{Li}_{7-3x}\text{Al}_x\text{La}_3\text{Zr}_2\text{O}_{12} + 1.25x(\text{Li}_2\text{O})$ samples (series C) with the nominal Al contents x as indicated. (b) Corresponding ^{27}Al MAS NMR spectra which were recorded at a magnetic field of 14.1 T and an MAS spinning rate of 30 kHz. See text for further explanation.

The corresponding XRPD patterns and ^{27}Al MAS NMR spectra of series B are shown in Figure 3. The XRPD data point to phase-pure LLZ up to a value of about $x = 0.3$. The incorporation of small amounts of Al in the LLZ phase goes along with the emergence of a ^{27}Al MAS NMR line at 64 ppm, which again represents the aliovalent exchange of Al for Li. At higher Al levels, XRPD peaks of a second phase, viz. $\text{La}_2\text{Zr}_2\text{O}_7$, are observed. Again, this results in a garnet phase depleted in La and Zr. Concomitantly, the NMR line at 78 ppm emerges with both increasing x and the formation of $\text{La}_2\text{Zr}_2\text{O}_7$ (see above). Exemplarily, a Rietveld refinement of the sample with $x = 1.2$ revealed that it is composed of ~ 33 wt % $\text{La}_2\text{Zr}_2\text{O}_7$ and ~ 66 wt % Al-doped LLZ. With these values the actual stoichiometry $\text{Li}_{7-3x+z}\text{Al}_{x+y+z}\text{La}_{3-y}\text{Zr}_{2-z}\text{O}_{12}$ of the sample can be determined to be $\text{Li}_{6.68}\text{Al}_{1.54}\text{La}_{2.55}\text{Zr}_{1.26}\text{O}_{12}$ with $x \approx 0.35$, $y \approx 0.45$, and $z \approx 0.74$. These values are in good agreement with those estimated from ^{27}Al MAS NMR: the three distinct NMR lines showing up at 64, 78, and 82 ppm are assumed to be related to three distinct doping mechanisms (α), (β), and (γ). While (α) denotes aliovalent doping (see above), (β) is described by $\text{La}^{3+} \Rightarrow \text{Al}^{3+}$ and (γ) denotes $\text{Zr}^{4+} \Rightarrow \text{Li}^+ + \text{Al}^{3+}$. Assuming $x + y + z = 1.54$, as calculated from Rietveld analysis, a rough deconvolution of the corresponding ^{27}Al MAS NMR spectrum of the sample with $x = 1.2$ (series B) yields $x = 0.33$, $y = 0.42$, and $z = 0.80$.

It should be mentioned that ^{27}Al MAS NMR signals around 80 ppm were also observed by Geiger et al.²³ From their ^{27}Al MQMAS NMR measurements they concluded that these signals result from a single NMR line which is perturbed by second-order quadrupolar effects. However, judging from the ^{27}Al MAS NMR spectra of some of our samples (see below), we may not rule out that these signals could also originate from two separate NMR lines representing different crystallographic sites in the structure of the garnet.

Compared with series B, the samples of series C show very similar results (see Figure 4a): phase-pure LLZ is obtained but up to Al levels of $x = 0.6$; at even higher values of x the formation of $\text{La}_2\text{Zr}_2\text{O}_7$ is observed. Interestingly, the ^{27}Al MAS NMR line at 78 ppm (and 82 ppm) emerges with significant intensity although the XRPD patterns do not reveal any indications for the formation of $\text{La}_2\text{Zr}_2\text{O}_7$, see Figure 4b. This might be considered as an argument against the above-given assignment that this NMR line reflects the replacement of Zr and La with Al. It is worth noting that no residual Li_2O can be detected by XRPD which does not rule out that it may be X-ray amorphous. However, assuming that the excess of Li_2O has been incorporated into the garnet and disregarding the formation of oxygen vacancies, the LLZ formed should be characterized by smaller ratios of Al, La, and Zr. In the case of series C with $\text{Li}_{7-3x}\text{Al}_x\text{La}_3\text{Zr}_2\text{O}_{12} + 1.25x(\text{Li}_2\text{O})$ this would lead to $[(12 + 1.25x)/12]\text{Li}_{(7-0.5x)[12/(12+1.25x)]}\text{Al}_{x[12/(12+1.25x)]}\text{La}_3[12/(12+1.25x)]\text{Zr}_2[12/(12+1.25x)]\text{O}_{12}$. This assumption would explain why for series C garnet-type LLZ is obtained phase pure up to higher Al contents ($x = 0.60$) than for series A ($x = 0.25$) and B ($x = 0.30$) as well as for series B compared to series A. This might be considered as another argument for the existence of the doping mechanisms $\text{La}^{3+} \Rightarrow \text{Al}^{3+}$ and $\text{Zr}^{4+} \Rightarrow \text{Al}^{3+} + \text{Li}^+$, respectively.

C. Mixed Doping Mechanisms. In order to check the assumption that Al replaces La and Zr in LLZ as mentioned above, we synthesized several LLZ samples with very high Al contents, which can be described with the formula $\text{Li}_{7-3x+z}\text{Al}_{x+y+z}\text{La}_{3-y}\text{Zr}_{2-z}\text{O}_{12}$. Indeed, it is possible to synthesize nearly phase-pure LLZ with nominal Al contents up to $n(\text{Al}) = x + y + z \approx 2$ whereby considerable amounts of La and Zr are replaced by Al. Selected results are shown in Figure 6.

In Figure 7 three different compositions with very high Al contents are presented. Interestingly, both the XRPD pattern and ^{27}Al MAS NMR spectrum of a sample with the nominal

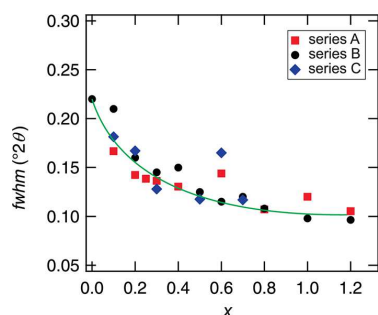


Figure 5. Width of the XRPD peak (full width at half-maximum (fwhm)) at $2\theta \approx 17^\circ$ (see Figures 2a, 3a, and 4a) as a function of Al content x . The solid line is drawn to guide the eye.

composition “ $\text{Li}_{6.95}\text{Al}_2\text{La}_{2.15}\text{Zr}_{1.15}\text{O}_{12}$ ” are very similar to those of the sample with $x = 0.60$ of series A. However, in the case of $\text{Li}_{6.36}\text{Al}_{1.78}\text{La}_{2.26}\text{Zr}_{1.38}\text{O}_{12}$ besides a small amount of $\gamma\text{-LiAlO}_2$ almost phase pure LLZ is obtained. The corresponding ^{27}Al MAS NMR spectrum reveals a signal with a very low intensity at 11 ppm (see inset in Figure 7). It probably indicates the formation of a small amount of LaAlO_3 . Increasing the nominal amounts of La and Zr up to a composition of approximately $\text{Li}_{5.73}\text{Al}_{1.78}\text{La}_{2.36}\text{Zr}_{1.47}\text{O}_{12}$, the formation of $\text{La}_2\text{Zr}_2\text{O}_7$ can be observed. Hence, the maximum amount of Al which can substitute La and/or Zr in the LLZ seems to be $n(\text{Al}) \approx 1.78$ while $n(\text{Al}) = 2$ leads to the formation of, e.g., $\gamma\text{-LiAlO}_2$ and $\text{La}_2\text{Li}_{0.5}\text{Al}_{0.5}\text{O}_4$. Interestingly, the XRPD peaks of these three samples are considerable broader than those found for the other LLZ samples with a large Al content. Therefore, it seems plausible to assume a characteristic Al content at which the stabilization of the cubic LLZ is at its maximum. If the amount of Al is increased further, the cubic LLZ is destabilized once again.

For comparison, the aliovalently Al-doped sample (mechanism (α) assumed) with $x = 1.20$ (series B) is also shown in Figure 6. Note that the intensity of the NMR line at 82 ppm of

this sample is higher than those found for the other samples (see Figure 6). Assuming that the signal at 82 ppm reflects mechanism (γ) $\text{Zr}^{4+} \Rightarrow \text{Li}^+ + \text{Al}^{3+}$, a very large amount of Al has been substituted for Zr, which is in agreement with the calculated chemical formula $\text{Li}_{6.68}\text{Al}_{1.54}\text{La}_{2.55}\text{Zr}_{1.26}\text{O}_{12}$ (*vide supra*). However, this seems to be an exception since generally we observed a preference of the substitution mechanism connected to the ^{27}Al NMR line at 78 ppm over that one ascribed to the signal at 82 ppm.

From the results presented up to here, two main conclusions can be drawn: (i) the doping mechanisms $\text{La}^{3+} \Rightarrow \text{Al}^{3+}$ and $\text{Zr}^{4+} \Rightarrow \text{Al}^{3+} + \text{Li}^+$ do take place, and (ii) the ^{27}Al NMR lines showing up at 64, 78, and 82 ppm result from Al residing on different crystallographic sites in the garnet. Hereby, the line at 64 ppm represents the replacement of Li by Al while the other lines reflect the replacement of La and Zr. NMR chemical shifts of the three signals lie in the range being typical of tetrahedral coordination. The signal at 64 ppm might well be Al on the tetrahedral Li1 position. For the substitution of Al for La and Zr the situation is probably different. In garnet-type LLZ La resides in a dodecahedral site and Zr in an octahedral site. The ^{27}Al NMR lines with chemical shifts of 78 and 82 ppm, which emerge with the exchange of La and Zr by Al, rather point to 4-fold oxygen coordination.⁴⁰ Therefore, Al probably does not occupy the La or Zr sites but resides on tetrahedral sites next to a vacancy created. So far, the correct assignment of the various NMR signals turns out to be a difficult task because no clear relation between isotropic ^{27}Al MAS NMR chemical shifts and both the coordination number and the Al–O distance d can be found in the literature.³⁸

By comparing the different doping mechanisms, there is a qualitative difference between the aliovalent doping mechanism and the mixed doping mechanism. This can be rationalized by considering the structure of the garnets stuffed with Li. $\text{Li}_7\text{La}_3\text{Zr}_2\text{O}_{12}$ should be understood as $\text{Li}_7^+[\text{La}_3\text{Zr}_2\text{O}_{12}]^{7-}$, i.e., a negatively charged garnet network being filled with Li ions compensating for the negative charge. The aliovalent doping mechanism then leads to $\text{Li}_{7-3x}^+\text{Al}_x^{3+}[\text{La}_3\text{Zr}_2\text{O}_{12}]^{7-}$. In this case, the stoichiometry of the garnet network is not affected by

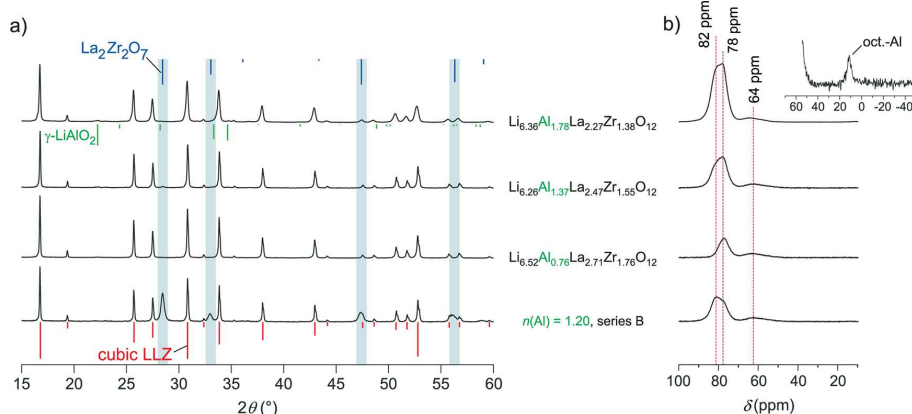


Figure 6. (a) XRPD patterns of a sample of series B with $x = 1.2$ as well as of selected samples systematically reduced in La and Zr. (b) Corresponding ^{27}Al MAS NMR spectra recorded at a field of 14.1 T and an MAS spinning rate of 30 kHz. The inset shows a magnification of a part of the NMR spectra of the sample with the composition $\text{Li}_{6.36}\text{Al}_{1.78}\text{La}_{2.27}\text{Zr}_{1.38}\text{O}_{12}$. It exhibits a small amount of octahedrally coordinated Al (see text).

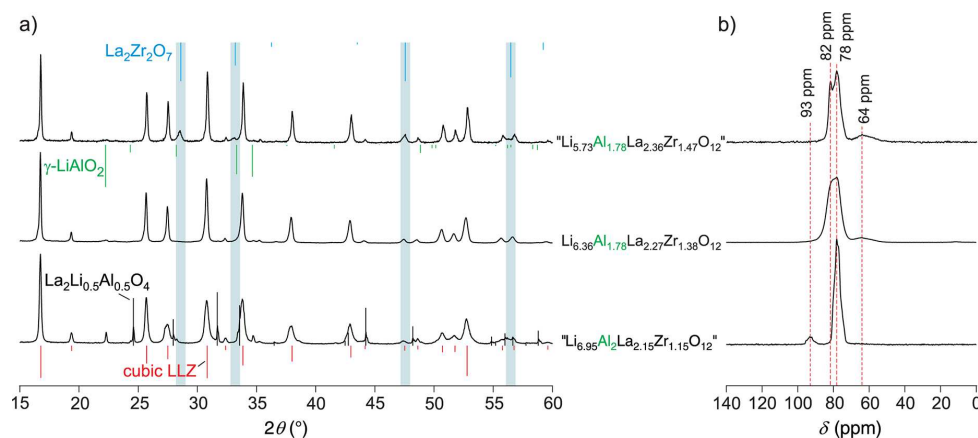


Figure 7. (a) XRPD patterns of three samples systematically reduced in La and Zr but with a very high Al content. (b) Corresponding ^{27}Al MAS NMR spectra recorded at a field of 14.1 T and an MAS spinning rate of 30 kHz.

doping, and a significant impact on the Li dynamics is not to be expected. The replacement of La and Zr by Al, however, directly affects the garnet network itself, leading to $\text{Li}_{7-3x+z}^+\text{Al}_x^{3+}[\text{La}_{3-y}\text{Al}_y\text{Zr}_{2-z}\text{Al}_2\text{O}_{12}]^{z-7}$. It is obvious that this kind of doping will more likely have a significant impact on the garnet structure as well as on the Li ion dynamics.

D. Li Ion Dynamics As Probed by NMR and Impedance Spectroscopy. 1. NMR Line Narrowing. Li ion dynamics of the samples were roughly characterized by static ^7Li NMR line narrowing measurements. Such measurements are useful when short-ranged dynamics have to be studied. As an example, in Figure 8a the ^7Li NMR lines of the sample with $x = 0.30$ of series B are shown. At low T the NMR line is dipolarly broadened and can be described with a Gaussian line shape. At higher temperatures, as the jump rate of the Li spins exceeds the dipolar coupling constant, the dipole–dipole interactions are averaged, resulting in a motionally narrowed NMR line.⁴¹ Here, a two-step narrowing is observed pointing to a heterogeneous Li ion dynamics.^{11,17}

By plotting the line width (full width at half-maximum, fwhm) vs T , a so-called motional narrowing (MN) curve is obtained which can be used to roughly estimate the Li^+ diffusivity. In Figure 8b, the corresponding narrowing curve of cubic LLZ (series B, $x = 0.30$) is shown together with those of the previously studied tetragonal¹⁶ and cubic¹⁷ LLZ prepared by conventional solid-state synthesis. The Li diffusivity of the mechanothesized material is nearly as high as that of cubic LLZ synthesized conventionally but significantly higher than that of the Al-free LLZ crystallizing with tetragonal symmetry.

At the inflection point ($T = T_{\text{MN}}$) of the NMR MN curve the mean Li jump rate τ_{MN}^{-1} is approximately given by the relation $\tau_{\text{MN}}^{-1} \approx \Delta\omega_{\text{d}}$, where $\Delta\omega_{\text{d}}$ denotes the rigid lattice line width in radians. Here, $\Delta\omega_{\text{d}}(T \rightarrow 0)$ is approximately $5.7 \times 10^4 \text{ s}^{-1}$. In Figure 8b, the temperature T_{MN} is marked by a vertically drawn dashed line. To compare the dynamic properties of the samples prepared, in Figure 8c T_{MN} is shown as a function of $n(\text{Al})$ (which is x for series A, B, and C) together with the T_{MN} values of both cubic LLZ¹⁷ and Al-free tetragonal LLZ¹⁶ prepared via high-temperature solid-state synthesis. Most of the samples prepared exhibited T_{MN} values ranging from 235 to 315 K and,

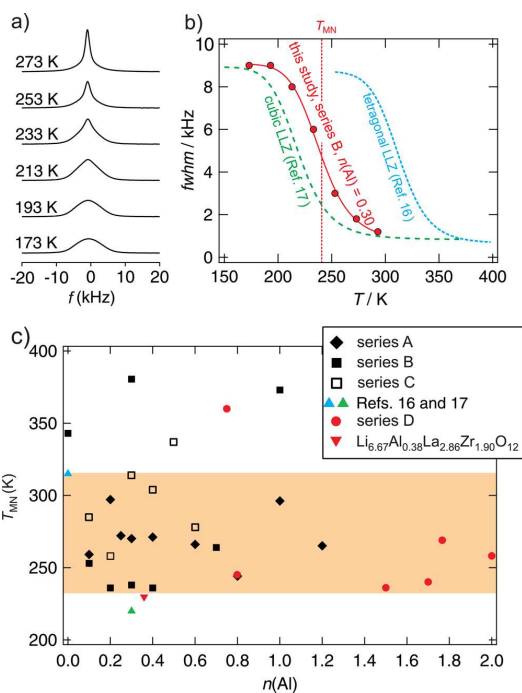


Figure 8. (a) ^7Li NMR lines of mechanothesized, aliovalently doped LLZ with $x = 0.30$ (series B). Data were recorded under static conditions at $\omega_0/2\pi = 155.4 \text{ MHz}$. (b) Motional narrowing (MN) of the corresponding line width (red data points). For comparison, the MN curves of cubic (dashed black line, data taken from ref 17) and tetragonal (dashed blue line, data taken from ref 16) LLZ prepared by conventional solid-state syntheses are included as well. (c) T_{MN} (deduced from the curves shown in (b)) as a function of the nominal composition $n(\text{Al})$. Series D marks the samples systematically reduced in La and Zr. The data point at $n(\text{Al}) = 1.78$ refers to the sample $\text{Li}_{6.36}\text{Al}_{1.78}\text{La}_{2.26}\text{Zr}_{1.38}\text{O}_{12}$. The green and blue triangles mark the inflection points of cubic and tetragonal LLZ.^{16,17}

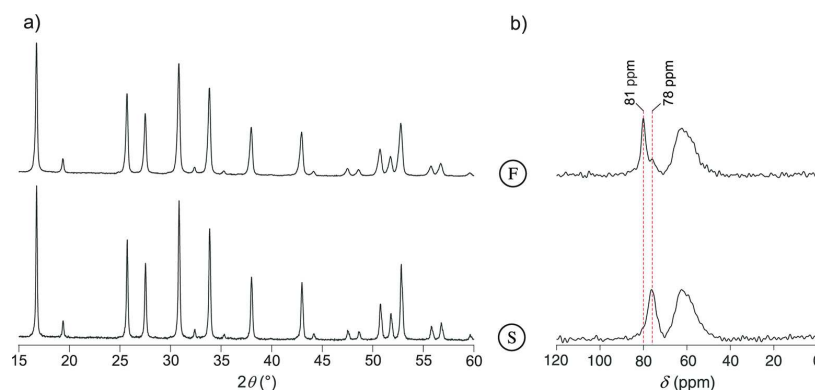


Figure 9. (a) XRPD patterns of two different samples of series B with $x = 0.30$. The XRPD peak widths of the sample labeled as “F” are broader than those found for the sample labeled as “S”. (b) ^{27}Al MAS NMR spectra of the two materials which were recorded at a field of 14.1 T and a spinning rate of 30 kHz.

thus, show higher diffusivities than the samples free of Al (see Figure 8c).

Regarding $T_{\text{MN}}(n(\text{Al}))$, the characteristic temperature seems to pass through a broad minimum located between $n(\text{Al}) = 0.20$ and $n(\text{Al}) = 0.60$ for the samples of series A and B. It points to a maximum Li ion diffusivity for samples with these compositions. At $n(\text{Al}) \approx 1.00$ there seems to be a minimum of the Li diffusivity for these two series. Interestingly, the Li diffusivity increases once more when the Al content is increased further. For comparison, the value of a very fast sample with a nominal composition of $\text{Li}_{6.67}\text{Al}_{0.38}\text{La}_{2.86}\text{Zr}_{1.90}\text{O}_{12}$ is also shown.

Obviously, the Al content itself is not the only parameter determining the Li ion dynamics. Possible explanations could be (i) a correlation with the Li concentration,⁴² (ii) the occurrence of oxygen vacancies as presumed by Murugan et al.,⁴² or (iii) a strong influence of the relative contributions of the different doping mechanisms. As to (i), we did not observe a clear correlation between the Li content and the ion diffusivity of the samples prepared which was evaluated by comparing the integrals of the ^7Li NMR lines. Concerning (ii), with the analytical tools available we are not able to decide whether oxygen vacancies, which have been assumed in, e.g., refs 26 and 42, are present to a significant extent. As to (iii), it is important to consider the different types of doping which definitely have a different impact on the garnet structure as pointed out above.

It is worth mentioning that some of the samples were prepared several times in different batches to check the reproducibility of the results. It turned out that T_{MN} varied by up to ~ 140 K for some equally prepared samples. Exemplarily, in Figure 9a the XRPD patterns of two samples with $x = 0.30$ of series B are shown.

The sample labeled as “F” (fast) is characterized by $T_{\text{MN}} = 240$ K while the slower one labeled as “S” is shifted toward higher T , yielding $T_{\text{MN}} = 380$ K (see Figure 8c). Interestingly, the XRPD peak widths of sample “F”, which is also included in Figure 5, are larger than those obtained for sample “S”. In Figure 9b, the corresponding ^{27}Al MAS NMR spectra are shown to check for any differences of the two samples. Whereas the NMR spectrum of sample “S”, which has already been included in Figure 3b, reveals a distinct signal at 78 ppm presumably reflecting the doping mechanism (β), in the

corresponding NMR spectrum of sample “F” a signal at 81 ppm shows up. Tentatively, the latter can be ascribed to doping mechanism (γ). Independently of these differences, the two spectra show very similar NMR intensities at 64 ppm ascribed to the aliovalent doping (α). Thus, as already proposed above, the relative contributions of the different doping mechanisms (β) and (γ) seem to significantly affect Li ion dynamics in LLZ.

However, it should be mentioned that there are also some samples with a similar composition prepared more than one time which revealed besides similar XRPD patterns very comparable dynamic properties.

Since some of the samples of series B reveal the highest Li diffusivities observed in this study, only samples of these series were chosen for additional conductivity measurements and NMR experiments.

2. ^7Li NMR Spin–Lattice Relaxation Rates. When plotted as a function of inverse temperature, the ^7Li NMR spin–lattice relaxation (SLR) rate R_1 passes through a maximum at the temperature at which the Li jump rate τ^{-1} is in the order of the Larmor frequency: $\tau^{-1} \approx \omega_0$. Exemplarily, in Figure 10 the SLR

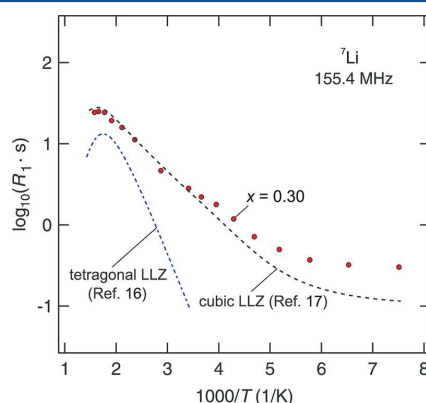


Figure 10. ^7Li NMR SLR rates R_1 of LLZ with $x = 0.30$ (series B) recorded at $\nu_0 = \omega_0/2\pi = 155.4$ MHz. For comparison, those of cubic and tetragonal LLZ prepared by a solid-state synthesis are also included (data were taken from refs 16 and 17).

rates R_1 of LLZ with $x = 0.30$ (series B) are shown. The diffusion-induced NMR SLR rates are very similar to those of conventionally synthesized cubic LLZ which has been studied by some of us quite recently (see ref 17). For comparison, the corresponding data are indicated in Figure 10 by a dashed line. Below 180 K the rate R_1 is governed by nondiffusion induced background relaxation, which is characterized by a very weak temperature dependence. At elevated temperatures the low- T flank of the diffusion-induced rate peak $R_1(1/T)$ is visible. For the sake of completeness also the NMR SLR rates recently obtained for Al-free LLZ crystallizing with tetragonal symmetry¹⁶ are included (see dashed-dotted line).

Independent of $n(\text{Al})$, diffusion-induced rate maxima show up between 573 and 623 K pointing to jump rates in the order of 10^9 s^{-1} (see the Arrhenius plot of Figure 12 where τ^{-1} is plotted vs $1/T$). Taking into account the estimated jump rate from NMR motional narrowing measurements, which has also been included in Figure 12, an activation energy E_a of 0.33(2) eV can be deduced. This value is in good agreement with the results from recently published studies on cubic LLZ.^{1,17} For comparison, the corresponding Arrhenius lines of cubic and Al-free tetragonal LLZ are also shown in Figure 12 (see the dashed lines).

3. Static Field-Gradient NMR Measurements. The Li jump rate deduced from ^7Li SLR NMR is very similar to that extracted from preliminary static field-gradient (SFG) NMR measurements which were exemplarily carried out using the mechano-synthesized sample with $x = 0.30$ (series B). In general, SFG NMR probes macroscopic Li diffusion coefficients D in the micrometer range.^{43–46} In order to compare D with the Li jump rates probed by SLR NMR, the diffusion coefficients recorded at various temperatures were converted into τ^{-1} values with the help of the Einstein–Smoluchowski equation. Here, we assumed uncorrelated motion and a jump distance of $\sim 0.25 \text{ nm}$. Although the absolute value of the so-obtained rates included in Figure 12 is fraught with an uncertainty of up to a factor of ~ 5 , good agreement is found with the data obtained from motional narrowing and SLR NMR (see, e.g., ref 47 for comparison with other studies).

For the sake of completeness, additional SFG NMR measurements were carried out on cubic and Al-free tetragonal LLZ studied in refs 17 and 16, respectively. Once again, the values probed are in very good agreement with the corresponding Arrhenius lines of Figure 12.

4. Impedance Measurements. Impedance spectroscopy measurements were carried out at room temperature for selected samples. In Figure 11, the real part σ' of the complex impedance of the sample with $x = 0.30$ (series B) is shown as a function of frequency f . While at low frequencies σ' is influenced by the effects of ion-blocking electrodes, at $f = 1 \text{ Hz}$ the conductivity reaches a plateau which passes into a dispersive regime. At even higher frequencies ($f > 10 \text{ MHz}$) a second plateau shows up which reflects the bulk conductivity being in the order of 10^{-5} – $10^{-4} \text{ S cm}^{-1}$. The exact value of σ' associated with this shallow plateau turns out to depend on $n(\text{Al})$ as well as the synthesis conditions chosen. A similar behavior of σ' was found for all the samples prepared by sintering the high-energy ball milled powders at 873 K for 6 h.

Most likely, the low-frequency plateau observed is governed by grain boundary effects significantly blocking long-range ion transport in LLZ. This can be easily verified by sintering the samples at temperatures much higher than 873 K. As an example, in Figure 11 the impedance spectrum of a

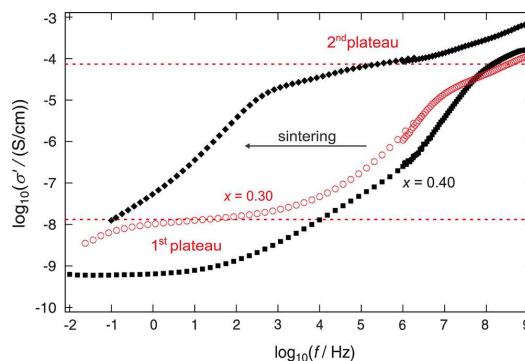


Figure 11. Impedance spectra of mechano-synthesized LLZ with $x = 0.30$ (red circles) measured at ambient temperature. For comparison, the black squares represent two impedance spectra of a sample with a nominal Al content of $x(\text{Al}) = 0.40$. As indicated by the arrow, sintering at 1500 K for 15 h, which was immediately carried out after the milling step, significantly affects the electrical response.

mechano-synthesized sample of LLZ with $x = 0.40$ is shown which was annealed at 873 K for 6 h. For comparison, the electrical response of a sample with $n = 0.40$ is included which has been annealed at 1500 K for 15 h. Its composition is “ $\text{Li}_{7.75}\text{Al}_{0.40}\text{La}_3\text{Zr}_2\text{O}_{12}$ ”, i.e., an excess of Li was intentionally added to compensate for Li loss during annealing (see Figure S2 in the Supporting Information for the XRPD pattern and the corresponding ^{27}Al MAS NMR spectrum). As can be clearly seen in Figure 11, sintering drastically changes the impedance response: the plateau associated with the bulk conductivity is significantly shifted toward higher frequencies dominating σ' in the range from 10 kHz to 10 MHz. $\sigma'(T)$ of the bulk response follows Arrhenius behavior with an activation energy of 0.28(3) eV (see Figure S3, Supporting Information), which is in fair agreement with literature data.¹⁷ Conversely, when the pellet sintered at 1500 K is thoroughly ground in an agate mortar and the obtained powder is cold pressed to a new pellet, a conductivity spectrum very similar to the original one is obtained. For comparison, samples which were not annealed after mechanical activation show a rather low Li diffusivity and conductivity, respectively.

Finally, coming back to the sample with an Al content of $n(\text{Al}) = 0.30$, in analogy to ref 16, the conductivity values of the two plateaus seen in Figure 11 have been converted into Li jump rates using the Nernst–Einstein equation and the Einstein–Smoluchowski equation. The values calculated are included in the Arrhenius plot of Figure 12. It is evident that the plateau showing up at higher frequencies reflects the fast transport process. The solid line included in the figure represents a least-squares fit taking into account also NMR data. The activation energy turned out to be $\sim 0.33 \text{ eV}$.

IV. CONCLUSIONS

Phase pure Al-doped $\text{Li}_7\text{La}_3\text{Zr}_2\text{O}_{12}$ crystallizing with cubic symmetry with an Al content of almost up to $n(\text{Al}) = 1.78$ can easily be prepared by high-energy ball milling and subsequent annealing carried out at rather low temperatures. In contrast to conventional high-temperature solid-state synthesis the low-temperature mechano-synthesis avoids Li loss and allows the precise adjustment of the samples' stoichiometry. This turned out to be beneficial to study the effect of various kinds of

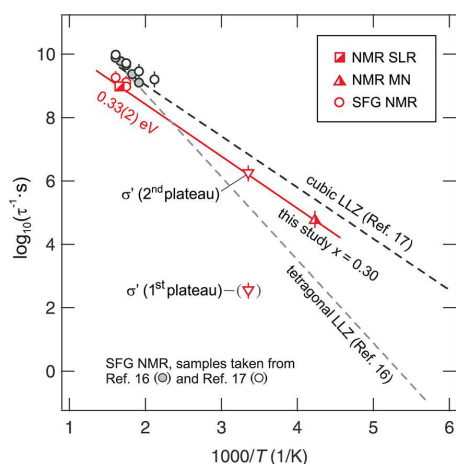


Figure 12. Arrhenius plot of the Li jump rates of the mechano-synthesized sample with $x = 0.30$ (series B). The rates were obtained from various NMR methods, including ^7Li SLR NMR, SFG NMR, and line shape measurements (see key) as well as deduced from the impedance spectrum $\sigma'(f)$ shown in Figure 11. For comparison, the Arrhenius lines of cubic,¹⁷ and Al-free tetragonal LLZ,¹⁶ prepared by solid-state synthesis are also included. See text for further explanation.

doping on both structural and dynamic properties of garnet-type LLZ. The comprehensive structural investigation of various Al-doped LLZ samples by XRPD and ^{27}Al MAS NMR reveals that the three distinct NMR lines showing up appear to be connected to three different doping mechanisms whereby Al replaces Li (preferred at low dopant concentrations), La, and Zr. The impact of the Al dopant on the stuffed garnet $\text{Li}_7^+[\text{La}_3\text{Zr}_2\text{O}_{12}]^{7-}$ is not restricted to the Li sublattice but does directly affect the garnet network itself, leading to $\text{Li}_{7-3x+z}^+\text{Al}_x^{3+}[\text{La}_{3-y}\text{Al}_y\text{Zr}_{2-z}\text{Al}_z\text{O}_{12}]^{z-7}$ or $\text{Li}_{7-3x}^+\text{Al}_x^{3+}[\text{La}_{3-y}\text{Al}_y\text{Zr}_{2-z}\text{Al}_z\text{O}_{12-2z}]^{z-7}$. This rationalizes the large impact of Al doping on the Li ion diffusivity as well as ion conductivity of cubic LLZ.

Appropriate Al doping results in highly conducting LLZ with a bulk conductivity in the order of 10^{-4} S cm^{-1} similar to that reported by Murugan et al.¹ Using an LLZ sample with $n(\text{Al}) = 0.30$ (series B), the fast Li diffusion process was exemplarily probed by various NMR techniques and impedance spectroscopy altogether covering a dynamic range of many decades. In agreement with recent investigations, the activation energy turned out to be ~ 0.3 eV. Impedance spectroscopy measurements revealed that the grain boundaries of a cold-pressed nonsintered powder sample have a significant blocking effect on Li ion transport. This can be overcome by appropriate high-temperature sintering of the garnets.⁴⁸

Certainly, further studies are needed to investigate the relationship between synthesis conditions and the relative contributions of the various doping mechanisms taking place. Small variations of the preparation parameters seem to have a significant effect on this ratio which, in turn, is expected to affect Li ion transport.

■ ASSOCIATED CONTENT

Supporting Information

Additional figures showing XRPD patterns and ^{27}Al MAS NMR spectra of some of the samples as well as the dc conductivity in

an Arrhenius representation of one of the samples studied. This material is available free of charge via the Internet at <http://pubs.acs.org>.

■ AUTHOR INFORMATION

Corresponding Author

*E-mail: duevel@pci.uni-hannover.de; Alexander.Kuhn@pci.uni-hannover.de.

Present Addresses

[§]Solid State Chemical Crystallography/FB02, University of Bremen, Leobener Straße/NW2, D-28359 Bremen, Germany.

^{||}Institute for Chemistry and Technology of Materials, Graz University of Technology, Stremayrgasse 9, A-8010 Graz, Austria.

[†]Max Planck Institute for Solid State Research, Heisenbergstr. 1, D-70569 Stuttgart, Germany.

Notes

The authors declare no competing financial interest.

■ ACKNOWLEDGMENTS

We thank E. Merzlyakova for her help in sample preparation and M. Krey and M. Binnewies for the ICP OES measurements. We thank J. Caro and A. Feldhoff for access to the Edwards 306 evaporator as well as to the D8 Advance diffractometer. We are indebted to H. Buschmann, S. Berendts, J. Janek (University of Gießen), V. Thangadurai (University of Calgary), and F. Tietz (Forschungszentrum Jülich) for valuable discussions. In particular, we are grateful to J. Janek and V. Thangadurai for leaving us the samples of refs 16 and 17 for the preliminary SFG NMR measurements included here. Financial support by the Federal Ministry of Education and Research (BMBF) in the frame of the project “Kompetenzverbund Nord (KVN)” is highly appreciated. We further acknowledge financial support by the Deutsche Forschungsgemeinschaft (DFG) in the frame of the Research Unit 1277 molife (mobility of lithium ions in solids).

■ REFERENCES

- (1) Murugan, R.; Thangadurai, V.; Weppner, W. *Angew. Chem., Int. Ed.* **2007**, *46*, 7778–7781.
- (2) Thangadurai, V.; Kaack, H.; Weppner, W. *J. Am. Ceram. Soc.* **2003**, *86*, 437–440.
- (3) Liu, Z.; Huang, F.; Yang, J.; Wang, Y.; Sun, J. *Solid State Sci.* **2008**, *10*, 1429–1433.
- (4) Etacheri, V.; Marom, R.; Elazari, R.; Salitra, G.; Aurbach, D. *Energy Environ. Sci.* **2011**, *4*, 3243–3262.
- (5) Kumar, B.; Kumar, J.; Leese, R.; Fellner, J. P.; Rodrigues, S. J.; Abraham, K. M. *J. Electrochem. Soc.* **2010**, *157*, A50–A54.
- (6) Ramzy, A.; Thangadurai, V. *Appl. Mater. Interfaces* **2010**, *2*, 385–390.
- (7) Kotokubi, M.; Munakata, H.; Kanamura, K.; Sato, Y.; Yoshida, T. *J. Electrochem. Soc.* **2010**, *157*, A1076–A1079.
- (8) Thangadurai, V.; Weppner, W. *Adv. Funct. Mater.* **2005**, *15*, 107–112.
- (9) Thangadurai, V.; Weppner, W. *J. Power Sources* **2005**, *142*, 339–344.
- (10) Wuellen, L. v.; Echelmeyer, T.; Meyer, H.-W.; Wilmer, D. *Phys. Chem. Chem. Phys.* **2007**, *9*, 3298–3303.
- (11) Koch, B.; Vogel, M. *Solid State Nucl. Magn. Reson.* **2008**, *34*, 37–43.
- (12) Cussen, E. J. *Chem. Commun.* **2006**, 412–413.
- (13) Cussen, E. J. *J. Mater. Chem.* **2010**, *20*, S167–S173.
- (14) Rangasamy, E.; Wolfenstine, J.; Sakamoto, J. *Solid State Ionics* **2012**, *206*, 28–32.

- (15) Weppner, W. German patent number DE102004010892-B3.
- (16) Kuhn, A.; Narayanan, S.; Spencer, L.; Goward, G.; Thangadurai, V.; Wilkening, M. *Phys. Rev. B* **2011**, *83*, 094302–1–094302–11.
- (17) Buschmann, H.; Dolle, J.; Berendts, S.; Kuhn, A.; Bottke, P.; Wilkening, M.; Heitjans, P.; Senyshyn, A.; Ehrenberg, H.; Lottnyk, A.; et al. *Phys. Chem. Chem. Phys.* **2011**, *13*, 19378–19392.
- (18) Kim, K. H.; Iriyama, Y.; Yamamoto, K.; Kumazaki, S.; Asaka, T.; Tanabe, K.; Fisher, C. A. J.; Hirayama, T.; Murugan, R.; Ogumi, Z. *J. Power Sources* **2011**, *196*, 764–767.
- (19) Kumazaki, S.; Iriyama, Y.; Kim, K.-H.; Murugan, R.; Tanabe, K.; Yamamoto, K.; Hirayama, T.; Ogumi, Z. *Electrochem. Commun.* **2011**, *13*, 509–512.
- (20) Kanamura, K.; Kaeriyama, A.; Honda, A.; Yoshida, T.; Sato, Y. US patent application number 20110053000.
- (21) Kotobuki, M.; Kanamura, K.; Sato, Y.; Yoshida, T. *J. Power Sources* **2011**, *196*, 7750–7754.
- (22) Awaka, J.; Kijima, N.; Hayakawa, H.; Akimoto, J. *J. Solid State Chem.* **2009**, *182*, 2046–2052.
- (23) Geiger, C. A.; Alekseev, E.; Lazic, B.; Fisch, M.; Armbruster, T.; Langner, R.; Fechtelkord, M.; Kim, N.; Pettke, T.; Weppner, W. *Inorg. Chem.* **2011**, *50*, 1089–1097.
- (24) Kuhn, A.; Choi, J.-Y.; Robben, L.; Tietz, F.; Wilkening, M.; Heitjans, P. *Z. Phys. Chem.* **2012**, *226*, 525–537.
- (25) Kokal, I.; Somer, M.; Notten, P. H. L.; Hintzen, H. T. *Solid State Ionics* **2011**, *185*, 42–46.
- (26) Shimonishi, Y.; Toda, A.; Zhang, T.; Hirano, A.; Imanishi, N.; Yamamoto, O.; Takeda, Y. *Solid State Ionics* **2011**, *183*, 48–53.
- (27) Xie, H.; Alonso, J. A.; Li, Y.; Fernández-Díaz, M. T.; Goodenough, J. B. *Chem. Mater.* **2011**, *23*, 3587–3589.
- (28) Janani, N.; Ramakumar, S.; Dhivya, L.; Deviannapoorani, C.; Saranya, K.; Murugan, R. *Ionics* **2011**, *17*, 575–580.
- (29) Kosova, A. *Ann. Chim.* **2009**, *34*, 401–413.
- (30) Plesingerova, B.; Buchal, A.; Šepelák, V.; Tkacova, K. *Ceram.-Silik.* **1996**, *40*, 131–136.
- (31) Da Silva, K. L.; Šepelák, V.; Paesano, A., Jr.; Litterst, F. J.; Becker, K. D. *Z. Anorg. Allg. Chem.* **2010**, *636*, 1018–1025.
- (32) Da Silva, K. L.; Šepelák, V.; Düvel, A.; Paesano, A., Jr.; Hahn, H.; Litterst, F. J.; Heitjans, P.; Becker, K. D. *J. Solid State Chem.* **2011**, *184*, 1346–1352.
- (33) *Diffusion in Condensed Matter – Methods, Materials, Models*; Heitjans, P.; Kärger, J., Eds.; Springer: Berlin, 2005.
- (34) Fukushima, E.; Roeder, S. B. W. *Experimental Pulse NMR*; Addison-Wesley: Reading, MA, 1981.
- (35) Blanc, F.; Middlemiss, D. S.; Buannic, L.; Palumbo, J. L.; Farnan, I.; Grey, C. P. *Solid State Nucl. Magn. Reson.* **2012**, *42*, 87–97.
- (36) Abbattista, F.; Vallino, M.; Mazza, D. *Inorg. Chim. Acta* **1987**, *140*, 147–149.
- (37) Narayanan, S.; Epp, V.; Wilkening, M.; Thangadurai, V. *RSC Adv.* **2012**, *2*, 2553–2561.
- (38) Choi, M.; Matsunaga, K.; Oba, F.; Tanaka, I. *J. Phys. Chem. C* **2009**, *113*, 3869–3873.
- (39) Müller, D.; Gessner, W. *Polyhedron* **1983**, *11*, 1195–1198.
- (40) Müller, D.; Gessner, W.; Behrens, H.-J.; Scheler, G. *Chem. Phys. Lett.* **1981**, *79*, 59–62.
- (41) Bloembergen, N.; Purcell, E.; Pound, R. *Phys. Rev.* **1948**, *73*, 679–712.
- (42) Murugan, R.; Thangadurai, V.; Weppner, W. *Appl. Phys. A: Mater. Sci. Process.* **2008**, *91*, 615–620.
- (43) Stilbs, P. *Progr. NMR Spectrosc.* **1986**, *19*, 1–45.
- (44) Karlicek, R. F., Jr.; Lowe, I. J. *J. Magn. Reson.* **1980**, *37*, 75–91.
- (45) Fischer, D. M.; Duwe, P.; Indris, S.; Heitjans, P. *Solid State Nucl. Magn. Reson.* **2004**, *26*, 74–83.
- (46) Gutsze, A.; Masierak, W.; Geil, B.; Kruk, D.; Pahlke, H.; Fujara, F. *Solid State Nucl. Magn. Reson.* **2005**, *28*, 244–249.
- (47) Heitjans, P.; Indris, S. *J. Phys.: Condens. Matter* **2003**, *15*, R1257–R1289.
- (48) Wolfenstine, J.; Rangasamy, E.; Allen, J. L.; Sakamoto, J. *J. Power Sources* **2012**, *208*, 193–196.

Chapter 4

Structure and Dynamics in the Binary Zintl-type Silicide $\text{Li}_{12}\text{Si}_7$

4.1 The Li-Si system

The binary phase diagram (see Fig. 4.1) of Li and Si contains of 5 stable compounds: LiSi [154,155], $\text{Li}_{12}\text{Si}_7$ [156, 157], Li_7Si_3 [158–160], $\text{Li}_{13}\text{Si}_4$ [161], $\text{Li}_{21}\text{Si}_5$ [162]. Additionally, amorphous Li-Si [163–166] and the metastable $\text{Li}_{15}\text{Si}_4$ compound [167–170] which occur in electrochemical lithiation [166, 171–173] have been reported. The Zintl-type silicides contain different types of Zintl-anions. With increasing Li content more electrons are provided and the net charge per Si atom of the Zintl ions occurring in the silicides increases with increasing Li content as shown in Table 4.1.

The lithium silicides are not only interesting from a fundamental point of view: silicon might replace carbon as anode materials in Li-ion batteries in future battery concepts. Silicon as an anode material has been proposed 30 years ago already [163, 164, 171, 172, 174–177]. The theoretical specific capacity of silicon-based anodes is by nearly a factor of 10 larger than that of carbon-based ones, but the high volumetric changes led cracks in the material and, thus, to large irreversible capacity losses in the first cycles already. This problem is likely to be overcome in new Si-based anode concepts working with nano-wires, nano-particles, or nano-composite materials. [178–183] The future has to show whether it is possible to upscale the fabrication of these new prototype batteries.

In spite of the promising prospect of Li-Si materials, until a few years ago, hardly any data on the Li diffusivity in these materials were found in the literature. In 1960, the diffusion of Li atoms

Zintl anion	net charge per Si	LiSi	$\text{Li}_{12}\text{Si}_7$	Li_7Si_3	$\text{Li}_{13}\text{Si}_4$	$\text{Li}_{21}\text{Si}_5$	$\text{Li}_{15}\text{Si}_4$
$[\text{Si}^-]_n$ -network	-1	×	—	—	—	—	—
Si_5^{6-} -rings	-1.2	—	×	—	—	—	—
Si_4^{10-} -stars	-2.5	—	×	—	—	—	—
Si_2^{4-} -dumbbells	-2	—	—	×	×	—	—
isolated Si_4^-	-4	—	—	—	×	×	×

Table 4.1: Zintl anions in binary lithium silicides

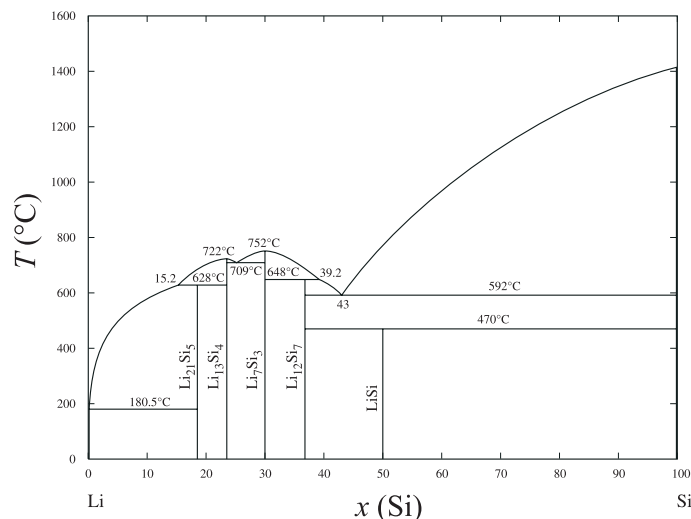


Figure 4.1: The binary phase diagram of Li and Si. Redrawn after Ref. [153] with corrected stoichiometry of the Li-richest compound $\text{Li}_{21}\text{Si}_5$.

in bulk Si was determined, [184, 185] in 1981, a GITT-study (galvanostatic intermittent titration technique) at high temperatures was presented. [186] RT-data on the Li diffusivity in Si half cells was added only recently. [187, 188] A fundamental study on the Li ion dynamics from a microscopic point of view was completely missing.

4.2 Li dynamics in $\text{Li}_{12}\text{Si}_7$

In this work, the binary silicide $\text{Li}_{12}\text{Si}_7$ was examined with ^7Li NMR relaxometry. The results are already published (A. Kuhn *et. al.*, “Li Ion Diffusion in the Anode Material $\text{Li}_{12}\text{Si}_7$: Ultrafast Quasi-1D Diffusion and Two Distinct Fast 3D Jump Processes Separately Revealed by ^7Li NMR Relaxometry”, *J. Amer. Chem. Soc.* 133 (2011) 11018, Ref. [189] and pages 121-125). The paper is shown below (page 122). Hereby, three dynamic processes occurring on well-separated time scales could be extracted. The NMR SLR rates of the fastest process exhibit properties typical of 1D diffusion processes. [78]

With the atomic-scale NMR relaxometry technique, it is neither possible to relate the process to structural features of the compound nor to decide whether the observed dynamic process is a local Li jump process or whether it gives rise to long-range Li diffusion - although the fastest process seen in NMR relaxometry was in good agreement with the high-temperature diffusion coefficient from the GITT study in the literature. [186]

Therefore, as a next step, FG-NMR measurements were performed. This nuclear method is capable of determining tracer-diffusion coefficients. In a first attempt, MAS-PFG-NMR were conducted in cooperation with Prof. Dr. D. Freude (University of Leipzig). However, here, the equipment was not sensitive enough to determine diffusion coefficients in the temperature range accessible with the probe. Therefore, I cooperated with Dr. M. Kunze (MEET, University of Münster) for PFG-NMR measurements with a commercial static PFG-probe (Bruker, Diff 30). Here, Li tracer diffusion coefficients could be determined at 298 K and 313 K. The results corroborated the assumption

that the fast diffusion process is of long-range nature. Very recently, I additionally performed SFG NMR measurements at high temperatures. These results are summarized in the poster presented on page 134 (Kuhn *et al.* “Insight into the Li ion dynamics in Li₁₂Si₇: Combining PFG NMR, 1D/2D MAS NMR, and NMR relaxometry”) shown below. The FG-NMR measurements did not show clear indications of a 1D diffusion process. On a macroscopic scale, the Li dynamics seems to be rather of 3D nature. Nevertheless, diffusion-time dependent PFG-NMR measurements are needed to clarify this beyond doubt. Hereby, the time-dependence of typical of single-file diffusion [190] which seems translate into SLR NMR might be detected.

4.3 Structural aspects of Li₁₂Si₇

In order to connect the processes observed in NMR relaxometry with the structural features of Li₁₂Si₇, ⁷Li and ⁶Li MAS NMR measurements were performed in December 2010. I observed the same ⁷Li NMR lines in the spectrum as already reported by Key *et al.* (see Ref. [191]) in 2007. Interestingly, a line appears at very low ppm-values, namely -17.2 ppm. Key *et al.* attributed it to an impurity. However, in my view, an alternative explanation was an aromatic shift of the Li6-position in Li₁₂Si₇ residing between two possibly aromatic Si₅⁶⁻-rings. This aromaticity has been proposed in theoretical studies ever since the compound was known. [157,192–195] Using ⁶Li and ⁷Li exchange NMR, I could show that the Li line at -17.2 ppm belongs to the same lattice as the other lines observed. Therefore, it could not be an impurity. The most reasonable assumption, thus, was the aromaticity of the Si₅⁶⁻-rings. The Si₅⁶⁻ Zintl ions also occur in the ternary silicide Li₈MgSi₆ [196,197]; the ⁷Li MAS spectrum of this compound also shows a line with a large upfield shift (about -16 ppm) which further corroborates the assignment of the shifted line to the Li site between the (aromatic) rings. This was the first experimental evidence of aromaticity of an per-sila ring - the publication is added on page 126 (A. Kuhn *et al.*, “Li NMR Spectroscopy on Crystalline Li₁₂Si₇: Experimental Evidence for the Aromaticity of the Planar Cyclopentadienyl-Analogous Si₅⁶⁻-rings” *Angew. Chem. Int. Ed.* 50 (2011) 12099, Ref. [198] and pages 126-133). The publication was recognized in scientific media (*Science* **334** (2011) 739, *Nachr. Chem.* **60** (2012) 107), *Nachr. Chem.* **60** (2012) 260).

As a next step, I performed ²⁹Si NMR on enriched samples as well as temperature-dependent ⁷Li MAS NMR. Some results are shown in Fig. 4.2. For a deeper understanding of the spectra, HETCOR NMR measurements are required. To this end, we profit from recent publications on structural NMR on Li₁₂Si₇ by the groups of C. P. Grey (Cambridge, UK) and H. Eckert (Münster, Germany). They mainly focused on resolving structural aspects of Li₁₂Si₇ with the help of advanced ²⁹Si and ^{6,7}Li MAS NMR techniques. [199,200]

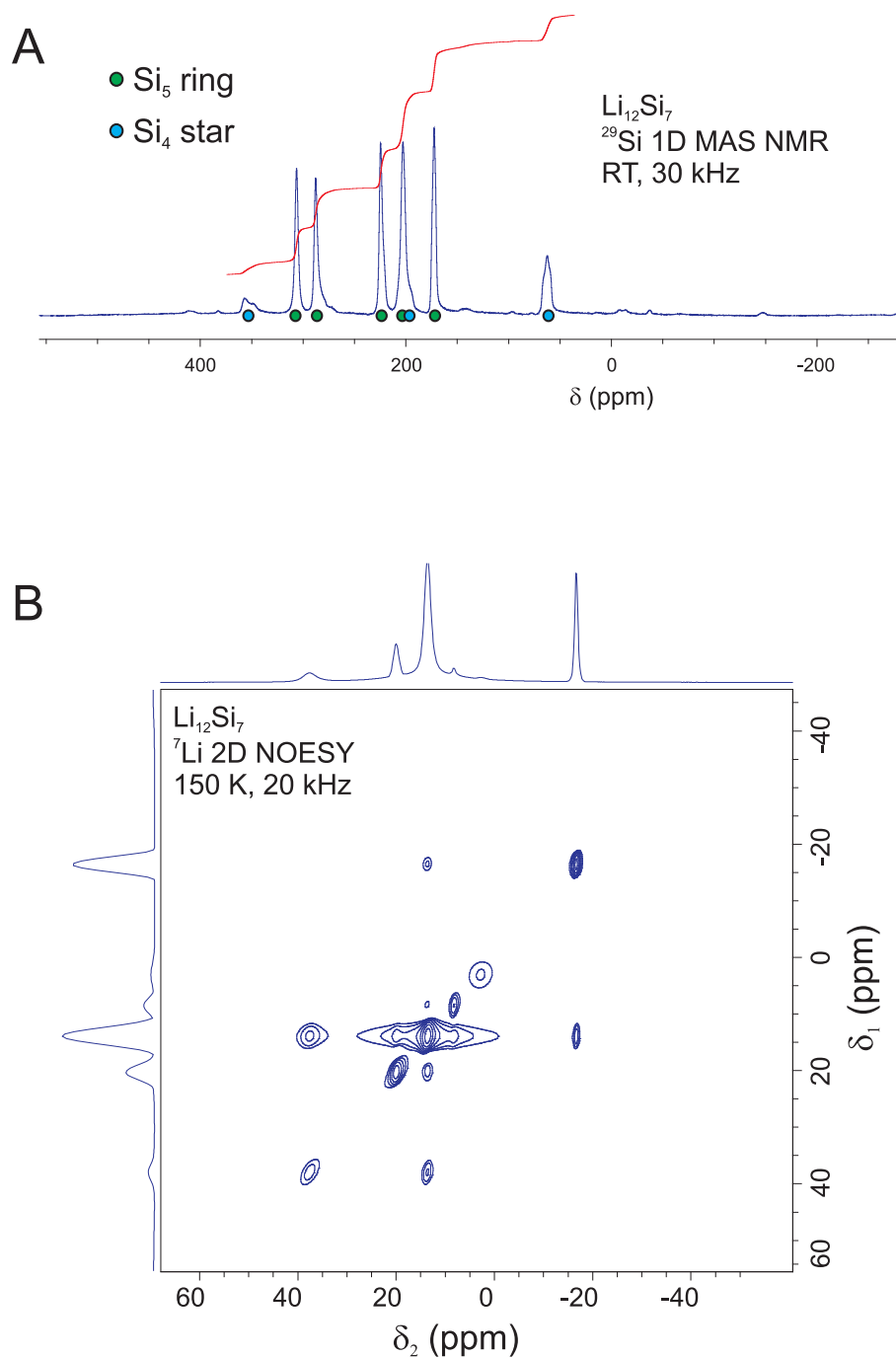


Figure 4.2: A: Room-temperature ²⁹Si MAS NMR spectrum of Li₁₂Si₇ measured at 14.1 T and a spinning rate of 30 kHz. The assignment of the lines to the Zintl anions was assumed from the integrals. B: Low-temperature ⁷Li 2D NOESY spectrum measured at 150 K, 11.7 T, a spinning rate of 20 kHz and a mixing time of 100 ms. Dipolar coupling and/or exchange is observed between all lines except the impurity at 0 ppm. This spectrum was recorded in the Bruker BioSpin labs by Dr. S. Wegner.

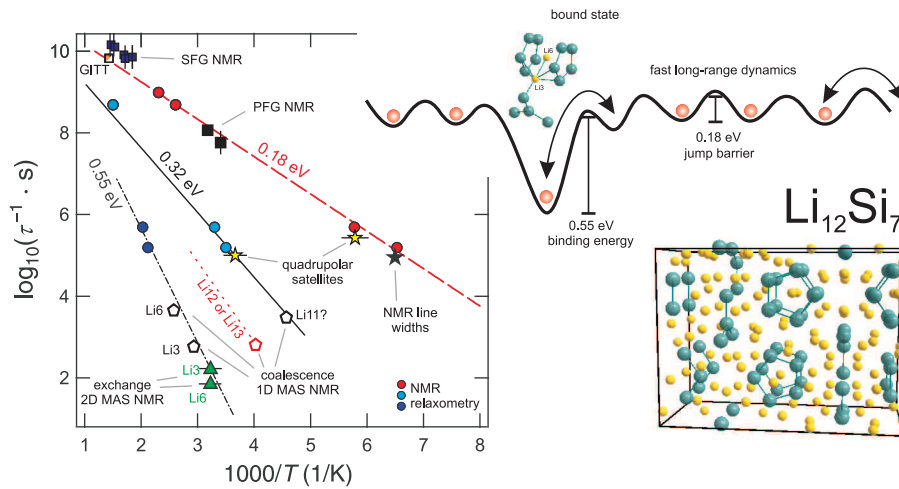


Figure 4.3: Li jump processes occurring in $\text{Li}_{12}\text{Si}_7$ as derived from various ^7Li NMR techniques. The fastest process activated by roughly 0.2 eV is relevant for long-range Li transport in $\text{Li}_{12}\text{Si}_7$. The other processes connect less mobile Li sites with the fast diffusing ion reservoir.

4.4 Correlating Structure and Dynamics in $\text{Li}_{12}\text{Si}_7$

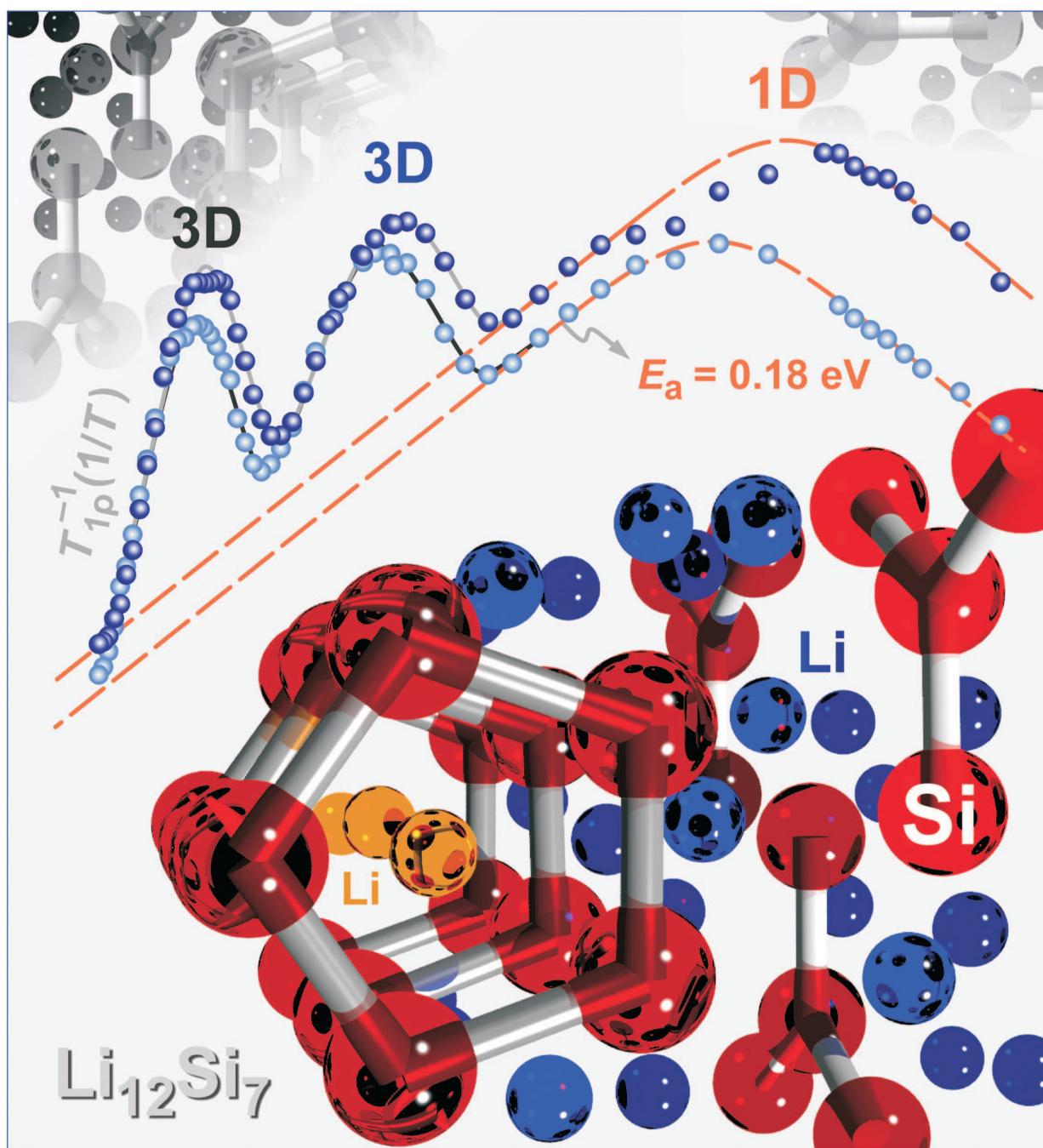
Taking together my results and those of the Refs. [199] and [200], a consistent picture of the structure and dynamics of $\text{Li}_{12}\text{Si}_7$ is obtained. This is outlined in the poster on page 134 already mentioned above (Kuhn *et al.* “Insight into the Li ion dynamics in $\text{Li}_{12}\text{Si}_7$: Combining PFG NMR, 1D/2D MAS NMR, and NMR relaxometry”). Here, additionally, exchange rates obtained from mixing-time dependent ^7Li MAS 2D exchange NMR measurements are added. Fig. 4.3 summarizes the progress in understanding the Li dynamics which has been obtained, so far.

Only few measurements are required to complete the picture: Low-temperature CP-MAS measurements would allow one to assign one more NMR line to a crystallographic site. However, due to principle technical limitations the 9 Li positions which take part in the very fast diffusion process cannot be resolved experimentally, so far. Here, MD simulations might be necessary in order to obtain a clearer picture of the single jump processes underlying the overall Li dynamics.

July 27, 2011
Volume 133
Number 29
pubs.acs.org/JACS

J | A | C | S

JOURNAL OF THE AMERICAN CHEMICAL SOCIETY



Li Ion Diffusion in the Anode Material $\text{Li}_{12}\text{Si}_7$: Ultrafast Quasi-1D Diffusion and Two Distinct Fast 3D Jump Processes Separately Revealed by ^7Li NMR Relaxometry

Alexander Kuhn,^{*,†} Puravankara Sreeraj,[‡] Rainer Pöttgen,[‡] Hans-Dieter Wiemhöfer,[‡] Martin Wilkening,[†] and Paul Heitjans^{*,†}

[†]Institute of Physical Chemistry and Electrochemistry, and ZFM - Center for Solid State Chemistry and New Materials, Leibniz University Hannover, Callinstr. 3-3a, 30167 Hannover, Germany

[‡]Institute of Inorganic and Analytical Chemistry, University of Münster, Corrensstr. 28-30, 48149 Münster, Germany

S Supporting Information

ABSTRACT: The intermetallic compounds Li_xSi_y have attracted considerable interest because of their potential use as anode materials in Li ion batteries. In addition, the crystalline phases in the Li–Si phase diagram turn out to be outstanding model systems for the measurement of fast Li ion diffusion in solids with complex structures. In the present work, the Li self-diffusivity in crystalline $\text{Li}_{12}\text{Si}_7$ was thoroughly probed by ^7Li NMR spin–lattice relaxation (SLR) measurements. Variable-temperature and -frequency NMR measurements performed in both the laboratory and rotating frames of reference revealed three distinct diffusion processes in $\text{Li}_{12}\text{Si}_7$. The diffusion process characterized by the highest Li diffusivity seems to be confined to one dimension. It is one of the fastest motions of Li ions in a solid at low temperatures reported to date. The Li jump rates of this hopping process followed Arrhenius behavior; the jump rate was $\sim 10^5 \text{ s}^{-1}$ at 150 K and reached 10^9 s^{-1} at 425 K, indicating an activation energy as low as 0.18 eV.

Silicon is intended to be used as negative electrode material for Li ion batteries. This is mainly due to its extraordinarily high specific capacity, which is a factor of 10 higher than that of conventionally used carbon anodes. Technological problems due to the high volumetric change of Si-based anodes and the resulting loss of capacity during cycling are likely to be overcome.^{1–4} In general, high Li diffusivity in electrode materials is greatly favorable for the development of rechargeable batteries with optimum performance. However, in spite of the technological significance of Si-based anodes within the scope of energy storage, data on the diffusion of Li in Li_xSi_y are still rare.^{5–7} In particular, there have been no studies of the jump processes by microscopic (i.e., atomic-scale) methods such as NMR spectroscopy.^{8,9} The available solid-state NMR techniques are capable of reliably probing Li diffusion parameters over a wide dynamic range.^{8–11} In addition to the aforementioned technological relevance in battery research, lithium silicides provide interesting model systems for fundamental ^7Li NMR diffusion studies. The phase diagram of lithium and silicon shows five crystalline intermetallic Zintl-like phases: Li_2Si_3 , Li_3Si_4 , Li_7Si_3 , $\text{Li}_{12}\text{Si}_7$, and LiSi .^{2,12,13} A metastable crystalline phase with the

composition $\text{Li}_{15}\text{Si}_4$ and amorphous Li_xSi_y also exist. The latter phases are obtained by electrochemical lithiation.^{14,15}

Here we report on the Li self-diffusivity in crystalline $\text{Li}_{12}\text{Si}_7$, which among the lithium silicides shows the most interesting crystallographic structure, containing a one-dimensional (1D) silicon backbone, in particular, which is filled with and surrounded by lithium ions on 13 different crystallographic sites.^{16–18} $\text{Li}_{12}\text{Si}_7$ was prepared from a melt of the elemental starting materials in a niobium tube under dry argon (see below). As confirmed by powder X-ray diffraction (XRD), a pure, crystalline product of orthorhombic $\text{Li}_{12}\text{Si}_7$ (space group *Pnma*) was obtained.

^7Li NMR spectroscopy performed under static conditions (i.e., on nonrotating samples) was used to probe microscopic Li diffusion parameters in the mixed conductor $\text{Li}_{12}\text{Si}_7$. ^7Li NMR line shape measurements are highly useful for classifying materials as ionic conductors in a qualitative manner.^{19–21} Quantitative information on the diffusive jump process can be obtained in a rather direct way via variable-temperature ^7Li NMR spin–lattice relaxation (SLR) measurements. From diffusion-induced NMR SLR rates, dynamic parameters (i.e., absolute jump rates and activation enthalpies) can be deduced.¹⁹ Moreover, frequency-dependent NMR SLR rate measurements, even when performed on a powder sample, contain valuable information on the dimensionality of the jump process under investigation.²²

^7Li NMR spectra (Figure 1) were recorded over the temperature range from 125 to 723 K at a resonance frequency ($\omega_0/2\pi$) of 155.4 MHz. At 125 K, the line is broad and has a complex shape due to (i) nonaveraged dipole–dipole interactions of the ^7Li nuclei, (ii) chemical shift anisotropies, and (iii) interactions of the quadrupole moment of ^7Li with the electric field gradients at the various crystallographic Li sites in $\text{Li}_{12}\text{Si}_7$. At low temperatures *T*, the line width $\Delta\omega/2\pi$ of the central transition is given by the so-called rigid lattice value $\Delta\omega_{\text{rl}}/2\pi$, which is ~ 16 kHz in the present case. With increasing temperature, dipole–dipole interactions are progressively averaged as a result of the thermally activated motion of the ^7Li ions. Significant line narrowing sets in when the Li jump rate (τ^{-1}) becomes comparable to the spectral width $\Delta\omega_{\text{rl}}/2\pi$. In the case of $\text{Li}_{12}\text{Si}_7$, the onset of this motional narrowing was observed at a very low temperature of ~ 130 K (see Figure 1B). From the inflection point of the corresponding

Received: March 4, 2011

Published: May 30, 2011

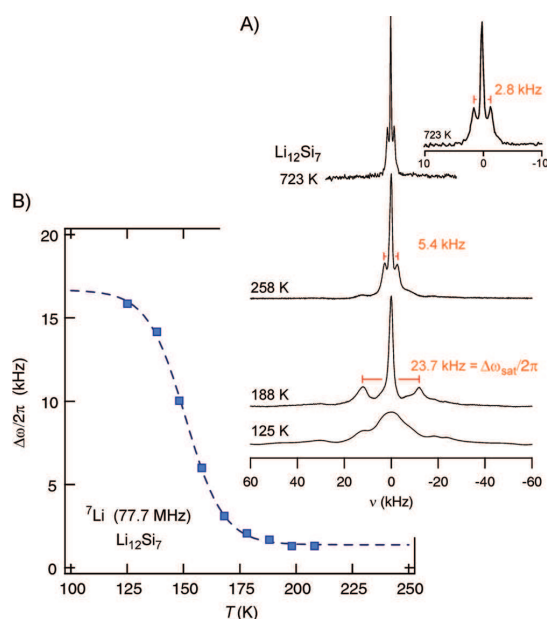


Figure 1. (A) ${}^7\text{Li}$ NMR spectra recorded at various temperatures (125, 188, and 258 K at $\omega_0/2\pi = 155.4$ MHz and 723 K at 77.7 MHz). The spectral distances of the quadrupolar satellites ($\Delta\omega_{\text{sat}}/2\pi$) are indicated. (B) Motional narrowing of the line width (full width at half-maximum) of the central ${}^7\text{Li}$ NMR transition.

narrowing curve $\Delta\omega(T)$ [obtained by plotting $\Delta\omega$ for the central transition (see below) as a function of T], it is possible to obtain a rough estimate of the Li jump rate at the respective temperature via the relation $\tau^{-1} \approx \Delta\omega_{\text{c}}$. It turned out that the rate τ^{-1} was on the order of 10^5 s^{-1} at 150 K.

The ${}^7\text{Li}$ NMR spectra at 188, 258, and 723 K showed the typical shape of the powder spectrum for a spin $3/2$ nucleus, consisting of a central transition line and quadrupolar satellite intensities. As can be clearly seen in Figure 1 A, the quadrupolar powder pattern (and thus the mean field gradient experienced by the Li ions) changed with increasing temperature. If it is assumed that the asymmetry parameter of the quadrupolar coupling tensor vanishes, the mean quadrupolar coupling constants δ_{Q} can be determined from the corresponding spectral distances $\Delta\omega_{\text{sat}}/2\pi$ (marked in Figure 1 A by vertical lines pointing to the singularities of the powder pattern) as $\delta_{\text{Q}} = 2 \times \Delta\omega_{\text{sat}}/2\pi$. In the present case, δ_{Q} did not exhibit a gradual change with increasing temperature, as might be ascribed to thermal expansion of the material. Here, as T increased, the satellite intensities gradually vanished, and new ones emerged at even higher temperatures. This behavior can be explained by a stepwise averaging of electric quadrupolar interactions due to Li jump processes between the distinct crystallographic sites in $\text{Li}_{12}\text{Si}_7$. Thus, at least three different jump processes, each one leading to a specific mean coupling constant δ_{Q} , were subsequently activated in the silicite, resulting in an intermittent reduction of the electric quadrupole interaction. The mean coupling constants δ_{Q} were found to be 47.4, 10.8, and 5.6 kHz at 188, 258, and 723 K, respectively.

NMR SLR measurements gave even clearer insight into the lithium dynamics of crystalline $\text{Li}_{12}\text{Si}_7$. In the Arrhenius

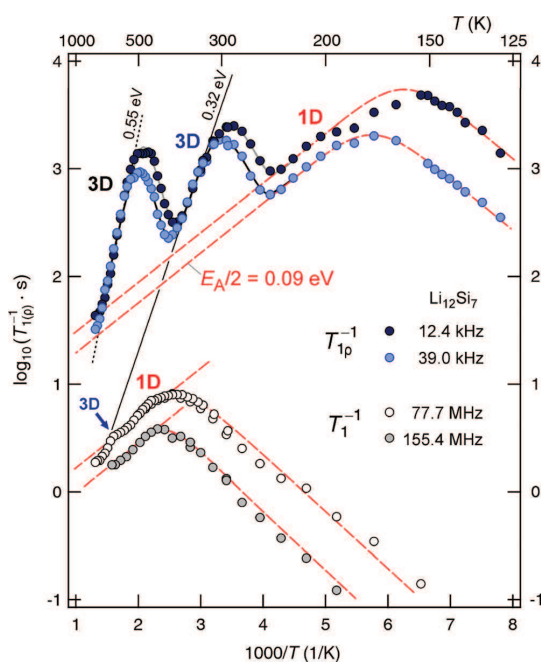


Figure 2. Arrhenius plots of the ${}^7\text{Li}$ NMR SLR rates in the laboratory frame, T_1^{-1} , at $\omega_0/2\pi = 155.4$ and 77.7 MHz and those in the rotating frame, $T_{1\rho}^{-1}$, at $\omega_1/2\pi = 39.0$ and 12.4 kHz. Dashed lines are guides to the eye. See the text for further explanation.

plots shown in Figure 2, ${}^7\text{Li}$ NMR SLR rates in the laboratory and rotating frames of reference (T_1^{-1} and $T_{1\rho}^{-1}$, respectively) are shown. The rates were recorded at different resonance ($\omega_0/2\pi = 77.7$ and 155.4 MHz) and locking ($\omega_1/2\pi = 12.4$ and 39.0 kHz) frequencies, respectively. Here the NMR SLR is induced solely by local fluctuations of magnetic dipolar or electric quadrupolar interactions due to the motion of the Li spins. As is well-known,²¹ these temporal fluctuations can be described in terms of a correlation function $G(\tau')$, and the NMR SLR rate is proportional to the Fourier transform of $G(\tau')$ [i.e., the spectral density $J(\omega_{(1)})$] at or close to the respective NMR frequency. When purely induced by diffusion processes, the NMR SLR rate passes through a maximum at a characteristic temperature T_{max} at which $1/\tau$, the correlation rate of the jump process (which is essentially the average jump rate τ^{-1}), equals the NMR frequency (i.e., $\omega \approx \tau^{-1}$). If the NMR SLR rates are measured as a function of T at different resonance frequencies, an absolute jump rate $\tau^{-1}(T_{\text{max}})$ can be deduced from each recorded rate peak $T_{1(\rho)}^{-1}(1/T)$. With the use of NMR SLR in the laboratory and rotating frames of reference, both the megahertz and kilohertz ranges can be covered, allowing the determination of the activation energies E_A and the lithium jump rates. The value of $\tau^{-1}(1/T)$ is expected to follow Arrhenius behavior according to the equation $\tau^{-1} = \tau_0^{-1} \exp(-E_A/k_B T)$, where τ_0^{-1} is the pre-exponential factor and k_B is Boltzmann's constant.

Obviously, the global maxima of the two $T_1^{-1}(1/T)$ curves and the low-temperature maxima of the two $T_{1\rho}^{-1}(1/T)$ curves in Figure 2 belong to the same ultrafast diffusion process. The corresponding flanks of the four SLR rate peaks show the same

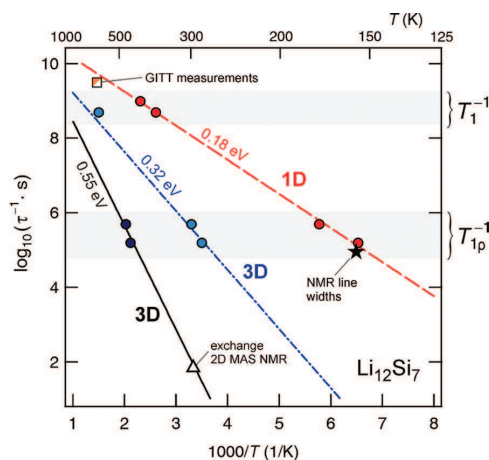


Figure 3. Li jump rates τ^{-1} extracted from the NMR SLR rate maxima of Figure 2; these jump rates are represented by circles. For comparison, the square shows a jump rate derived from literature data (GITT measurements⁵), the star a Li jump rate estimated from the ^7Li NMR line narrowing (see Figure 1), and the triangle a Li jump rate from a first 2D exchange MAS NMR measurement.

Table 1. High-Temperature (HT) and Low-Temperature (LT) Limits of the Spectral Density Function $J(\omega)$ for 1D, 2D, and 3D Diffusion^a

	HT limit	LT limit
1D	$(\tau/\omega)^{0.5}$	$\tau^{-1}\omega^{-\beta}$
2D	$\tau \ln(1/\omega\tau)$	$\tau^{-1}\omega^{-\beta}$
3D	τ	$\tau^{-1}\omega^{-\beta}$

^aThe model parameter β ranges between 1 and 2 and accounts for correlation effects due to Coulomb interactions of the jumping ion or to structural disorder (see ref 8).

slope. The jump rates associated with the peak maxima can be obtained using the maximum conditions $\omega_0 \approx \tau^{-1}$ and $2\omega_1 \approx \tau^{-1}$ (see above).^{19,22,23} The resulting rates $\tau^{-1}(T = T_{\text{max}})$ are shown in Figure 3 in an Arrhenius plot (red data points). The dashed line represents an Arrhenius fit to the four points, yielding $E_A = 0.18$ eV. The value of τ_0^{-1} turned out to be on the order of 10^{11} s^{-1} . For comparison, a Li jump rate deduced using galvanostatic intermittent titration technique (GITT) measurements (see ref 5) is also included.

The behavior of the NMR SLR rate flanks [i.e., for temperatures above that of the rate maximum ($\tau^{-1} \gg \omega$) or below it ($\tau^{-1} \ll \omega$)] requires a model-dependent examination. The high-temperature (HT) and low-temperature (LT) limits of $J(\omega)$ according to models for 1D,²² 2D,^{22,24} and 3D^{19,22} diffusion in solids are listed in Table 1 (see ref 8). In the case of 3D diffusion, the NMR SLR rate in the high-temperature limit ($\tau^{-1} \gg \omega$) is proportional to τ . As a result, the activation energy derived from that flank should be equal to that obtained from the jump rates $\tau^{-1}(T_{\text{max}})$ obtained from the maxima of the SLR rate peaks. Furthermore, the NMR SLR rate on the HT flank is expected to be independent of the resonance frequency applied.^{19,22} However, in the present case, *neither* of these predictions was met for the four diffusion-induced SLR rate peaks mentioned above and

highlighted in Figure 2 by dashed lines. Interestingly, the NMR SLR rates in the HT limit ($\tau^{-1} \gg \omega$) revealed a distinct frequency dependence. The corresponding HT flanks of the four rate peaks in Figure 2 seem to be parallel (cf. the dashed lines). The apparent activation energy deduced from the HT flanks was approximately half the actual activation energy that was obtained from the jump rates derived from the rate maxima (see the dashed line in Figure 3). These findings are clear indications that the ultrafast diffusion process observed for $\text{Li}_{12}\text{Si}_7$ is of a low-dimensional nature. According to the theoretical description for 1D diffusion given by Sholl,²² the diffusion-induced NMR SLR rate on the HT flank is proportional to $\tau^{0.5}\omega^{-0.5}$. Hereby, the factor $\tau^{0.5}$ is responsible for the smaller slope on the HT flank, which is expected to be half the slope in the Arrhenius plot. The factor $\omega^{-0.5}$ brings about the frequency dependence. Although there are many systems in which (quasi) 1D diffusion occurs, in none of these, except for the related phenomenon of 1D diffusion of electron spins,²⁵ could the theory be checked until now. Essentially, the lack of suitable data stemmed either from the circumstance that the HT flank was not accessible because the diffusion process was too slow or the fact that the HT flank was masked by strong interactions of Li^+ with paramagnetic ions dominating the NMR SLR rate. In the latter case, the NMR SLR rate would no longer be governed solely by Li diffusion. However, in the case of $\text{Li}_{12}\text{Si}_7$, the two predictions for 1D diffusion were met with satisfying agreement. The apparent activation energy (0.09 eV; see Figure 2) was approximately half the actual one, and the frequency dependence of the SLR rate on the HT flank turned out to be $\sim \omega^{-0.4}$, whereby a frequency range of more than 3 orders of magnitude was covered. Therefore, we assume that this diffusion process is a quasi-1D one. Preliminary considerations with regard to the crystal structure and electronic bonding properties of $\text{Li}_{12}\text{Si}_7$ (see refs 13, 18, and 33) make our assumptions plausible. In particular, the extended structural analysis by Nesper et al.¹⁸ clearly showed the existence of two well-separated 1D infinitesimal partial structure elements along the [100] direction, corresponding to the compositions $[\text{Li}_{12}\text{Si}_4]$ and $[\text{Li}_6\text{Si}_5]$. These findings support our conclusion about the quasi-1D or at least strongly anisotropic diffusion process. For comparison, the experimental verification of the predicted spectral density function for Li_xTiS_2 showing pure 2D diffusion was previously reported by our group.²⁶

Apart from this low-dimensional and very fast dynamic process in $\text{Li}_{12}\text{Si}_7$, the $T_{1\rho}^{-1}(1/T)$ data revealed two additional jump processes showing up as two well-separated ^7Li NMR SLR rate peaks at higher temperatures (see Figure 2). The jump rates derived from the corresponding rate maxima are also included in Figure 3 (see the solid and dashed-dotted lines).

The underlying motional processes of the two $T_{1\rho}^{-1}(1/T)$ rate peaks exhibit the characteristics of 3D diffusion, since in both cases the rates on the HT flanks coincide (i.e., the diffusion-induced SLR rates are independent of the locking frequency used). The faster of the two processes caused the $T_{1\rho}^{-1}$ rate to pass through characteristic peak maxima near room temperature (at 3.5 K^{-1} on the $1000/T$ scale; see Figure 2). Presumably, the same process led to the slight shoulder appearing at $1000/T \approx 1.5 \text{ K}^{-1}$ on the HT flank of the rate peak $T_{1\rho}^{-1}(1/T)$ measured at 77.7 MHz (see the arrow in Figure 2). For measurements at 155.4 MHz, only temperatures up to 633 K were accessible with our equipment. This was not high enough to clearly reach the corresponding rate maximum at the largest resonance frequency used. Still, the respective incipient rate peak seems to

be indicated in the SLR rates measured at the highest temperatures and 155.4 MHz. The activation energy of the faster 3D jump process obtained from the three rate maxima (dashed-dotted line in Figure 3) and the one taken from the slope of the HT flank of the rotating-frame SLR rates (solid line in Figure 2) are identical within experimental error (0.32 eV). Beyond doubt, this is expected for a 3D diffusion process (see above and Table 1).

The second 3D process, which is characterized by the highest activation energy, was visible only in the $T_{1\rho}^{-1}(1/T)$ data (see Figure 2). The corresponding Arrhenius line in Figure 3 (black line) is not a fit through the two points obtained from the SLR rate maxima. Here, the activation energy was taken from the HT flank of the rotating-frame SLR rates, yielding $E_A = 0.55$ eV for this 3D process. The Arrhenius line for this jump process is in very good agreement with the Li jump rate deduced from a first measurement by 2D exchange magic-angle-spinning (MAS) NMR spectroscopy.²⁷

As also found for the quasi-1D process, the pre-exponential factors τ_0^{-1} , which are interpreted as attempt frequencies of the two 3D processes, were on the order of 10^{11} s^{-1} . This value is ~ 2 orders of magnitude lower than the optical phonon Li modes of $\text{Li}_{12}\text{Si}_7$ obtained from ab initio calculations.¹³ Generally, the tendency to have lower pre-exponential factors in the Arrhenius relation in comparison with the phonon frequencies can be understood in terms of cooperative motions or strong anharmonicities of the potential landscape next to a vacancy; the latter might lead to lower vibrational frequencies than in the vacancy-free bulk (for a discussion of low pre-exponential factors obtained by NMR spectroscopy, see, e.g., refs 24, 28, and 29).

In summary, the low-dimensional hopping process found for polycrystalline $\text{Li}_{12}\text{Si}_7$ ($E_A = 0.18$ eV) is one of the fastest Li diffusion processes in solids known in the literature. Its quasi-1D nature has been revealed by frequency-dependent NMR SLR measurements. The fast 3D Li jump process ($E_A = 0.32$ eV), although much slower than the quasi-1D process, is nonetheless comparable to diffusion processes in typical superionic Li conductors.^{30–32} The slower 3D process has an activation energy of 0.55 eV, which is similar to that for self-diffusion in lithium metal.³³ To our knowledge, this is the first system in which three distinct Li jump processes, which are activated one after the other according to their increasing jump barriers, have been separately characterized using diffusion-induced NMR SLR measurements.

Subsequent studies will include the identification of the diffusion pathways and sites related to the revealed jump processes. From the structure, even many more than those three distinct jump processes are expected. Presumably, exchange processes between comparable crystallographic sites show similar jump barriers and therefore are not separately seen in NMR relaxometry. 1D and 2D MAS NMR measurements carried out at very low temperatures might help identify the crystallographic sites connected to the three main diffusion processes probed by NMR SLR.

■ ASSOCIATED CONTENT

S Supporting Information. Sample preparation and experimental details. This material is available free of charge via the Internet at <http://pubs.acs.org>.

■ AUTHOR INFORMATION

Corresponding Author

kuhn@pci.uni-hannover.de; heitjans@pci.uni-hannover.de

■ ACKNOWLEDGMENT

Financial support by the BMBF within Project HE-Lion as well as by the DFG (FOR 1277) is greatly appreciated. A.K. gratefully acknowledges financial support by the Studienstiftung des Deutschen Volkes e.V.

■ REFERENCES

- (1) Weydanz, W. J.; Wohlfahrt-Mehrens, M.; Huggins, R. A. *J. Power Sources* **1999**, *81*, 237.
- (2) Key, B.; Bhattacharyya, R.; Morcrette, M.; Seznéc, V.; Tarascon, J.-M.; Grey, C. P. *J. Am. Chem. Soc.* **2009**, *131*, 9239.
- (3) Chan, C. K.; Peng, H.; Liu, G.; McIlwrath, K.; Zhang, X. F.; Huggins, R. A.; Cui, Y. *Nat. Nanotechnol.* **2008**, *3*, 31.
- (4) Hertzberg, B.; Alexeev, A.; Yushin, G. *J. Am. Chem. Soc.* **2010**, *132*, 8548.
- (5) Wen, C. J.; Huggins, R. A. *J. Solid State Chem.* **1981**, *37*, 271.
- (6) Ding, N.; Xu, J.; Yao, Y. X.; Wegner, G.; Fang, X.; Chen, C. H.; Lieberwirth, I. *Solid State Ionics* **2009**, *180*, 222.
- (7) Yoshimura, K.; Suzuki, J.; Sekine, K.; Takamura, T. *J. Power Sources* **2007**, *174*, 653.
- (8) Heitjans, P.; Schirmer, A.; Indris, S. In *Diffusion in Condensed Matter: Methods, Materials, Models*; Heitjans, P., Kärger, J., Eds.; Springer: Berlin, 2005; Chapter 9, p 369.
- (9) Wontcheu, J.; Bensch, W.; Wilkening, M.; Heitjans, P.; Indris, S.; Sideris, P.; Grey, C. P.; Mankovsky, S.; Ebert, H. *J. Am. Chem. Soc.* **2008**, *130*, 288.
- (10) Kuhn, A.; Narayanan, S.; Spencer, L.; Goward, G.; Thangadurai, V.; Wilkening, M. *Phys. Rev. B* **2011**, *83*, No. 094302.
- (11) Wilkening, M.; Heitjans, P. *Phys. Rev. B* **2008**, *77*, No. 024311.
- (12) (a) Nesper, R. *Prog. Solid State Chem.* **1990**, *20*, 1. (b) Okamoto, H. *J. Phase Equilib. Diffus.* **2009**, *30*, 118.
- (13) Chevrier, V. L.; Zwanziger, J. W.; Dahn, J. R. *J. Alloys Compd.* **2010**, *496*, 25.
- (14) Kubota, Y.; Escano, M. C. S.; Nakanishi, H.; Kasai, H. *J. Appl. Phys.* **2007**, *102*, No. 053704.
- (15) Evers, J.; Oehlinger, G.; Sextl, G. *Angew. Chem., Int. Ed. Engl.* **1993**, *32*, 1442.
- (16) Axel, H.; Schäfer, H.; Weiss, A. *Z. Naturforsch., B* **1965**, *20*, 1302.
- (17) von Schnering, H. G.; Nesper, R.; Curda, J.; Tebbe, K.-F. *Angew. Chem., Int. Ed. Engl.* **1980**, *19*, 1033.
- (18) Nesper, R.; von Schnering, H. G.; Curda, J. *Chem. Ber.* **1986**, *119*, 3576.
- (19) Bloembergen, N.; Purcell, E.; Pound, R. *Phys. Rev.* **1948**, *73*, 679.
- (20) Hendrickson, J.; Bray, P. *J. Magn. Reson.* **1973**, *9*, 341.
- (21) Abragam, A. *The Principles of Nuclear Magnetism*; Oxford University Press: Oxford, U.K., 1961.
- (22) Sholl, C. A. *J. Phys. C: Solid State Phys.* **1981**, *14*, 447.
- (23) Look, D. C.; Lowe, I. J. *J. Chem. Phys.* **1966**, *44*, 2995.
- (24) Richards, P. M. *Top. Curr. Phys.* **1979**, *15*, 141.
- (25) Mizoguchi, M.; Kume, K.; Shirakawa, H. *Solid State Commun.* **1984**, *50*, 213.
- (26) Küchler, W.; Heitjans, P.; Payer, A.; Schöllhorn, R. *Solid State Ionics* **1994**, *70*, 434.
- (27) Kuhn, A.; Sreeraj, P.; Pöttgen, R.; Wiemhöfer, H.-D.; Wilkening, M.; Heitjans, P. Submitted.
- (28) Richards, P. M. *Solid State Commun.* **1978**, *25*, 1019.
- (29) Huberman, B. A.; Boyce, J. B. *Solid State Commun.* **1978**, *25*, 759.
- (30) Knauth, P. *Solid State Ionics* **2009**, *180*, 911.
- (31) Robertson, A. D.; West, A. R.; Ritchie, A. G. *Solid State Ionics* **1997**, *104*, 1.
- (32) Thangadurai, V.; Weppner, W. *Ionics* **2006**, *12*, 81.
- (33) Heitjans, P.; Koerblein, A.; Ackermann, H.; Dubbers, D.; Fujara, F.; Stoeckmann, H. *J. Phys. F: Met. Phys.* **1985**, *15*, 41.

Aromaticity

Li NMR Spectroscopy on Crystalline $\text{Li}_{12}\text{Si}_7$: Experimental Evidence for the Aromaticity of the Planar Cyclopentadienyl-Analogous Si_5^{6-} Rings**

Alexander Kuhn,* Puravankara Sreeraj, Rainer Pöttgen, Hans-Dieter Wiemhöfer, Martin Wilkening,* and Paul Heitjans*

Since the pioneering work of West et al. in 1981^[1] that questioned the well-known double-bond rule, chemists working in the field of organometallics have been trying to synthesize silicon analogues of organic compounds containing π bonds. However, most of these compounds inherently lack thermodynamic stability, thus making their preparation a very challenging task. In these compounds, Si=Si π bonds have to be kinetically stabilized by large, sterically hindering groups. Very recently, Abersfelder et al.^[2] reported the synthesis of a tricyclic isomer of hexasilabenzene containing a Si_6 ring. Theoretical calculations suggest a nonclassical “dismutational” aromaticity of the nonplanar hexasilabenzene.^[3] However, classical benzene-like aromaticity is characterized by planarity and equal bond lengths that lead to an optimum overlap of the p orbitals to result in a cyclic electron delocalization. This effect increases the corresponding diamagnetic susceptibility.

Nuclear magnetic resonance (NMR) spectroscopy is a powerful technique that can be used to experimentally assess whether a structure should be regarded as aromatic or not. Aromatic compounds show characteristic and relatively large chemical shifts δ_{iso} , which are explained by a ring current induced by the magnetic field.^[4] A probe nucleus residing inside the anisotropic cone above or below the aromatic ring will be subjected to a shielding effect (upfield shift) that causes the NMR signal to appear at lower δ_{iso} values. To the best of our knowledge, classical aromaticity characterized by the criteria mentioned above has not been reported to date for a structural unit solely composed of Si. Lee and Sekiguchi^[5] previously reported two probably aromatic, positively charged complex ligands containing Si_3 and Si_4

rings. The Si_4 ligands are nearly planar and their formal charge agrees with the Hückel rule;^[6] these features are a good argument for the aromaticity of these compounds. However, the ultimate proof of their (carbon-like) aromaticity is still missing.

In this work, the crystalline Zintl phase $\text{Li}_{12}\text{Si}_7$ was investigated by both 1D and 2D ^6Li as well as ^7Li high-resolution, that is, magic angle spinning (MAS) NMR spectroscopy. The crystal structure of the binary silicide contains semi-infinite 1D $^{\infty}[\text{LiSi}_{10/2}]$ sandwich complexes (Figure 1).^[7] Remarkably, the corresponding Li MAS NMR

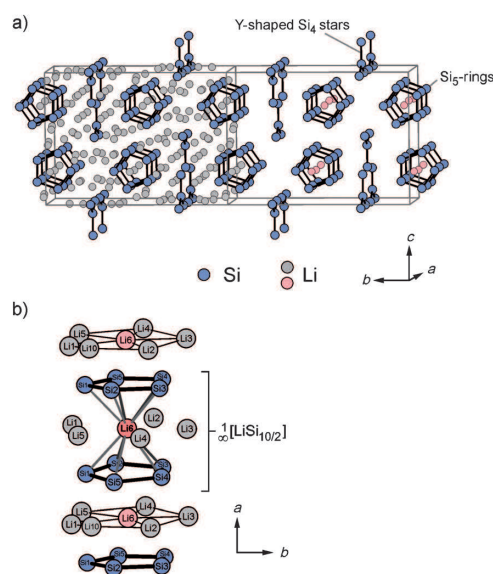


Figure 1. a) Crystal structure of the Zintl phase $\text{Li}_{12}\text{Si}_7$ ($Pnma$). In the right-hand unit cell, all Li atoms apart from Li6 are removed. b) Semi-infinite 1D sandwich complexes of $^{\infty}[\text{LiSi}_{10/2}]$ in $\text{Li}_{12}\text{Si}_7$. The notation follows that of Nesper et al., see Ref. [7b].

spectrum exhibits a distinct signal that is shifted upfield to -17.2 ppm. As we will show here, there is strong evidence that this NMR signal belongs to the Li ions sandwiched between the cyclopentadienyl-analogous Si_5^{6-} rings in $\text{Li}_{12}\text{Si}_7$. The suspected aromaticity of the planar Si_5^{6-} units, see for example Ref. [7b,c], results in a pronounced shielding of these

[*] A. Kuhn, Dr. M. Wilkening, Prof. Dr. P. Heitjans
Institute of Physical Chemistry and Electrochemistry
Leibniz University Hannover
Callinstrasse 3a, 30167 Hannover (Germany)
E-mail: kuhn@pci.uni-hannover.de
wilkening@pci.uni-hannover.de
heitjans@pci.uni-hannover.de

Dr. P. Sreeraj, Prof. Dr. R. Pöttgen, Prof. Dr. H.-D. Wiemhöfer
Institute of Inorganic and Analytical Chemistry
University of Münster
Corrensstrasse 28–30, 48149 Münster (Germany)

[**] Financial support by the DFG and the BMBF is gratefully acknowledged. A.K. acknowledges support by the Studienstiftung des deutschen Volkes e.V.

Supporting information for this article is available on the WWW under <http://dx.doi.org/10.1002/anie.201105081>.

Communications

Li ions. These rings, which are solely composed of silicon instead of carbon, meet the structural and magnetic criteria that are necessary for classical aromaticity.

Long before the work of West et al.,^[1] a large variety of Si-containing Zintl phases that show all kinds of Si–Si bonding situations were reported (see, for example, Ref. [8]). In a simple picture, in Zintl-type silicides, the silicon substructure is “forced” to distribute the additional electrons obtained from the electropositive metal. This process leads to a variety of different bonding situations including the formation of π bonds. While Si=Si π bonds in organometallic molecular compounds need to be kinetically stabilized and protected from electrophilic attack by large sterically hindering groups, Si=Si π bonds in Zintl-phase compounds are stabilized because of the mere absence of any electrophilic atom or group. Therefore, these compounds are not only kinetically stabilized but thermodynamically stable as long as the pure compound is considered.

Planar silicon rings^[7a,9] can be found in some of these phases. In particular, this is the case for the (nonparamagnetic) Zintl-type binary silicide $\text{Li}_{12}\text{Si}_7$ containing linear semi-infinite chains of $[\text{LiSi}_{10/2}]$ sandwich complexes (Figure 1.^[10] It is noteworthy that the latter structural motif is also present in the ternary compound Li_8MgSi_6 ^[9] (see the Supporting Information). The unit cell of the Zintl phase $\text{Li}_{12}\text{Si}_7$ is best described as $(\text{Li}_6^{6+}[\text{Si}_5]^{6-})_2 (\text{Li}_{12}^{10+}[\text{Si}_4]^{10-})_2$ and gives rise to two distinct arrangements of Si atoms, that is, planar Si_5 rings and ‘Y’-shaped Si_4 stars (see Figure 1). This structural model (Zintl ion concept) attributes the 26 electrons ($20\text{Si} + 6\text{Li}$) to the Si_5^{6-} ring, thus satisfying Hückel aromaticity.^[6] Theoretical studies predicted the aromaticity of the Si_5^{6-} ring (see Ref. [10] and references therein), however, this aromaticity has not been experimentally proven to date.

The Li NMR spectra shown here were recorded on a highly pure, polycrystalline $\text{Li}_{12}\text{Si}_7$ (natural abundance, 92.5% ^7Li , 7.5% ^6Li), which was prepared under Ar atmosphere in a niobium ampoule (for experimental details see the Supporting Information). The product was characterized by X-ray powder diffraction, and shows orthorhombic symmetry (*Pnma*). The refined lattice parameters are $a = 860.3(2)$, $b = 1976.9(4)$, $c = 1434.9(4)$ pm. These values are in very good agreement with the reported values. Variable-temperature Li MAS NMR spectra were recorded using a Bruker Avance III spectrometer in combination with a commercial 2.5 mm MAS probe (Bruker BioSpin). The spectrometer is connected to a cryomagnet with a shimmed magnetic field B_0 of 14.1 T. NMR spectra were recorded at a spinning frequency of 30 kHz.

^7Li and ^6Li MAS NMR spectra of $\text{Li}_{12}\text{Si}_7$ measured at room temperature (bearing gas temperature) are composed of four clearly resolved signals (Figure 2). Not all the crystallographic sites are resolved at room temperature because of extremely fast exchange processes of the Li ions residing outside the chains^[11] shown in Figure 1. In particular, the ^7Li MAS NMR spectra recorded at temperatures as low as 140 K (not shown here for the sake of brevity) show that the signal with the highest intensity (see Figure 2) is a coalesced signal with a mean chemical shift of $\delta = 16.1$ ppm at room temperature. As mentioned above, the Li NMR spectra show a clearly recognizable signal at $\delta_{\text{iso}} = -17.2$ ppm, which is

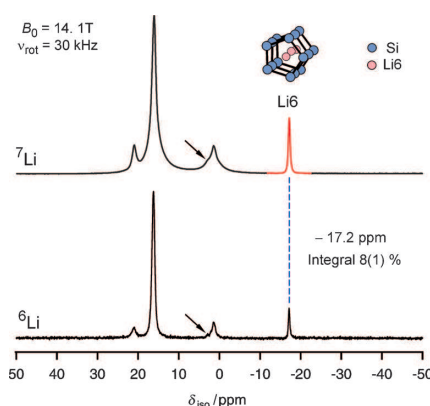


Figure 2. 1D ^7Li and ^6Li MAS NMR spectra of $\text{Li}_{12}\text{Si}_7$ at room temperature (bearing gas temperature) recorded at an external magnetic field B_0 of 14.1 T and a spinning frequency ν_{rot} of 30 kHz. The integral under the NMR signal at -17.2 ppm amounts to 8(1)% of the total integral of the spectrum. The arrow denotes a minor decomposition phase arising from unavoidable air contact in the MAS rotor.

independent of temperature (140–335 K). In general, the chemical shifts of Li^+ ions in nonparamagnetic and non-metallic compounds are very small (i.e., well below ± 10 ppm; see, for example, Ref. [12]). In our opinion, the existence of a ring current in the cyclopentadienyl-like Si_5^{6-} units in $\text{Li}_{12}\text{Si}_7$, which are isoelectronic with P_5^- ,^[13] is the simplest explanation for an upfield shift as large as -17.2 ppm. This explanation is in good agreement with previous considerations of Nesper, von Schnering, and Curda^[7b] (see also Ref. [7c]). Indeed, the reported calculated values are in the same range as investigated here: the calculated so-called nucleus-independent chemical shift NICS(1)^[14] of isoelectronic P_5^- amounts to values between -16 and -18 ppm depending on the procedure for calculating applied; the NICS_{zz}(1) value is reported to be -39.2 ppm.^[15] The corresponding NICS_{zz}(1) value of Si_5H_5^- (-32.1 ppm) is similar to that of Cp^- (-33.7 ppm; Cp = cyclopentadienyl) while the calculated diamagnetic shielding in slightly distorted (nonplanar) Si_5H_5^- was much smaller (-19.3 ppm).^[16] Based on these results, we conclude that the chemical shift of -17.2 ppm found in $\text{Li}_{12}\text{Si}_7$ is largely due to an aromatic ring current.^[17] Thus, the signal has to be identified with that of Li6 (see Figure 1 b), representing the Li site between the Si_5^{6-} rings. For comparison, the experimental value δ_{iso} of ^6Li in LiCp_2^- amounts to -13.1 ppm.^[18] This assignment is further corroborated by the fact that the integral under the corresponding NMR line amounts to 8(1)%, which is in excellent agreement with the expected value of 8.3% determined from the crystal structure. The same explanation is valid for the similarity of the corresponding Li NMR spectrum of ternary Li_8MgSi_6 ^[9] to that of $\text{Li}_{12}\text{Si}_7$ (see the Supporting Information).

Finally, in order to exclude that the signal observed at $\delta_{\text{iso}} = -17.2$ ppm belongs to a second phase that is possibly present, 2D exchange Li MAS NMR experiments were carried out. The room-temperature ^7Li NMR spectra as well as ^6Li exchange NMR spectra of $\text{Li}_{12}\text{Si}_7$, which were recorded

at mixing times of 100 ms (^7Li) and 1 s (^6Li), respectively, are shown in Figure 3. Off-diagonal intensities clearly indicate slow chemical exchange between all of the peaks visible in the NMR spectrum. Cross-peaks are either caused by spin

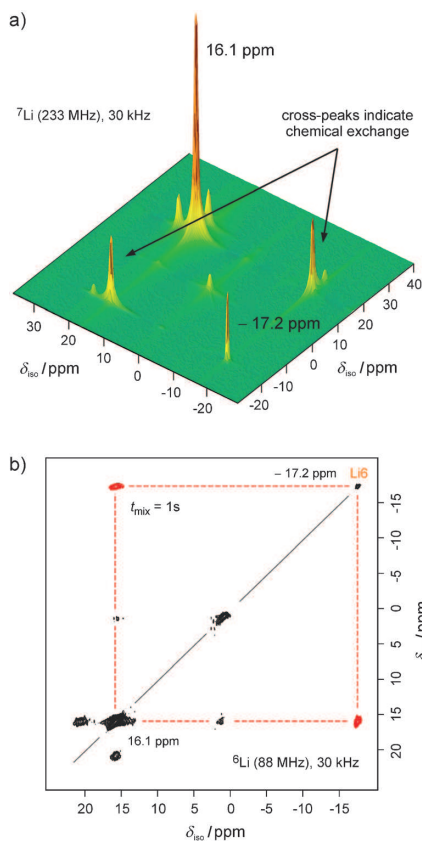


Figure 3. a) ^7Li 2D exchange MAS NMR spectrum of $\text{Li}_{12}\text{Si}_7$ at room temperature (bearing gas temperature) recorded at a magnetic field of 14.1 T and a spinning rate of 30 kHz using a mixing time of $t_m = 100$ ms. b) ^6Li 2D exchange MAS NMR spectrum recorded under the same conditions. The mixing time was 1 s. Dashed lines highlight the Li exchange between the signals showing up at 16.1 and -17.2 ppm. The corresponding off-diagonal intensities are shown in red.

diffusion or translational jumps of the Li ions from one crystallographic site to another. Irrespective of their nature, their appearance unequivocally proves that the Li sites involved belong to the same structure. If the NMR signal at -17.2 ppm belonged to a separate phase, as recently assumed by the NMR study of Key et al.,^[19] no off-diagonal intensities would be expected.

A comparison of results from ^7Li with those from ^6Li 2D NMR shows that the cross-peaks detected are mainly due to Li jump processes rather than spin diffusion. The latter process is largely suppressed in the case of ^6Li 2D NMR because of the spatial separation of the ^6Li nuclei leading to a

reduction of homonuclear dipole–dipole interactions. This enables the estimation of the Li exchange rate from mixing-time-dependent 2D NMR spectra. Here, as expected, the exchange rate associated with the signals that appear at -17.2 ppm and 16.1 ppm (see Figure 3a) turns out to be rather low and amounts to be $70(5) \text{ s}^{-1}$. Obviously, the Li6 ions are locked by multiple interactions with the Si5 rings to result in such a small jump rate.

In conclusion, the Li MAS NMR spectrum of the Zintl phase $\text{Li}_{12}\text{Si}_7$ shows a distinct signal at -17.2 ppm. Usually, such a large upfield shift serves as a criterion for aromaticity. Indeed, the NMR signal can be unambiguously assigned to the Li6 ions located between the cyclopentadienyl-like Si_5^{6-} rings. These units are characterized by the typical structural and magnetic features of classical aromaticity known for carbon compounds, namely planarity, (nearly) equal bond lengths, and overlap between the p orbitals perpendicular to the Si_5^{6-} ring. Thus, the chemical shift observed experimentally confirms earlier studies that predict classical Hückel aromaticity of these rings that are composed solely of silicon instead of carbon.

Received: July 20, 2011

Published online: October 24, 2011

Keywords: aromaticity · lithium · NMR spectroscopy · silicon · Zintl ions

- [1] R. West, M. J. Fink, J. Michl, *Science* **1981**, 214, 1343.
- [2] K. Abersfelder, A. J. P. White, H. S. Rzepa, D. Scheschke, *Science* **2010**, 327, 564.
- [3] R. J. F. Berger, H. S. Rzepa, D. Scheschke, *Angew. Chem.* **2010**, 122, 10203; *Angew. Chem. Int. Ed.* **2010**, 49, 10006.
- [4] a) P. Lazzaretti, *Prog. Nucl. Magn. Reson. Spectrosc.* **2000**, 36, 1; b) J. A. N. F. Gomes, R. B. Mallion, *Chem. Rev.* **2001**, 101, 1349.
- [5] V. Y. Lee, A. Sekiguchi, *Angew. Chem.* **2007**, 119, 6716; *Angew. Chem. Int. Ed.* **2007**, 46, 6596.
- [6] W. v. E. Doering, F. L. Detert, *J. Am. Chem. Soc.* **1951**, 73, 876.
- [7] a) H. G. von Schnering, R. Nesper, J. Curda, K. F. Tebbe, *Angew. Chem.* **1980**, 92, 1070; *Angew. Chem. Int. Ed. Engl.* **1980**, 19, 1033; b) R. Nesper, H. G. von Schnering, J. Curda, *Chem. Ber.* **1986**, 119, 3576; c) W. Tiznado, N. Perez-Peralta, R. Islas, A. Toro-Labbe, J. M. Ugalde, G. Merino, *J. Am. Chem. Soc.* **2009**, 131, 9426.
- [8] a) R. Nesper, *Prog. Solid State Chem.* **1990**, 20, 1; b) H. Axel, H. Schäfer, A. Weiss, *Angew. Chem.* **1965**, 77, 379; *Angew. Chem. Int. Ed. Engl.* **1965**, 4, 358.
- [9] R. Nesper, J. Curda, H. G. von Schnering, *J. Solid State Chem.* **1986**, 62, 199.
- [10] V. L. Chevrier, J. W. Zwanziger, J. R. Dahn, *J. Alloys Compd.* **2010**, 496, 25.
- [11] A. Kuhn, P. Sreeraj, R. Pöttgen, H.-D. Wiemhöfer, M. Wilkening, P. Heitjans, *J. Am. Chem. Soc.* **2011**, 133, 11018.
- [12] H. Günther in *Encyclopedia of Nuclear Magnetic Resonance*, Vol. 5 (Eds.: D. M. Grant, R. K. Harris), Wiley, Chichester, **1996**, p. 2807.
- [13] E. Urnezus, W. W. Brennessel, J. C. Cramer, J. E. Ellis, P. von R. Schleyer, *Science* **2002**, 295, 832.
- [14] P. von R. Schleyer, C. Maerker, A. Dransfeld, H. Jiao, N. J. R. van Eikema Hommes, *J. Am. Chem. Soc.* **1996**, 118, 6317.
- [15] J. O. C. Jiménez-Halla, E. Matito, J. Robles, M. Solà, *J. Organomet. Chem.* **2006**, 691, 4359.

Communications

- [16] A. P. Sergeeva, A. I. Boldyrev, *Organometallics* **2010**, *29*, 3951.
- [17] Most recently, we have also found large NMR upfield shifts (up to -35 ppm) in the nonparamagnetic Zintl phases Li_7Si_3 and $\text{Li}_{13}\text{Si}_4$ containing Si_2 dumbbell units. The signals appear at low temperatures only and with low intensity. It is most likely that some of the Li ions form π complexes with the Si_2 dumbbells to result in a pronounced upfield shift. The preliminary NMR results point to a much more complex structure of these Zintl phases than those reported to date. It is worth mentioning that the corresponding shifts are absent for Li_2Si_5 containing isolated Si only.
- [18] L. A. Paquette, W. Bauer, M. R. Sivik, M. Bühl, M. Feigel, P. von R. Schleyer, *J. Am. Chem. Soc.* **1990**, *112*, 8776.
- [19] B. Key, R. Bhattacharyya, M. Morcrette, V. Seznéc, J.-M. Tarascon, C. P. Grey, *J. Am. Chem. Soc.* **2009**, *131*, 9239.
-



Supporting Information

© Wiley-VCH 2011

69451 Weinheim, Germany

Li NMR Spectroscopy on Crystalline $\text{Li}_{12}\text{Si}_7$: Experimental Evidence for the Aromaticity of the Planar Cyclopentadienyl-Analogous Si_5^{6-} Rings**

Alexander Kuhn, Puravankara Sreeraj, Rainer Pöttgen, Hans-Dieter Wiemhöfer, Martin Wilkening,* and Paul Heitjans**

anie_201105081_sm_miscellaneous_information.pdf

Preparation details (as already described in ref. [S1]):

The starting materials for the preparation were lithium rods (Merck, >99%) and silicon lumps (Wacker, >99.9%). The lithium rods were cut into smaller pieces under dry paraffin oil and washed with *n*-hexane. They were kept in Schlenk tubes under argon prior to the reaction. Argon was purified with a titanium sponge (900 K), silica gel, and molecular sieves. The lithium pieces and silicon pieces were mixed in the required stoichiometric ratio under flowing argon and then arc-welded^[S2] in a niobium ampoule under an argon pressure of about 700 mbar. Subsequently, the niobium ampoule was placed in a water-cooled sample chamber^[S3] of an induction furnace. At first, the sample was rapidly heated to 1170 K, kept at that temperature for 20 min, and then quenched to 900 K. The sample was annealed at that temperature for another 3 h, followed by quenching, *i. e.*, by switching off the power supply. The brittle product could easily be separated from the niobium tube. No reaction with the container was observed.

The polycrystalline sample was analyzed on a Guinier camera (equipped with an image plate system Fujifilm BAS-1800) using Cu $K\alpha_1$ radiation and α -quartz as an internal standard. The powder data was analyzed using the programs LAZY PULVERIX^[S4] and a standard least-squares routine. The obtained product is crystalline and pure up to the level of x-ray diffraction and has an orthorhombic unit cell, space group *Pnma*, with the refined parameters $a = 860.3(2)$, $b = 1976.9(4)$, $c = 1434.9(4)$ pm, which is in good agreement with the reported data.^[S5]

Experimental details:

⁶Li and ⁷Li magic angle spinning (MAS) NMR measurements were performed with a Bruker Avance III spectrometer connected to a shimmed Bruker cryomagnet with a nominal field of 14.1 T. A commercial Bruker standard probe (rotor diameter 2.5 mm, MAS spinning rate 30 kHz) was used. The ⁷Li MAS NMR spectrum at 140 K (see below) was recorded in the laboratory of Bruker BioSpin using a magnet of 11.7 T and a newly developed ultra-low-temperature MAS probe (MAS spinning rate 20 kHz). ⁶Li and ⁷Li 1D MAS NMR spectra were recorded using a single, short $\pi/2$ -pulse and a suitable phase cycle. ⁶Li and ⁷Li 2D exchange MAS NMR spectra were performed with the pulse sequence described in, *e. g.*, ref. [S6]. All Li NMR spectra were referenced to a 1N aqueous solution of LiCl.

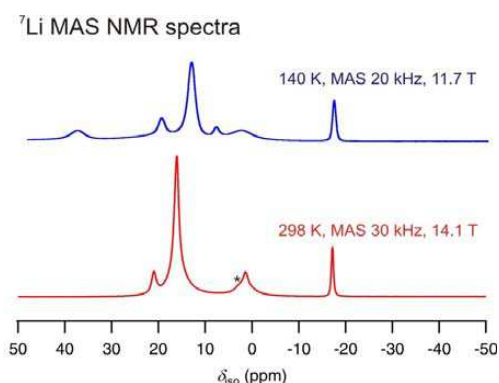
Additional data:

Figure S1. ⁷Li MAS NMR spectra of Li₁₂Si₇ measured at 298 K and 140 K (bearing gas temperature). Note that the line at -17.2 ppm is hardly affected by temperature.

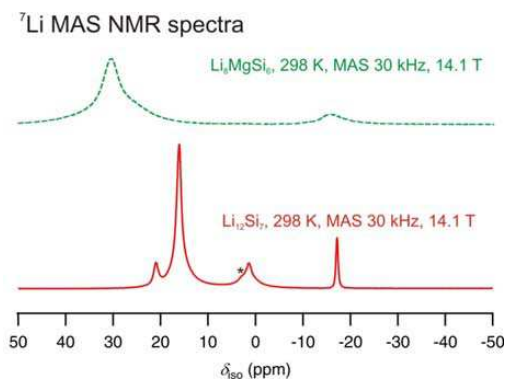


Figure S2. ⁷Li MAS NMR spectra of Li₁₂Si₇ and Li₈MgSi₆^[S7] measured at 298 K (bearing gas temperature) and a spinning rate of 30 kHz. The aromatically shifted line appears as well for the Mg-containing compound which exhibits the same semi-infinite sandwich complexes. In the Mg compound, the lines are somewhat broader, probably due to the disorder present in the Mg sub-lattice. The lines connected to the Li positions outside the sandwich complexes appear at 25 - 30 ppm at room temperature. Most probably, this is due to (i) lower electron density in the surroundings of these ions leading to deshielding and (ii) aromatic downfield shifts for the ions outside of the rings. In the case of Li₁₂Si₇, the Si₄-stars give rise to additional upfield shifts (as compared to the Mg containing compound) whose origin still needs to be clarified in combination with theoretical calculations. Note that also for these stars, aromaticity was suggested by some theoretical studies (*cf.* ref. [S8]).

References

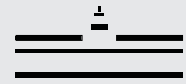
[S1] A. Kuhn et al., *J. Amer. Chem. Soc.* **2011**, *133*, 11018.

- [S2] R. Pöttgen, T. Gulden, A. Simon, *GIT Labor-Fachzeitschrift* **1999**, 43, 133.
- [S3] D. Kußmann, R.-D. Hoffmann, R. Pöttgen, *Z. Anorg. Allg. Chem.* **1998**, 624, 1727.
- [S4] K. Yvon, W. Jeitschko, E. Parthé, *J. Appl. Crystallogr.* **1977**, 10, 73.
- [S5] R. Nesper, H. G. v. Schnering, J. Curda, *Chem. Ber.* **1986**, 119, 3576.
- [S6] C. Schmidt, B. Blümich, H. W. Spiess, *J. Magn. Res.* **1988**, 79, 269.
- [S7] R. Nesper, J. Curda, H. G. v. Schnering, *J. Solid State Chem.* **1986**, 62, 199.
- [S8] V. L. Chevrier, J. W. Zwanziger, J. R. Dahn, *J. Alloy. Compd.* **2010**, 25, 496.

Insight into the Li ion dynamics in $\text{Li}_{12}\text{Si}_7$: Combining PFG NMR, 1D/2D MAS NMR, and NMR relaxometry



A. Kuhn, M. Wilkening, P. Heitjans, Leibniz University Hannover, Germany
 M. Kunze, M. Winter, S. Passerini, University of Münster, Germany
 P. Sreeraj, H.-D. Wiemhöfer, University of Münster, Germany
 D. Freude, University of Leipzig, Germany



The STRUCTURE of the Zintl phase $\text{Li}_{12}\text{Si}_7$ ^[1,2]

- orthorhombic space group $Pnma$
- two different types of Zintl anions:
 - Si_5^{6-} rings
 - Si_4^{10-} stars
- 13 different Li sites with very different environments

→ different mean residence times of Li expected
 → several dynamic processes expected

^6Li MAS NMR coalescence

figure and data taken from S. Dupke et al. *Solid State Nucl. Magn. Reson.* **42** (2012) 17.

^7Li NMR static line shape^[3]

^{29}Si NMR, ^6Li NMR structural information

S. Dupke et al. *Solid State Nucl. Magn. Reson.* **42** (2012) 17.
 T. Köster et al. *Angew. Chem. Int. Ed.* **50** (2011) 12591.
 A. Kuhn et al. *Angew. Chem. Int. Ed.* **50** (2011) 12099.

^7Li PFG NMR (pushed field gradient)

DYNAMICS: Li jump processes in $\text{Li}_{12}\text{Si}_7$

Key features in the plot:
 - 0.55 eV (exchange 2D MAS NMR)
 - 0.32 eV (Li6 → Li6)
 - 0.18 eV (Li2 ↔ Li3)
 - 0.18 eV (Li117)
 - quadrupolar satellites
 - coalescence 1D MAS NMR
 - NMR line widths

^7Li NMR relaxometry^[3]

Legend:
 $T_{1\rho}^-1$: 12.4 kHz, 39.0 kHz
 T_1^-1 : 77.7 MHz, 155.4 MHz

^7Li SFG NMR (static field gradient)

Parameters: $P = 220 \text{ W}$, $f_0 = 2.8 \text{ GHz}$, $g = 63 \text{ T/m}$

^7Li 2D MAS exchange NMR

Fast reservoir sites: 1a, 1b, 2a, 2b, 3a, 3b, Li6

STRUCTURE-DYNAMICS RELATION

[1] H.G. von Schnering et al. *Angew. Chem. Int. Ed.* **19** (1980)1033.
 [2] R. Nesper et al. *Chem. Ber.* **119** (1986) 3576.
 [3] A. Kuhn et al. *J. Am. Chem. Soc.* **133** (2011) 11018.

Chapter 5

Conclusion

The Li ion dynamics occurring in model systems being relevant for battery applications (the electrolyte LLZ, and the anode material $\text{Li}_{12}\text{Si}_7$) was thoroughly characterized from a fundamental point of view over a wide temperature range covering a vast dynamic range. The combination of long-range and short-range methods, nuclear and non-nuclear methods allowed one to unequivocally trace back the macroscopic Li transport to the single correlated Li hop with Haven ratios and correlation factors in the order of unity.

The garnet-type electrolyte $\text{Li}_7\text{La}_3\text{Zr}_2\text{O}_{12}$ (LLZ) crystallizes in tetragonal symmetry at room temperature unless it is doped with Al. The diffusivity of Li in pure LLZ is very similar to that of many other oxide-based electrolytes: the Li ion dynamics is traced back to correlated hops activated by roughly $E_A \approx 0.53$ eV; the prefactor $\tau_0^{-1} \approx 10^{14}$ s⁻¹ is in the range typical of phonon frequencies as confirmed over 10 orders of magnitude via ⁷Li NMR relaxometry and ⁷Li SAE NMR (short-range nuclear methods), ⁷Li SFG NMR (long-range nuclear method), and dc conductivity (long-range non-nuclear). The parameter n describing the deviation from random hopping within the KWW-stretched-exponential model amounts to $n \approx 0.5$. The diffusion process seems to be nearly 3D isotropic. The phase transition to cubic symmetry which occurs at temperatures above 400 K, does not seem to have an influence on the ion dynamics. This is corroborated by a study on an Al-doped LLZ crystallizing with cubic symmetry at room temperature which showed nearly the same diffusion parameters as the tetragonal LLZ.

Nevertheless, there exist Al-doped samples of $\text{Li}_7\text{La}_3\text{Zr}_2\text{O}_{12}$ (LLZ) which show a decisively higher Li diffusivity at low temperatures. The dynamics in a highly conductive Al-doped LLZ sample was thoroughly studied by means of ⁶Li NMR relaxometry and ⁷Li NMR relaxometry (short-range nuclear methods), ⁷Li SFG NMR (long-range nuclear method) and dc conductivity (long-range non-nuclear). Over a dynamic range of 12 orders of magnitude, the macroscopic Li transport can be traced back to correlated Li hops activated with $E_A \approx 0.29$ eV. The prefactor is in the order of $\tau_0^{-1} \approx 10^{11}$ s⁻¹. This value is lower than usual phonon frequencies which might *e. g.* reflect cooperative dynamics. In the studied regime, the motional correlation function is well described by a KWW stretched exponential with $n \approx 0.5$.

In addition to this long-range jump process, jump processes which are characterized by similar values as the long-range dynamics in pure LLZ occur in the material. These do not give rise to

long-range dynamics, *i. e.* the jump process is not percolated but occurs either isolated on an atomic scale (as an alternative to the lower-activated jump process) or in slightly larger domains in the material.

The grain-boundaries in well-crystallized Al-doped LLZ cause a slightly higher long-range activation energy of roughly 0.35 eV in polycrystalline LLZ.

An important result of this study is also that electrode polarization processes may contain thermally activated processes which lead to plateaus in the conductivity that can be mistaken for grain-boundary processes. Additional care has to be taken in interpreting impedance spectroscopy results. True dc conductivity measurements with reversible Li electrodes should be considered for all materials that are stable against Li.

In a systematic study, the influence of Al on the structure and dynamics in LLZ was examined. Using XRD and ^{27}Al MAS NMR, it could be shown that Al replaces not only Li but also La and Zr in the garnet. Thus, the garnet network is altered by Al. Presumably, the oxygen sublattice is considerably distorted by the incorporation of Al. This might explain the high conductivity in Al-doped samples of LLZ. The exact distribution of Al in the lattice seems to have a decisive impact on the ion dynamics. This might be understood as follows: if it is not the simple phase transition to cubic symmetry that is responsible for the extraordinarily high Li diffusivity but local distortions of the lattice, percolation of these defects is necessary for an effect on long-range dynamics.

Further studies on the structural features of Al-doped LLZ are required to clarify the exact reasons for the high diffusivity. Hereby, IR and Raman spectroscopy might be useful. ^{27}Al NMR relaxometry might also be helpful. The possible role of oxygen vacancies has to be ruled out or corroborated by experiments, *e. g.* TG, oxygen partial pressure dependence of diffusivity.

The Zintl phase $\text{Li}_{12}\text{Si}_7$ which transitionally occurs in Si anodes under charging and discharging shows a rather complex structure with two types of Zintl anions, Si_5^{6-} -rings and Si_4^{10-} -stars surrounded by Li. The Li ions reside on 13 different crystallographic sites with very different binding energies. 9 of the Li sites take part in a very fast long-range Li jump process activated by roughly 0.2 eV with a prefactor in the order of $\tau_0^{-1} \approx 10^{11} \text{ s}^{-1}$ as determined over a dynamic range of 6 orders of magnitude with ^7Li NMR relaxometry (the short-range nuclear method) and ^7Li SFG NMR and ^7Li PFG NMR (long-range nuclear methods) - in good accordance with GITT measurements from the literature (long-range non-nuclear method). In NMR relaxometry, this jump process seems to show characteristics of single-file diffusion. Presumably, this is connected to motion on diffusion pathways confined by the Zintl-anionic network and less mobile Li. With the measurements available it is hard to exactly determine the expected anisotropy of the diffusivity. Li residing on the other sites (Li6, Li3, Li11(?), and Li12 or Li13) is bound more tightly to the anionic network with binding energies between 0.34 and 0.55 eV. Jumping over these barriers connects the Li ions with the fast diffusing ion reservoir. The respective jump processes are observed in ^7Li NMR relaxometry, ^6Li MAS NMR line coalescence, and $^{6,7}\text{Li}$ 2D exchange NMR.

Li is most tightly bound on the Li6 site between two Si_5^{6-} -rings in a η^5 -sandwich coordination. The large upfield shift (-17.2 ppm) of Li on this site points to the aromaticity the Si_5^{6-} -rings which is the first experimental evidence of the aromaticity in a ring solely composed of Si. Interestingly, the aromaticity of a third-period element occurs even in thermodynamically stable compounds

and thus is not a chemical oddity like some organometallic compounds violating the double bond rule. The same Si_5^{6-} -ring occurs in Li_8MgSi_6 . As expected, here again, a similar upfield shift is observed.

Altogether, a rather consistent picture of structure and dynamics in $\text{Li}_{12}\text{Si}_7$ is obtained. Low-temperature CP-MAS studies should clarify whether Li12 or Li13 is more tightly bound and whether the assignment of Li11 is correct. Furthermore, theoretical studies on the hopping barriers between each site and the neighboring sites will be required to determine the exact diffusion pathways.

Bibliography

- [1] A. Einstein, *Annalen der Physik* **17**, pp. 549 (1905).
- [2] R. A. Huggins, *Electrochimica Acta* **22**, pp. 773 (1977).
- [3] H.-J. Steiner and H. D. Lutz, *Z. anorg. allg. Chem.* **613**, pp. 26 (1992).
- [4] A. D. Robertson, A. R. West, and A. G. Ritchie, *Solid State Ionics* **104**, pp. 1 (1997).
- [5] V. Thangadurai and W. Weppner, *Ionics* **8**, pp. 281 (2002).
- [6] S. Stramare, V. Thangadurai, and W. Weppner, *Chem. Mater.* **15**, pp. 3974 (2003).
- [7] V. Thangadurai and W. Weppner, *Ionics* **12**, pp. 81 (2006).
- [8] P. Knauth, *Solid State Ionics* **180**, pp. 911 (2009).
- [9] B. Kumar and L. G. Scanlon, *J. Electroceram.* **5**, pp. 127 (2000).
- [10] K. Noriaki, H. Kenji, Y. Yuichiro, M. Hirayama, R. Kanno, M. Yonemura, T. Kamiyama, Y. Kato, S. Hama, K. Kawamoto, and A. Mitsui, *Nature Materials* **10**, pp. 682 (2011).
- [11] A. Sakuda, A. Hayashi, T. Ohtomo, S. Hama, and M. Tatsumisago, *J. Power Sources* **196**, pp. 6735 (2011).
- [12] A. Rabenau, *Solid State Ionics* **6**, pp. 277 (1982).
- [13] B. Heed, A. Lundén, and K. Schroeder, *Electrochimica Acta* **22**, pp. 705 (1977).
- [14] Y. Inaguma, L. Chen, M. Itho, T. Nakamura, T. Uchida, H. Ikuta, and M. Wakihara, *Solid State Commun.* **86**, pp. 689 (1993).
- [15] U. v. Alpen, A. Rabenau, and G. H. Talat, *Appl. Phys. Lett.* **30**, pp. 621 (1977).
- [16] M. Murayama, N. Sonoyama, A. Yamada, and R. Kanno, *Solid State Ionics* **170**, pp. 173 (2004).
- [17] Y. Tomita, A. Fuji-i, H. Ohki, K. Yamada, and T. Okuda, *Chem. Lett.* **3**, pp. 223 (1998).
- [18] R. Murugan, V. Thangadurai, and W. Weppner, *Angew. Chem. Int. Ed.* **46**(41), pp. 7778–7781 (2007).
- [19] H. Buschmann, J. Doelle, S. Berendts, A. Kuhn, P. Bottke, M. Wilkening, P. Heitjans, A. Senyshyn, H. Ehrenberg, A. Lotnyk, V. Duppel, L. Kienle, and J. Janek, *Phys. Chem. Chem. Phys.* **13**, pp. 19378 (2011).

- [20] J. Awaka, N. Kijima, H. Hayakawa, and J. Akimoto, *J. Solid State Chem.* **182**(8), pp. 2046 – 2052 (2009).
- [21] A. Kuhn, S. Narayanan, L. Spencer, G. Goward, V. Thangadurai, and M. Wilkening, *Phys. Rev. B* **83**(9), pp. 094302 (2011).
- [22] Y.-W. Hu, Raistrick. I.D., and R. A. Huggins, *Mat. Res. Bull.* **11**, pp. 1227 (1976).
- [23] Y.-W. Hu, Raistrick. I.D., and R. A. Huggins, *J. Electrochem. Soc.* **124**, pp. 1240 (1977).
- [24] U. v. Alpen, M. F. Bell, and W. Wichelhaus, *Electrochimica Acta* **23**, pp. 1395 (1978).
- [25] M. Witschas, H. Eckert, D. Wilmer, R. D. Banhatti, and K. Funke, *Z. Phys. Chem.* **214**, pp. 643 (2000).
- [26] A. Kuhn, V. Epp, G. Schmidt, S. Narayanan, V. Thangadurai, and M. Wilkening, *J. Phys.: Condens. Matter* **24**, pp. 035901 (2012).
- [27] K. H. Kim, , Y. Iriyama, K. Yamamoto, S. Kumakazi, T. Asaka, K. Tanabe, C. A. J. Fisher, T. Hirayama, R. Murugan, and Z. Ogumi, *J. Power Sources* **196**, pp. 764 (2011).
- [28] C. A. Geiger, E. Alekseev, B. Lazic, M. Fisch, T. Armbruster, R. Langner, M. Fechtelkord, N. Kim, T. Pettke, and W. Weppner, *Inorganic Chemistry* **50**(3), pp. 1089 (2011).
- [29] M. Kotokubi, H. Munakata, K. Kanamura, Y. Sato, and T. Yoshida, *J. Electrochem. Soc.* **157**, pp. A1076 (2010).
- [30] M. Kotokubi, K. Kanamura, Y. Sato, and T. Yoshida, *J. Power Sources* **196**, pp. 7750 (2011).
- [31] S. Kumakazi, Y. Iriyama, Kim. K.-H., R. Murugan, K. Tanabe, T. Yamamoto, T. Hirayama, and Z. Ogumi, *Electrochem. Commun.* **13**, pp. 509 (2011).
- [32] J. Tan and A. Tiwari, *Electrochem. Solid-State Lett.* **15**, pp. A37 (2012).
- [33] S. Ohta, T. Kobayashi, and T. Asaoka, *J. Power Sources* **196**, pp. 3342 (2011).
- [34] S. Ohta, T. Kobayashi, J. Seki, and T. Asaoka, *Journal of Power Sources* **202**, pp. 332 (2012).
- [35] M. Matsuo, Y. Nakamori, S.-I. Orimo, H. Maekawa, and H. Takamura, *Appl. Phys. Lett.* **91**, pp. 224103 (2007).
- [36] V. Epp and M. Wilkening, *Phys. Rev. B* **82**, pp. 020301 (2010).
- [37] R. Kubo, *J. Phys. Soc. Jpn.* **12**, pp. 570 (1957).
- [38] R. Kubo, M. Toda, and N. Hashitsume, *Statistical Physics II*, Springer (1991).
- [39] H. Ackermann, P. Heitjans, and H.-J. Stöckmann, *Top. Curr. Phys.* **31**, pp. 291 (1983).
- [40] P. Heitjans, *Solid State Ionics* **18/19**, pp. 50 (1986).
- [41] P. Heitjans, W. Faber, and A. Schirmer, *J. Non-Cryst. Solids* **131-133**, pp. 1053 (1991).

- [42] P. Freiländer, P. Heitjans, H. Ackermann, B. Bader, G. Kiese, A. Schirmer, H.-J. Stoeckmann, C. van der Marel, A. Magerl, and H. Zabel, *Z. Phys. Chem. NF* **151**, pp. 93 (1987).
- [43] H. Estrade, J. Conrad, P. Lauginie, P. Heitjans, F. Fujara, W. Buttler, G. Kiese, H. Ackermann, and D. Guerard, *Physica* **99B**, pp. 531 (1980).
- [44] A. Schirmer, P. Heitjans, W. Faber, and J. E. Fischer, *Materials Science Forum* **91-93**, pp. 589 (1992).
- [45] A. Schirmer, P. Heitjans, W. Faber, and D. Clausen, *Solid State Ionics* **53-56**, pp. 426 (1992).
- [46] A. Köblein, P. Heitjans, H.-J. Stöckmann, F. Fujara, H. Ackermann, W. Buttler, K. Dörr, and H. Grupp, *J. Phys. F: Met. Phys.* **15**, pp. 561 (1985).
- [47] R. Kimmich, *NMR Tomography, Diffusiometry, Relaxometry*, Springer, Berlin (1997).
- [48] R. Kimmich and E. Anoardo, *Prog. Nucl. Magn. Res. Sp.* **44**, pp. 257 (2004).
- [49] J. Rahn, E. Huger, L. Dorrer, B. Ruprecht, P. Heitjans, and H. Schmidt, *Phys. Chem. Chem. Phys.* **14**, pp. 2427 (2012).
- [50] A.-M. Welsch, H. Behrens, I. Horn, S. Ross, and P. Heitjans, *J. Phys. Chem. A* **116**, pp. 309 (2012).
- [51] R. de L. Kronig, *J. Opt. Soc. Am.* **12**, pp. 547 (1926).
- [52] D. L. Sidebottom, B. Roling, and K. Funke, *Phys. Rev. B* **63**, pp. 024301 (2000).
- [53] J. R. Macdonald, *J. Non-Cryst. Solids* **197**, pp. 83 (1996).
- [54] A. Kuhn, Master's thesis Leibniz Universität Hannover, Germany (2008).
- [55] A. Abragam, *The principles of Nuclear Magnetism*, Oxford University Press (1961).
- [56] C. P. Slichter, *Principles of Magnetic Resonance*, Springer (1978).
- [57] M. J. Duer, *Solid-State NMR Spectroscopy*, Blackwell Publishing, Oxford (2004).
- [58] M. H. Levitt, *spin dynamics - Basics of Nuclear Magnetic Resonance*, John Wiley & Sons (2008).
- [59] D. Wolf, *Spin-Temperature and Nuclear-Spin Relaxation in Matter*, Clarendon Press, Oxford (1979).
- [60] M. E. Rose, *Elementary theory of angular momentum*, J. Wiley (1957).
- [61] A. R. Edmonds, *Angular momentum in quantum mechanics*, Princeton University Press (1957).
- [62] M. Tinkham, *Group theory and quantum mechanics*, McGraw-Hill (1964).
- [63] D. Brink and G. R. Satchler, *Angular momentum*, Oxford University Press (1962).

- [64] V. Heine, *Group theory*, Pergamon Press (1960).
- [65] H. W. Spiess, *NMR - Basic Principles and Progress* **15**, pp. 169 (1978).
- [66] K. Eichele, *Win Solids - NMR spectra simulation software* **Eberhard-Karls-Universität Tübingen** (2009).
- [67] C. P. Grey and N. Dupré, *Chem. Rev.* **104**, pp. 4493 (2004).
- [68] J. Korringa, *Physica* **16**, pp. 601 (1950).
- [69] N. Bloembergen, E. Purcell, and R. Pound, *Phys. Rev.* **73**, pp. 679 (1948).
- [70] J. H. van Vleck, *Phys. Rev.* **74**, pp. 1168 (1948).
- [71] D. Wolf and P. Jung, *Phys. Rev. B* **12**, pp. 3596 (1975).
- [72] D. Wolf, *Phys. Rev. B* **14**, pp. 932 (1976).
- [73] David Ailion and Charles P. Slichter, *Phys. Rev. Lett.* **12**(7), pp. 168–171 (1964).
- [74] D. C. Ailion and C. P. Slichter, *Phys. Rev.* **137**, pp. A235 (1965).
- [75] T. J. Rowland and F. Y. Fradin, *Phys. Rev* **182**, pp. 760 (1969).
- [76] D. C. Look and I. J. Lowe, *J. Chem. Phys.* **44**, pp. 2995 (1966).
- [77] P. M. Richards, *Top. Curr. Phys.* **25**, pp. 1019 (1979).
- [78] C. A. Sholl, *J. Phys. C: Solid State Phys.* **14**, pp. 447 (1981).
- [79] M. Grüne, PhD thesis University of Münster (1992).
- [80] C. P. Slichter and D. C. Ailion, *Phys. Rev.* **135**, pp. A1099 (1964).
- [81] J. W. Peng, W. Thanabal, and G. Wagner, *J. Magn. Reson.* **94**, pp. 82 (1991).
- [82] P. M. Richards, *J. Stat. Phys.* **30**, pp. 497 (1983).
- [83] N. Bloembergen, *Physica* **15**, pp. 386 (1949).
- [84] D. Tse and S. R. Hartmann, *Phys. Rev. Lett.* **21**, pp. 511 (1968).
- [85] W. E. Blumberg, *Phys. Rev.* **119**, pp. 79 (1960).
- [86] P. M. Richards, *Phys. Rev. B* **18**, pp. 6358 (1978).
- [87] M. Grüne and W. Müller-Warmuth, *Solid State Nucl. Magn. Reson.* **5**, pp. 145 (1995).
- [88] O. Abou-Ghaloun, S. Slough, and L. Trichet, *J. Phys. C: Solid State Phys.* **15**, pp. 5113 (1982).
- [89] R. D. Hogg, S. P. Vernon, and V. Jaccarino, *Phys. Rev. Lett.* **39**, pp. 481 (1977).
- [90] B. A. Huberman and J. B. Boyce, *Solid State Commun.* **25**, pp. 759 (1978).

- [91] G. B. Furman, A. M. Panich, A. Yochelis, E. M. Kunoff, and S. D. Goren, *Phys. Rev. B* **55**, pp. 439 (1997).
- [92] J. van Kranendonk, *Physica* **20**, pp. 781 (1954).
- [93] W. K. Lee, J. F. Liu, and A. S. Nowick, *Phys. Rev. Lett.* **67**, pp. 1559 (1991).
- [94] K. Funke, R. D. Banhatti, D. M. Laughman, L. G. Badr, M. Mutke, A. Santic, W. Wrobel, E. M. Fellberg, and C. Biermann, *Progress in Physical Chemistry Volume 4*, Oldenbourg Verlag (2011).
- [95] O. Kanert, R. Kuchler, J. Dieckhöfer, X. Lu, and H. Jain, *Phys. Rev. B* **49**, pp. 629 (1994).
- [96] K. Funke and R. D. Banhatti, *Solid State Sci.* **10**, pp. 790 (2008).
- [97] E. O. Stejskal and J. E. Tanner, *J. Chem. Phys.* **42**, pp. 288 (1965).
- [98] P. Stilbs, *Progress in NMR Spectroscopy* **19**, pp. 1 (1987).
- [99] D. M. Fischer, P. Duwe, S. Indris, and P. Heitjans, *Solid State Nucl. Mag. Reson.* **26**, pp. 74 (2004).
- [100] A. Gutsze, W. Masierak, B. Geil, D. Kruk, H. Pahlke, and F. Fujara, *Solid State Nucl. Magn. Reson.* **28**, pp. 244 (2005).
- [101] P. Duwe, PhD thesis University of Hannover (1995).
- [102] R. F. Jr. Karlicek and I. J. Lowe, *J. Magn. Reson.* **37**, pp. 75 (1980).
- [103] P. T. Callaghan, *Aust. J. Phys.* **37**, pp. 359 (1984).
- [104] W. S. Price, *Concepts Magn. Reson.* **9**, pp. 299 (1997).
- [105] Y. Cohen, L. Avram, and L. Frish, *Angew. Chem.* **117**, pp. 524 (2005).
- [106] J. Jeener and P. Broekaert, *Phys. Rev.* **157**, pp. 232 (1967).
- [107] R. Böhmer, T. Jorg, F. Qi, and A. Titze, *Chem. Phys. Lett.* **316**, pp. 419 (2000).
- [108] F. Qi, T. Jorg, and R. Böhmer, *Solid State Nucl. Magn. Reson.* **22**, pp. 484 (2002).
- [109] M. Wilkening and P. Heitjans, *Solid State Ionics* **177**, pp. 3031 (2006).
- [110] M. Wilkening, W. Kuechler, and P. Heitjans, *Phys. Rev. Lett.* **97**, pp. 065901 (2006).
- [111] M. Wilkening, A. Kuhn, and P. Heitjans, *Phys. Rev. B* **78**, pp. 054303 (2008).
- [112] S. Faske, B. Koch, S. Murawski, R. Kuchler, R. Böhmer, J. Melchior, and M. Vogel, *Phys. Rev. B* **84**, pp. 024202 (2011).
- [113] M. Wilkening and P. Heitjans, *Chem. Phys. Chem.* **13**, pp. 53 (2012).
- [114] A. Medek, J. S. Harwood, and L. Frydman, *J. Amer. Chem. Soc.* **117**, pp. 12779 (1995).
- [115] V. Thangadurai, H. Kaack, and W. Weppner, *J. Amer. Chem. Soc.* **86**, pp. 437 (2003).

- [116] Z. Liu, F. Huang, J. Yang, Y. Wang, and J. Sun, *J. Solid State Sci.* **10**, pp. 1429 (2008).
- [117] V. Thangadurai and W. Weppner, *Adv. Funct. Mater.* **15**, pp. 107 (2005).
- [118] V. Thangadurai and W. Weppner, *J. Power Sources* **142**, pp. 339 (2005).
- [119] A. Ramzy and V. Thangadurai, *Appl. Mater. Interfaces* **2**, pp. 385 (2010).
- [120] L. v. Wüllen, T. Echelmeyer, H.-W. Meyer, and D. Wilmer, *Phys. Chem. Chem. Phys.* **9**, pp. 3298 (2007).
- [121] B. Koch and M. Vogel, *Solid State Nucl. Magn. Reson.* **34**, pp. 37 (2008).
- [122] E. J. Cussen, *Chem. Commun.* , p. 412 (2006).
- [123] M. P. O'Callaghan and E. J. Cussen, *Chem. Commun.* , p. 2048 (2007).
- [124] E. J. Cussen, *J. Mater. Chem.* **20**, pp. 5167 (2010).
- [125] X. P. Wang, W. G. Wang, Y. X. Gao, T. Zhang, and Q. F. Fang, *Mater. Sci. Engin. A* **521-522**, pp. 87 (2009).
- [126] W. G. Wang, X. P. Wang, Y. X. Gao, and Q. F. Fang, *Solid State Ionics* **180**, pp. 1252 (2009).
- [127] V. Thangadurai and W. Weppner, *J. Solid State Chem.* **179**, pp. 974 (2006).
- [128] S. Thangadurai, V. Adams and W. Weppner, *Chem. Mater.* **16**, pp. 2998 (2004).
- [129] M. Nyman, T. Alam, S. K. McIntyre, and D. Bleier, G. C. Ingersoll, *Chem. Mater.* **22**, pp. 5401 (2010).
- [130] J. Percival, E. Kendrick, R. I. Smith, and P. R. Slater, *Dalton Trans.* , p. 5177 (2009).
- [131] M. P. O'Callaghan, A. S. Powell, J. J. Titman, Chen. G. Z., and E. J. Cussen, *Chem. Mater.* **20**, pp. 2360 (2008).
- [132] R. Murugan, W. Weppner, P. Schmid-Beurmann, and V. Thangadurai, *Mater. Res. Bull.* **43**, pp. 2579 (2008).
- [133] S. Narayanan and V. Thangadurai, *J. Power Sources* **196**, pp. 8085 (2011).
- [134] C. Galven, J.-L. Fourquet, M.-P. Crosnier-Lopez, and F. Le Berre, *Chem. Mater.* **23**, pp. 1892 (2011).
- [135] J. Awaka, N. Kijima, K. Kataoka, H. Hayakawa, K.-i. Ohshima, and J. Akimoto, *J. Solid State Chem.* **183**, pp. 180 (2010).
- [136] L. Truong and V. Thangadurai, *Inorganic Chemistry* **3**, pp. 1222 (51).
- [137] W. Weppner (2009).
- [138] E. Rangasamy, J. Wofenstine, and J. Sakamoto, *Solid State Ionics* **206**, pp. 28 (2012).
- [139] K. Kanamura, A. Kaeriyama, A. Honda, T. Yoshida, and Y. Sato (2011).

- [140] I. Kokal, M. Somer, P. H. Notten, and H. T. Hintzen, *Solid State Ionics* **185**, pp. 42 (2011).
- [141] H. Xie, J. A. Alonso, Li Y., M. T. Fernández-Díaz, and J. B. Goodenough, *Chem. Mater.* **23**, pp. 3587 (2011).
- [142] N. Janani, S. Ramakumar, L. Dhivya, C. Deiannapoorani, K. Saranya, and R. Murugan, *Ionics* **17**, pp. 575 (2011).
- [143] Y. Shimonishi, A. Toda, T. Zhang, A. Hirano, N. Imanishi, O. Yamamoto, and Y. Takeda, *Solid State Ionics* **183**, pp. 48 (2011).
- [144] S. Narayanan, V. Epp, M. Wilkening, and V. Thangadurai, *RSC Advances* **2**, pp. 2553 (2012).
- [145] E. A. Il'ina, O. L. Andreev, B. D. Antonov, and N. N. Batolov, *J. Power Sources* **201**, pp. 169 (2012).
- [146] A. Gupta, R. Murugan, M. P. Paranthaman, Z. Bi, C. A. Bridges, M. Nakanishi, A. P. Sokolov, K. S. Han, E. W. Hagaman, H. Xie, C. B. Mullins, and J. B. Goodenough, *J. Power Sources* **209**, pp. 184 (2012).
- [147] J. Wolfenstine, J. L. Rangasamy, E. Allen, and J. Sakamoto, *J. Power Sources* **208**, pp. 193 (2012).
- [148] Y. T. Li, J. T. Han, C. A. Wang, S. C. Vogel, H. Xie, M. W. Xu, and J. B. Goodenough, *J. Power Sources* **209**, pp. 278 (2012).
- [149] J. L. Allen, J. Wolfenstine, E. Rangasamy, and J. Sakamoto, *J. Power Sources* **206**, pp. 315 (2012).
- [150] M. Xu, M. S. Park, J. M. Lee, T. Y. Kim, Y. S. Park, and E. Ma, *Phys. Rev. B* **85**, pp. 052301 (2012).
- [151] M. Kotokubi, K. Kanamura, Y. Sato, K. Yamamoto, and T. Yoshida, *J. Power Sources* **199**, pp. 246 (2012).
- [152] H. Buschmann, S. Berendts, B. Mogwitz, and J. Janek, *J. Power Sources* **206**, pp. 236 (2012).
- [153] H. Okamoto, *J. Phase Equilib. Diffus.* **30**, pp. 118 (2009).
- [154] J. Evers, G. Oehlinger, and G. Sextl, *Angew. Chem. Int. Ed.* **32**, pp. 1442 (1993).
- [155] L. A. Stearns, J. Gryko, J. Diefenbacher, G. K. Ramachandran, and P. F. McMillan, *J. Solid State Chem.* **173**, pp. 251 (2003).
- [156] H. G. v. Schnering, R. Nesper, J. Curda, and F. Tebbe, *Angew. Chem. Int. Ed.* **19**, pp. 1033 (1980).
- [157] R. Nesper, J. Curda, and H. G. v. Schnering, *Chem. Ber.* **119**, pp. 3576 (1986).
- [158] H. Axel, H. Schäfer, and A. Weiss, *Angew. Chem. Int. Ed.* **4**, pp. 358 (1965).

- [159] H.-G. v. Schnering, R. Nesper, K.-F. Tebbe, and J. Curda, *Z. Metallkd.* **71**, pp. 357 (1980).
- [160] I. Barvik, *Chzech J. Phys. B* **33**, pp. 1338 (1983).
- [161] U. Frank, W. Müller, and H. Schäfer, *Z. Naturforsch.* **30b**, pp. 10 (1975).
- [162] R. Nesper and H.-G. v. Schnering, *J. Solid State Chem.* **70**, pp. 48 (1987).
- [163] P. Limthongkul, Y.-I. Jang, N. J. Dudney, and Y.-M. Chiang, *J. Power Sources* **119-121**, pp. 604 (2003).
- [164] P. Limthongkul, Y.-I. Jang, N. J. Dudney, and Y.-M. Chiang, *Acta Mater.* **51**, pp. 1103 (2003).
- [165] V. L. Chevrier and J. R. Dahn, *J. Electrochem. Soc.* **2010**, pp. A392 (157).
- [166] B. Key, M. Morcrette, J. M. Tarascon, and C. P. Grey, *J. Amer. Chem. Soc.* **133**, pp. 503 (2011).
- [167] M. N. Obrovac and L. Christensen, *Solid-State Lett.* **7**, pp. A93 (2004).
- [168] T. D. Hatchard and Dahn. J. R., *J. Electrochem. Soc.* **151**, pp. A838 (2004).
- [169] Y. Wang and J. Dahn, *J. Electrochem. Soc.* **153**, pp. A2314 (2006).
- [170] Y. Kubota, M. C. S. Escano, H. Hakanishi, and H. Kasai, *J. Appl. Phys.* **102**, pp. 053704 (2007).
- [171] R. Seefurth and R. Sharma, *J. Electrochem. Soc.* **127**, pp. 1101 (1980).
- [172] T. Zhang, H. P. Zhang, L. C. Yang, B. Wang, Y. P. Wu, and T. Takamura, *Electrochimica Acta* **53**, pp. 5660 (2008).
- [173] C. K. Chan, H. Peng, G. Liu, K. McIlwrath, X. F. Zhang, R. A. Huggins, and Y. Cui, *Nature Nanotechn.* **3**, pp. 31 (2008).
- [174] B. A. Boukamp, G. C. Lesh, and R. A. Huggins, *J. Electrochem. Soc.* **1981**, pp. 725 (128).
- [175] R. A. Huggins and A. A. Anani (1990).
- [176] W. J. Weydanz, M. Wohlfahrt-Mehres, and R. A. Huggins, *J. Power Sources* **81**, pp. 237 (1999).
- [177] H. Li, Z. Wang, L. Chen, and X. Huang, *Adv. Mater.* **21**, pp. 4593 (2009).
- [178] D. P. Yu, C. S. Lee, I. Bello, X. S. Sun, Y. H. Tang, G. W. Zhou, Z. G. Bai, and Z. Zhang, *Solid State Commun.* **105**, pp. 403 (1998).
- [179] F. W. Zhou, H. Li, P. Sun, D. P. Yu, Y. Q. Wang, X. J. Huang, L. Q. Chen, and Z. Zhang, *Appl. Phys. Lett.* **75**, pp. 2447 (1999).
- [180] H. Li, X. J. Huang, L. Q. Chen, G. W. Zhou, Z. Zhang, D. P. Yu, and Y. J. Mo, *Solid State Ionics* **135**, pp. 181 (2000).

- [181] R. Ruffo, S. S. Hong, C. K. Chan, R. A. Huggins, and Cui. Y., *J. Phys. C* **113**, pp. 11390 (2009).
- [182] C. K. Chan, R. Ruffo, S. S. Hong, R. A. Huggins, and Cui. Y., *J. Power Sources* **189**, pp. 34 (2009).
- [183] B. Hertzberg, A. Alexeev, and G. P. Yushin, *J. Amer. Chem. Soc.* **132**, pp. 8548 (2010).
- [184] E. M. Pell, *Phys. Rev.* **119**, pp. 1222 (1960).
- [185] E. M. Pell, *Phys. Rev.* **119**, pp. 1014 (1960).
- [186] C. J. Wen and R. A. Huggins, *J. Solid State Chem.* **37**, pp. 271 (1981).
- [187] K. Yoshimura, J. Suzuki, and T. Sekine, K. Takamura, *J. Power Sources* **2007**, pp. 653 (174).
- [188] N. Ding, J. Xu, Y. X. Yau, G. Wegner, X. Fang, C. H. Chen, and I. Lieberwirth, *Solid State Ionics* **180**, pp. 222 (2009).
- [189] A. Kuhn, P. Sreeraj, R. Pöttgen, H.-D. Wiemhöfer, M. Wilkening, and P. Heitjans, *J. Amer. Chem. Soc.* **133**, pp. 11018 (2011).
- [190] P. S. Burada, P. Hänggi, F. Marchesoni, G. Schmid, and P. Talkner, *Phys. Chem. Phys.* **10**, pp. 45 (2009).
- [191] B. Key, R. Bhattacharyya, M. Morcrette, V. Seznec, J. M. Tarascon, and C. P. Grey, *J. Amer. Chem. Soc.* **131**, pp. 9232 (2009).
- [192] J. F. Liebman and J. S. Vincent, *Angew. Chem. Int. Ed.* **21**, pp. 632 (1982).
- [193] M. C. Böhm, R. Ramirez, R. Nesper, and H.-G. v. Schnering, *Phys. Rev. B* **30**, pp. 4870 (1984).
- [194] H. van Leuken, F. A. de Wijs, and W. van der Lugt, *Phys. Rev. B* **53**, pp. 10599 (1996).
- [195] V. L. Chevrier, J. W. Zwanziger, and J. R. Dahn, *J. Alloy Compd.* **496**, pp. 25 (2010).
- [196] R. Nesper, J. Curda, and H.-G. v. Schnering, *J. Solid State Chem.* **62**, pp. 199 (1986).
- [197] R. Ramirez, R. Nesper, and H.-G. v. Schnering, *Chem. Phys.* **95**, pp. 17 (1985).
- [198] A. Kuhn, P. Sreeraj, R. Pöttgen, H.-D. Wiemhöfer, M. Wilkening, and P. Heitjans, *Angew. Chem. Int. Ed.* **50**, pp. 12099 (2011).
- [199] T. K.-J. Köster, E. Salager, A. J. Morris, B. Key, V. Seznec, M. Morcrette, C. J. Pickard, and C. P. Grey, *Angew. Chem. Int. Ed.* **50**, pp. 12591 (2011).
- [200] S. Dupke, T. Langer, R. Pöttgen, M. Winter, and H. Eckert, *Solid State Nucl. Magn. Reson.* **42**, pp. 17 (2011).
- [201] D. Massiot, F. Fayon, M. Capron, I. King, S. Le Calvé, B. Alonso, J.-O. Durand, B. Bujoli, Z. Gan, and G. Hoatson, *Magnetic Resonance in Chemistry* **40**, pp. 70 (2002).

Appendix A

Experimental

A.1 Equipment

A.1.1 Impedance spectroscopy measurements

- Novocontrol Concept 80 broadband impedance spectrometer:
for usual frequency range (0.1 Hz ... 10 MHz):
 - BDMS1200 cell
 - Alpha AN Analyzer (Novocontrol)for high frequencies (1 MHz ... 3 GHz):
 - RF extension line (Agilent)
 - shielded RF cell (Agilent)
 - RF Analyzer 4991 (Agilent)
 - temperature control: QUATRO cryosystem
- home-built impedance setup:
 - home-built impedance cell
 - HP 4192A Impedance analyzer
 - Loba oven
 - Eurotherm 818 Temperature Controller, thermocouple Type K

A.1.2 NMR spectroscopy measurements

- **MSL 100** spectrometer (Bruker), Kalmus RF amplifier (500 W)
tunable Oxford cryomagnet (0-8 T, here **4.7 T**)
 - Oxford ITC4 temperature controller, thermocouple Type K, resistive heater with EA-PS 8360-15 T dc supply
 - Bruker broad-band probe (Teflon, 150 K...350 K)
 - home-built high-temperature probe (RT...1250 K, see Fig. A.1)
- **MSL 400** spectrometer (Bruker)
Oxford cryomagnet (**9.4 T**)
 - Oxford ITC4 temperature controller, thermocouple Type K, resistive heater with EA-PS

8360-15 U dc supply

- Bruker broad-band probes (Teflon: 150 K...350 K, ceramic: 150 K...623 K)

- **Avance III** spectrometer (Bruker)

Bruker Ultrashield Plus cryomagnet (**14.1 T**)

- Bruker BVT temperature unit

- Bruker 2.5 mm MAS probe (35 kHz) probe (213 K...343 K)

- Bruker broad-band probe (Teflon, 150 K...350 K)

- for SFG: ceramic broad-band probe from MSL 400, temperature equipment from MSL 400

- **Avance III** spectrometer (Bruker), at MEET, University of Münster

Bruker Ultrashield Plus cryomagnet (**4.7 T**)

- Bruker BVT temperature unit - Bruker Diff 30 PFG probe

A.1.3 Miscellaneous

- XRD: Bruker D8 Advance x-ray diffractometer (Cu K_{α} radiation at 40 kV and 40 mA)

- IR: Tensor 27 (Bruker)

- planetary mill P7 premium line, ZrO₂ vial set, 140 balls of 5mm diameter (Fritsch)

- muffle oven Typ LM 412 (Linn High Therm)

- Au evaporator (Edwards 306)

- pellet pressing set, press (P-O-Weber)

- quartz tubes, borate glass tubes for NMR measurements

- Ar-filled glove box (Braun)

A.2 Pulse sequences

- **single pulse** $90^\circ_{\phi_1} - FID_{\phi_2}$
 ϕ_1 : 0213
 ϕ_2 : 0213

- **spin-lock** $90^\circ_{\phi_1} - \text{lockingpulse}_{\phi_2} - FID_{\phi_3}$
 ϕ_1 : 02
 ϕ_2 : 13
 ϕ_3 : 02

- **echo** $90^\circ_{\phi_1} - \Phi_{\phi_2} - \text{echo}_{\phi_3}$
Hahn echo ($\Phi = 180^\circ$):
 ϕ_1 : 0022
 ϕ_2 : 1313
 ϕ_2 : 0022
solid echo ($\Phi = 64^\circ$):
 ϕ_1 : 03210321
 ϕ_2 : 32101032
 ϕ_3 : 32103210
quadrupolar echo ($\Phi = 64^\circ$):
 ϕ_1 : 01010101
 ϕ_2 : 11223300
 ϕ_2 : 02310231

- **stimulated echo** $90^\circ_{\phi_1} - \Phi_{\phi_2} - \Phi_{\phi_3} - \text{echo}_{\phi_4}$
NOESY, used for 2D exchange ($\Phi = 90^\circ$):
 ϕ_1 : 0202020202020202
 ϕ_2 : 0000000022222222
 ϕ_3 : 0022113300221133
 ϕ_4 : 0220133120023113
spin-alignment echo (SAE) for $I = 3/2$ ($\Phi = 45^\circ$):
 ϕ_1 : 02021313020213130202131302021313
 ϕ_2 : 1133002211330022113300221133002211330022
 ϕ_3 : 00000000111111112222222233333333
 ϕ_4 : 20020220311313310220200213313113
stimulated echo used in SFG/PFG NMR ($\Phi = 90^\circ$):
 ϕ_1 : 0000222211113333
 ϕ_2 : 1302130213021302
 ϕ_3 : 1302130213021302
 ϕ_4 : 0022220033111133

$$0 = X, 1 = Y, 2 = -X, 3 = -Y$$

A.3 Software

- LaTeX, MIKTEX, TeXnicCenter, JabRef, and the template of “DissOnlineTutor” (DFG-project, HU Berlin, Deutsche Nationalbibliothek)
- Igor Pro 6.22 A (wavemetrics)
- HATARI (V. Epp, TU Graz, program for Igor)
- Corel Draw X3
- WinSolids (Dr. Eichele, Universität Tübingen)
- TopSpin 3.0 (Bruker BioSpin)
- WinDeta (Novocontrol)
- Office 7 (Microsoft)
- EC-Lab demo (Bio-Logic Science Instruments)
- LabView 6.0 student version
- 1DWinNMR (Bruker BioSpin)
- DMFit2007 [201]
- Diamond 3.2 (crystal impact)

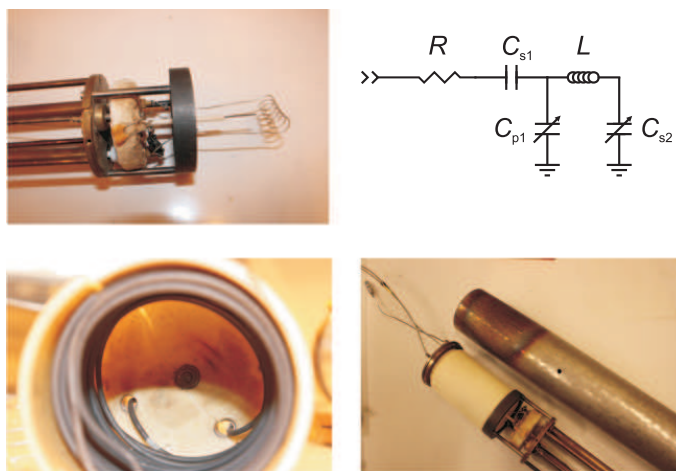


Figure A.1: Home-built high-temperature probe (cooperation project of B. Ruprecht and me). The preexisting but not functioning probe (originally built by W. Franke) was restored and improved. The probe was stabilized mechanically, the electrical circuiting was completely replaced, and the thermal isolation of the passive elements (glimmer capacitor, carbon resistors) was improved. Either an Ag-coated Cu coil (for temperatures below 1000 K) or a Pt coil (for temperatures up to 1300 K) were used. The photographs show anticlockwise: top section of probe head with NMR coil and circuit elements, bifilar heating coil inside alumina insulation, complete probe. The circuit of the probe is also shown. C_{s1} is a glimmer capacitor of 15 pF, R are 3-6 parallel non-magnetic carbon resistors of 3.3Ω , L is a coil with 6 turns and a diameter of 10 mm, C_{p1} and C_{s2} are tubular capacitors whose capacity can be adjusted (approx. in the range from 10-30 pF by inserting quartz tubes as dielectric medium). Like this, the probe is adjustable for 60-90 MHz. By adequately replacing L or C_x , the range can be extended easily. For much lower frequencies, the first series capacitor should be replaced by a parallel one.

Curriculum Vitae

Personal details

Name: Alexander Kuhn
Date of Birth: 16/04/1984
Place of Birth: Freiburg i. Br., Germany
Nationality: German

Employment

since 05/2012 Max Planck Institute for Solid State Research, Stuttgart/Germany

Education

2009-2012 PhD in the group of Prof. Dr. P. Heitjans, Institute of Physical Chemistry and Electrochemistry, Leibniz University Hannover/Germany. Topic: "Fundamental Studies on Li Dynamics in Materials Considered for Battery Applications"
2008 diploma degree in chemistry (1.0), Leibniz University of Hannover/Germany; diploma thesis: "Li diffusion in nanocrystalline and nanoglassy spodumene $\text{LiAlSi}_2\text{O}_6$ "
2005 first diploma (1.1), Eberhard-Karls-Universität Tübingen/Germany
2003 Abitur (1.0), Andreae-Gymnasium Herrenberg/Germany
2001-2003 Andreae-Gymnasium Herrenberg/Germany
1994-2001 Schickhardt-Gymnasium Herrenberg/Germany
1990-1994 Pfalzgraf-Rudolph-Grundschule Herrenberg/Germany

Teaching

2011 in charge of the "Physikalisch-Chemisches Praktikum I"
2008-2011 teaching in the "Physikalisch-Chemisches Praktikum I"
2009 complete revision of the script of the "Physikalisch-Chemisches Praktikum I"

Political Engagement

2011 elected member of the council of the Institute of Physical Chemistry, Leibniz University of Hannover/Germany.
2004-2005 elected member of the city parliament of Herrenberg/Germany. Deputy chairman of a parliamentary group.

Scholarships/Prices

2009-2012 scholarship of the German National Academic Foundation (Studienstiftung des

	deutschen Volkes e.V.)
2009	participation at the meeting of nobel laureates as young scientist
2008	price of the department of chemistry (Leibniz University of Hannover) for best diploma (donated by Honeywell)
since 2003	online scholarship of e-fellows.net
2003	participation at the meeting of nobel laureates as young scientist as prize for result in the third round of the national qualification of the Chemistry Olympics
2003	price of the federal state (Baden-Württemberg) for result in the Chemistry Olympics (second round of the national qualification)
1996/2000/2001	school prizes for various projects
1998/2002	music competition "Jugend musiziert" (violin), 2 nd /3 rd price, federal state level
2000	maths competition of the federal state (Baden-Württemberg), 1 st price

List of Publications - Alexander Kuhn

Articles

A. Düvel, A. Kuhn, L. Robben, M. Wilkening, P. Heitjans, "Mechanosynthesis of Solid Electrolytes for Lithium-Ion Batteries - Li^+ Transport Properties of Garnet-Type Al-Doped $\text{Li}_7\text{La}_3\text{Zr}_2\text{O}_{12}$ ", *J. Phys. Chem. C* **116** (2012) 15192.

A. Kuhn, J.-Y. Choi, L. Robben, F. Tietz, M. Wilkening, P. Heitjans, "Li ion dynamics in Al-doped garnet-type $\text{Li}_7\text{La}_3\text{Zr}_2\text{O}_{12}$ crystallizing with cubic symmetry" *Z. Phys. Chem.* **262** (2012) 525.

A. Kuhn, M. Kunze, P. Sreeraj, H.-D. Wiemhöfer, V. Thangadurai, M. Wilkening, P. Heitjans, "NMR relaxometry as a versatile tool to study Li ion dynamics in potential battery materials" *Solid State Nucl. Magn. Reson.* **42** (2012) 2.

A. Kuhn, V. Epp, G. Schmidt, S. Narayanan, V. Thangadurai, M. Wilkening, "Spin-Alignment Echo NMR: Probing Li^+ hopping motion in the solid electrolyte $\text{Li}_7\text{La}_3\text{Zr}_2\text{O}_{12}$ with garnet-type tetragonal structure" *J. Phys.: Condens. Matter* **24** (2012) 035901.

A. Kuhn, P. Sreeraj, R. Pöttgen, H.-D. Wiemhöfer, M. Wilkening, P. Heitjans, "Li NMR spectroscopy on crystalline $\text{Li}_{12}\text{Si}_7$: experimental evidence for aromaticity of the planar cyclopentadienyl-analogous Si_5^{6-} rings", *Angew. Chem. Int. Ed.* **50** (2011) 12099.

Henrik Buschmann, Janis Dölle, Stefan Berendts, Alexander Kuhn, Patrick Bottke, Martin Wilkening, Paul Heitjans, Anatoliy Senyshyn, Helmut Ehrenberg, Andriy Lottnyk, Viola Duppel, Lorenz Kienle, Jürgen Janek, "Structure and dynamics of the fast lithium ion conductor " $\text{Li}_7\text{La}_3\text{Zr}_2\text{O}_{12}$ ", *Phys. Chem. Chem. Phys.* **13** (2011) 19378.

A. Kuhn, P. Sreeraj, R. Pöttgen, H.-D. Wiemhöfer, M. Wilkening, P. Heitjans, "Li Ion Diffusion in the Anode Material $\text{Li}_{12}\text{Si}_7$: Ultrafast Quasi-1D Diffusion and Two Distinct Fast 3D Jump Processes Separately Revealed by ^7Li NMR Relaxometry", *J. Amer. Chem. Soc.* **133** (2011) 11018.

A. Kuhn, S. Narayanan, L. Spencer, G. Goward, V. Thangadurai, M. Wilkening, "Li self-diffusion in garnet-type $\text{Li}_7\text{La}_3\text{Zr}_2\text{O}_{12}$ as probed directly by diffusion-induced ^7Li spin-lattice relaxation NMR spectroscopy", *Phys. Rev. B* **83** (2011) 094302.

A. Kuhn, P. Heitjans, "Slow Li Exchange in a Li_3N Single Crystal Measured by $^{6,7}\text{Li}$ NMR Selective Quadrupole Satellite Inversion", *Diffusion Fundamentals* **12** (2010) 97 (extended abstract).

K. Efimov, T. Halfer, A. Kuhn, P. Heitjans, J. Caro, A. Feldhoff, "Novel cobalt-free oxygen-permeable perovskite-type membrane", *Chem. Mater.* **22** (2010) 1540.

A. Kuhn, E. Tobschall, P. Heitjans, "Li ion diffusion in nanocrystalline and nanoglassy $\text{LiAlSi}_2\text{O}_6$ and LiBO_2 - structure-dynamics relations in two glass forming compounds", *Z. Phys. Chem.* **223** (2009) 1359.

A. Kuhn, M. Wilkening, P. Heitjans, "Mechanically induced decrease of the Li conductivity in an aluminosilicate glass", *Solid State Ionics* **180** (2009) 302.

M. Wilkening, A. Kuhn, P. Heitjans, "Atomic-scale measurement of ultraslow Li motions in glassy $\text{LiAlSi}_2\text{O}_6$ by two-time ^6Li spin-alignment echo NMR correlation spectroscopy", *Phys. Rev. B* **78** (2008) 054303.

Oral Presentations at Conferences

A. Düvel, A. Kuhn, M. Wilkening, P. Heitjans, "Mechanosynthesis and Li^+ Dynamics of Al-doped $\text{Li}_7\text{La}_3\text{Zr}_2\text{O}_{12}$ ", *111. Jahrestagung der Bunsengesellschaft*, 2012, Leipzig.

A. Kuhn, P. Sreeraj, H.-D. Wiemhöfer, M. Wilkening, P. Heitjans, "Three distinct Li diffusion processes in $\text{Li}_{12}\text{Si}_7$: ultrafast 1D diffusion and two different fast 3D diffusion processes revealed separately by ^7Li NMR relaxometry", *18th International Conference on Solid State Ionics (SSI 18)*, 2011, Warszawa.

A. Kuhn, G. Goward, V. Thangadurai, M. Wilkening, "Li diffusion in garnet-type $\text{Li}_7\text{La}_3\text{Zr}_2\text{O}_{12}$ crystallizing with tetragonal symmetry at room temperature - ^7Li NMR study", *18th International Conference on Solid State Ionics (SSI 18)*, 2011, Warszawa.

A. Kuhn, P. Sreeraj, H.-D. Wiemhöfer, P. Heitjans, "Li ion diffusion in $\text{Li}_{12}\text{Si}_7$ - ultrafast 1D diffusion and two different fast 3D diffusion processes revealed separately by ^7Li NMR relaxometry", *110. Jahrestagung der Bunsengesellschaft*, 2011, Berlin.

A. Kuhn, M. Wilkening, "Li dynamics in tetragonal $\text{Li}_7\text{La}_3\text{Zr}_2\text{O}_{12}$ - application-oriented challenges meet fundamental research probed directly by diffusion-induced ^7Li spin-lattice relaxation NMR spectroscopy", *110. Jahrestagung der Bunsengesellschaft*, 2011, Berlin.

A. Kuhn, M. Wilkening, P. Heitjans, "Li diffusion in nanocrystalline and nanoglassy spodumene $\text{LiAlSi}_2\text{O}_6$ ", *DPG-Frühjahrstagung*, 2008, Berlin.

Poster Presentations at Conferences

Bunsentagung 2012 (Leipzig): "Insight into the Li ion dynamics in $\text{Li}_{12}\text{Si}_7$: Combining PFG NMR, 1D/2D MAS NMR, and NMR relaxometry"

Bunsentagung 2012 (Leipzig): "Li diffusion in anodic titania nanotubes probed by ^7Li NMR spectroscopy"

Bunsenkolloquium 2011 (Hannover): "From NCL-type caged dynamics to long-range transport: Li dynamics in $\text{Li}_3\text{PO}_4:\text{Li}_4\text{SiO}_4$ (ss) as probed by ^6Li , ^7Li , and ^{31}P NMR relaxometry and impedance spectroscopy"

Bunsenkolloquium 2011 (Hannover): “Li diffusivity in garnet-type $\text{Li}_7\text{La}_3\text{Zr}_2\text{O}_{12}$ (LLZ) with cubic and tetragonal symmetry”

Bunsenkolloquium 2011 (Goslar): “The determination of Li self-diffusion coefficients of the solid electrolyte $\text{Li}_3\text{PO}_4:\text{Li}_4\text{SiO}_4$ (ss) using ^7Li and ^{31}P relaxometry”

Bunsenkolloquium 2011 (Goslar): “Ceramic solid electrolytes: Li dynamics in $\text{Li}_7\text{La}_3\text{Zr}_2\text{O}_{12}$ ”

Bunsentagung 2010 (Bielefeld): “Slow Li exchange in Li_3N measured by SQSI-NMR”

Bunsenkolloquium 2009 (Hannover): “Slow Li exchange in Li_3N measured by SQSI-NMR”

Bunsentagung 2008 (Saarbrücken): “Li diffusion in nanoglassy and nanocrystalline $\text{LiAlSi}_2\text{O}_6$ ”

Acknowledgment

I would like to express my deepest gratitude to my family, friends, colleagues, supervisors, cooperation partners, and the Studienstiftung des deutschen Volkes e.V. for their indispensable support. First of all, I would like to thank Prof. Dr. P. Heitjans and Prof. Dr. M. Wilkening for their active support during the last years and for the unique opportunity to profit from a free and open research atmosphere.

Additionally, I am very grateful to Prof. Dr. J. Caro for his support.

I am thankful for many scientific discussions with Benjamin Ruprecht which in many cases led to a deeper understanding.

Thanks to Viktor Epp, not only for programming the HATARI software but also for being helpful to everybody.

Thanks to Andre Düvel for spending many weekends in the lab with me and for the fruitful cooperation.

Thanks to the rest of the group.

Thanks to the groups of Prof. Dr. J. Caro (especially Dr. K. Efimov), Prof. Dr. P. Behrens, Prof. Dr. M. Binnewies, and Prof. Dr. C. Vogt for helping out with XRD, IR, ICP-OES, and μ -RFA.

Thanks to Prof. Dr. O. Kanert, Prof. Dr. K. Funke, and Prof. Dr. W. Dieterich for valuable discussions.

I am indebted to our cooperation partners without whom this work would not have been possible:

- Dr. P. Sreeraj, Prof. Dr. H.-D. Wiemhöfer, Prof. Dr. R. Pöttgen (preparation of the silicide samples)
- S. Narayanan, Prof. Dr. V. Thangadurai (preparation of tetragonal LLZ)
- L. Spencer, Prof. Dr. G. Goward (high-resolution NMR of tetragonal LLZ at 21 T)
- S.-Y. Choi, Dr. F. Tietz (preparation of various LLZ samples, discussions)
- H. Buschmann, J. Reinacher, Dr. S. Berendts, Prof. Dr. J. Janek (preparation of cubic LLZ, discussions)
- Dr. M. Kunze, Prof. Dr. S. Passerini, Prof. Dr. M. Winter (PFG-NMR measurements)
- Prof. Dr. D. Freude (MAS-PFG-NMR measurements)
- Dr. L. Robben (XRD, Rietveld analyses)
- A. Düvel (mechanosynthesis of LLZ)

Thanks for not only financial support by the Studienstiftung des deutschen Volkes e.V. for my PhD scholarship.

Thanks to my mother, my father, my brothers and sisters, and to my grandmother - for everything. Thanks to Luis for support during writing this thesis and for a beautiful time. Thanks to my WG and my friends in Hannover and elsewhere for the time we spent together during the last years.